

Ultrafast Dynamic Ellipsometry of Laser Driven Shock Waves

by

Cynthia Anne Bolme

B.S., Chemistry
University of California--San Diego, 2002

Submitted to the Department of Chemistry
In partial fulfillment of the requirements for the degree of

Doctor of Philosophy in Physical Chemistry

at the

Massachusetts Institute of Technology
September 2008

© 2008 Cynthia Anne Bolme. All rights reserved.

The author hereby grants to MIT permission to reproduce and distribute publicly paper
and electronic copies of this thesis document in whole or in part in any medium now
known or hereafter created.

Signature of Author _____
Department of Physical Chemistry
August 12, 2008

Certified by _____
Keith A. Nelson
Professor of Chemistry
Thesis Supervisor

Accepted by _____
Robert W. Field
Chairman, Departmental Committee on Graduate Studies

This doctoral thesis has been examined by a committee of the Department of Chemistry as follows:

Professor Jainshu Cao _____
Chairman

Professor Keith A. Nelson _____
Thesis Supervisor

Professor Andrei Tokmakoff _____

Ultrafast Dynamic Ellipsometry of Laser Driven Shock Waves

by

Cynthia Anne Bolme

Submitted to the Department of Chemistry on August 12, 2008
in partial fulfillment of the requirements for the degree of
Doctor of Philosophy at the Massachusetts Institute of Technology

Abstract

The experimental measurement technique of ultrafast dynamic ellipsometry (UDE) was developed for measuring material motion and changes in optical properties of samples under laser driven shock loading. Ultrafast dynamic ellipsometry, a technique based on space-shifted spectral interferometry, uses the time-dependent frequency of a chirped laser pulse to provide time encoding, allowing the picosecond probing of material dynamics in a single shot. With this technique, the sample is probed at two different incident angles with both s- and p-polarized light, which measures the motion of the material and any change in its complex refractive index. Ultrafast dynamic ellipsometry was first used to ascertain the Hugoniot and the shocked refractive indices of thin polymer films of polycarbonate, poly(methyl methacrylate) (PMMA), poly(chlorotrifluoroethylene-co-vinylidene fluoride) (Kel-F 800), and polydimethylsiloxane (Sylgard 184). Next, UDE was used to measure the Hugoniots of liquid samples over a range of nearly one-dimensional stresses in a single laser shot by capitalizing on the spatial energy distribution of the shock generating laser beam. Using the spatially resolved UDE data, the Hugoniots and shocked refractive indices of cyclohexane, toluene, methanol, and water were measured, each in a single laser shot. Two additional liquids, nitromethane and carbon disulfide, were also investigated with UDE, and both liquids showed evidence of chemical reaction in the first 200 ps after the arrival of the shock wave. Ultrafast dynamic ellipsometry was used in conjunction with high-speed schlieren imaging to determine the nature of the insult provided by ablation of a thin titanium film in optical detonators. We found that the titanium ablates in fragmented sections, which impact the explosive material to initiate the optical detonators. Finally, UDE was applied to the study of metallic phase transitions. The change in the complex refractive index of crystalline silicon was measured during ultrafast laser induced melting. The fabrication of thin metal films of iron and cerium is described, and preliminary UDE data were recorded in an attempt to probe the α - ϵ phase transformation in iron and the γ - α transformation in cerium.

Thesis Supervisor: Keith A. Nelson
Title: Professor of Chemistry

Acknowledgments

I cannot even begin to properly express my gratitude to the countless people who have helped me during this journey that is called graduate school. First, I would like to thank Dave Funk and David Moore, my advisors at Los Alamos National Laboratory (LANL). Through these years, Dave Funk has continuously guided and encouraged me, both scientifically and professionally, and I hope that he is proud of the work I have done and the scientist I am become. Herr Moore imparted to me his inexhaustible enthusiasm, creativity, wisdom, experience, and humility, and his infectious optimism has inspired me when I have needed it most. I can't imagine where I would be without the encouragement, support, and scientific guidance bestowed on me by these two extraordinary men. I would also like to thank Shawn McGrane, who has spent much time in the lab with me, assisting me with the many aspects of laser driven shock waves and helping me develop ultrafast dynamic ellipsometry. Shawn is an exceptional example of a scientist who sees no obstacles, only opportunities for further areas of investigation. I hope that I have inherited some of his passion for pure science and that I can show the same intellectual endurance despite how "sub-optimal" the situation. Additionally, I wish to thank my MIT advisor Keith Nelson for his support, understanding, and flexibility. It is his support that has allowed me to learn and grow. I once heard that one should be careful when choosing advisors because the student often takes on the same characteristics as his advisor. I have been incredibly lucky to have so many exceptional advisors, and I would consider myself truly blessed to have inherited some of their characteristics.

I must thank my first scientific mentor Steve Son and his playful enthusiasm that first started my love for science, and Prof. John C. Wheeler who first introduced me to physical chemistry and strongly influenced my decision to join the field. I would also like to thank Thomas Feurer who helped me during my first foray into a laser lab, Von Whitley who performed the CTH calculations in support of the single shot Hugoniot work, Chad Meserole who made the Cr and Au samples for the study of the shock rise times, and Steve Clarke, Adrian Akinci, and Mike Murphy, with whom the schlieren and detonator studies were performed. Frank Archuleta has provided invaluable support to me, both with his exceptional machining skills and his patience in working with my vacuum bell jar system. I express my gratitude to Dana Dattelbaum for imparting to me some of her vast knowledge of polymers and for providing me with the Kel-F, to Andrew Dattelbaum for assisting me with spectroscopic ellipsometry at LANL's Center for Integrated Nanotechnologies (CINT), to Darrick Williams for helping me with the x-ray diffraction at CINT, and to Rob Dickerson for the orientation imaging microscopy. Jim Glowia is the principle investigator for the research through which most of this work was funded and also a man of infinite ideas. I wish to thank all of the members of the Shock and Detonation Physics group at LANL who have supported me during this work and from whom I have learned so much and the members of the Nelson group at MIT who have provided encouragement and friendship. Of course, I must specifically mention the folks with whom I have worked closely: Andrew Grieco, Dan Eakins, Jason Scharff, Margo Greenfield, Jay Quenneville, Dean Preston, Gagan Saini, and Steve Kooi.

Finally, I want to thank my family. It is only with your eternal and unwavering support that I have accomplished this. I am at a loss for how I can express the depth of my gratitude. All I can say is this: Thank you.

Table of Contents

Abstract.....	5
Acknowledgments.....	7
1. Introduction.....	13
2. Laser and Shock Generation	
2.1. Laser system.....	19
2.2. Shock generation.....	24
3. Shock Rise Times in Layered Metal Films	
3.1. Introduction.....	31
3.2. Experiment.....	32
3.3. Results.....	36
3.3.1. Data Analysis	
3.3.2. Chirped drive pulse	
3.3.3 fs drive pulse	
3.4. Discussion.....	48
4. Ultrafast Dynamic Ellipsometry (UDE)	
4.1. Introduction.....	52
4.2. Ultrafast dynamic ellipsometry interferometric probe.....	55
4.3 Analysis of the interferograms	59
4.4 Benefits of a single shot diagnostic	63
5. UDE of polymers	
5.1. Introduction.....	68
5.2. Thin film model and fitting routine for transparent materials.....	69
5.3. Dependence of data on experimental parameters.....	76
5.3.1. Calculation method	
5.3.2. Simulated data with various thicknesses	
5.3.3. Simulated data with various pressures	
5.3.4. Simulated data with various initial refractive indices	
5.4. Polycarbonate.....	96
5.5. Poly(methyl methacrylate) (PMMA)	105
5.6. Poly(chlorotrifluoroethylene- <i>co</i> -vinylidene fluoride) (Kel-F 800).....	108
5.7. Polydimethylsiloxane (Sylgard 184)	115
5.8. Conclusions.....	120

6.	UDE of deposited dielectrics	
6.1.	Introduction.....	122
6.2.	Window deposition.....	123
6.3.	Fused silica.....	124
6.4.	Aluminum oxide.....	125
6.5.	Discussion.....	126
6.6.	Conclusions.....	128
7.	Single Shot Hugoniot Using a Spatially Shaped Pressure Wave	
7.1.	Introduction.....	130
7.2.	CTH hydrocode simulation.....	131
7.3.	Single shot Hugoniot data of liquids.....	134
	7.3.1. Experiment	
	7.3.2. Cyclohexane	
	7.3.3. Toluene	
	7.3.4. Methanol	
	7.3.5. Water	
7.4.	Single shot Hugoniot data of a polycarbonate thin film.....	147
7.5.	Discussion.....	150
8.	Hugoniot Measurements of Reactive Liquids	
8.1.	Introduction.....	155
8.2.	Nitromethane.....	156
	8.2.1. Introduction	
	8.2.2. Experiment	
	8.2.3. Results	
	8.2.4. Discussion	
8.3.	Carbon disulfide.....	168
	8.3.1. Introduction	
	8.3.2. Experiment	
	8.3.3. Results	
	8.3.4. Discussion	
8.4.	Conclusions.....	176
9.	Laser Ablation of Titanium	
9.1.	Introduction.....	180
9.2.	Schlieren.....	181
	9.2.1. Introduction	
	9.2.2. Experiment	
	9.2.3. Schlieren results	
9.3.	Laser ablation with ultrafast dynamic ellipsometry.....	192
	9.3.1. Introduction	
	9.3.2. Spectroscopic ellipsometry of Ti films	
	9.3.3. Experiment	
	9.3.4. Ultrafast dynamic ellipsometry results	

9.4.	Conclusion.....	204
10.	Metallic Phase Transition	
10.1.	Introduction.....	207
10.2.	Ultrafast laser induced melting of silicon.....	208
	10.2.1. Introduction	
	10.2.2. Experiment	
	10.2.3. Results	
	10.2.4. Discussion	
10.3.	Iron and cerium metal films.....	216
	10.3.1. Fabrication of metal films	
	10.3.2. Preliminary UDE data	
10.4.	Discussion.....	223

Chapter 1

Introduction

Traditionally, shock waves have been created with gas guns, which launch projectiles into targets, and with high explosives, which use the chemical energy from the explosives to push impactors into samples. Both of these methods use macroscopic samples and are controlled with electrical timing systems, which limits the time resolution of the diagnostics that are usually used to probe the samples.

The continual improvements in molecular dynamics and electronic structure calculations coupled with increasing computational speed have allowed calculations of materials under shock loading. The difference in temporal and spatial resolution between the calculations and the experimental data from traditional shock techniques has made evident a void in experimental techniques. This thesis describes an effort toward filling that void with the development of an experimental method, ultrafast dynamic ellipsometry (UDE), that provides data concerning the optical properties and material motion of laser shocked materials with picosecond time resolution and micron spatial resolution. The data that UDE provides can be used to validate computational results and to refine empirical potentials. By probing optical properties at 800 nm, UDE is sensitive to changes in the electronic structure of the materials, which can be especially insightful when investigating chemical reactions or phase transitions.

The intense study of acoustics in the 1800s naturally led to the basic principles of shock waves, which were derived separately by W. J. M. Rankine and P. H. Hugoniot. The Rankine-Hugoniot equation (hereafter, called the Hugoniot equation) is the equation that describes the change in the thermodynamic properties of shocked materials and is derived from the conservation of mass, momentum, and energy across the shock boundary. The principle Hugoniot for a material is the locus of all final states achieved from compression by a single shock wave. Using the measurement of the velocity of the shock front, u_s , and the measurement of the velocity of the material behind the shock front (particle velocity), u_p , the pressure and volume of the material are given by Eqs. (1.1) and (1.2):

$$\frac{\Delta V}{V} = 1 - \frac{u_p}{u_s}, \quad (1.1)$$

where ΔV is the change in volume and V is the initial volume.

$$P = P_0 + \rho_0 u_s u_p, \quad (1.2)$$

where P is the pressure, P_0 is the initial pressure, and ρ_0 is the initial density. In this thesis, the Hugoniot will be provided as the relationship between the shock and particle velocities.

This thesis builds off of previous work done at Los Alamos National Laboratory with laser driven shock waves. The principle scientists who performed the previous work were D. S. Moore, D. J. Funk, and S. D. McGrane, all of who were intimately involved with the work presented here. With co-workers, these gentlemen developed a technique to create sustained shock waves for several hundred ps by frustrated laser ablation using a spectrally shaped, chirped, ultrafast laser pulse,¹ which will be described in more detail in

Chapter 2. They also measured the shock wave rise times in thin metal films with Gahagan using ultrafast interferometric microscopy.^{2,3} A series of experiments with a similar interferometric diagnostic that investigated the shock wave rise times in layered thin metal films is described in Chapter 3. Additionally, the same group at Los Alamos initiated the experiments using multiple angles and both polarizations of light to measure the optical properties and motion of shocked aluminum⁴ and poly(methyl methacrylate).⁵ It is significant advances on this technique and the resulting data on many different materials that form the basis of this thesis.

Chapter 2 provides an introduction to the experimental technique with a detailed description of the laser system used for the experiments and an explanation of the method of shock generation using frustrated laser ablation of thin metal films.

Chapter 3 describes a series of experiments to measure the shock wave rise times in layered thin metal films of chromium and gold with ultrafast interferometric microscopy.

Chapter 4 presents the technique of ultrafast dynamic ellipsometry (UDE) that was used for the rest of the experiments in this thesis. Ultrafast dynamic ellipsometry probes the time dependent evolution of both the material motion and the optical properties of the shocked sample in a single laser shot.

In Chapter 5, UDE is applied to thin polymer films fabricated by spin casting. The analysis of the data from the transparent films is described and the influence of the physical properties of film thickness, shock pressure, and initial film refractive index on the UDE data is calculated. The Hugoniot data and shocked refractive indices as measured with UDE for polycarbonate, poly(methyl methacrylate) (PMMA),

poly(chlorotrifluoroethylene-*co*-vinylidene fluoride) (Kel-F 800), and polydimethylsiloxane (Sylgard 184) are presented.

In Chapter 6, the fabrication of and UDE data for electron beam deposited films of fused silica and alumina are described. These two materials are of interest as window materials for later studies of shock induced phase transformations in metals.

To create the shock waves, a laser pulse with a Gaussian spatial profile is used. Chapter 7 presents the concept of using the spatially resolved UDE data to measure a range of pressures across the Gaussian profile. Hydrodynamic simulations are provided that support the validity of this experiment, and Hugoniot and refractive index data measured with UDE are presented for 4 liquids: cyclohexane, toluene, methanol, and water.

In Chapter 8, UDE is applied to two materials that undergo shock-induced reaction: nitromethane and carbon disulfide. The UDE data from both of these materials provide information about the time scales on which these reactions occur and will contribute to better understanding of these reactions.

Chapter 9 describes a series of experiments investigating the underlying mechanism for initiation of an optical detonator. First, schlieren imaging with a fast framing camera is used to study the ablation of a thin titanium film and the shock wave that results from the ablation of an identical film into an explosive detonator. Then, UDE is applied to the laser ablation of the titanium in an effort to understand the nature of the insult provided by the titanium ablation to initiate the explosive pentaerythritol tetranitrate (PETN) in the detonator.

Finally, Chapter 10 presents the application of UDE to the ultrafast laser induced melting of silicon, which demonstrates its ability to detect metallic phase transitions. The fabrication and characterization of thin metal films of iron and cerium, two materials with interesting solid-solid phase transitions, is described, and some initial UDE data from the shocked iron and cerium are shown. This thesis concludes with a discussion of the next steps that should be taken to measure the kinetics of shock-induced metallic phase transformations.

References

- ¹ S. D. McGrane, D. S. Moore, D. J. Funk, and R. L. Rabie, "Spectrally modified chirped pulse generation of sustained shock waves," *Appl. Phys. Lett.* **80**, 3919-21 (2002).
- ² K. T. Gahagan, D. S. Moore, D. J. Funk, R. L. Rabie, S. J. Buelow, and J. W. Nicholson, "Measurement of shock wave rise times in metal thin films," *Phys. Rev. Lett.* **85**, 3205-8 (2000).
- ³ K. T. Gahagan, D. S. Moore, D. J. Funk, J. H. Reho, and R. L. Rabie, "Ultrafast interferometric microscopy for laser-driven shock wave characterization," *J. Appl. Phys.* **92**, 3679-82 (2002).
- ⁴ D. J. Funk, D. S. Moore, K. T. Gahagan, S. J. Buelow, J. H. Reho, G. L. Fisher, and R. L. Rabie, "Ultrafast measurement of the optical properties of aluminum during shock-wave breakout," *Phys. Rev. B* **64**, 115114-5 (2001).
- ⁵ S. D. McGrane, D. S. Moore, and D. J. Funk, "Sub-picosecond shock interferometry of transparent thin films," *J. Appl. Phys.* **93**, 5063-8 (2003).

Chapter 2

Laser System and Shock Generation

This chapter describes the laser used for the shock experiments and the method of shock generation using frustrated laser ablation via a chirped and spectrally shaped pulse.

2.1 Laser system

The laser system used for the shock experiments in this thesis was a commercially available Ti:sapphire chirped pulse amplification system, operating at a repetition rate of 10 Hz. The major components of the laser system and the pump lasers are shown in Fig. 2-1.

A Spectra-Physics Millennia V, composed of a solid state Nd:YVO₄ laser with a 3.5 - 4 W continuous wave output at 532 nm, pumped a KMLabs Chinook oscillator, with a typical output pulse duration of 35 fs running at a frequency of 86 MHz. A typical wavelength spectrum is shown in Fig. 2-2.

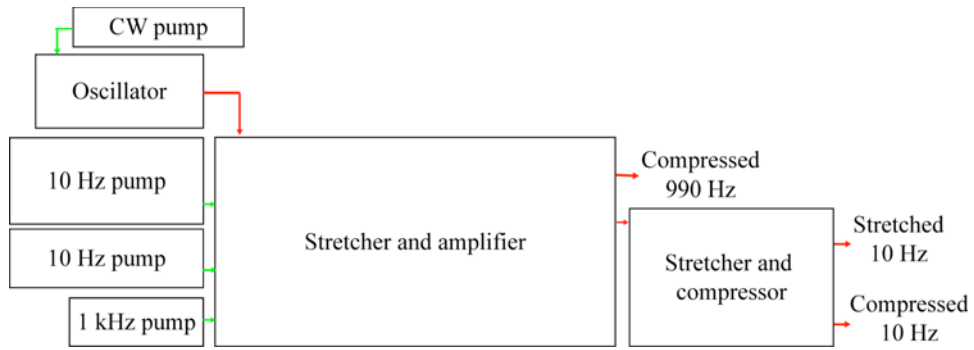


Fig. 2-1. Schematic of the laser system, showing the major components and pump lasers. A continuous wave laser pumped the oscillator, providing the seed for amplification. A 1 kHz laser pumped the regenerative amplifier, and two 10 Hz lasers pumped two multi-pass amplifiers. The 990 Hz beam was compressed after amplification, and the 10 Hz was split into portions that were stretched and compressed in an external stretcher/compressor.

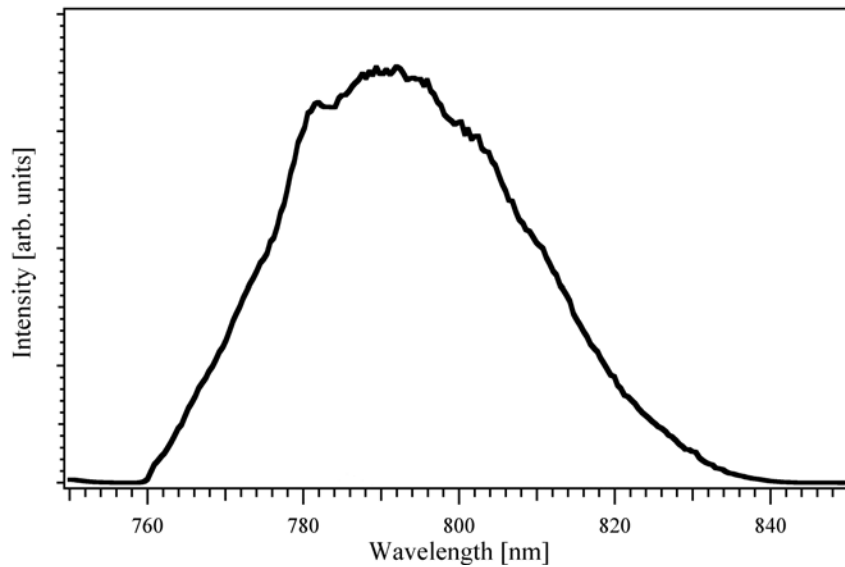


Fig. 2-2. A plot of intensity vs. wavelength for a typical spectrum from the KMLabs Chinook oscillator.

Chirped pulse amplification¹⁻³ of the Chinook output was performed with a Spectra-Physics TSA-50 that had been extensively modified. A schematic of the amplifier is shown in Fig. 2-3. In brief, the oscillator output pulse entered the amplifier

and was stretched using a grating stretcher to approximately 80 ps before undergoing amplification. The first stage of amplification operated at 1 kHz using a regenerative amplifier (regen), pumped with approximately 10 W output of a frequency-doubled Nd:YLF laser. The regen pump laser for the experiments discussed in Chapter 3 was a Spectra-Physics Merlin, which was replaced by a Coherent Evolution for the remainder of the experiments. The amplified output of the regen was typically 1.8 - 2.0 W, or 1.8 to 2 mJ/pulse.

After regenerative amplification, the 1 kHz beam was separated into a 990 Hz beam and a 10 Hz beam. To accomplish this separation, the polarization of the s-polarized 1 kHz beam was rotated by a half-wave plate and sent through a “double” pockels cell. The timing of the double pockels cell was controlled by a digital delay generator that was triggered by the timing of the pockels cells in the regen. The double pockels cell rotated the polarization of every hundredth pulse. The rotated pulse was reflected by a polarizing beamsplitter cube immediately after the double pockels cell and sent for further amplification. The remaining 990 Hz pulses that passed through the double pockels cell unchanged were rotated back to their original polarization by a half-wave plate and were sent to a compressor. The 990 Hz beam was then used for unrelated experiments. The 10 Hz beam was further amplified in two double-pass amplification stages. The first double-pass rod was pumped by approximately 250 mJ from a frequency-doubled Nd:YAG Spectra-Physics GCR-170. The second double-pass rod was pumped by approximately 350 mJ from a frequency-doubled Nd:YAG Spectra-Physics GCR-190. The maximum energy in the amplified 10 Hz beam was 35 mJ per pulse. A typical spectrum of the amplified 10 Hz beam is shown in Fig. 2-4.

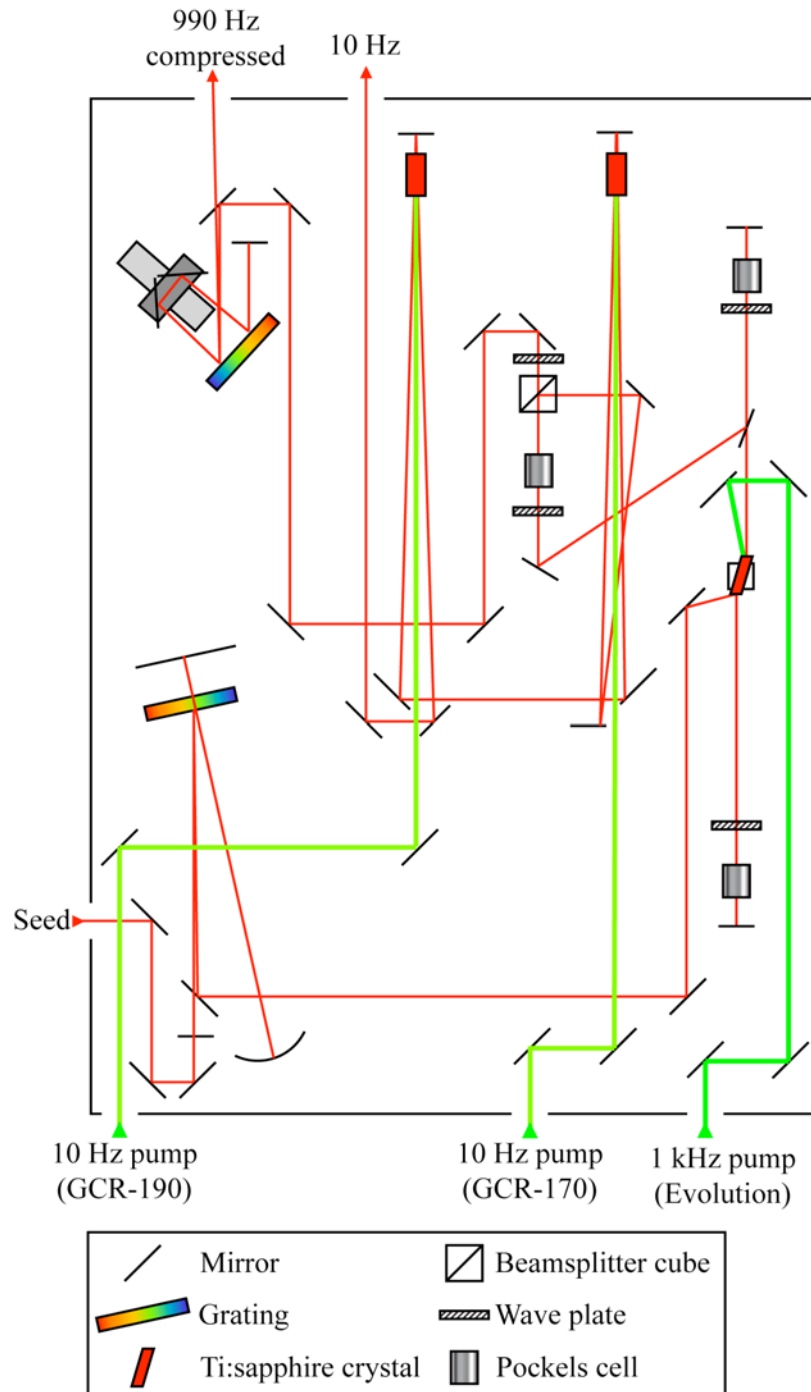


Fig. 2-3. Schematic of the Ti:sapphire amplification system. The seed pulse enters at the lower left, is stretched to eliminate the potential of damage from a high intensity pulse, is regeneratively amplified at 1 kHz to the mJ level and subsequently multi-pass amplified at 10 Hz to tens of mJ prior to a portion of the beam being recompressed to close to the original pulse width.

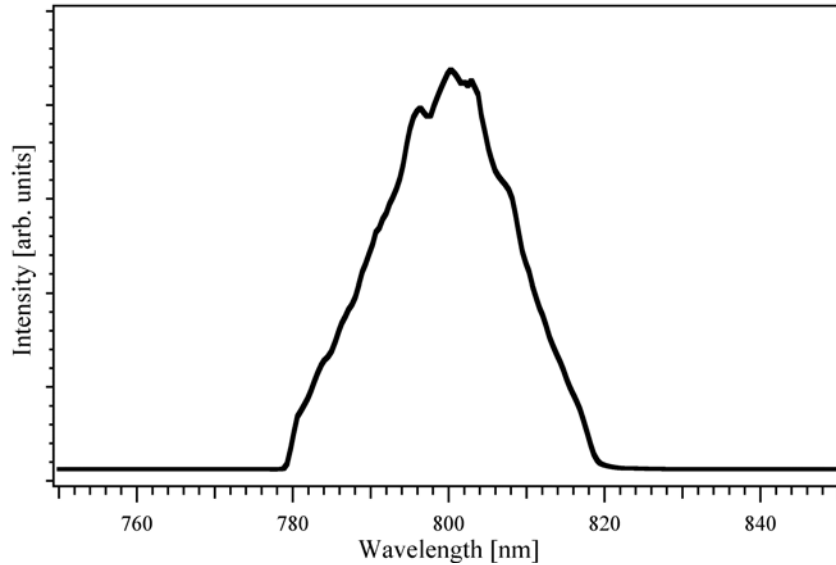


Fig. 2-4. Typical spectrum of the amplified 10 Hz beam.

After completing the amplification, an interferometer flat reflected 7% of the energy into a compressor. The output of the compressor was used as a time gated probe and for performing cross-correlation measurements, and the desired duration of the probe was varied according to its application. The width of the spectrum was adjusted in the compressor to obtain the desired bandwidth-limited pulse duration. Further details of the compressed pulse characteristics and uses will be presented in the relevant chapters.

The 93% remaining energy of the 10 Hz beam was directed into a grating-based stretcher. The pulses were further stretched and spectrally shaped for driving a supported shock wave. The details of the shaping and shock generation are presented in §2.2. A schematic of the 10 Hz stretcher and compressor is given in Fig. 2-5.

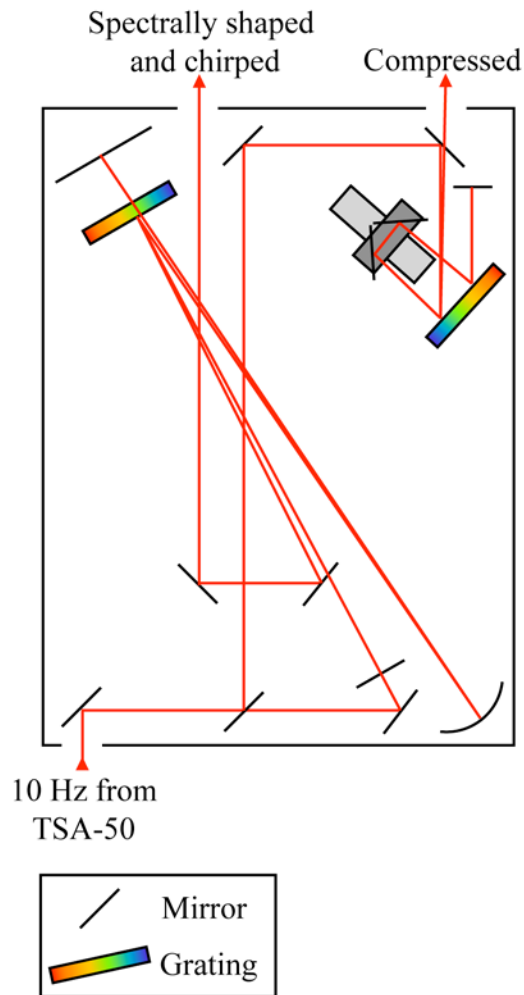


Fig. 2-5. Schematic of the 10 Hz post-amplification stretcher and compressor. The pulse enters the stretcher/compressor at the lower left from the amplifier shown in Fig. 2-3. Approximately 7% of the pulse is sent into the compressor, and the remainder is stretched and spectrally shaped.

2.2 Shock generation

For the shock experiments in this thesis, shock waves were generated in thin metal films using frustrated laser ablation. The samples for creating the shock waves consisted of thin metal films deposited on dielectric substrates, most commonly 2 μm of Al on 120 μm thick amorphous glass cover slips. Typically, the laser was focused

through the dielectric substrate on to the metal film, where the laser energy heated the electrons in the skin depth of the metal, and the hot electrons traveled ballistically through the cold metal lattice to approximately the electron-phonon coupling length of the metal. The thermal energy in the electrons was coupled into the metal lattice via electron-phonon interactions, heating the metal lattice, which expanded in response to the temperature jump to create the shock wave in the metal. The dielectric substrate acted as a tamper, preventing rapid expansion of the material back toward the incident laser pulse and forcing the expansion into the metal film. Sketches depicting these steps are shown in Fig. 2-6.

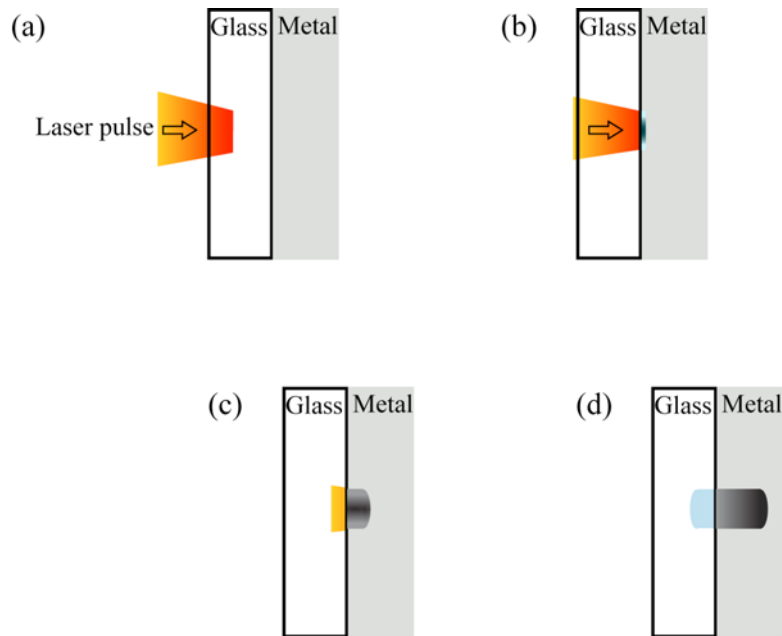


Fig. 2-6. Conceptual illustrations of frustrated laser ablation method of shock wave generation in thin metal films. (a) Laser pulse was focused through a dielectric substrate on to the metal film. (b) Laser energy was absorbed creating a hot electron gas. (c) The hot electron gas traveled through the material to the electron-phonon coupling length, where the energy was transferred from the electrons to the lattice. (d) The hot lattice expanded to generate a shock wave in the metal film (and in the dielectric substrate).

To create a shock wave that closely resembled the temporal shape of shock waves generated by the impact of a projectile, the intensity of the laser pulse was temporally shaped to yield a supported shock wave with a sharp (short rise time) shock front. To create the desired shape, a knife edge was inserted into the low-frequency (temporally-leading) side of the spectrum at the Fourier plane in the post-amplification stretcher. This spectral shaping of the chirped pulse translated into the shaping of the temporal intensity of the beam, by clipping a portion of the spectrum and yielding a shaped output with a sharp rise of ~ 5 ps, followed by a relatively constant intensity for >150 ps. A typical spectrum of the shaped laser pulse for shock generation is shown in Fig. 2-7.

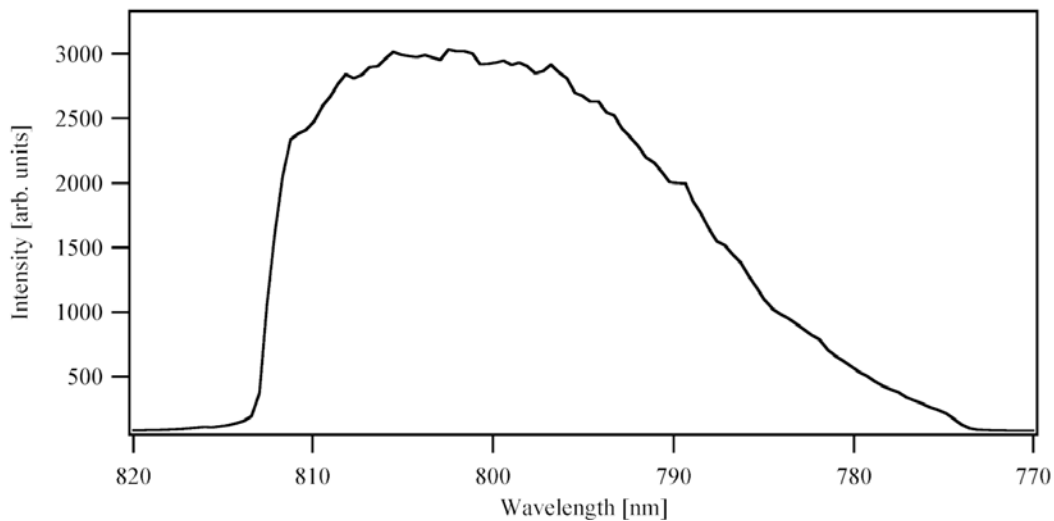


Fig. 2-7. Spectrum of the spectrally shaped and chirped laser pulse.

The time-dependent intensity of the pulse was measured using a cross-correlation frequency resolved optical gating (XFROG)⁴ method. The portion of the 10 Hz pulse that was compressed was spectrally narrowed to a FWHM bandwidth of 2.5 nm and compressed to approximately 400 fs. This compressed pulse was combined with the

chirped pulse in a 50 μm thick, Type I β -barium borate (BBO) crystal to generate the sum frequency of the two pulses. The spectrum of the resulting pulse was recorded while scanning the time delay between the two pulses. The resulting XFROG data provided a measurement of the time-dependent frequency of the shaped pulse. Typical XFROG data are shown in Fig. 2-8.

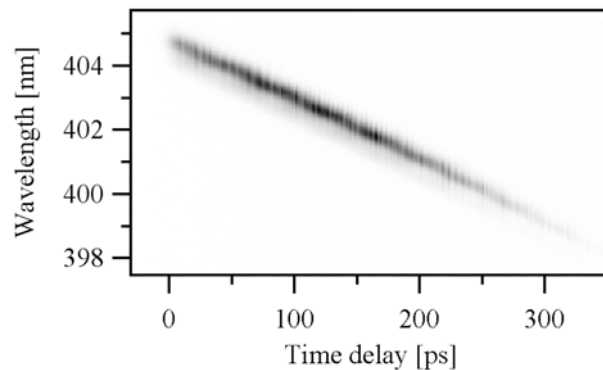


Fig. 2-8. XFROG trace of the spectrally shaped laser pulse used for shock generation as measured by the compressed pulse centered at 806.6 nm with 2.5 nm FWHM bandwidth.

The sharp increase in intensity at the beginning of the shock driving laser pulse created a short rise time shock wave in the material. The long duration of the laser pulse was required to generate a supported shock wave that could travel through several microns of material without being eroded by release waves from the laser heated expansion region. Figure 2-9 shows the interferometrically measured⁵ free surface position of a 250 nm thick Al film that was shocked using the chirped and temporally shaped pulse discussed above and contrasted with a shock generated by the compressed 120 fs long pulse. For the first several picoseconds, the free surface position of the material was the same using the two different pump pulses. This indicates that the

material limited the rise time of the shock, primarily through the electron-phonon coupling parameters yielding a rise time that was much longer (approximately 6 ps) than the 120 fs pulse. After the initial rise, the free surface of the Al pumped with the chirped pulse moved with an approximately constant velocity, while the motion of the Al surface pumped with the compressed pulse quickly decreased. The chirped pulse continued to provide energy to the Al film, which forced the continued expansion of the film. This resulted in a sustained pressure wave, similar to a pressure wave resulting from the impact of a projectile. The compressed pulse created a shock wave in the same way as the chirped pulse; however, since the laser did not continue to drive the shock wave, a release wave formed behind the shock. The release wave traveled faster than the shock wave through the material that was compressed from the shock wave and had a higher sound speed. The release wave overtook the shock wave, at which point the material stopped moving.

Further information about the spectral shaping for shock wave generation can be found in McGrane *et al.*,⁶ and additional information about the shock rise times in thin metal films can be found in Gahagan *et al.*⁷

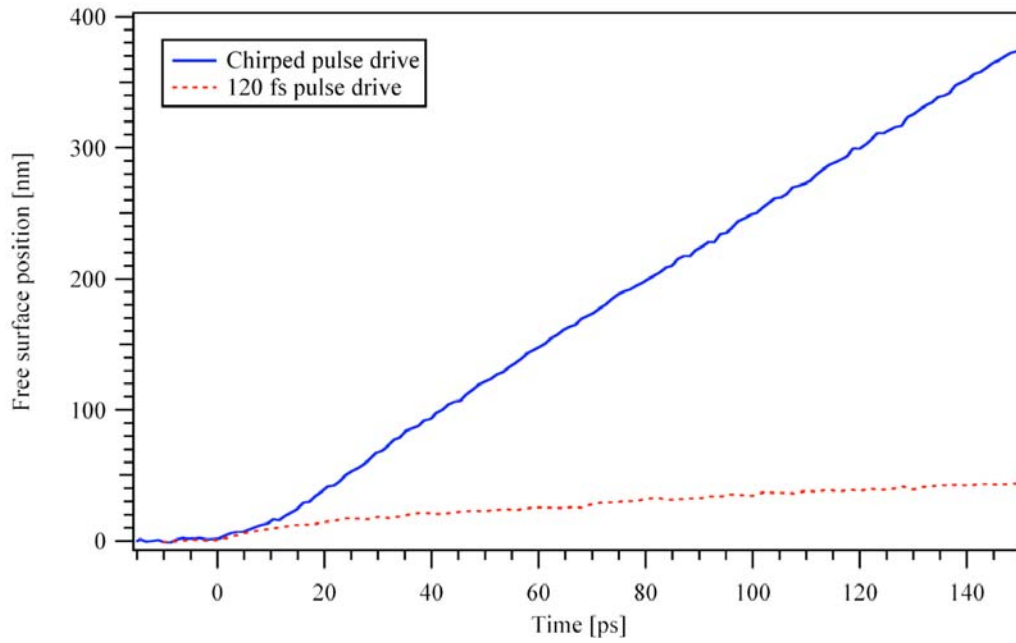


Fig. 2-9. Interferometrically determined free surface position versus time for shocks in a 250 nm thick bare Al film. Data courtesy of S. D. McGrane.

References

- ¹ D. Strickland and G. Mourou, "Compression of amplified chirped optical pulses," *Opt. Commun.* **56**, 219-221 (1985).
- ² M. Pessot, P. Maine, and G. Mourou, "1000 times expansion/compression of optical pulses for chirped pulse amplification," *Opt. Commun.* **62**, 419-21 (1987).
- ³ P. Maine and G. Mourou, "Amplification of 1-nsec pulses in Nd:glass followed by compression to 1 psec," *Opt. Lett.* **13**, 467-9 (1988).
- ⁴ S. Linden, H. Giessen, and J. Kuhl, "XFROG--a new method for amplitude and phase characterization of weak ultrashort pulses," *Phys. Status Solidi B* **206**, 119-24 (1998).
- ⁵ K. T. Gahagan, D. S. Moore, D. J. Funk, J. H. Reho, and R. L. Rabie, "Ultrafast interferometric microscopy for laser-driven shock wave characterization," *J. Appl. Phys.* **92**, 3679-82 (2002).
- ⁶ S. D. McGrane, D. S. Moore, D. J. Funk, and R. L. Rabie, "Spectrally modified chirped pulse generation of sustained shock waves," *Appl. Phys. Lett.* **80**, 3919-21 (2002).
- ⁷ K. T. Gahagan, D. S. Moore, D. J. Funk, R. L. Rabie, S. J. Buelow, and J. W. Nicholson, "Measurement of shock wave rise times in metal thin films," *Phys. Rev. Lett.* **85**, 3205-8 (2000).

Chapter 3

Shock Rise Time in Layered Metal Films

3.1 Introduction

The short temporal duration and high temporal resolution of laser driven shock waves, such as the 300 ps duration of the laser driven shocks described in the previous chapter, impose tight constraints on the sample dimensions and on the uniformity of the materials that are investigated. For studying chemistry that is initiated by a shock wave in an energetic material, it would be ideal to have a thin single crystal sample of the energetic material on a substrate that would convert the laser energy into a shock wave. Metals tend to be poor surfaces on which to grow organic crystals, but they often function well as laser driven shock drive layers. Therefore, one could imagine fabricating a sample by attaching a self-assembled monolayer (SAM) to a gold film¹⁻³ and growing the energetic crystal on the SAM. However, due to the weak electron-phonon coupling in gold (electron-phonon coupling constant, $g=2.1 \times 10^{16} \text{ Wm}^{-3}\text{K}^{-1}$),⁴ laser driven thin gold films produce ramp waves instead of shock waves.⁵ In an effort to find a more suitable substrate for energetic crystal studies, a series of experiments was performed to study the shock rise times of chromium and gold layered thin films, with the expectation that a shock could be generated in a chromium film and transferred mechanically to a gold film.

Ultrafast laser pulses of 180 fs have been used to drive shock waves in thin film

metal targets of aluminum and nickel on glass substrates.⁶ After shock runs of 0.25 to 1 μm , the time constants of the rise times in these vapor-plated films have been observed as approximately 2.5 ps. The rise times and shapes of the pressure pulses are determined by many factors, including the temporal shape of the laser pulse, optical skin depth, electron-phonon coupling parameters, heat conduction, and the viscosity of the material. Recently, graded density impactors have been developed for light gas guns, which can be used to tailor the resulting compression wave.^{7,8} For laser driven shocks, the same manipulation of the wave should be possible using the properties of the materials and the shape of the laser pulse itself.

For this study, we have created layered thin films of chromium and gold, and measured the rise times as a function of the thicknesses of the two layers. These materials were chosen with the notion that the strong electron-phonon coupling in chromium ($g=42 \times 10^{16} \text{ Wm}^{-3}\text{K}^{-1}$)⁹ would create a shock with a short rise time that could be carried through to the gold layer and propagate as a sharp shock wave in the gold.

3.2 Experiment

The laser used for these experiments is described in §2.1. The shocks were driven with either of two pulses, one of which was stretched to approximately 80 ps, chirped, and spectrally shaped to have a 10-90% rise time of <3 ps on the temporally-leading edge and the other compressed to 180 fs. Both pulses were focused onto the sample to create shock waves as described in §2.2. The XFROG¹⁰ trace of the spectrally shaped pulse used for driving the shocks is shown in Fig. 3-1.

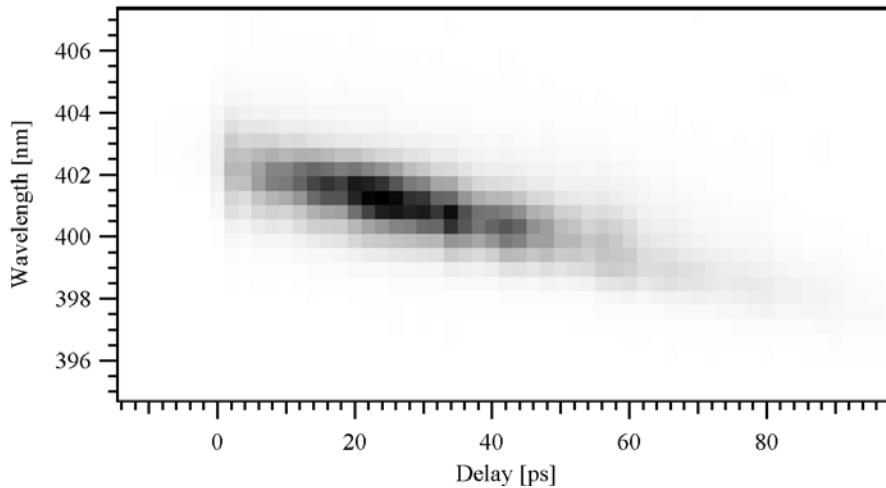


Fig. 3-1. XFROG trace of the spectrally shaped laser pulse used for shock generation as measured by a compressed pulse centered at 804.8 nm with 6.5 nm FWHM bandwidth.

The full bandwidth of the probe pulse did not permit the formation of interference fringes across the necessary area of the sample. To increase the coherence length of the probe pulse, the bandwidth of the probe was narrowed, increasing the pulse duration. To decrease the bandwidth while maintaining a Gaussian shaped pulse for better compression, two birefringent filters with thicknesses 5T and 6T were inserted into the beam at Brewster's angle before the compressor. A polarizer after the birefringent filters removed the wavelengths for which the polarization had been rotated, and knife edges in the compressor removed the intensity of the peaks away from the central wavelength. The resulting spectrum is shown in Fig. 3-2. This beam was compressed to 180 fs and was used as the pump pulse in the experiments with the fs drive. It was also used to probe the sample from the side opposite the pump beam with both the chirped drive and the fs drive.

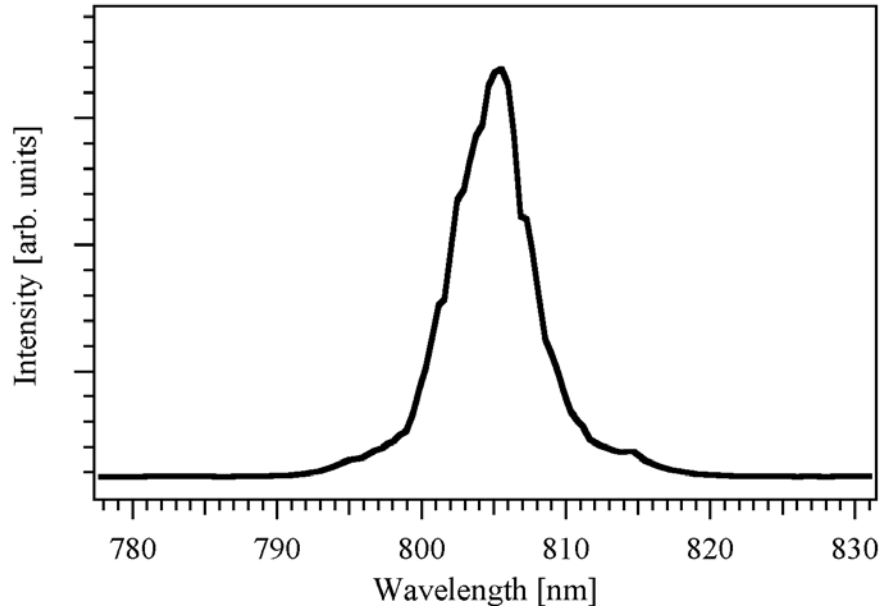


Fig. 3-2. Typical spectrum of the interferometric microscopy probe pulse that had been spectrally narrowed with 5T and 6T birefringent filters prior to compression.

Interferometric microscopy was used to measure the motion of the metal at the free surface. The compressed pulse shown above was variably delayed with respect to the pump pulse and was sent into a Mach-Zehnder interferometer that probed the free surface of the sample at 31° from normal. An experimental schematic is shown in Fig. 3-3. The two legs of the interferometer were recombined at a small angle on a charge-coupled-device camera, which recorded interferograms before, during, and after each event. Typical interferograms are shown in Fig. 3-4. Since the shock destroyed a portion of the material with each shot, the sample was rastered to a pristine area between each shot. A photo of one of the samples displaying the holes created by the laser driven shock is shown in Fig. 3-5.

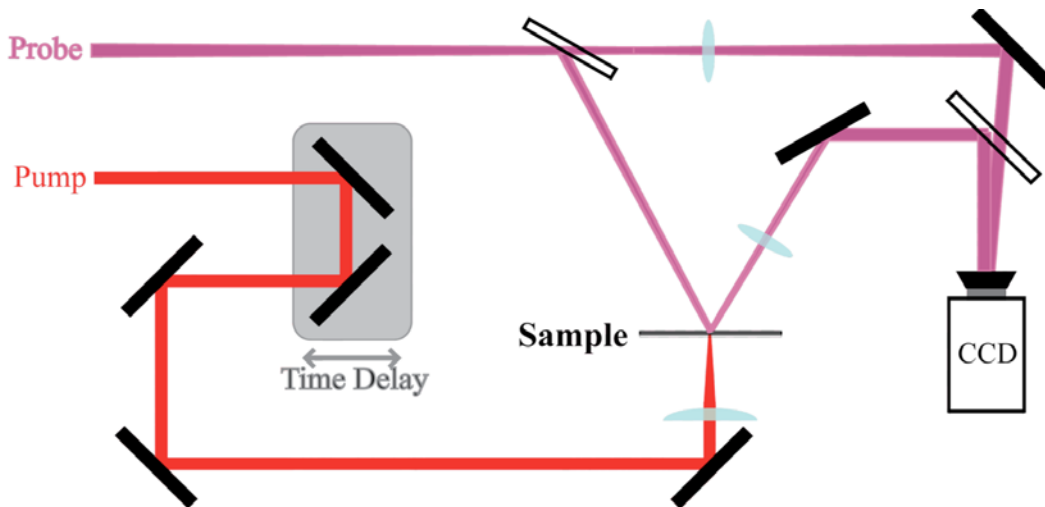


Fig. 3-3. Experimental schematic of the laser shock generation as probed using interferometric microscopy.

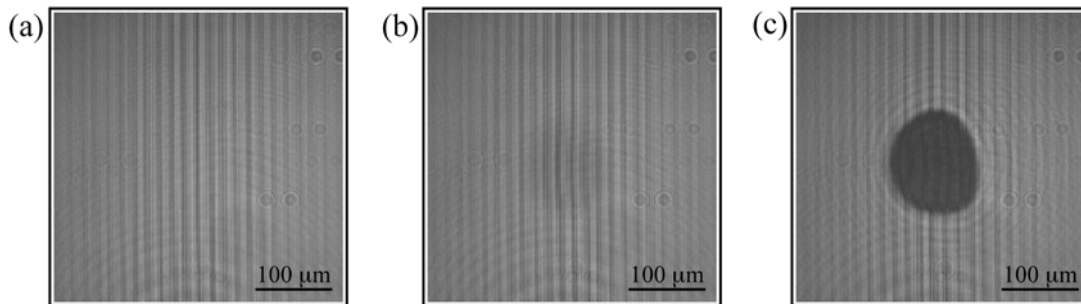


Fig. 3-4. Interferograms of the surface of a Cr and Au sample (a) before the shock is in the material, (b) 60 ps after shock breakout at the surface (the ripple and darkening at the center of the image indicate the presence of motion in the thin film), and (c) after the completion of the shock event, showing the hole left in the metal film.

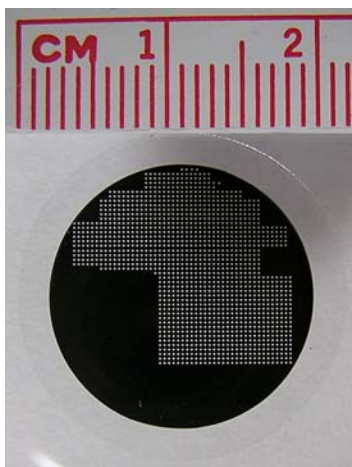


Fig. 3-5. Photograph of a Cr and Au layered sample that was vapor deposited on 120 μm of glass. The holes in the metal film were generated by the laser shocks.

The Cr and Au thin film samples were grown in a high vacuum bell jar system equipped with two electron beam deposition sources operated at a pressure during deposition of 1×10^{-7} Torr (or better). A quartz crystal microbalance was located in the center of the planetary and was used as an *in situ* film thickness monitor. The chromium and gold layers were sequentially grown on 120 μm glass substrates that were 22 mm in diameter. Prior to introduction into the vacuum, the substrates were rinsed with methanol and air-dried. The typical deposition rate for both materials was approximately 1-2 $\text{\AA}/\text{s}$ and was controlled by manipulating the emission current of the source.

3.3 Results

3.3.1 Data Analysis

The displacement of the surface of the films was extracted from the interferograms with a Fourier transform method in the fashion of Takeda *et al.* as

described below.¹¹ The fringe pattern of the interferograms is of the form:

$$g(x, y) = a(x, y) + b(x, y) \cos[2\pi f_0 x + \varphi(x, y)], \quad (3.1)$$

where x and y are the coordinates of the interferogram, $a(x, y)$ is unwanted spatial variation in the interferogram intensity, $b(x, y)$ is the spatial variation in intensity of the interferogram that contains information about the reflectivity of the sample, f_0 is the frequency of the interferometric fringes, and φ is the phase shift of the light from the movement of the sample. Equation (3.1) can be written as

$$g(x, y) = a(x, y) + \frac{1}{2} b(x, y) e^{i[2\pi f_0 x + \varphi(x, y)]} + \frac{1}{2} b^*(x, y) e^{-i[2\pi f_0 x + \varphi(x, y)]}, \quad (3.2)$$

which may be further simplified as

$$g(x, y) = a(x, y) + c(x, y) e^{i2\pi f_0 x} + c^*(x, y) e^{-i2\pi f_0 x} \quad (3.3)$$

with the substitution

$$c(x, y) = \frac{1}{2} b(x, y) e^{i\varphi(x, y)}, \quad (3.4)$$

where c^* indicates the complex conjugate of c . Equation (3.3) is Fourier transformed in x with a Fast Fourier Transform (FFT) algorithm to become

$$G(f, y) = A(f, y) + C(f - f_0, y) + C^*(f + f_0, y), \quad (3.5)$$

where the capital letters denote the Fourier spectra of the lower case counterparts and f is the frequency in the x direction. The three parts of Eq. (3.5) are separated in frequency at the locations f , $f-f_0$, and $f+f_0$. This separation allows the isolation of a single part, $C(f-f_0, y)$, which is inverse Fourier transformed to return $c(x, y)$ as written in Eq. (3.4). The desired quantity is the displacement of the sample surface, which is given by the change in the phase. To acquire that quantity, $c(x, y)$ is normalized after performing the above

analysis using an interferogram of the same sample area that was recorded prior to the surface displacement, as follows:

$$\frac{c(x, y)}{c_0(x, y)} = \frac{\frac{1}{2}b(x, y)e^{i\varphi(x, y)}}{\frac{1}{2}b_0(x, y)e^{i\varphi_0(x, y)}} = \frac{b(x, y)}{b_0(x, y)} e^{i[\varphi(x, y) - \varphi_0(x, y)]}, \quad (3.6)$$

where the subscript 0 indicates values from an interferogram recorded before surface displacement. From Eq. (3.6), both the relative reflectivity, $R(x, y)$, and the phase shift from the surface displacement, $\phi(x, y)$, may be extracted as shown in Eqs. (3.7) and (3.8).

$$R(x, y) = \left(\frac{b(x, y)}{b_0(x, y)} \right)^2 \quad (3.7)$$

$$\phi(x, y) = \varphi(x, y) - \varphi_0(x, y) \quad (3.8)$$

The phase shift is obtained modulo- 2π , so the phase is unwrapped to remove any 2π discontinuities, and then the phase in the region of the interferogram that remains stationary is set to 0.

This analysis was performed on the interferograms in Fig. 3-4. The real portion of the Fourier spectra of the interferogram in Fig. 3-4(b) is shown in Fig. 3-6. Clearly evident is the separation of the three distributions of Eq. (3.5) along the horizontal axis, where $A(f, y)$ is in the center of the plot, $C(f-f_0, y)$ to the left of center, and $C^*(f+f_0, y)$ is to the right.

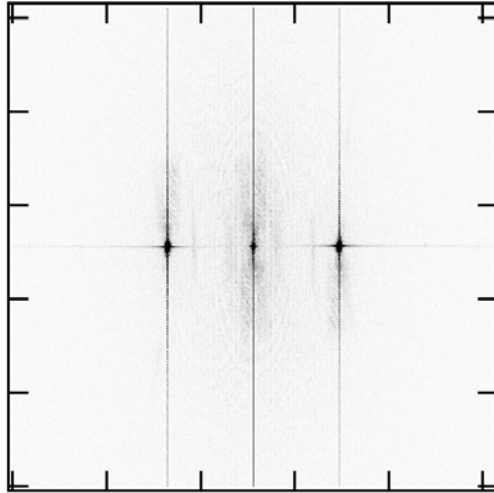


Fig. 3-6. Plot of the real component of the Fourier spectrum from the interferogram shown in Fig. 3-4(b).

The peak to the left of center in Fig. 3-6 was isolated with an elliptically shaped mask and inverse Fourier transformed. The remainder of the analysis was conducted to yield the phase shift and reflectivity results shown in Fig. 3-7.

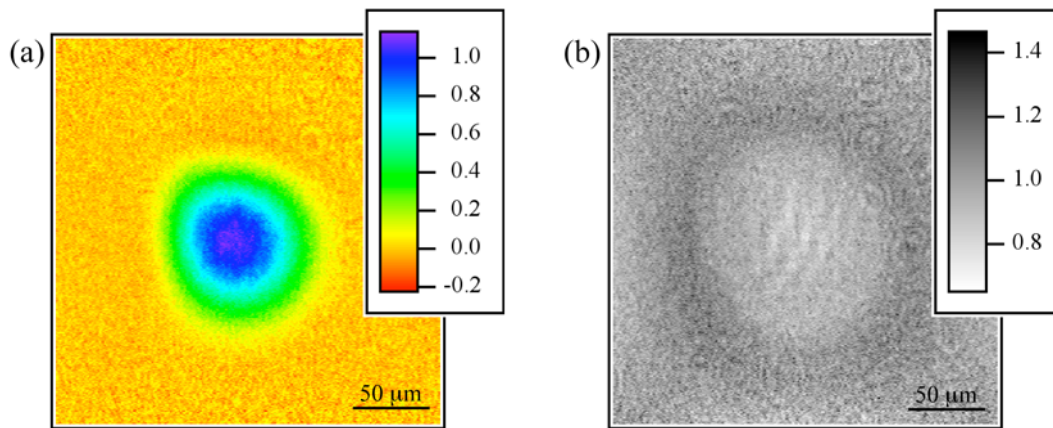


Fig. 3-7. (a) Optical phase shift and (b) relative reflectivity calculated from the interferogram shown in Fig. 3-4(b) and zeroed/normalized by the interferogram in Fig. 3-4(a).

The phase shift data were used as a measurement of the displacement $z(x,y)$ of the surface of the metal film, which is calculated from:

$$z(x,y) = \frac{\lambda}{4\pi \cos\theta} \phi(x,y), \quad (3.9)$$

where λ is the probe wavelength, θ is the incident angle of the probe, and ϕ is the phase shift. The surface displacement calculated from the phase shift data in Fig. 3-7(a) is depicted in Fig. 3-8.

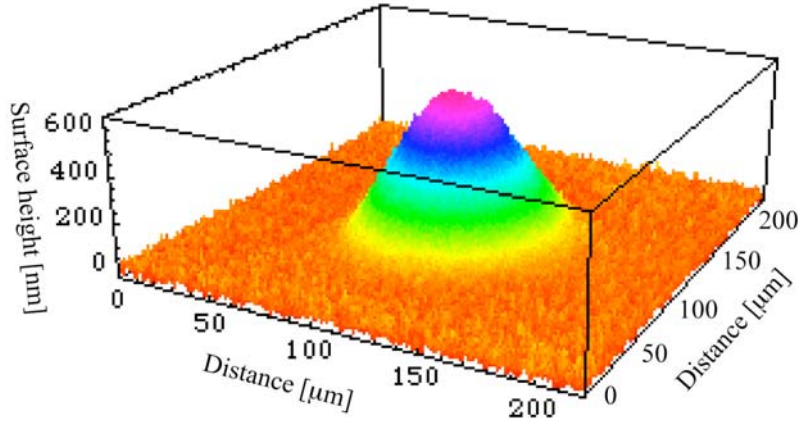


Fig. 3-8. Three-dimensional representation of the surface position of the Cr and Au film, calculated from Eq. (3.9) using the phase shift data shown in Fig. 3-7(a).

In previous studies of shock rise times in thin metal films, the surface displacement was fit well by the following function:

$$z(t) = \int \frac{1}{2} \left[1 + \tanh \left(\frac{t-t_0}{\tau} \right) \right] u_{fs} dt, \quad (3.10)$$

where t is time, t_0 is the time at the center of the material acceleration, τ is the time constant of the material acceleration, and u_{fs} is the free surface velocity. The phase shift

from the center 30 μm of the shocked area was averaged and plotted against the time delay of the probe pulse relative to the pump pulse. To use the phase shift data, Eq. (3.9) was substituted for z in Eq. (3.10), and Eq. (3.10) was integrated to yield

$$\phi(t) = \frac{4\pi \cos\theta}{\lambda} u_p \left[t - t_0 + \tau \ln \left(\cosh \frac{t - t_0}{\tau} \right) \right] + \phi_0, \quad (3.11)$$

where $\phi(t)$ is the time-dependent phase shift, u_p is the particle velocity in the material, and ϕ_0 is any phase shift present before the arrival of the pump pulse, commonly a result of a small amount of pre-pulse in the laser output. The phase shift as a function of time was fit to Eq. (3.11) to acquire τ , the time constant of the material free surface velocity, with the 10%-90% shock wave rise time as approximately 2.3τ .

3.3.2 Chirped drive pulse

For the experiments that used a chirped pulse to drive the shock wave in the metal films, combinations of four Cr thicknesses and three Au thicknesses were investigated. The Cr thicknesses were 5 nm, 15 nm, 30 nm and 50 nm. At the wavelength of 800 nm, Cr has an optical penetration depth of 18 nm, and the Cr thicknesses were chosen to range from significantly below the penetration depth to well above it. The Au thicknesses were 100 nm, 250 nm, and 500 nm. These thicknesses were chosen to determine if the Au disperses the shock front and to determine if a sharp shock can be propagated in the gold film.

Phase shift versus time data for the samples with 100 nm Au and the four thicknesses of Cr are shown in Fig. 3-9 along with the fits to the data using Eq. (3.11). For all the data recorded with the chirped drive pulse, the phase shift data at each time are

the averages of five shots. The accelerations of the free surfaces as a function of time are shown in Fig. 3-10. It is evident from the widths of the acceleration curves that the shock rise time is similar for the films with 5 and 15 nm of Cr, shorter for the 30 nm Cr film, and shortest for the 50 nm Cr film.

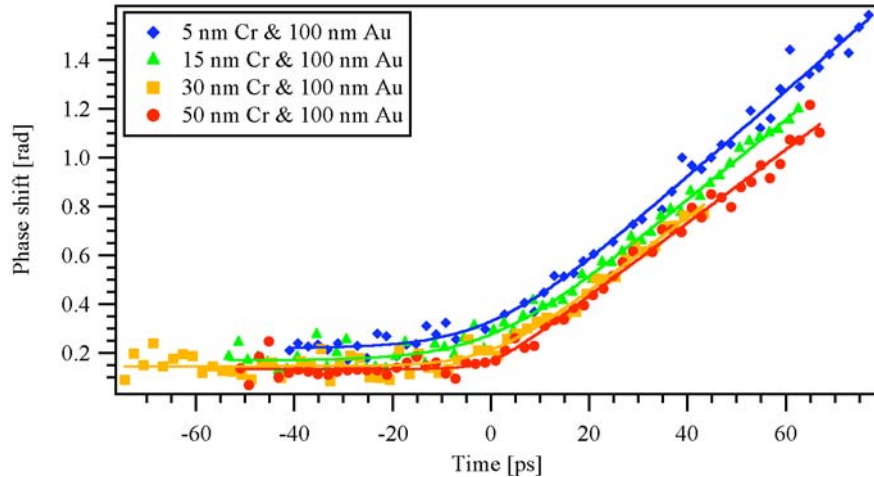


Fig. 3-9. Interferometric microscopy phase shift for films with various thicknesses of Cr underneath 100 nm Au averaged over the central 30 μm of the shock breakout region as a function of delay between the pump and probe pulses.

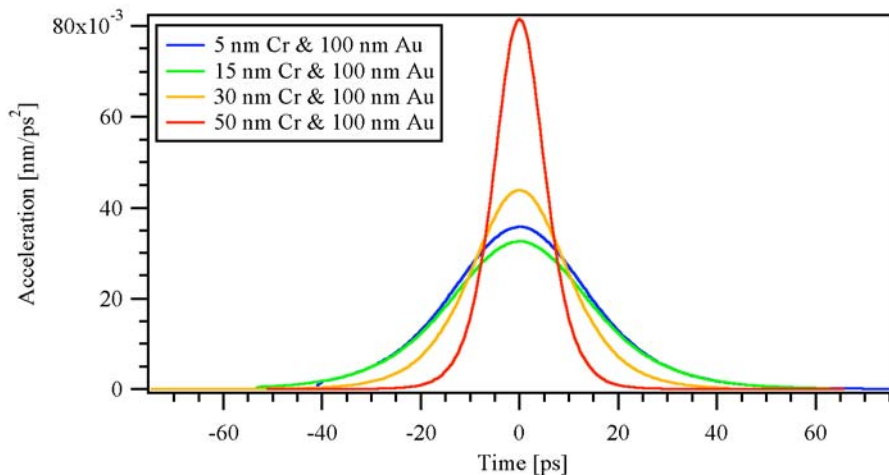


Fig. 3-10. Acceleration of the free surfaces of films with various thicknesses of Cr underneath 100 nm Au determined from the fit of phase shift data obtained as a function of delay between the pump and probe pulses.

Phase shift versus time data and fits for the samples with 250 nm Au and four different thicknesses of Cr are shown in Fig. 3-11. It can be seen from the acceleration curves in Fig. 3-12 that the data with 250 nm Au do not show a clear correlation between Cr thickness and rise time.

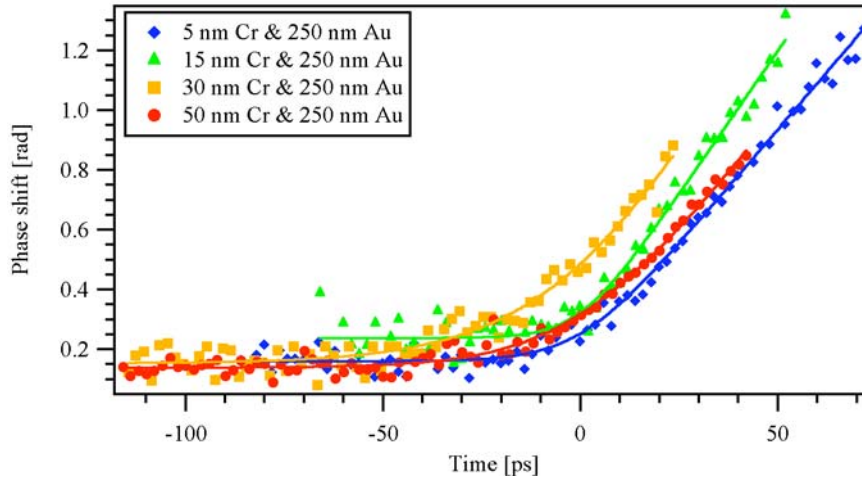


Fig. 3-11. Interferometric microscopy phase shift for films with various thicknesses of Cr underneath 250 nm Au averaged over the central 30 μm of the shock breakout region as a function of delay between the pump and probe pulses.

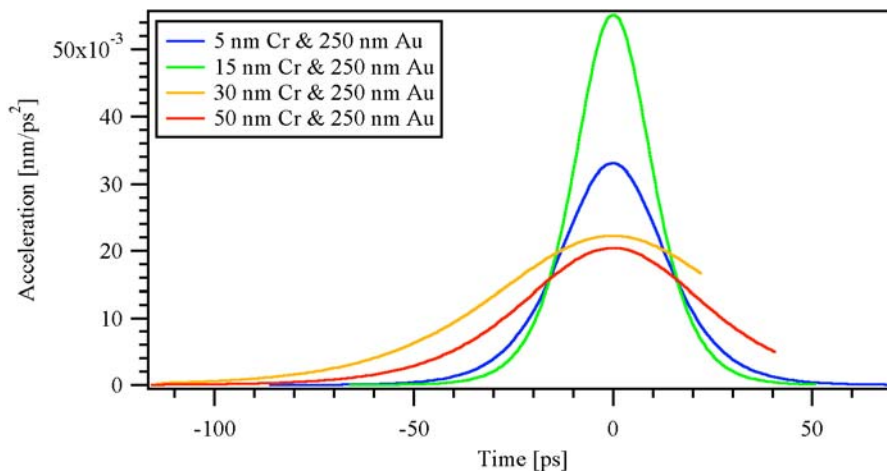


Fig. 3-12. Acceleration of the free surfaces of films with various thicknesses of Cr underneath 250 nm Au determined from the fit of phase shift data obtained as a function of delay between the pump and probe pulses.

The phase shift versus time data and fits for the films with 500 nm Au and four different thicknesses of Cr are shown in Fig. 3-13. The accelerations of the free surfaces of the films in Fig 3-14 are similar to those for the films with 250 nm Au in that there is not a clear correlation between thickness of the Cr film and rise time.

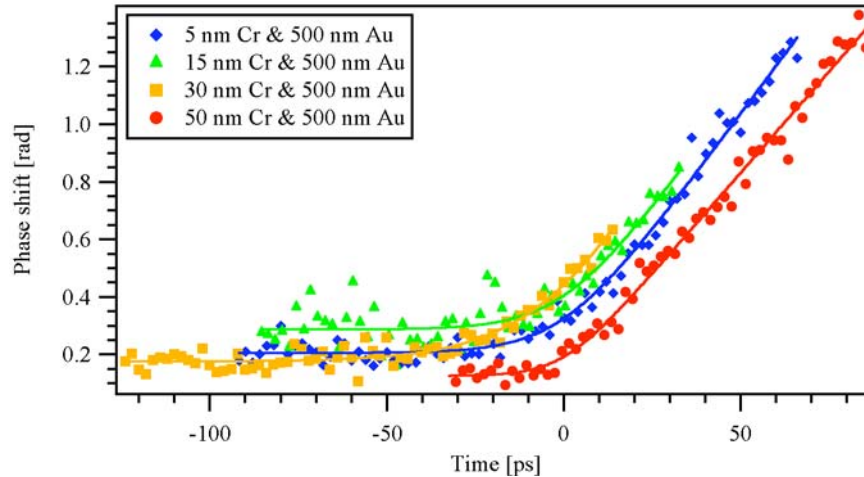


Fig. 3-13. Interferometric microscopy phase shift for films with various thicknesses of Cr underneath 500 nm Au averaged over the central 30 μm of the shock breakout region as a function of delay between the pump and probe pulses.

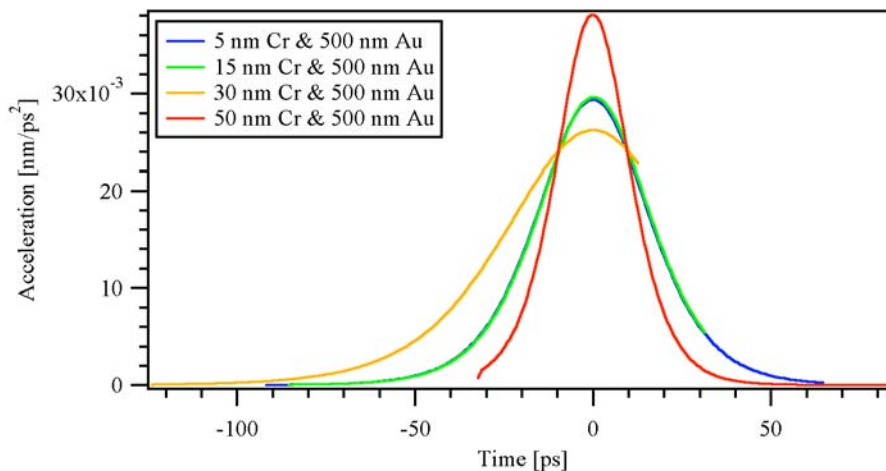


Fig. 3-14. Acceleration of the free surfaces of films with various thicknesses of Cr underneath 500 nm Au determined from the fit of phase shift data obtained as a function of delay between the pump and probe pulses.

The rise times for all the thicknesses of Cr and Au measured are given in Table 3-

1. As mentioned earlier, the films with 250 nm and 500 nm Au do not show the expected trend of shorter rise time with thicker Cr layers, however, the films with 100 nm Au do show this trend.

Table 3-1. Rise time, τ , in ps of the shock wave in films with various thicknesses of Cr and Au. The shock wave was generated with a stretched and spectrally shaped laser pulse of approximately 80 ps.

		Au thickness [nm]:		
		100	250	500
Cr thickness [nm]:	5	18±9	18±6	21±7
	15	19±7	13±9	21±19
	30	13±9	40.±18	32±14
	50	7±8	31±8	14±10.

250 nm Al and 250 nm Au films were also measured with the chirped drive pulse. The phase shift data and fits are shown in Fig. 3-15, and the accelerations are shown in Fig. 3-16. The 250 nm Al film was measured to compare the rise times of the Cr-Au samples to the rise time in Al, the typical metallic drive layer used in laser driven shock experiments. The rise time in the 250 nm Al film was 7±4 ps. The 250 nm Au film was measured to determine if adding a Cr layer to generate the shock shortened the rise time. The rise time in the 250 nm Au film was 20.±4 ps.

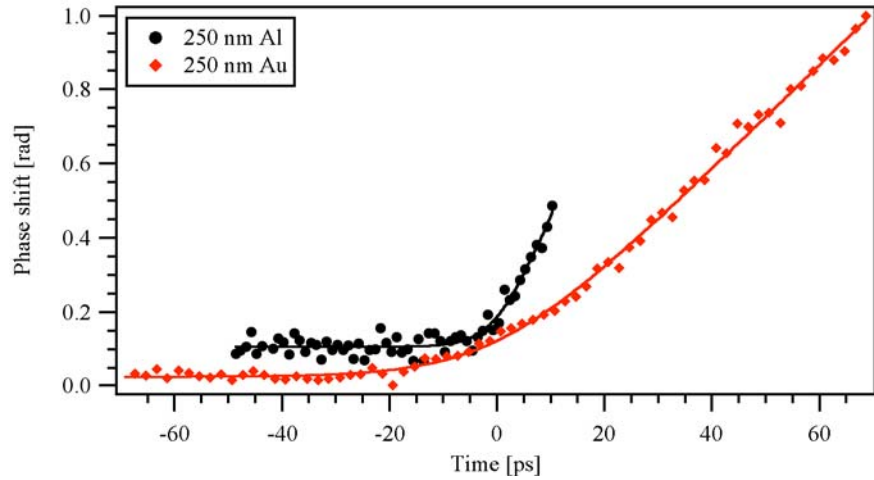


Fig. 3-15. Interferometric microscopy phase shift for a 250 nm Al film and a 250 nm Au film averaged over the central 30 μm of the shock breakout region as a function of delay between the pump and probe pulses. The Al data were recorded for a shorter time than the Au data because the Al free surface accelerates in a shorter time.

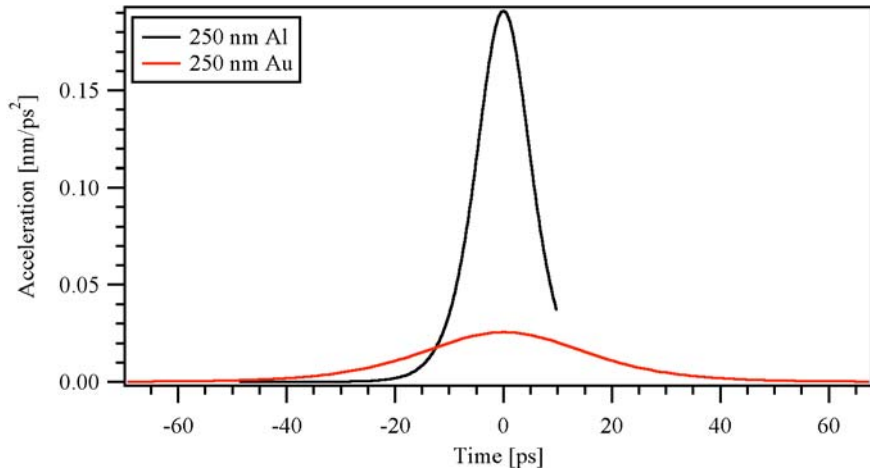


Fig. 3-16. Acceleration of the free surfaces of a 250 nm Al film and a 250 nm Au film determined from the fit of phase shift data obtained as a function of delay between the pump and probe pulses.

3.3.3 fs drive pulse

Due to the inconsistencies of the rise times in the data taken with the chirped drive pulse, especially in the 250 nm and 500 nm Au films, the rise times of some Cr-Au

films were measured with a 180 fs drive pulse. The ultrafast drive pulse insured that the rise time of the free surface velocity was exclusively due to the materials in the sample and not from the rise time of the laser pulse intensity. The rise times of four films were measured with the 180 fs drive pulse. All four films had 100 nm of Au, and the Cr layers were 15nm, 50 nm, 100 nm, and 300 nm thick. The phase shift data at each time is the average of 10 shots. The phase shift data and fits are shown in Fig. 3-17, and the accelerations calculated from the fits are shown in Fig. 3-18. Additionally, the rise times for the four films are given in Table 3-2. Clearly the free surface velocity rise time for the film with 15 nm Cr was much longer than the rise times for the other three films. The variances in the rise times of the 50 nm and 100 nm Cr films show that there was not a statistically significant difference in the rise times of those films, and the rise time of the 300 nm Cr film was slightly longer but still much shorter than the rise time of the 15 nm Cr film.

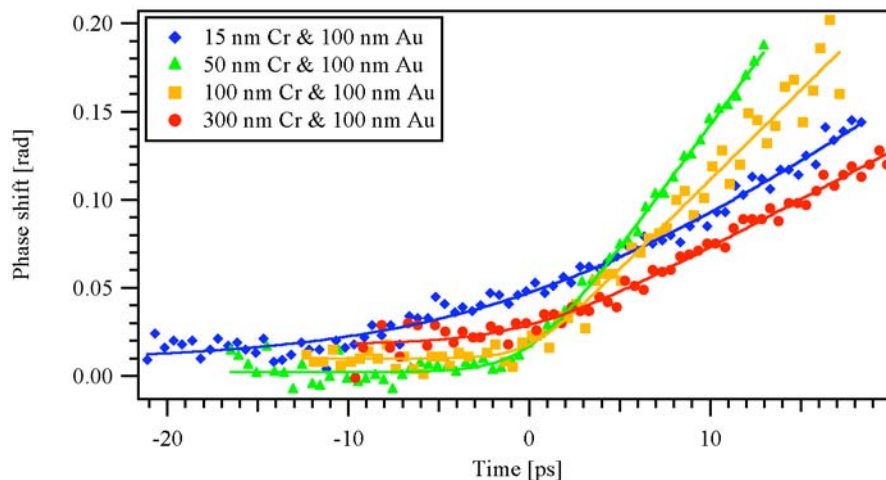


Fig. 3-17. Interferometric microscopy phase shift for films with various thicknesses of Cr underneath 100 nm Au averaged over the central 30 μm of the shock breakout region as a function of delay between the pump and probe pulses.

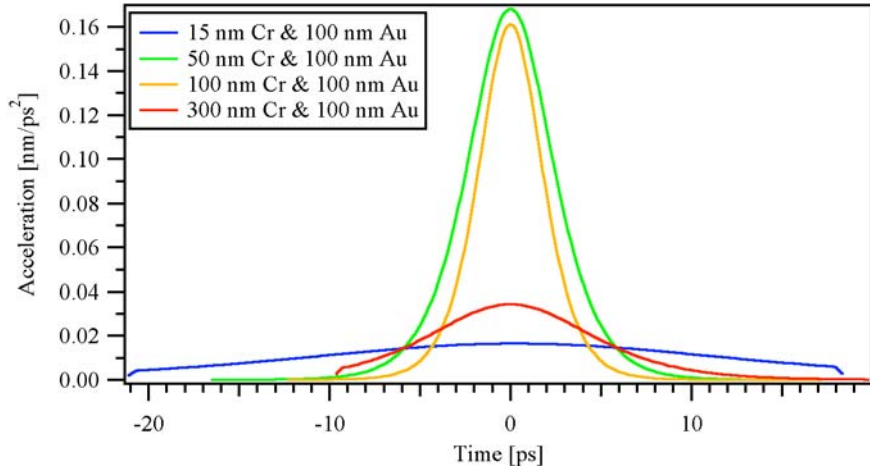


Fig. 3-18. Acceleration of the free surfaces of films with various thicknesses of Cr underneath 100 nm Au determined from the fit of phase shift data obtained as a function of delay between the pump and probe pulses.

Table 3-2. Rise time, τ , of the shock wave in films with various thicknesses of Cr underneath 100 nm Au. The shock wave was generated with a 180 fs laser pulse.

	100 nm Au
15 nm Cr	15.7±3.4
50 nm Cr	3.1±0.6
100 nm Cr	2.3±1.3
300 nm Cr	5.9±2.0

3.4 Discussion

The free surface velocity rise time data of the samples with 100 nm Au taken with the chirped drive pulse show a clear decrease in rise time with increased Cr film thickness from 5 nm to 50 nm of Cr. The 5 nm and 15 nm thick Cr films produced rise times similar to the rise time in the 250 nm Au with no Cr layer; all had rise times of approximately 20 ps. Since the optical penetration depth at a wavelength of 800 nm in Cr is 18 nm, a significant portion of the light passed through the Cr layer and was absorbed in the Au. The shock wave was formed in both the thin Cr layer and the Au layer, but the

weak electron-phonon coupling in the Au created the relatively long rise time. As hypothesized in §3.1, increasing the thicknesses of the Cr to 30 nm and 50 nm made the rise times progressively shorter as almost all of the light was absorbed in the Cr, and the shock was formed in the Cr layer and then mechanically transferred to the Au layer. In fact, the rise time in the sample with 50 nm of Cr and 100 nm of Au was the same as the rise time in the 250 nm thick Al film, 7 ps.

The shock wave rise times varied for the samples with 250 nm and 500 nm thick Au layers, and they did not show a consistent trend with Cr thickness. For the samples with Cr layers 5 nm and 15 nm thick, the rise times of the samples with 250 nm and 500 nm thick Au layers were very similar to those with the 100 nm thick Au layer and similar to the 250 nm film of only Au. These rise times resulted from the same mechanism as explained earlier in the samples with 100 nm Au layers in that the light for driving the shock wave penetrated through the Cr layer and the shock wave was formed in both the Cr and the Au layers. For the samples with 30 nm and 50 nm of Cr and 250 nm and 500 nm of Au, the rise times did not decrease like they did in the samples with 100 nm thick Au layers. The most probable explanation is that there was dispersion of the shock front in the thicker Au layer, which lengthened the rise time.

Using the 180 fs drive pulse to generate a shock in films with 100 nm Au and various thicknesses of Cr, it was possible to create a sharp shock front when the Cr thickness was 50 nm or larger. The monotonic decrease in rise time when the Cr thickness was varied from 15 nm to 100 nm was a product of increasing amounts of the light being absorbed in the Cr layer and the larger thicknesses permitting the formation of the shock wave fully in the Cr layer before it was mechanically transferred to the Au

layer. The rise time was slightly longer with the 300 nm Cr film, possibly due to dispersion at the shock front as it traveled through more material or due to the rarefaction wave eroding the shock at later times. There was no evidence that a sharper shock front was created by Cr thicknesses greater than 50 nm.

In conclusion, it has been shown that short rise times in free surface velocity of Au films are achievable with layered metal structures. Layers of Cr 50 nm or more thick underneath a 100 nm Au film produced sharp shock fronts with free surface velocity rise times similar to those previously seen by Gahagan *et al.*⁶ in Al and Ni.

References

- 1 E. Sabatani and I. Rubinstein, "Organized self-assembling monolayers on electrodes. 2. Monolayer-based ultramicroelectrodes for the study of very rapid electrode kinetics," *J. Phys. Chem.* **91**, 6663-9 (1987).
- 2 C. D. Bain and G. M. Whitesides, "Molecular-level control over surface order in self-assembled monolayer films of thiols on gold," *Science* **240**, 62-63 (1988).
- 3 G. M. Whitesides and P. E. Laibinis, "Wet chemical approaches to the characterization of organic surfaces. Self-assembled monolayers, wetting, and the physical-organic chemistry of the solid-liquid interface," *Langmuir* **6**, 87-96 (1990).
- 4 J. Hohlfeld, S. S. Wellershoff, J. Gudde, U. Conrad, V. Jahnke, and E. Matthias, "Electron and lattice dynamics following optical excitation of metals," *Chem. Phys.* **251**, 237-58 (2000).
- 5 D. J. Funk, D. S. Moore, J. H. Reho, K. T. Gahagan, S. D. McGrane, and R. L. Rabie, "Ultrafast measurement of the optical properties of shocked nickel and laser heated gold" in *Shock Compression of Condensed Matter--2001*, edited by M. D. Furnish, N. N. Thadhani, and Y. Horie (American Institute of Physics, Melville, NY, 2002), p. 1227-1230.
- 6 K. T. Gahagan, D. S. Moore, D. J. Funk, R. L. Rabie, S. J. Buelow, and J. W. Nicholson, "Measurement of shock wave rise times in metal thin films," *Phys. Rev. Lett.* **85**, 3205-8 (2000).
- 7 L. P. Martin, J. H. Nguyen, J. R. Patterson, D. Orlikowski, P. P. Asoka-Kumar, and N. C. Holmes, "Tape casting technique for fabrication of graded-density impactors for tailored dynamic compression" in *Materials Research at High Pressure*; Vol. 987, edited by M. R. Manaa, A. F. Goncharov, R. J. Hemley, and R. Bini (Mater. Res. Soc. Symp. Proc., Warrendale, PA, 2007), p. 45-50.
- 8 R. T. Krone, L. P. Martin, J. R. Patterson, D. Orlikowski, and J. H. Nguyen, "Fabrication and characterization of graded impedance impactors for gas gun experiments from hot-pressed magnesium and polyethylene powders," *Mater. Sci. Eng., A* **479**, 300-305 (2008).
- 9 S. S. Wellershoff, J. Gudde, J. Hohlfeld, J. G. Muller, and E. Matthias, "The role of electron-phonon coupling in femtosecond laser damage of metals," *Proc. SPIE Int. Soc. Opt. Eng.* **3343**, 378-2 (1998).
- 10 S. Linden, H. Giessen, and J. Kuhl, "XFROG--a new method for amplitude and phase characterization of weak ultrashort pulses," *Phys. Status Solidi B* **206**, 119-24 (1998).
- 11 M. Takeda, H. Ina, and S. Kobayashi, "Fourier-transform method of fringe pattern analysis for computer-based topography and interferometry," *J. Opt. Soc. Am.* **72**, 156-60 (1982).

Chapter 4

Ultrafast Dynamic Ellipsometry

4.1 Introduction

There are many diagnostics available to probe shock induced material dynamics. These diagnostics vary both in the instrumentation that is used and in the material properties that are interrogated. The most commonly used diagnostic in shock physics is the velocity interferometer system for any reflector (VISAR),¹ which uses fiber-coupled continuous-wave laser light to measure the velocity of a free or windowed surface of a shocked material. The probe light is reflected from a sample at normal incidence to the sample surface and then recombined with light that has been optically delayed. The oscillations in the intensity of the resulting light provide a measurement of the velocity of the sample surface. Recently, photon Doppler velocimetry (PDV)² has been developed, a technique that also probes the sample surface at normal incidence (most frequently) to extract velocities. Due to the use of normal incidence of the probe light in both VISAR and PDV, these diagnostics are unable to discriminate between shock induced optical changes and material motion as we will show below. Changes in the optical properties of the shocked material can impact the measured velocity, especially for experiments that are probed through a window. In most window materials, shock compression causes an increase in the refractive index, which changes the optical path length. Due to the long-

standing use of VISAR, the refractive index changes for many common window materials have been measured, and those results are applied to VISAR data in the form of VISAR correction factors. However, since the optical changes in the window material are not measured for each shot, they can lead to error in the velocity measurement, particularly if there is a nonlinear dependence of the refractive index with pressure. This possible introduction of error is of special concern as large laser facilities expand the region of accessible shock pressures to a few TPa (10s of Mbars), significantly beyond the pressures at which the correction factors were determined.

Although velocity is the most common property measured during a shock experiment, x-ray diffraction (XRD) has been used to probe both shock compression³⁻⁷ and shock-induced phase changes.⁸⁻¹⁰ Its sensitivity to nuclear position provides important and definitive information about lattice structure, but its use has been limited to materials with simple crystal structures, with readily available single crystals, and with low x-ray absorption cross-sections. Despite the definitive nature of XRD data, it cannot be used alone as a shock diagnostic because velocity information is still required to relate the XRD data to a shock pressure.

Infrared spectroscopy has been used to look at reactivity in shocked materials by probing specific vibrational modes.¹¹ It is sensitive to molecular configurations but provides little if any information about the electronic states of the materials.

Reflectivity provides information regarding electronic structure, and the reflectivity of shocked materials has been previously measured,¹²⁻¹⁴ yielding information about the material's electronic changes but without providing information about the material motion. Fourier domain interferometry has produced space and time resolved

measurements of materials subjected to laser driven shocks¹⁵⁻¹⁹ and plasmas.²⁰⁻²² Blanc *et al.*²¹ noted dependence on the polarization of their probe light and on the incident angle in their plasma studies, and Quoix *et al.*²² used the difference in the phase between s- and p-polarized probes in the measurement of plasma density and electronic temperature.

The optical properties of a material in the visible wavelength range result from its electronic structure. Thus, ultrafast dynamic ellipsometry (UDE), which is sensitive to changes in the electronic structure as manifested through changes in the material's index of refraction, may be used in some cases as a non-invasive probe of the phase of a material or its chemical reactivity.

Ultrafast dynamic ellipsometry measures the space and time resolved phase shift and reflectivity of laser light incident at two angles to the shocked surface, each containing s- and p-polarized light. The use of off-normal probe angles allows the separation of the optical effects from the material motion as we show below. Previously, UDE of shocked materials has been performed using multiple laser shots to build up a time history, similar to the method used in the shock rise time experiments in the previous chapter. In other experiments, Funk *et al.*²³ measured the optical effects of shocked Al at 800 nm using the phase shifts at multiple angles to extract the particle velocity and the shocked refractive index, and McGrane *et al.*²⁴ used optical phase shift information to determine the shocked refractive index, the particle velocity, and the shock velocity for shocks traveling in transparent poly(methyl methacrylate) (PMMA). This thesis presents a dramatic advancement by allowing the simultaneous determination of the optical properties and the material motion using chirped pulse interferometry to acquire a complete time profile in a single shot. The benefit of acquiring this information

in a single shot is greatly decreased noise in the data, which permits a more accurate determination of the material response to shock loading. A comparison between single shot data and data acquired by building up a time history will be given in §4.4, along with a discussion of the value added. Another benefit of a single shot technique is the ability to apply it to larger experiments, such as those driven by high power lasers, high explosives, and gas guns.

Ultrafast dynamic ellipsometry is a powerful technique for measuring the Hugoniot of transparent materials, as will be demonstrated in the next several chapters. By separating changes in the optical properties from the material motion of thin films, the film thickness, the refractive indices of the pristine and shocked materials, and the shock and particle velocities are determined. This work marks the first time that all of these parameters have been determined simultaneously.

4.2 Ultrafast dynamic ellipsometry interferometric probe

Shown in Fig. 4-1 is a schematic of the shock generation/probe apparatus. As noted in Chapter 2, a portion of the chirped and spectrally shaped pulse was used to probe the material properties. Approximately 30% of the laser pulse energy from the chirped pulse was split off after the post-amplification stretcher. This pulse was equally split into two Mach-Zehnder interferometers that probed the sample at two different angles, $25.0 \pm 0.1^\circ$ and $63.4 \pm 0.3^\circ$ from normal. The probes were loosely focused onto the same region of the sample, illuminating an area approximately 600 μm in diameter and circumscribing the shock breakout region. In each arm of each interferometer, a half-wave plate was inserted before the sample and rotated such that each beam contained

both s- and p-polarized light of equal intensity at the detectors after the spectrometers. Achromatic doublet lenses imaged the sample surface onto the entrance slits of two home-built imaging spectrometers, one for each angle. Identical lenses in the reference arms balanced the interferometers. The reference and probe beams were crossed at a slight angle on the slits of the spectrometers, creating interference fringes perpendicular to the spectrometer slit. An adjustable delay built into the reference arms of each interferometer allowed temporal overlap of the beams at the spectrometer entrance slits as measured with the spectrometer grating at zero order. This space-shifted implementation of Fourier domain interferometry was chosen because it gave less noise in this experiment than the more common time-delayed variation. Each slit was positioned to sample through the center of the shock breakout region. At the output of each spectrometer, a Wollaston prism separated the orthogonal polarizations into separate images on 12-bit charge-coupled-device (CCD) cameras.

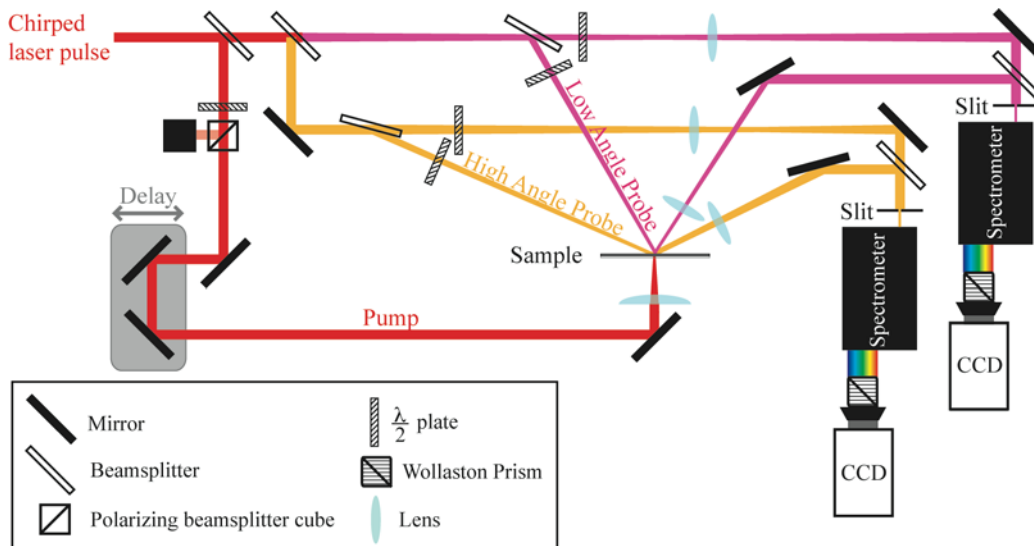


Fig. 4-1. Experimental schematic for shock generation and ultrafast dynamic ellipsometry diagnostic. The same chirped laser pulse was used to drive the shock wave in the material and to probe the resulting material dynamics with two Mach-Zehnder spectral interferometers.

An image of the hole created in an Al sample by the laser generated shock wave probed at 26.0° is shown in Fig. 4-2. Shown in Fig. 4-3 are interferograms recorded before and during a shock in a 1530 nm film of polycarbonate. For the low angle data, the calibrated sample dimension of length per CCD pixel was $0.685 \mu\text{m}$ for s-polarization and $0.526 \mu\text{m}$ for p-polarization. For the high angle data, it was $1.136 \mu\text{m}$ for s-polarization and $0.877 \mu\text{m}$ for p-polarization. (The difference in magnification results from astigmatism due to the large split angle of the Wollaston prisms, $\sim 15^\circ$.²⁵)

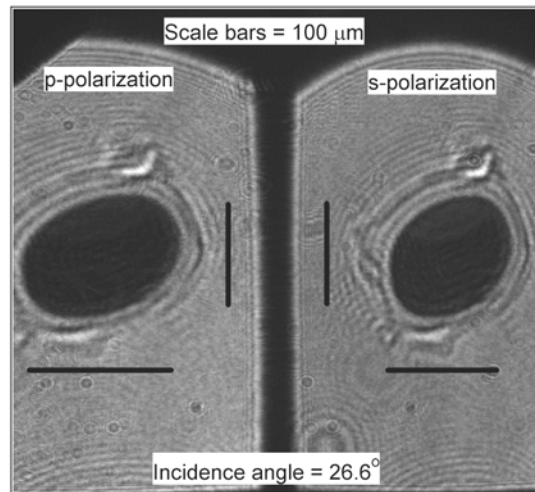


Fig. 4-2. Images of the holes produced by a laser generated shock wave in a $2 \mu\text{m}$ Al film grown on a glass substrate. A Wollaston prism splits the s- and p-polarized light for imaging onto separate areas of the CCD camera.

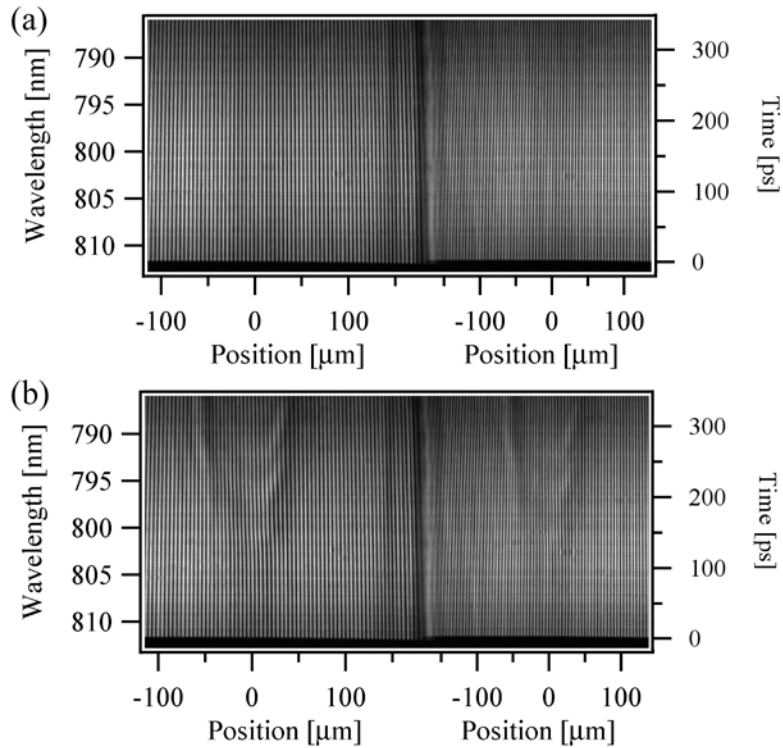


Fig. 4-3. Interferograms of the 25.0° probe with the p-polarized light on the left and the s-polarized light on the right. Interferograms were recorded (a) before and (b) during an 8.7 ± 0.2 GPa shock in 1530 nm of polycarbonate on 2 μm of Al. The ripples observed in (b) are indicative of surface motion and/or changes in the optical properties of the sample.

Care was taken in using the same configuration of mirrors to image the shock into each spectrometer and in aligning the spectrometer slits to the same area on the sample in both arms, using a visible defect or feature on the sample for alignment. Since the data were spatially resolved, it was critical that the data collected at each angle be taken from the same place on the sample. In addition, the images were rotated before the entrance slit of the spectrometer so that the slit was sampling horizontally through the center of the shock, allowing accurate centering of the elliptical image obtained at high incident angle and reducing any error introduced by movement of the pump beam between shots.

4.3 Analysis of the Interferograms

To measure the time-dependent frequency of the shaped laser pulse and to calibrate the time dependence of the probe, a cross-correlation frequency resolved optical gating (XFROG)²⁶ measurement was performed. The stretched and spectrally shaped pulse was combined with the compressed and spectrally narrowed pulse of 400 fs in a 50 μm thick β -barium borate (BBO) crystal to create the sum frequency of the two pulses. The sum frequency was recorded with a spectrometer while the delay between the two pulses was scanned. A typical XFROG trace is shown in Fig. 4-4.

The resulting XFROG data were analyzed, using a peak fitter at each time step. The peak wavelength was transformed into frequency. The peak frequency as a function of time is shown in Fig. 4-5, along with a linear and a second order polynomial fit. There are oscillations in the residual of the fits that result from interference in the BBO crystal, which did not impact the second order polynomial fit that was used to generate an accurate description of the time-dependent frequency.

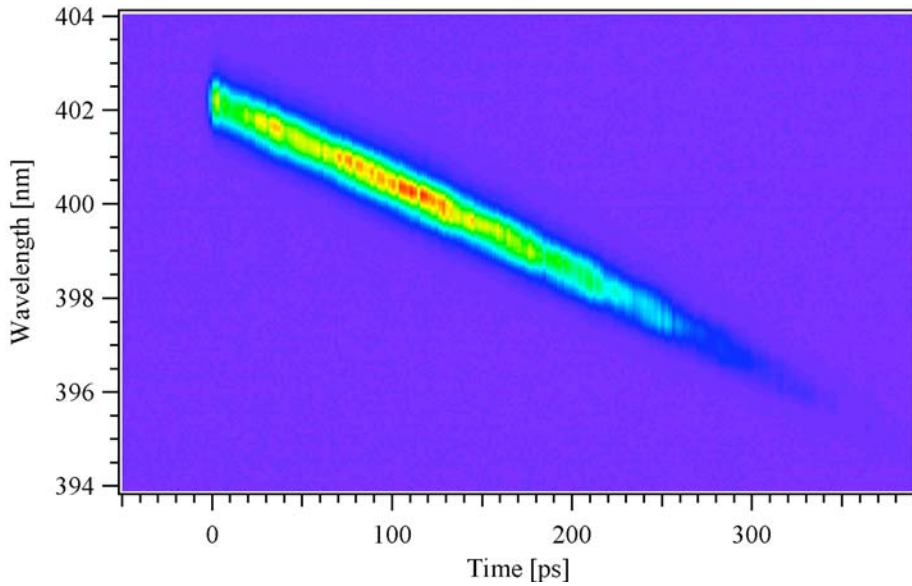


Fig. 4-4. Typical XFROG trace of the spectrally shaped laser pulse used for shock generation as measured by a compressed pulse centered at 799.9 nm with 3.5 nm FWHM bandwidth.

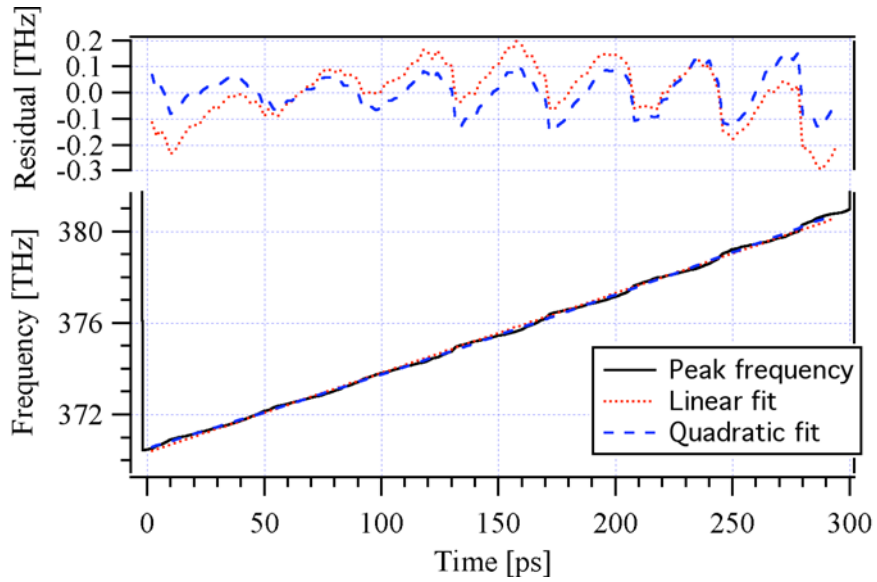


Fig. 4-5. Frequency of the peak intensity of the XFROG shown in Fig. 4-4 as a function of time delay between the stretched and compressed pulses. Linear and quadratic fits are shown overlapping the peak frequency data. Although the quality of the fits cannot be distinguished in the plot, the residuals of those fits are plotted above, showing that the quadratic fit better matches the data. The oscillations in the residuals (and also in the peak frequency data) result from interference in the sum frequency generating crystal.

The spectrometers were calibrated with an argon spectral calibration lamp (Oriel). This calibration, combined with the measured nonlinear time dependent frequency from the XFROG, was used to interpolate the interferograms onto an evenly spaced time grid. The interferograms were inverse fast Fourier transformed (FFT) along the spatial axis, and a cosine tapered filter mask excluded all but the relevant signal peak. An FFT returned a complex value from which the imaginary part gave the desired phase shift and the square of the real part yielded the reflectivity. The analysis is the same as explained in §3.3.1. The data were subtracted or divided by the phase shift or reflectivity, respectively, from an interferogram recorded of the same sample area before the shock. The effects of air currents and beam pointing fluctuations on the background were reduced by subtraction (phase shift) or division (reflectivity) of any planar tilt and by the removal of a second order polynomial fit to the background along a line in the temporal direction. Figure 4-6 shows the phase shift and reflectivity data for a shock with a maximum pressure at the peak of the Gaussian of 9.5 ± 0.2 GPa traveling through 1580 nm of polycarbonate.

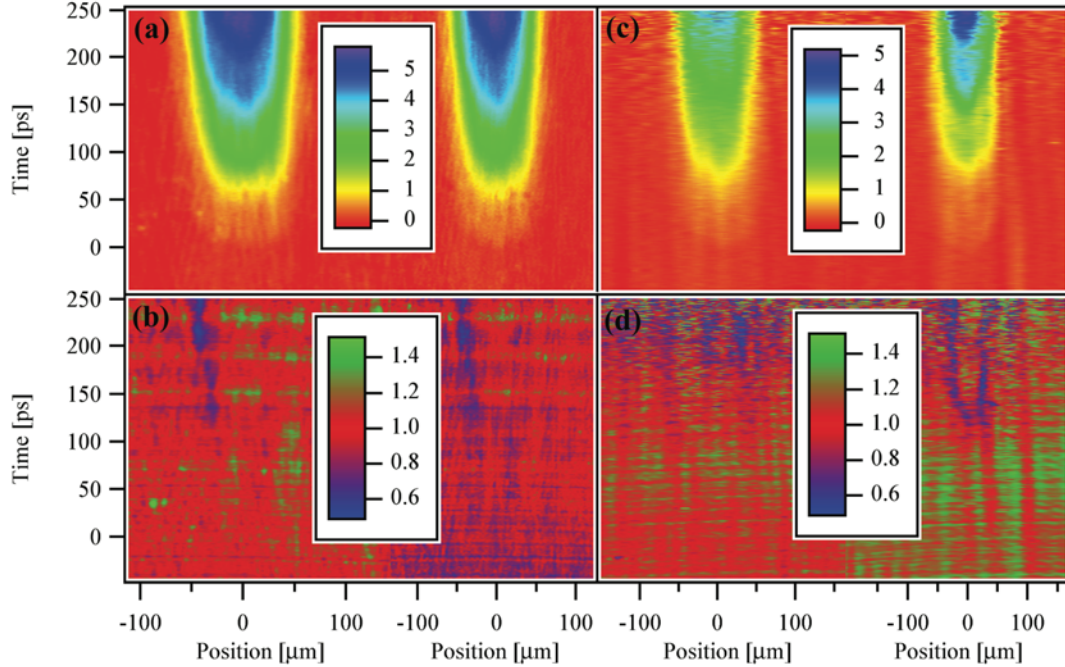


Fig. 4-6. Phase shift and reflectivity data for a 9.5 ± 0.2 GPa shock propagating through a 1580 nm thick polycarbonate film coated onto a 2 μm thick Al film. In each of the four images, the data from the p-polarized probe is on the left and from the s-polarized probe is on the right. (a) Phase shift data at 25.0° . (b) Reflectivity data at 25.0° . (c) Phase shift data at 63.4° . (d) Reflectivity data at 63.4° .

In the analysis of the data, a second-order polynomial related frequency and time. In these experiments, the spectral resolution of the spectrometers determined the time resolution to be 3.5 ps, which is sufficiently short to capture the shock dynamics. If a higher time resolution is desired, a time resolution comparable with the bandwidth-limited probe pulse duration (<50 fs) is achievable with signal reconstruction described by Geindre *et al.*²⁷

4.4 Benefits of a single shot diagnostic

In previous experiments,²⁴ ultrafast interferometric microscopy was applied in a similar fashion to UDE to measure a shock wave in PMMA. (Ultrafast interferometric microscopy is described in Chapter 3.) This technique required several hundred shots, which were averaged for each time step and used to build a time history of the phase shift. Due to fluctuations in laser power and inhomogeneities or thickness variations of the sample over the large area that was needed for so many shots, the phase data were somewhat noisy and the reflectivity data were too noisy to be of use in the analysis. Figure 4-7 gives a comparison between the interferometric microscopy phase shift data acquired from multiple shots and the single shot UDE phase shift data, in which we note the improved signal-to-noise ratio for the single shot technique.

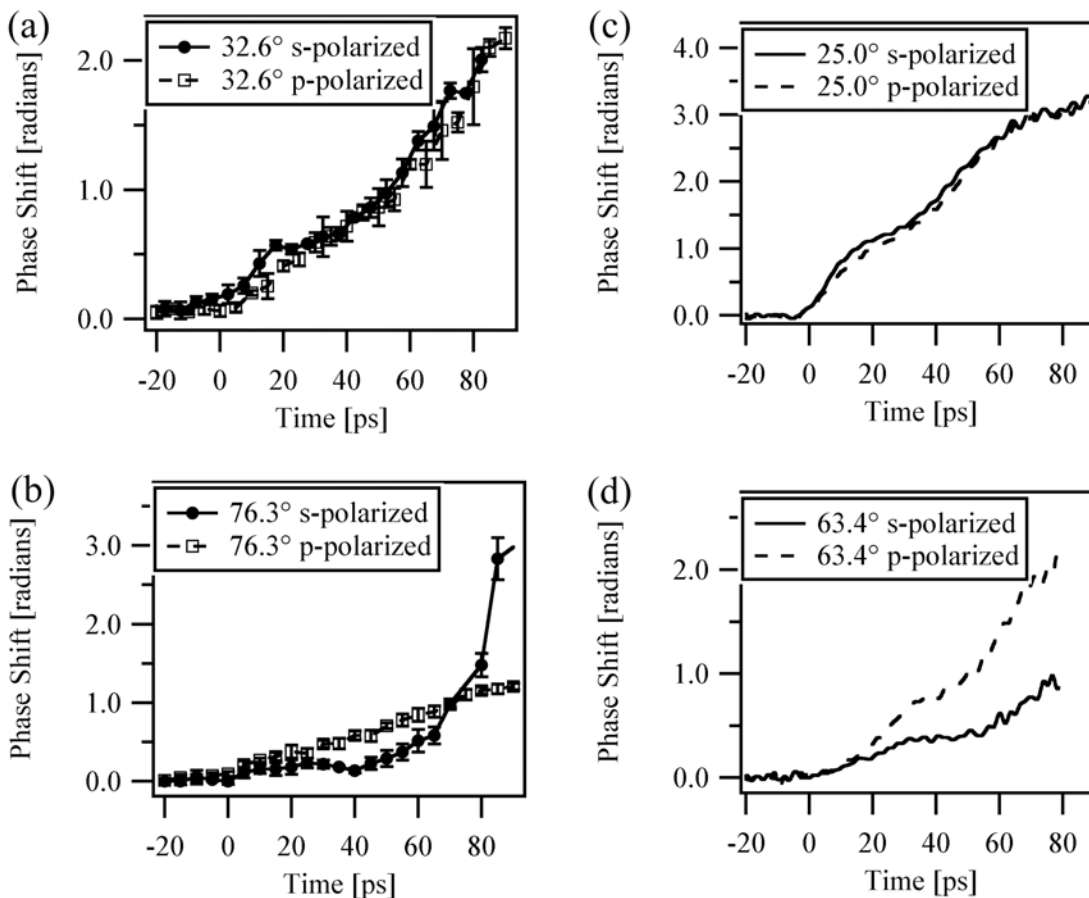


Fig. 4-7. Comparison of multiple shot interferometric microscopy phase shift data from reference [24] (a)-(b) and single shot UDE phase shift data (c)-(d) for a PMMA film of approximately 700 nm.

The UDE approach is well suited for measurement of shock-induced chemical reaction dynamics. For reactive materials, such as high explosives, photo-induced reactions, or layered nano-composites, or for inhomogeneous samples, the technique presented here demonstrates value in its single shot sensitivity, which is required in the case where the sample is destroyed or consumed. Often, reactive samples are difficult to prepare and can be impossible to create in large quantities with few enough variations to allow signal averaging. In addition, the picosecond time resolution of this chirped pulse

technique is the appropriate time scale for probing shock-induced reaction dynamics in many systems, which will be done in Chapter 8 on nitromethane and carbon disulfide.

Finally, the use of a spatially varying shock pulse with a well-characterized Gaussian profile creates a corresponding Gaussian distribution of pressures in the material. The acquisition of a range of Hugoniot data from each laser shot using the spatially resolved data across the pressure distribution will be shown in Chapter 7.

By separating the material motion from the shock-induced optical effects, ultrafast dynamic ellipsometry is a powerful technique to probe material dynamics that are not accessed with other methods. In addition to the investigations in this thesis, it will prove valuable in future studies of material dynamics due to its ability to concurrently ascertain multiple parameters of the dynamic material without the need for reference experiments and with the high time resolution necessary to capture fast material dynamics.

References

- ¹ L. M. Barker and R. E. Hollenbach, "Laser interferometer for measuring high velocities of any reflecting surface," *J. Appl. Phys.* **43**, 4669-75 (1972).
- ² O. T. Strand, L. V. Berzins, D. R. Goosman, W. W. Kuhlow, P. D. Sargis, and T. L. Whitworth, "Velocimetry using heterodyne techniques" in *26th International Congress on High-Speed Photography and Photonics*, edited by D. L. Paisley, S. Kleinfelder, D. R. Snyder, and B. J. Thompson (SPIE--International Society for Optical Engineering, Bellingham, WA, 2005), p. 593-599.
- ³ Q. Johnson, L. Evans, and A. C. Mitchell, "X-ray diffraction study of single crystals undergoing shock-wave compression," *Appl. Phys. Lett.* **21**, 29-30 (1972).
- ⁴ J. S. Wark, R. R. Whitlock, A. A. Hauer, J. E. Swain, and P. J. Solone, "Subnanosecond X-ray diffraction from laser-shocked crystals," *Phys. Rev. B* **40**, 5705-14 (1989).
- ⁵ P. A. Rigg and Y. M. Gupta, "Real-time X-ray diffraction to examine elastic-plastic deformation in shocked lithium fluoride crystals," *Appl. Phys. Lett.* **73**, 1655-7 (1998).
- ⁶ P. A. Rigg and Y. M. Gupta, "Multiple X-ray diffraction to determine transverse and longitudinal lattice deformation in shocked lithium fluoride," *Phys. Rev. B* **63**, 094112-12 (2001).
- ⁷ P. A. Rigg and Y. M. Gupta, "Time-resolved x-ray diffraction measurements and analysis to investigate shocked lithium fluoride crystals," *J. Appl. Phys.* **93**, 3291-8 (2003).
- ⁸ Q. Johnson and A. C. Mitchell, "First X-ray diffraction evidence for a phase transition during shock- wave compression," *Phys. Rev. Lett.* **29**, 1369-71 (1972).
- ⁹ D. H. Kalantar, J. F. Belak, G. W. Collins, J. D. Colvin, H. M. Davies, J. H. Eggert, T. C. Germann, J. Hawreliak, B. L. Holian, K. Kadau, P. S. Lomdahl, H. E. Lorenzana, M. A. Meyers, K. Rosolankova, M. S. Schneider, J. Sheppard, J. S. Stolken, and J. S. Wark, "Direct observation of the alpha - epsilon transition in shock-compressed iron via nanosecond X-ray diffraction," *Phys. Rev. Lett.* **95**, 075502-4 (2005).
- ¹⁰ T. d'Almeida and Y. M. Gupta, "Real-time X-ray diffraction measurements of the phase transition in KCl shocked along [100]," *Phys. Rev. Lett.* **85**, 330-3 (2000).
- ¹¹ S. D. McGrane, D. S. Moore, and D. J. Funk, "Shock induced reaction observed via ultrafast infrared absorption in poly(vinyl nitrate) films," *J. Phys. Chem. A* **108**, 9342-9347 (2004).
- ¹² D. Partouche-Sebban, J. L. Pelissier, F. G. Abeyta, W. W. Anderson, M. E. Byers, D. Dennis-Koller, J. S. Esparza, R. S. Hixson, D. B. Holtkamp, B. J. Jensen, J. C. King, P. A. Rigg, P. Rodriguez, D. L. Shampine, J. B. Stone, D. T. Westley, S. D. Borrer, and C. A. Kruschwitz, "Measurement of the shock-heated melt curve of lead using pyrometry and reflectometry," *J. Appl. Phys.* **97**, 043521-11 (2005).
- ¹³ G. Huser, M. Koenig, A. Benuzzi-Mounaix, E. Henry, T. Vinci, B. Faral, M. Tomasini, B. Telaro, and D. Batani, "Temperature and melting of laser-shocked iron releasing into an LiF window," *Phys. Plasmas* **12**, 60701-1 (2005).

- 14 T. de Ressguier, L. Signor, A. Dragon, M. Boustie, G. Roy, and F. Llorca, "Experimental investigation of liquid spall in laser shock-loaded tin," *J. Appl. Phys.* **101**, 013506 (2007).
- 15 R. Evans, A. D. Badger, F. Fallies, M. Mahdieh, T. A. Hall, P. Audebert, J. P. Geindre, J. C. Gauthier, A. Mysyrowicz, G. Grillon, and A. Antonetti, "Time- and space-resolved optical probing of femtosecond-laser-driven shock waves in aluminum," *Phys. Rev. Lett.* **77**, 3359-62 (1996).
- 16 A. Benuzzi-Mounaix, M. Koenig, J. M. Boudenne, T. A. Hall, D. Batani, F. Scianitti, A. Masini, and D. Di Santo, "Chirped pulse reflectivity and frequency domain interferometry in laser driven shock experiments," *Phys. Rev. E* **60**, R2488-91 (1999).
- 17 D. M. Gold, P. M. Celliers, G. W. Collins, K. S. Budil, R. Cauble, L. B. daSilva, M. E. Foord, R. E. Stewart, R. J. Wallace, and D. Young, "Interferometric and chirped optical probe techniques for high-pressure equation-of-state measurements," *Astrophys. J. Suppl.* **127**, 333-7 (2000).
- 18 K. T. Gahagan, D. S. Moore, D. J. Funk, R. L. Rabie, S. J. Buelow, and J. W. Nicholson, "Measurement of shock wave rise times in metal thin films," *Phys. Rev. Lett.* **85**, 3205-8 (2000).
- 19 J. P. Chen, R. X. Li, Z. N. Zeng, X. T. Wang, W. Y. Wang, Y. H. Jiang, C. F. Cheng, and Z. Z. Xu, "Simultaneous measurement of laser-induced shock wave and released particle velocities at Mbar pressure," *J. Appl. Phys.* **94**, 858-62 (2003).
- 20 J. P. Geindre, P. Audebert, A. Rousse, F. Fallies, J. C. Gauthier, A. Mysyrowicz, A. Dossantos, and G. Hamoniaux, "Frequency-domain interferometer for measuring the phase and amplitude of a femtosecond pulse probing a laser-produced plasma," *Opt. Lett.* **19**, 1997-9 (1994).
- 21 P. Blanc, P. Audebert, F. Fallies, J. P. Geindre, J. C. Gauthier, A. DosSantos, A. Mysyrowicz, and A. Antonetti, "Phase dynamics of reflected probe pulses from sub-100-fs laser-produced plasmas," *J. Opt. Soc. Am. B* **13**, 118-24 (1996).
- 22 C. Quoix, G. Hamoniaux, A. Antonetti, J. C. Gauthier, J. P. Geindre, and P. Audebert, "Ultrafast plasma studies by phase and amplitude measurements with femtosecond spectral interferometry," *J. Quant. Spectrosc. Radiat. Transfer* **65**, 455-62 (2000).
- 23 D. J. Funk, D. S. Moore, K. T. Gahagan, S. J. Buelow, J. H. Reho, G. L. Fisher, and R. L. Rabie, "Ultrafast measurement of the optical properties of aluminum during shock-wave breakout," *Phys. Rev. B* **64**, 115114-5 (2001).
- 24 S. D. McGrane, D. S. Moore, and D. J. Funk, "Sub-picosecond shock interferometry of transparent thin films," *J. Appl. Phys.* **93**, 5063-8 (2003).
- 25 M. C. Simon, "Wollaston prism with large split angle," *Appl. Opt.* **25**, 369-76 (1986).
- 26 S. Linden, H. Giessen, and J. Kuhl, "XFROG-a new method for amplitude and phase characterization of weak ultrashort pulses," *Phys. Status Solidi B* **206**, 119-24 (1998).
- 27 J. P. Geindre, P. Audebert, S. Rebibo, and J. C. Gauthier, "Single-shot spectral interferometry with chirped pulses," *Opt. Lett.* **26**, 1612-14 (2001).

Chapter 5

Ultrafast Dynamic Ellipsometry of Polymers

5.1 Introduction

The method of ultrafast dynamic ellipsometry (UDE) was developed using thin polymer film samples. The polymer films were chosen because of the relative ease of sample fabrication, the accessibility of the materials, and the large compression created in polymers by relatively low shock pressures. The compression creates significant changes in the refractive index of the polymers, resulting in strong changes in the measured reflectance.

In this chapter, the UDE model and the fitting routine used on the polymer samples are explained, and the dependence of the material properties on the resulting UDE data is discussed. Then, UDE is applied to four different polymers: polycarbonate, poly(methyl methacrylate), poly(chlorotrifluoroethylene-*co*-vinylidene fluoride), and Sylgard 184. The accompanying analysis yields data on the shock equation of state, provided in the form of the shock velocity-particle velocity Hugoniot, and on the shock compressed refractive index for each material.

5.2 Thin film model and fitting routine for transparent materials

A shock traveling through a polymer causes compression, which increases the material's density and refractive index. This new compressed layer creates an additional optical interface (Fresnel surface) in the sample. The thickness of this layer grows as the shock travels further into the material, and the thickness of the pristine polymer layer decreases correspondingly. The time-dependent thicknesses of these two layers (the shocked and unshocked) give rise to changes in the reflectance from the material. By measuring the change in reflectance as a function of time at 2 angles and with 2 orthogonal polarizations of light, the optical properties and velocities of the material layers in the sample can be determined. Figure 5-1 depicts the two layers that are formed in a polymer and the reflections of the probe light at the layer interfaces.

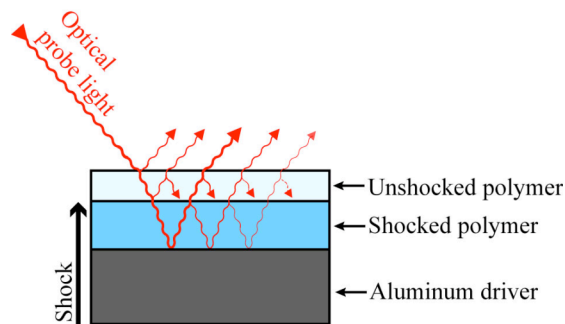


Fig. 5-1. Sketch of the optical layers in the sample showing some of the multiple reflections of the probe light. The shock is traveling upwards from the Al through the polymer. The change in density due to shock compression splits the polymer into two layers, shocked and unshocked, generating an optical interface at the shock front.

To calculate the reflectance, the matrix formalism for light propagating in stratified media was used.¹ The characteristic matrix that captures how light propagates in a medium is given by Eq. (5.1):

$$M(d) = \begin{bmatrix} \cos\left(\frac{2\pi}{\lambda_0} nd \cos\theta\right) & \frac{i}{q} \sin\left(\frac{2\pi}{\lambda_0} nd \cos\theta\right) \\ iq \sin\left(\frac{2\pi}{\lambda_0} nd \cos\theta\right) & \cos\left(\frac{2\pi}{\lambda_0} nd \cos\theta\right) \end{bmatrix}. \quad (5.1)$$

Here, d is the thickness of the material, n is the refractive index, θ is the incident angle in the material, and λ_0 is the wavelength in vacuum. In Eq. (5.1), q is defined separately for each polarization. For s-polarized light

$$q = n \cos\theta. \quad (5.2)$$

For p-polarized light

$$q = \frac{\cos\theta}{n}. \quad (5.3)$$

When a structure consists of multiple layers, the characteristic matrix for the entire structure is obtained by multiplying the characteristic matrices for each individual layer in the order in which they are encountered by the probe light. This matrix is written in Eq. (5.4).

$$M(d) = M_1(d_1)M_2(d_2)\cdots M_N(d_N). \quad (5.4)$$

Using the condition that the electric and magnetic fields are continuous across each boundary, it can be shown that the reflectance from the media is

$$r = \frac{(m_{11} + m_{12}q_N)q_1 - (m_{21} + m_{22}q_N)}{(m_{11} + m_{12}q_N)q_1 + (m_{21} + m_{22}q_N)} = \rho e^{i\phi}, \quad (5.5)$$

where m denotes the elements of the characteristic matrix, q_1 is the q defined in equation (5.2) or (5.3) for the first layer, and q_N is the q for the last layer. In Eq. (5.5), the phase shift of the light upon reflection is ϕ , and the reflectivity is ρ^2 .

In this experiment, the absolute reflectance of the light is not measured, but rather the measured quantity is the change in reflectance. The phase shift is a function of both the change in the path length of the reflected light and changes due to interference of the light at multiple boundaries. The phase shift arises from changes in the optical properties of the material, changes in the thicknesses of the layers, and movement of the material layers. This is shown in Fig. 5-2, which plots the phase change for a shock emerging from a bare Al film and for a shock in a polycarbonate layer on an Al film.

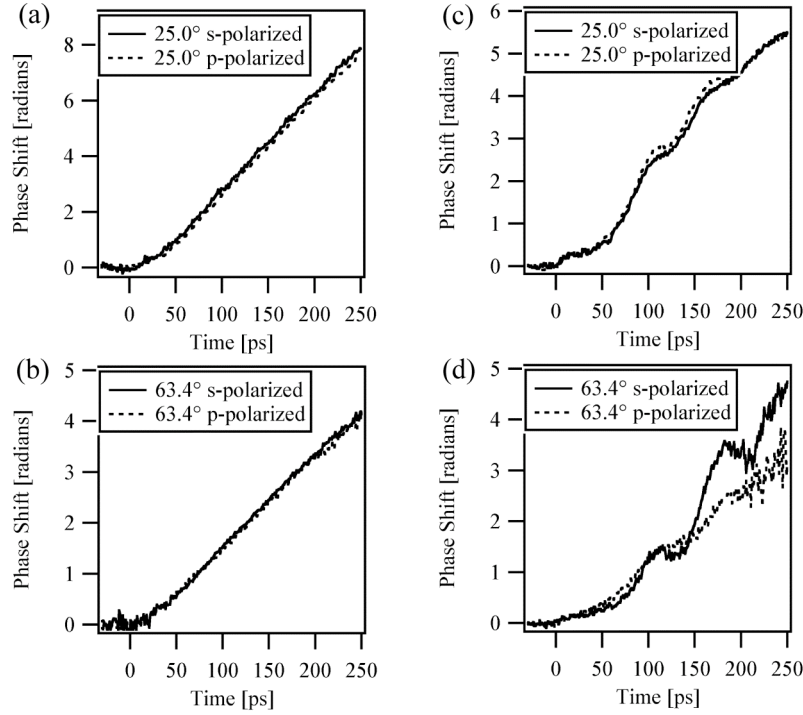


Fig. 5-2. The phase shift versus time of light reflected by a shock emerging from a bare Al film and in polycarbonate covering an Al film. The phase shift in (a)-(b) is due to movement of the Al free surface. Using the phase shift versus time to find the free surface velocity, the pressure was calculated to be 20.5 ± 0.7 GPa. In (c)-(d), the positive phase shift is primarily from the movement of the interface between the Al and the shocked polycarbonate, which results from the particle velocity of the polycarbonate. The oscillations in the phase shift are from the thin film effects arising from the time-dependent thicknesses of the shocked and unshocked layers of the polycarbonate.

A measurement of the reflected light from a bare Al surface as a shock wave emerges yields a phase shift that is primarily a result of the movement of the free surface (Funk *et al.*² measured phase shifts due to Al optical properties at the peak of the pressure wave in Al, but they are orders of magnitude smaller than the phase shifts due to surface motion discussed here). The free surface velocity, u_{fs} , is calculated using the change in the phase shift, $\Delta\phi$, and the change in time, Δt , as given in the following equation:

$$u_{fs} = \frac{\lambda}{4\pi \cos \theta} \frac{\Delta \phi}{\Delta t}, \quad (5.6)$$

where λ is the wavelength of the light and θ is the incident angle. For a free surface at low shock pressures, the particle velocity is well approximated as half of the free surface velocity.³ The shock velocity is calculated from the Al Hugoniot⁴ $u_s = 5.38 + 1.34u_p$, where u_s is the shock velocity and u_p is the particle velocity. The pressure of the Al shock shown in Fig. 5-2 was calculated using Eq. (5.7).

$$P = P_0 + \rho_0 u_s u_p, \quad (5.7)$$

where P is the shock pressure, P_0 is the initial pressure, and ρ_0 is the initial density. A more extensive discussion of free surface velocity measurements in thin metal films is available from Gahagan *et al.*⁵

For a shock in a polymer thin film, the reflectance was calculated using equations (5.1)-(5.5), in which the shocked and unshocked materials are treated as layers with different refractive indices. The majority of the phase shift is due to the movement of the interface between the Al and the shocked polymer, similar to the movement of the Al free surface, with the oscillations in the phase shift resulting from the changing thicknesses of the shocked and unshocked polymer layers.

On the timescale of this experiment, the acceleration of the material at the shock front was not instantaneous. This acceleration has been studied in Al and other metals,⁵ in which the free surface position of the metal fit very well to a function of the following form:

$$x(t) = \int \frac{1}{2} [1 + \tanh(\frac{t-t_0}{\tau})] u_{fs} dt, \quad (5.8)$$

where x is the surface position, t is time, t_0 is the time of maximum material acceleration, τ is the time constant of the rise, and u_{fs} is the free surface velocity. For bare Al films, τ was previously measured as 5.5 ps.⁵ In the model used to analyze the data, the function in equation (5.8) describes the acceleration of the Al and of the polymer at the shock front, and the rise time constant of both was set at 5.5 ps.

To model the time dependence of the material motion, the thicknesses of the shocked and unshocked polymer layers were allowed to vary as a function of the shock and particle velocities. The time-dependent thickness of the unshocked polymer layer, d_u , was given by

$$d_u(t) = d_0 - \int \frac{1}{2} [1 + \tanh(\frac{t-t_0}{\tau})] u_s dt, \quad (5.9)$$

where d_0 is the original thickness of the film. As the shock moved through the polymer, the material behind the shock wave began moving at the particle velocity. The resulting change in thickness of the shocked layer is a function of the difference between the shock and particle velocities. For the shocked polymer layer, the thickness started at zero and grew in time as given by

$$d_s(t) = \int \frac{1}{2} [1 + \tanh(\frac{t-t_0}{\tau})] (u_s - u_p) dt, \quad (5.10)$$

where d_s is the thickness of the shocked polymer film.

For the analysis of the data, a five layer time-dependent structure was assumed. The first layer was air with a refractive index set to 1. The second layer was the unshocked polymer for which the initial refractive index and initial thickness were fitting parameters. The third layer was the shocked polymer with a refractive index that also was a fitting parameter. The fourth layer was Al₂O₃, resulting from the surface oxidation

of the vapor-plated Al. The thickness of this layer was set at 7 nm, which was the typical thickness measured with spectroscopic ellipsometry, and the index was set to 1.76.⁶ The final layer was 2 μm of Al with the refractive index of $2.8 + i 8.45$.⁷

Phase shift and reflectivity data were taken along a single pixel row across the center of each Gaussian shaped shock. Using equations (5.1)-(5.5) and (5.8)-(5.10), all eight sets of data were simultaneously fit for the initial refractive index, the shocked refractive index, the initial thickness of the film, the shock velocity, and the particle velocity using the Levenberg-Marquardt least squares fitting algorithm. A set of polycarbonate data and its fit are shown in Fig. 5-3. The errors reported are obtained from the diagonal elements of the covariance matrix of the least squares fit.

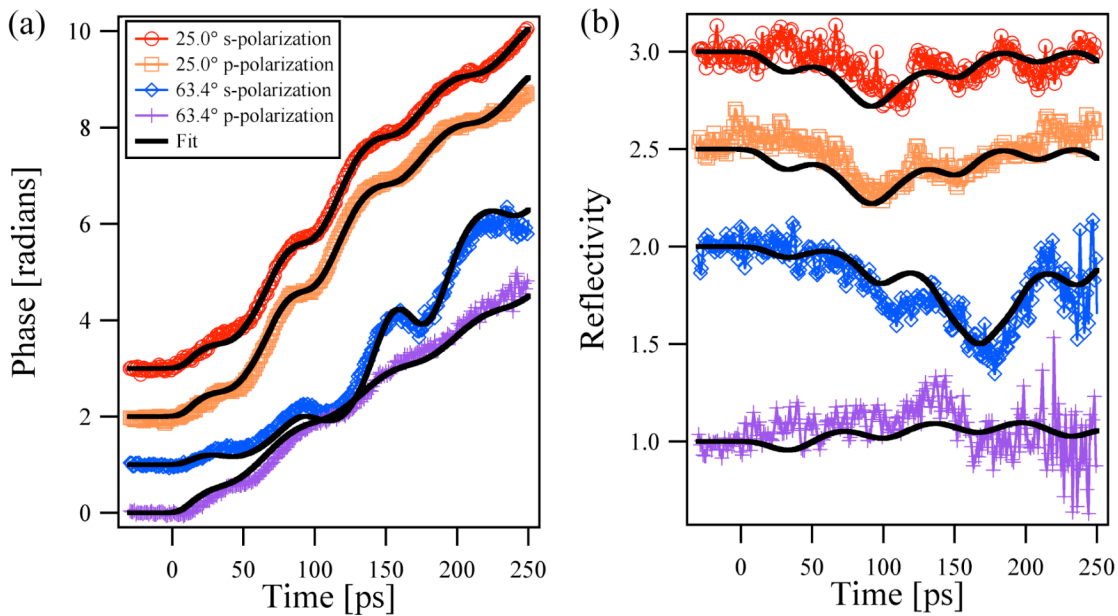


Fig. 5-3. (a) Phase shift and (b) reflectivity data from the two angles and both polarizations along with the fit to the data for a 13.6 ± 0.2 GPa shock in a 1620 nm polycarbonate film on 2 μm Al. Data are vertically offset for clarity.

Over the range of time for which the data were fit, the shock and particle velocities were assumed to be constant, also making pressure constant by equation (5.7). The agreement between the data and the fit in Fig. 5-3 indicates that this assumption is reasonable for the pressure wave propagating in the polycarbonate.

Also embedded in the analysis was the assumption that the initial refractive index and the density of the thin films were constant throughout the thickness of the films. The shocked refractive index of the polymers was also assumed to be constant as a function of thickness and time. These assumptions for the refractive indices greatly simplified the analysis by allowing only two layers in the polymers (shocked and unshocked) that had changing thicknesses with time.

5.3 Dependence of data on experimental parameters

5.3.1 Calculation method

During the first experiments with thin polymer films, it was observed that the data produced from some films showed very strong oscillations, while data from other films showed substantially weaker oscillations. The data with stronger oscillations were much more desirable because the oscillations more tightly constrained the fit, resulting in increased precision of the Hugoniot data and optical properties. To determine which sample traits were influencing the data so that they could be appropriately manipulated to provide the desired data, a series of calculations was performed, in which data were simulated while the characteristics of the sample were varied. The data were simulated for a polycarbonate sample using the thin film model described in the previous section.

The same five layers as described earlier were used to simulate the data (air, unshocked polycarbonate, shocked polycarbonate, alumina, and aluminum). For a good estimate of how the thicknesses of the shocked and unshocked layers would vary with time, shock and particle velocities were used from the LASL Shock Hugoniot Data.⁴ The initial thicknesses of the layers are given in Eq. (5.11), where $d_{0,u}$ is the initial thickness of the polycarbonate layer.

$$d_0[\text{nm}] = \begin{bmatrix} d_{\text{air}} \\ d_{0,u} \\ d_{0,s} \\ d_{\text{Al}_2\text{O}_3} \\ d_{\text{Al}} \end{bmatrix} = \begin{bmatrix} 10^7 \\ d_{0,u} \\ 0 \\ 7 \\ 2000 \end{bmatrix} \quad (5.11)$$

The thicknesses at time t are given by Eq. (5.12), where $d_u(t)$ is given by (5.9), and $d_s(t)$ is given by (5.10). Both equations are integrated from 0 to t .

$$d(t)[\text{nm}] = \begin{bmatrix} 10^7 \\ d_u(t) \\ d_s(t) \\ 7 \\ 2000 \end{bmatrix} \quad (5.12)$$

In this model, the refractive indices do not vary with time, so the refractive indices at any time are the same as the initial refractive indices.

$$n = n_0 = \begin{bmatrix} n_{\text{air}} \\ n_u \\ n_s \\ n_{\text{Al}_2\text{O}_3} \\ n_{\text{Al}} \end{bmatrix} = \begin{bmatrix} 1 \\ 1.549 \\ n_s \\ 1.76 \\ 2.8 + i8.45 \end{bmatrix} \quad (5.13)$$

The refractive indices are set to literature values for the unshocked polycarbonate ($n=1.549^8$), the alumina ($n=1.76^6$), and the aluminum ($n=2.8+i8.45^7$). For some

materials, the Gladstone-Dale relation has been used to describe the change in refractive index with the change in density due to shock compression. The Gladstone-Dale relation can be simply stated as:

$$\frac{n-1}{\rho} = \text{constant} , \quad (5.14)$$

where n is the refractive index and ρ is the density.⁹ As the refractive indices of many dielectrics, especially polymers, conform well to the Gladstone-Dale model upon compression, it was used to calculate the shocked refractive index of the polycarbonate film as shown in Eq. (5.15).

$$n_s = 1 + \frac{(n_0 - 1)}{\left(1 - \frac{u_p}{u_s}\right)} + i0 \quad (5.15)$$

The angle of light propagation in each layer was calculated with Snell's Law, starting with the incident angle of the light in air (63.4° or 26.6°) and using the refractive indices from Eq. (5.13).

$$\theta_i = \sin^{-1}\left(\frac{n_{i-1} \sin \theta_{i-1}}{n_i}\right) \quad (5.16)$$

Since a chirped pulse was used to probe the sample, the wavelength was adjusted as a function of time. The time-dependence of the probe wavelength using XFROG data fit well to a second order polynomial, which had a small second order dependence.

$$\lambda(t) = \lambda_0 + \lambda_1 t + \lambda_2 t^2 \quad (5.17)$$

The typical starting wavelength was approximately 810 nm, and the wavelength spanned approximately 20 nm in 300 ps.

$$\lambda(t) = 810\text{nm} + \frac{20\text{nm}}{300\text{ps}}t + \frac{0\text{nm}}{\text{ps}^2}t^2 \quad (5.18)$$

Using these parameters, the complex reflectance r was calculated with Eqs. (5.1) - (5.5). The measured quantity is the change in reflectance, so the phase shift and the change in reflectivity were calculated by

$$\Delta\phi = \text{Im}\{r[n_0, d_0, \theta, \lambda(t)]\} - \text{Im}\{r[n, d(t), \theta, \lambda(t)]\} \quad (5.19)$$

and

$$\Delta R = \frac{|\text{Re}\{r[n_0, d_0, \theta, \lambda(t)]\}|^2}{|\text{Re}\{r[n, d(t), \theta, \lambda(t)]\}|^2}, \quad (5.20)$$

where r is from Eq. (5.5).

5.3.2 Simulated data with various film thicknesses

In cases where the thickness of a film is on the same order as the wavelength of light used to probe it, the thickness of the film often has a strong influence. With that in mind, the first parameter explored was the film thickness.

For a shock pressure of 11.1 GPa in polycarbonate, the shock velocity was 5.12 km/s, and the particle velocity was 1.82 km/s.⁴ The phase shift and reflectivity were calculated at each ps from 50 ps before the arrival of the shock at the Al/polycarbonate interface to 200 ps after. This time profile was calculated for initial thicknesses of the polycarbonate layer from 1000 to 2000 nm in 5 nm steps. The results of these calculations are shown in Figs. 5-4 through 5-7.

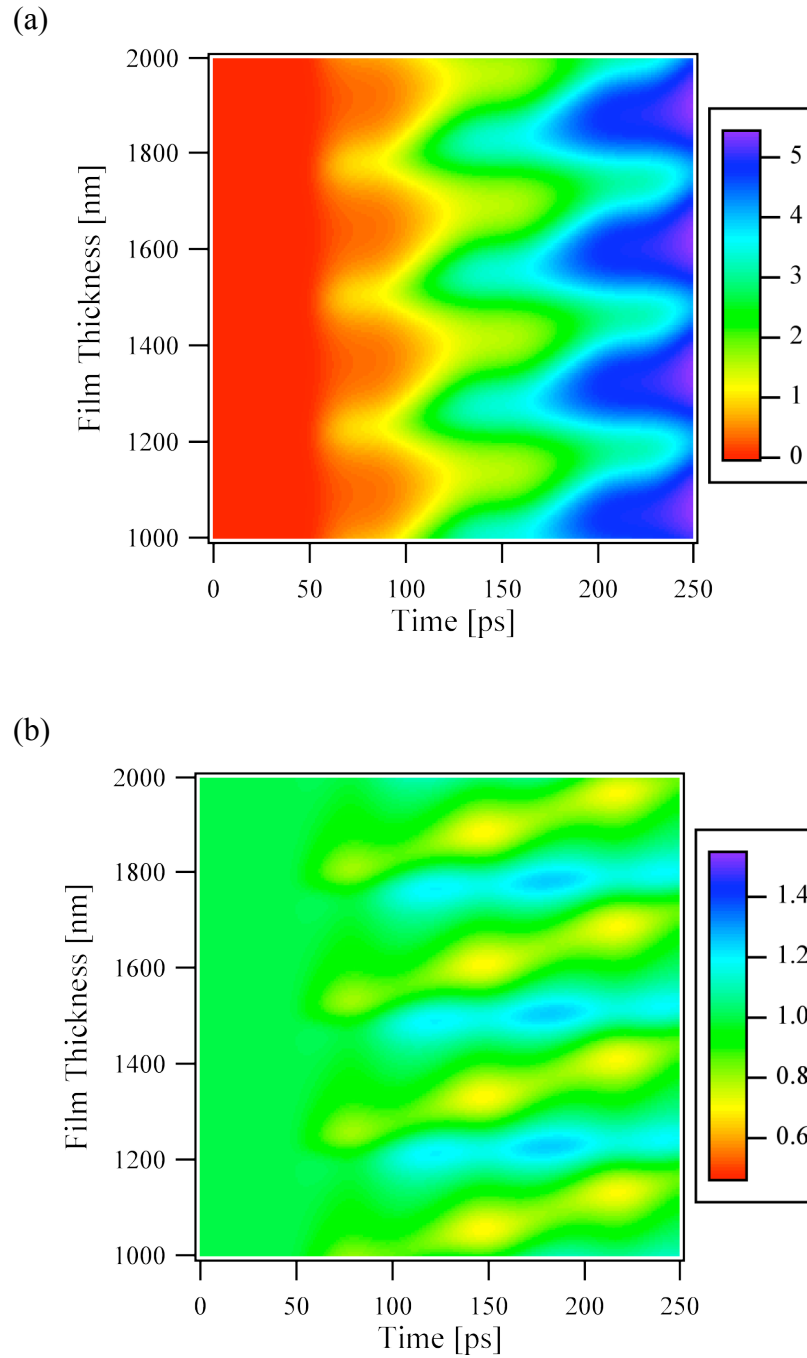


Fig. 5-4. (a) Phase shift and (b) reflectivity vs. time as a function of polycarbonate film thickness for s-polarized probe light at 26.6° incident angle.

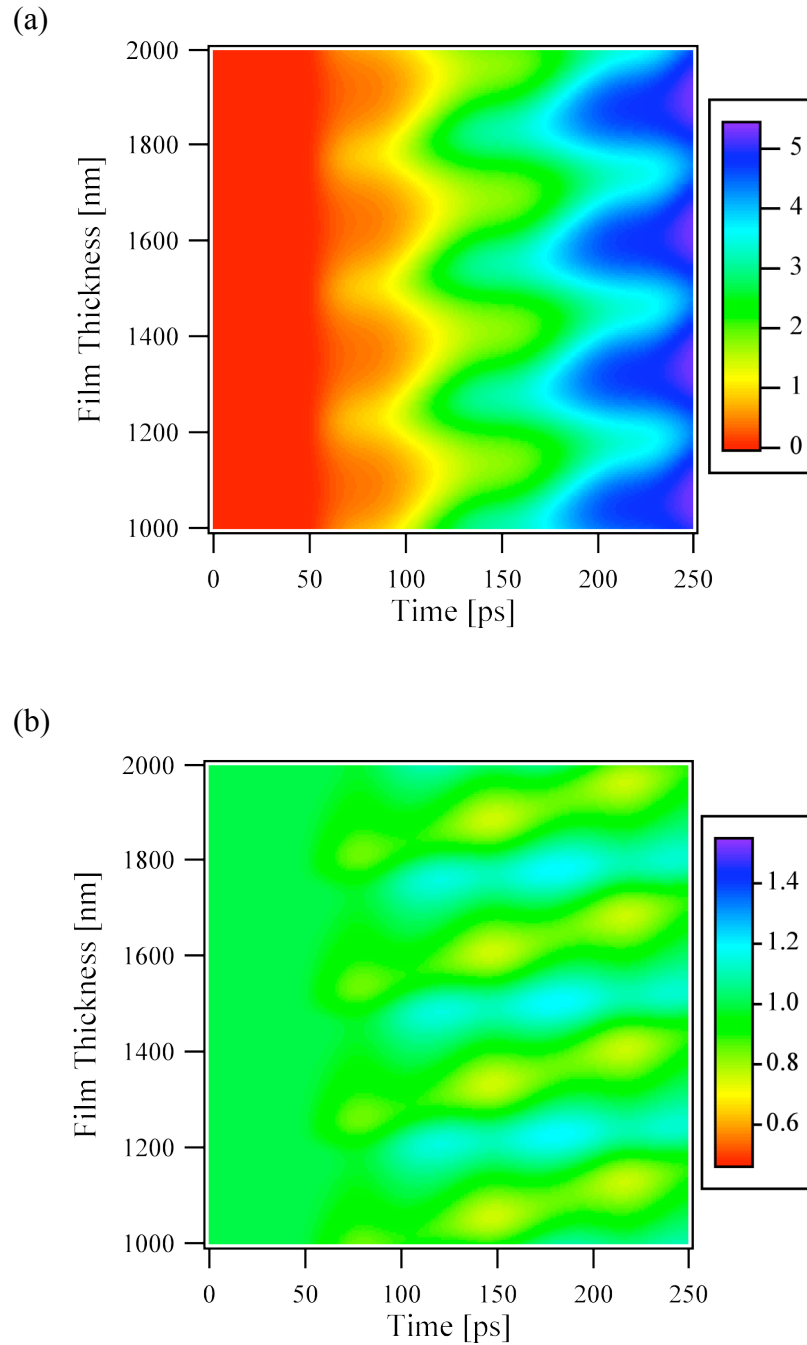


Fig. 5-5. (a) Phase shift and (b) reflectivity vs. time as a function of polycarbonate film thickness for p-polarized probe light at 26.6° incident angle.

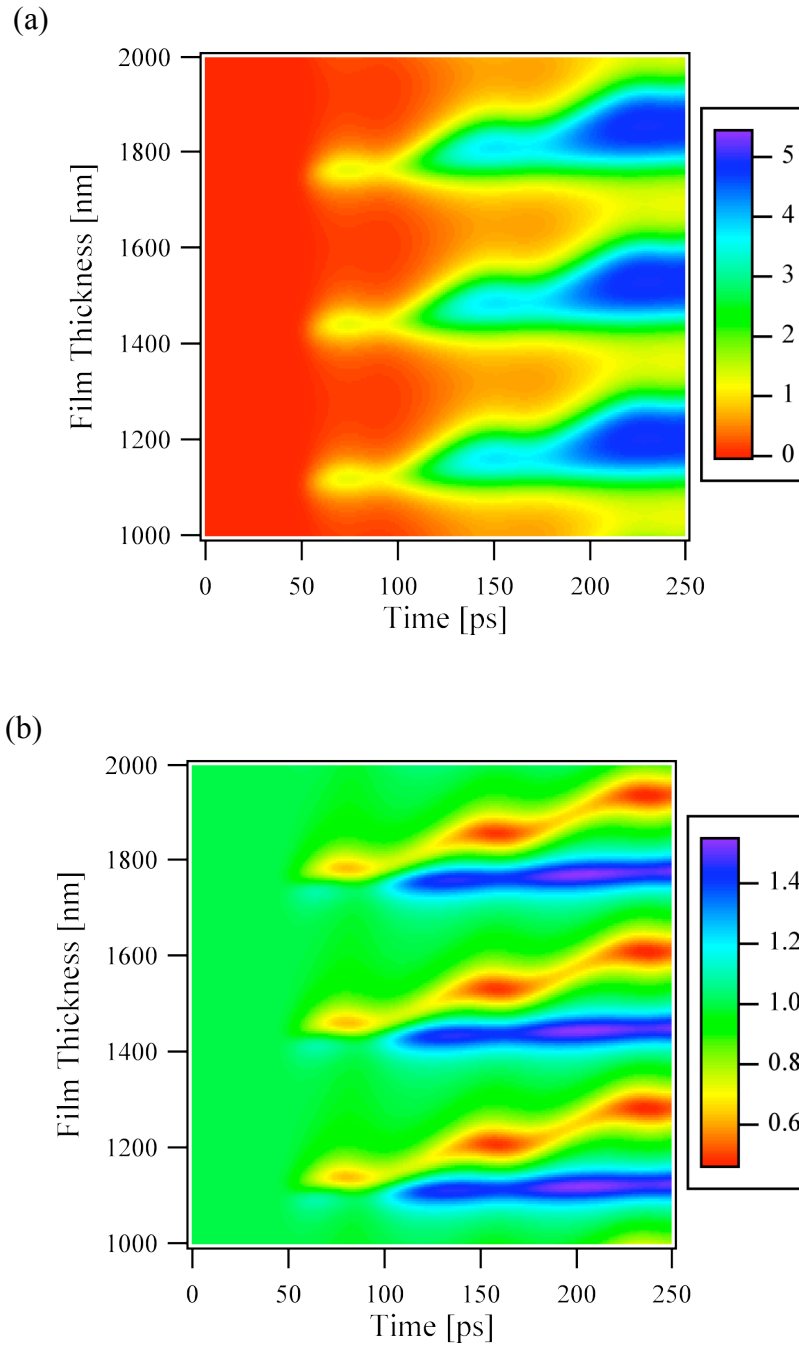


Fig. 5-6. (a) Phase shift and (b) reflectivity vs. time as a function of polycarbonate film thickness for s-polarized probe light at 63.4° incident angle.

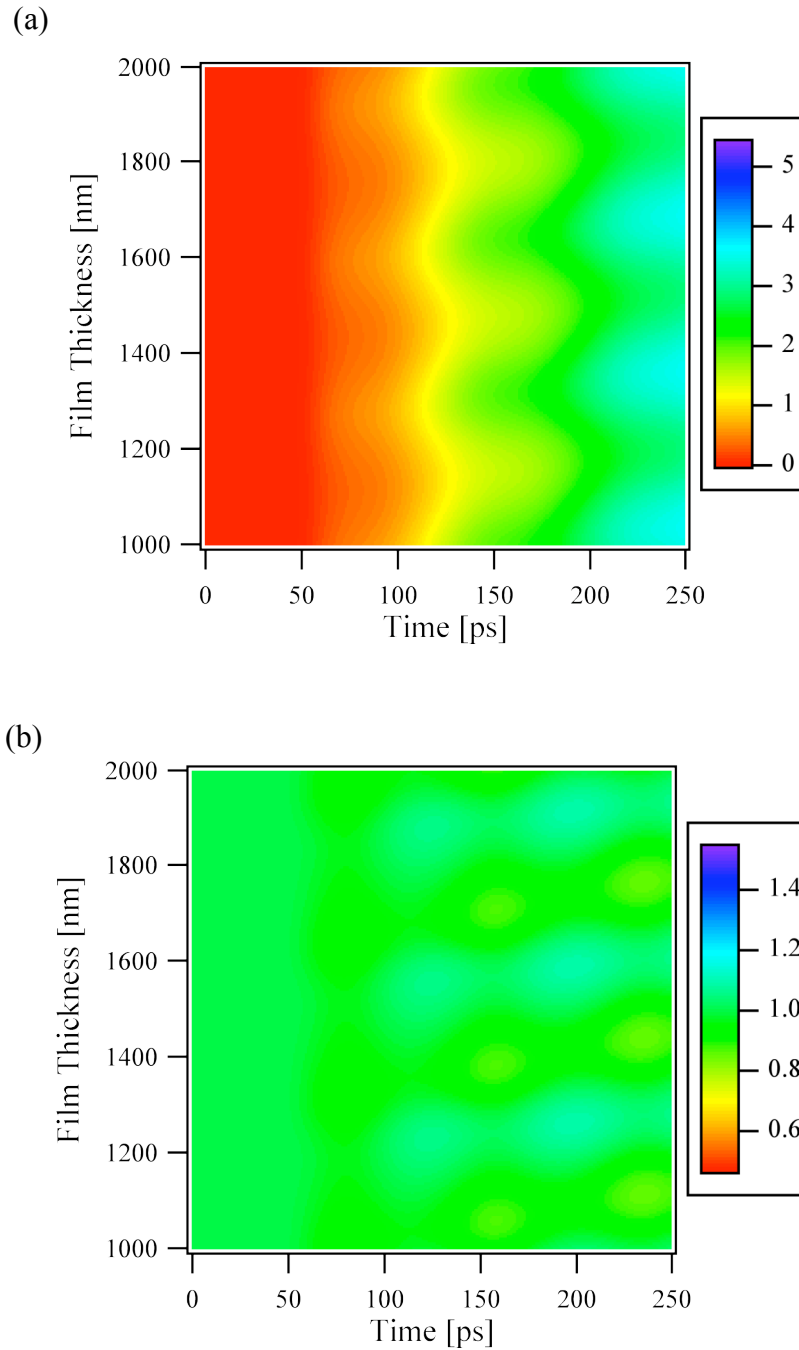


Fig. 5-7. (a) Phase shift and (b) reflectivity vs. time as a function of polycarbonate film thickness for p-polarized probe light at 63.4° incident angle.

To show how dramatically the data vary at different thicknesses, the time profiles (from the calculations in Figs. 5-4 to 5-7) for 1850 nm and 2000 nm thick films are shown in Figs. 5-8 and 5-9.

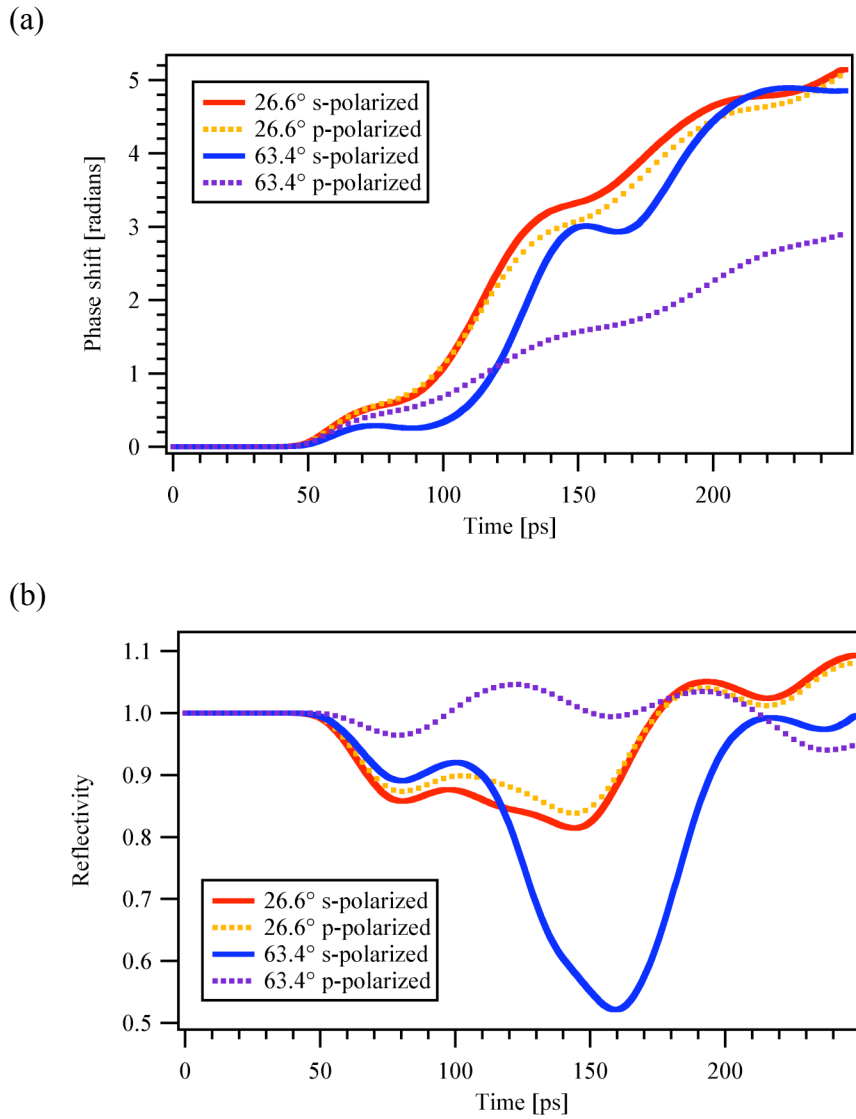


Fig. 5-8. Simulated (a) phase shift and (b) reflectivity data from the calculations shown in Figs. 5-4 – 5-7 for a polycarbonate thickness of 1850 nm.

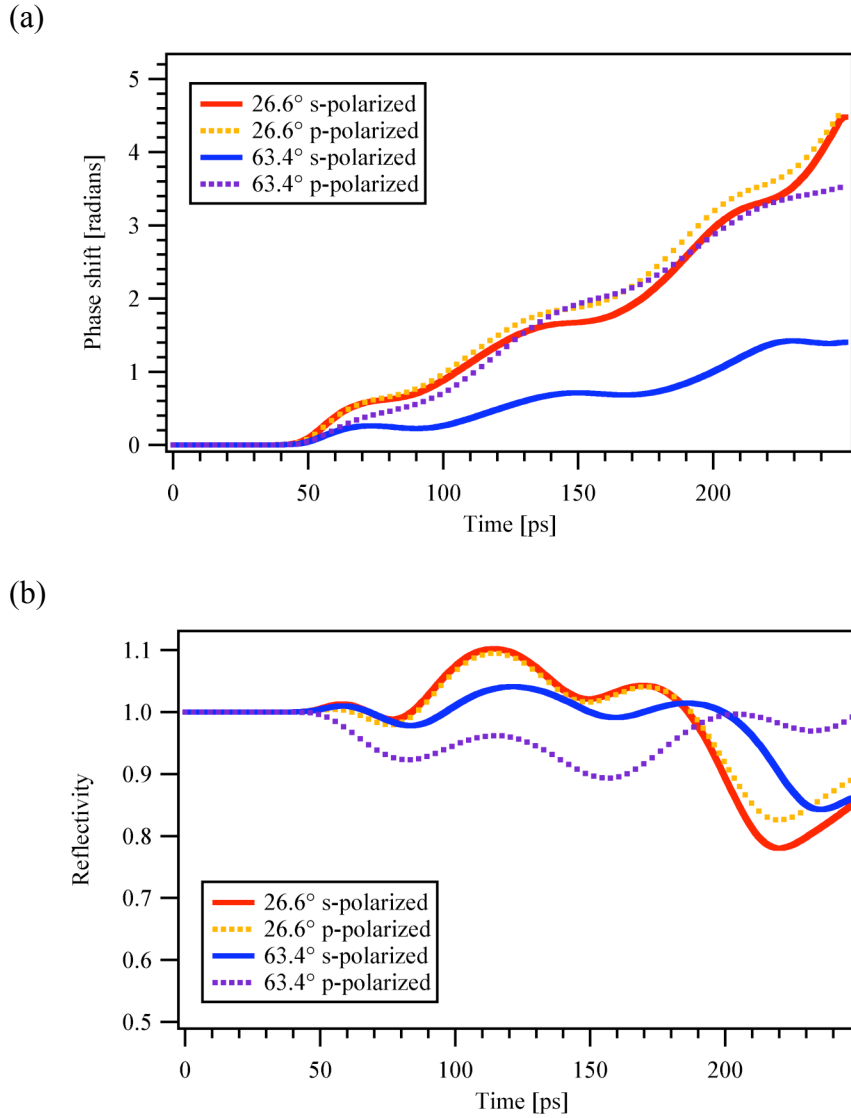


Fig. 5-9. Simulated (a) phase shift and (b) reflectivity data from the calculations shown in Figs. 5-4 – 5-7 for a polycarbonate thickness of 2000 nm.

These calculations show that the film thickness has a substantial effect on the magnitudes of the oscillations in the data. Therefore, the samples should be fabricated to produce a layer whose thickness will provide data that more tightly constrains the fit parameters.

5.3.3 Simulated data with various pressures

To better plan the sample fabrication, the calculations shown in the previous section were repeated to explore the effect of shock pressure on the desired thicknesses. The calculations were performed with shock and particle velocities from the LASL Shock Hugoniot Data⁴ corresponding to different pressures. The following pressures and velocities were chosen.

Table 5-1. Pressures and corresponding velocities used to simulate data.

Pressure [GPa]	Shock velocity [km/s]	Particle velocity [km/s]
4.32	3.86	0.94
6.58	4.32	1.28
7.73	4.54	1.43
9.99	4.98	1.68

The results of these calculations are shown in Figs. 5-10 through 5-13. The pressure does not change which thicknesses show stronger oscillations.

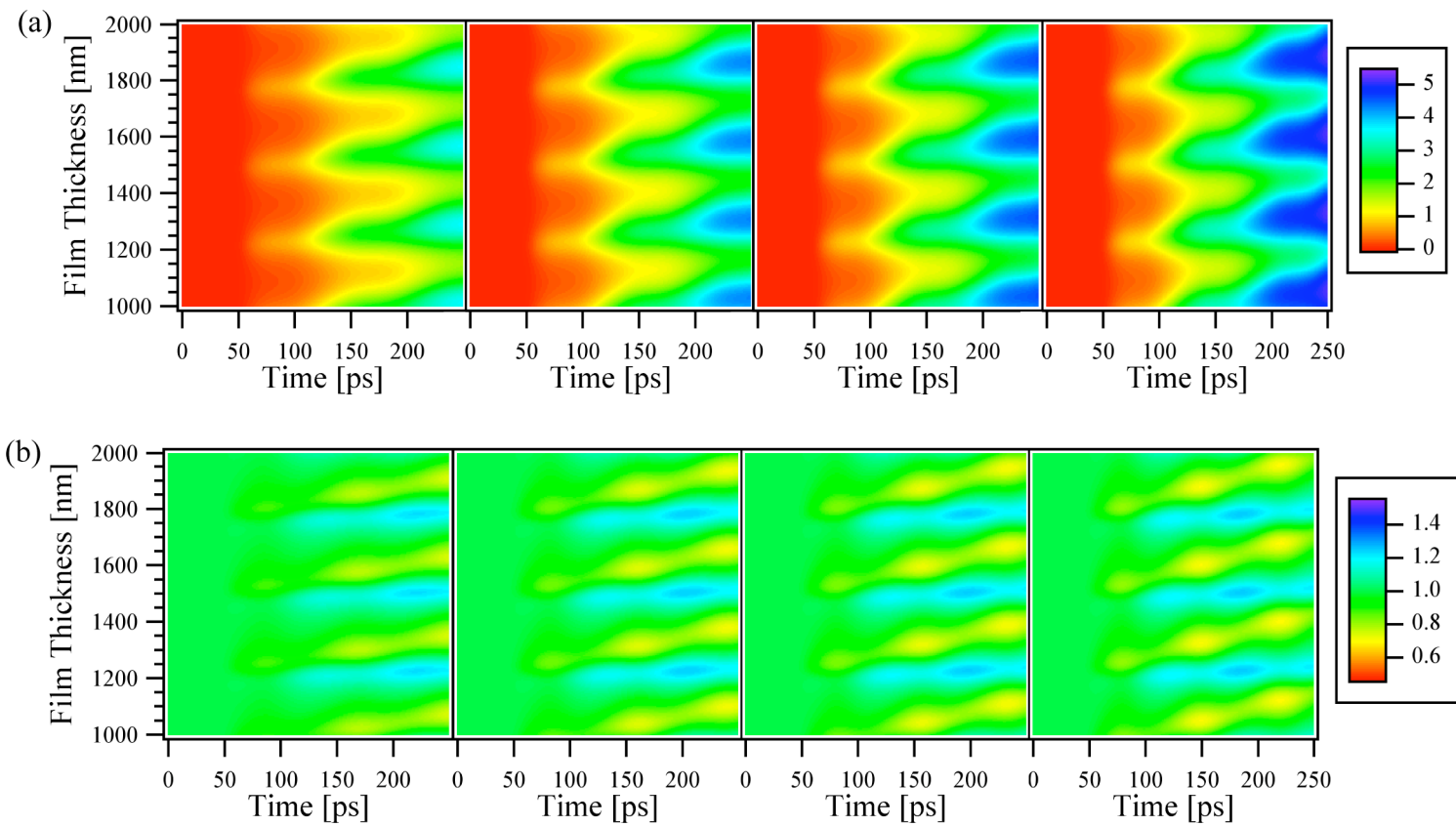


Fig. 5-10. (a) Phase shift and (b) reflectivity data simulated for different shock pressures at 26.6° incident angle and s-polarized probe light as a function of the initial thickness of the polycarbonate layer. From left to right, the pressures are 4.32, 6.58, 7.73, and 9.99 GPa.

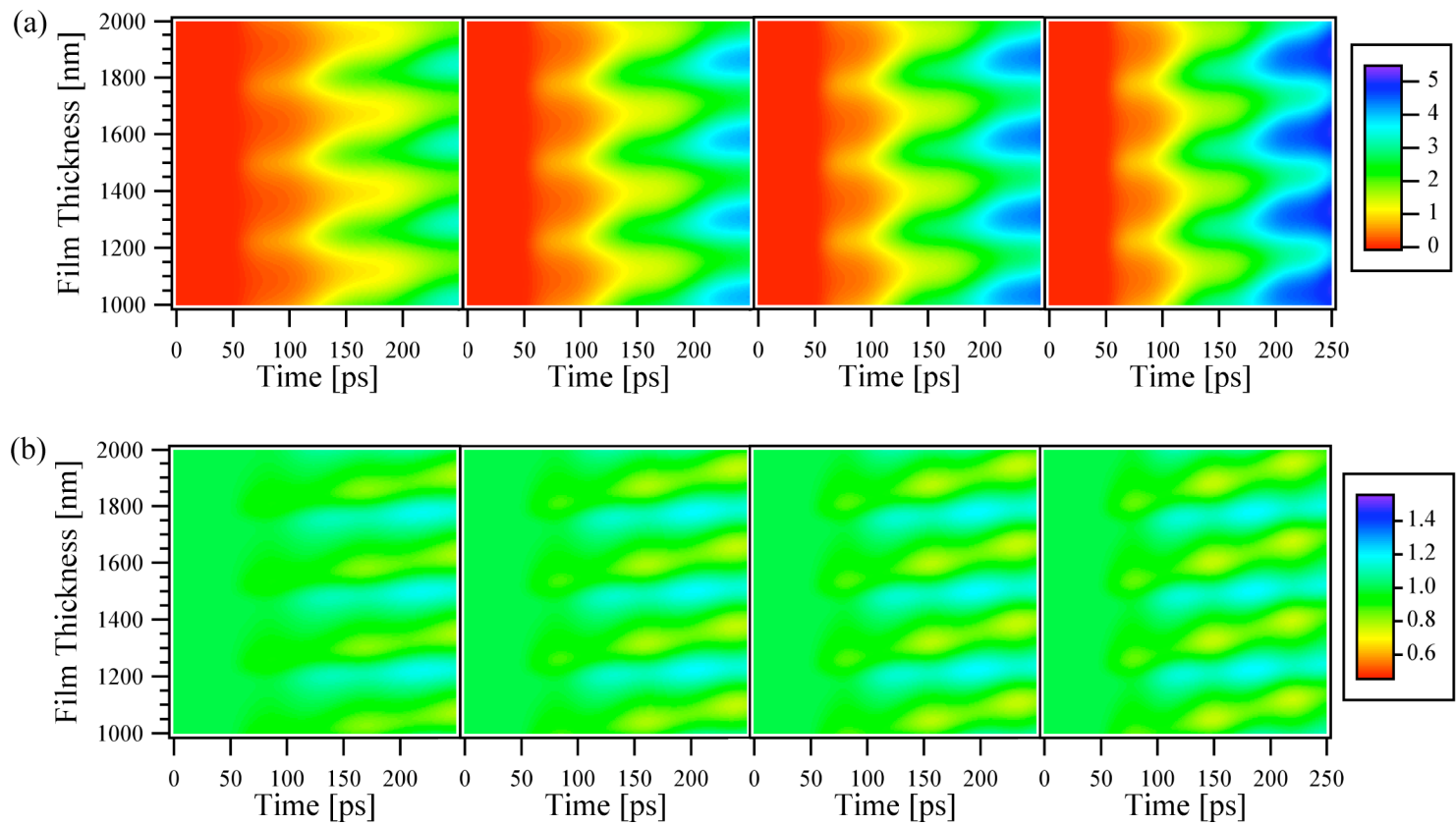


Fig. 5-11. (a) Phase shift and (b) reflectivity data simulated for different shock pressures at 26.6° incident angle and p-polarized probe light as a function of the initial thickness of the polycarbonate layer. From left to right, the pressures are 4.32, 6.58, 7.73, and 9.99 GPa.

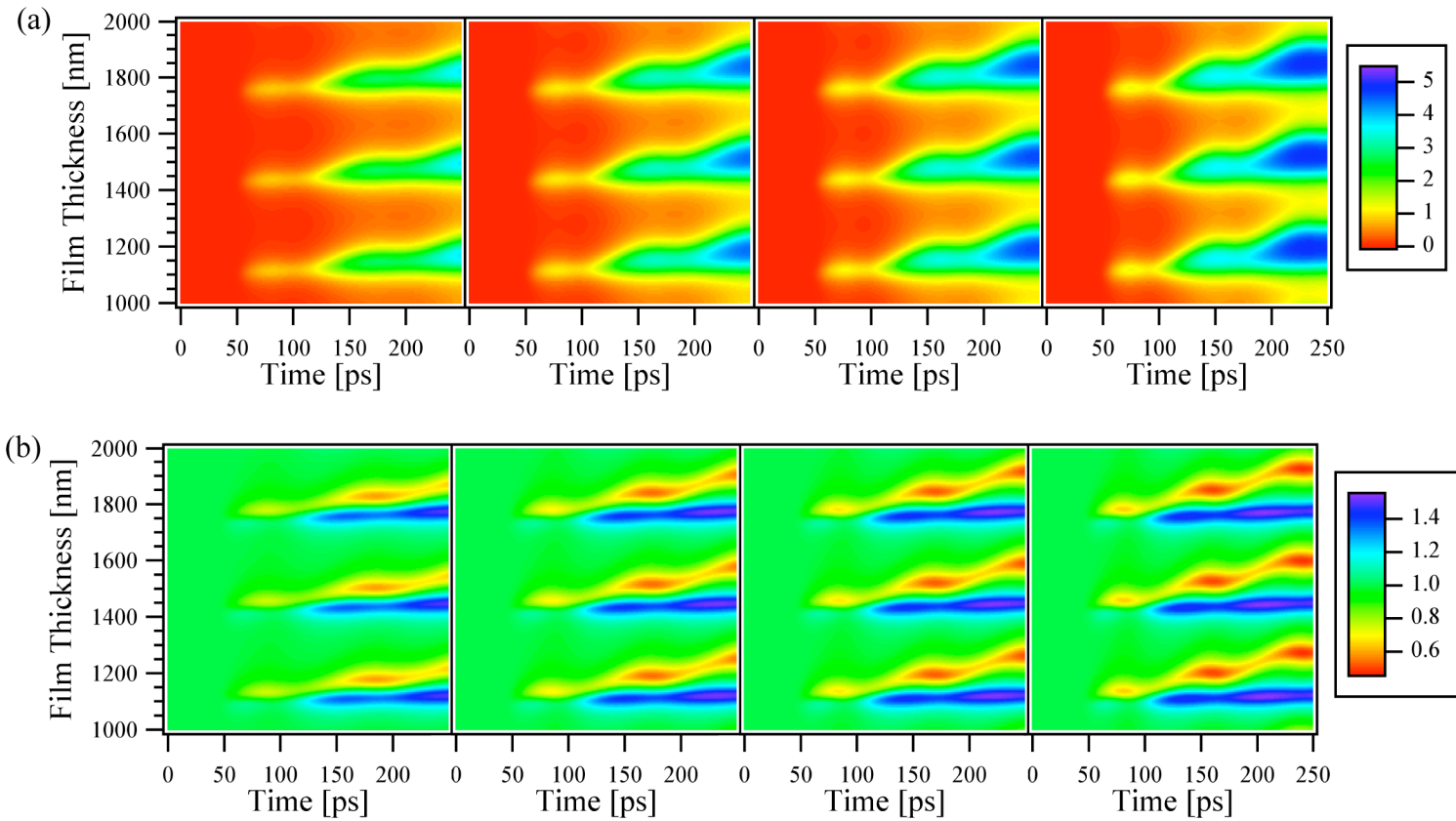


Fig. 5-12. (a) Phase shift and (b) reflectivity data simulated for different shock pressures at 63.4° incident angle and s-polarized probe light as a function of the initial thickness of the polycarbonate layer. From left to right, the pressures are 4.32, 6.58, 7.73, and 9.99 GPa.

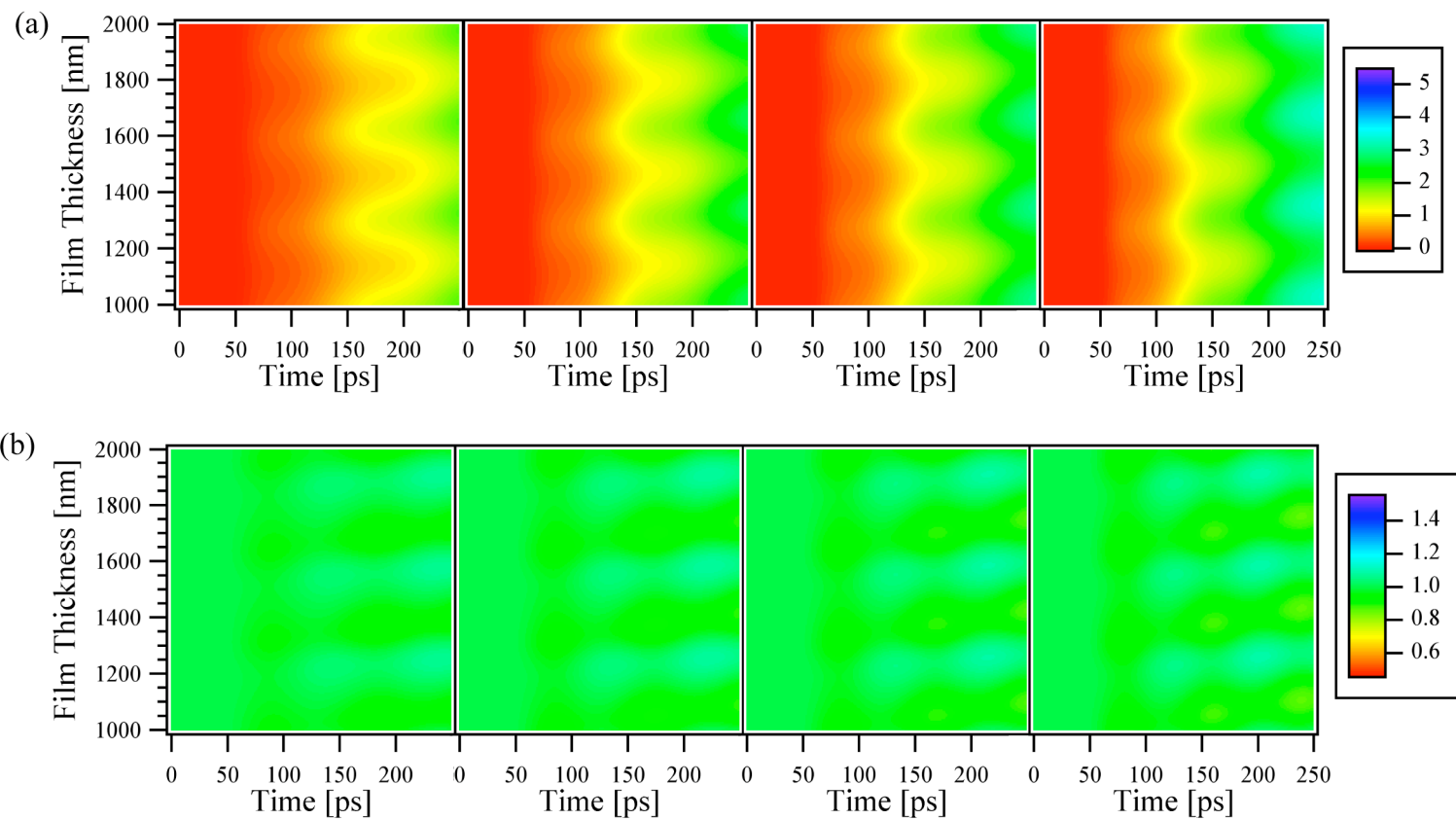


Fig. 5-13. (a) Phase shift and (b) reflectivity data simulated for different shock pressures at 63.4° incident angle and p-polarized probe light as a function of the initial thickness of the polycarbonate layer. From left to right, the pressures are 4.32, 6.58, 7.73, and 9.99 GPa.

5.3.4 Simulated data with various initial refractive indices

While fitting the data from the first experiments, it was discovered that the spin-coated polymer films did not have the same refractive index as bulk samples of the polymers. Due to the sample preparation, which involved dissolving the polymer in an organic solvent before spin coating, the films usually had a lower density and a lower refractive index than bulk samples. To identify how this difference would affect the optimal thicknesses for data collection, the previous calculations were repeated with various initial refractive indices of the unshocked film. The initial refractive indices used were 1.450, 1.500, 1.525, and 1.549. The results of the calculations are shown in Figs. 5-14 through 5-17. The results show that the optimum thicknesses depend slightly on the different refractive indices. This effect is readily explained in terms of the change in optical path length of the probe light as it travels through materials with different optical properties.

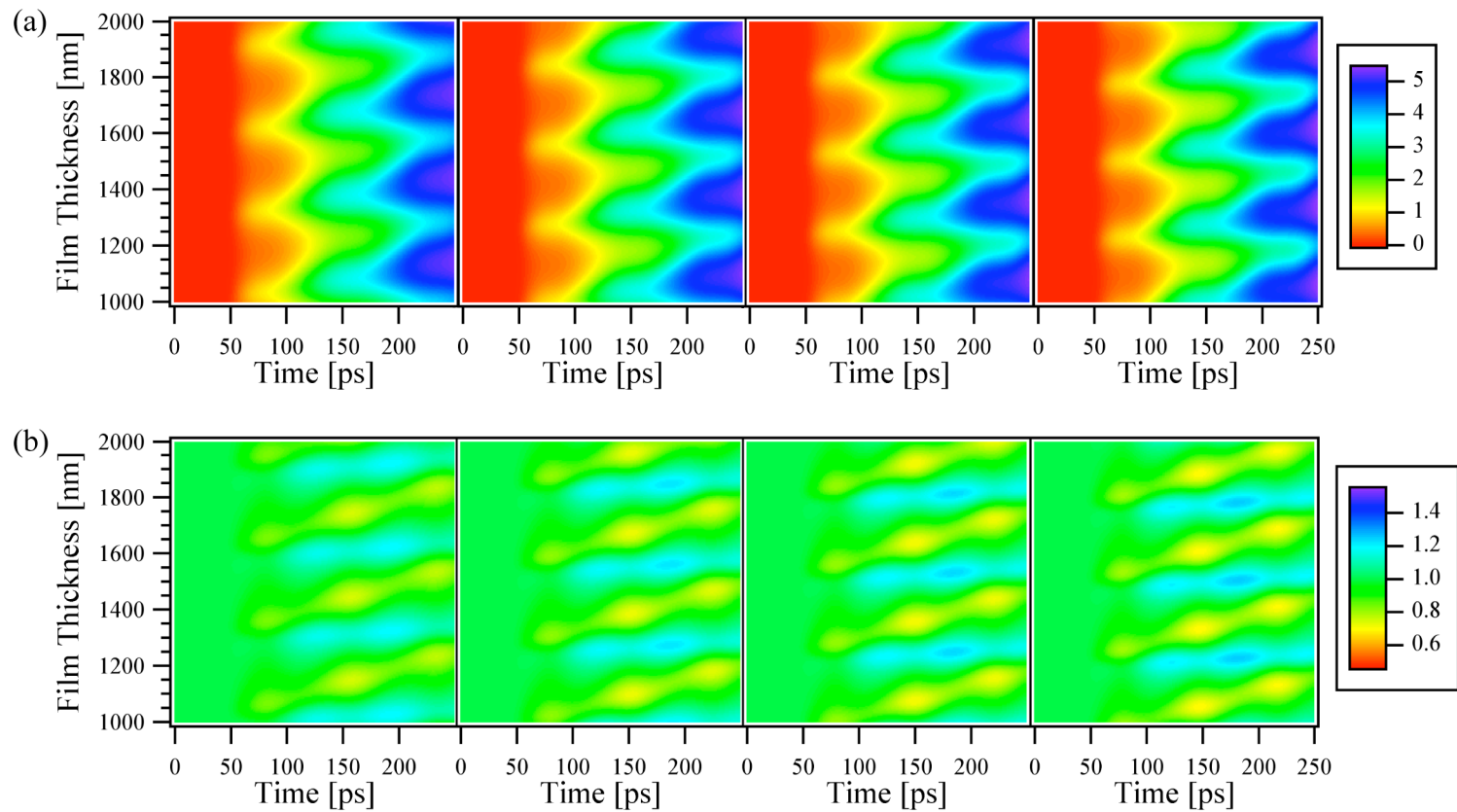


Fig. 5-14. (a) Phase shift and (b) reflectivity data simulated for polycarbonate films with different refractive indices at 26.6° incident angle and s-polarized probe light as a function of the initial thickness of the polycarbonate film. From left to right, the initial refractive indices are 1.450, 1.500, 1.525, and 1.549.

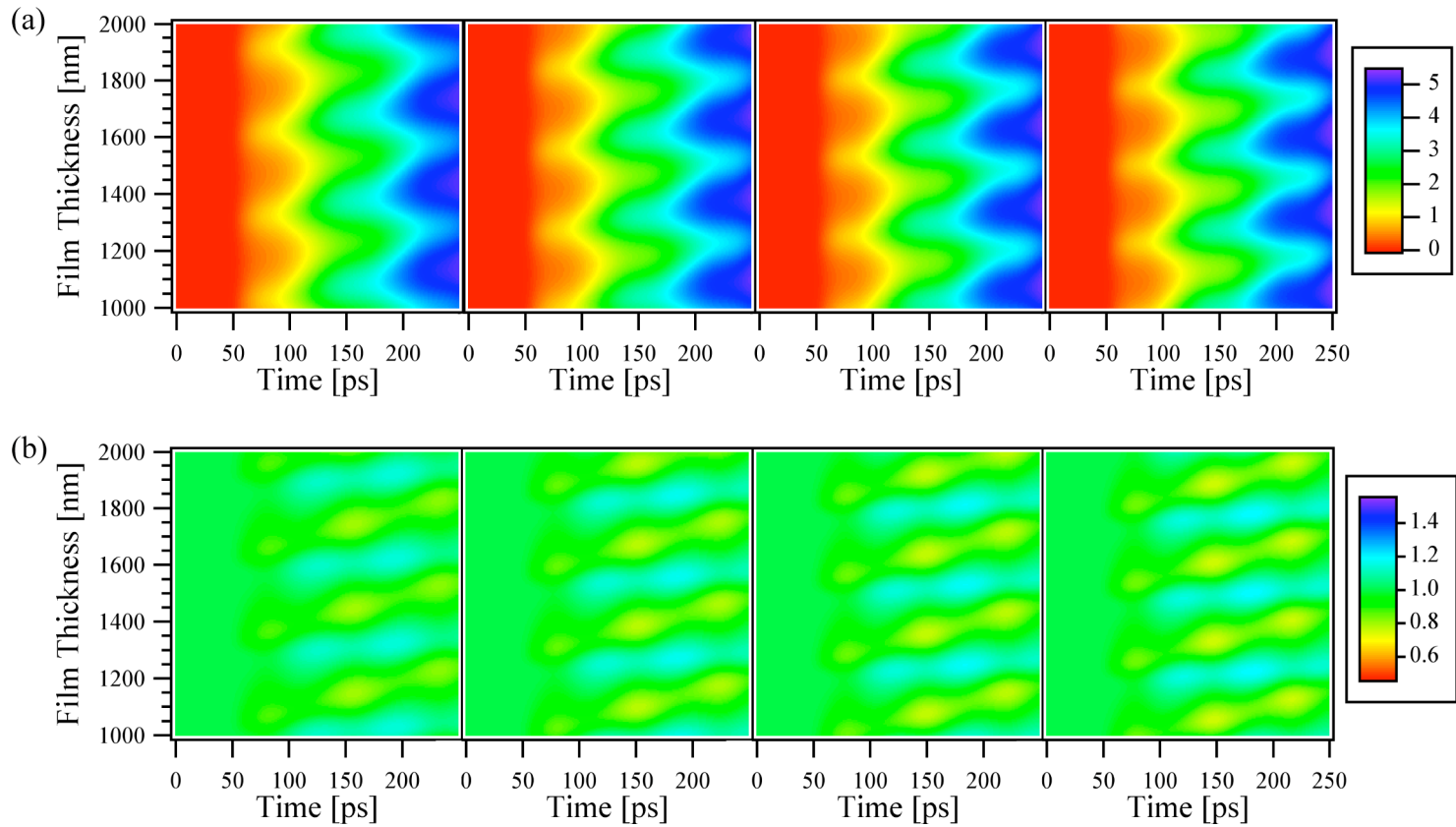


Fig. 5-15. (a) Phase shift and (b) reflectivity data simulated for polycarbonate films with different refractive indices at 26.6° incident angle and p-polarized probe light as a function of the initial thickness of the polycarbonate film. From left to right, the initial refractive indices are 1.450, 1.500, 1.525, and 1.549.

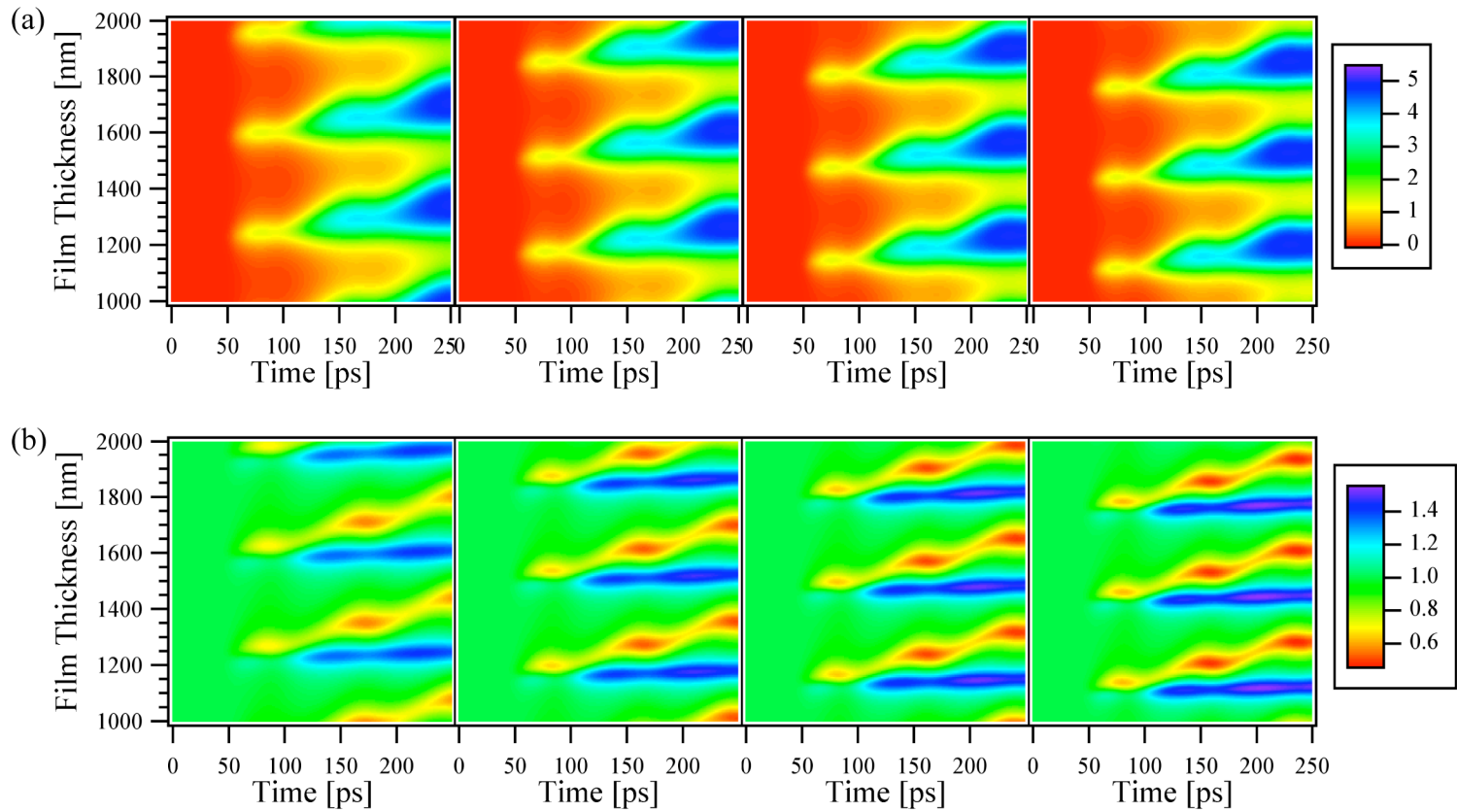


Fig. 5-16. (a) Phase shift and (b) reflectivity data simulated for polycarbonate films with different refractive indices at 63.4° incident angle and s-polarized probe light as a function of the initial thickness of the polycarbonate film. From left to right, the initial refractive indices are 1.450, 1.500, 1.525, and 1.549.

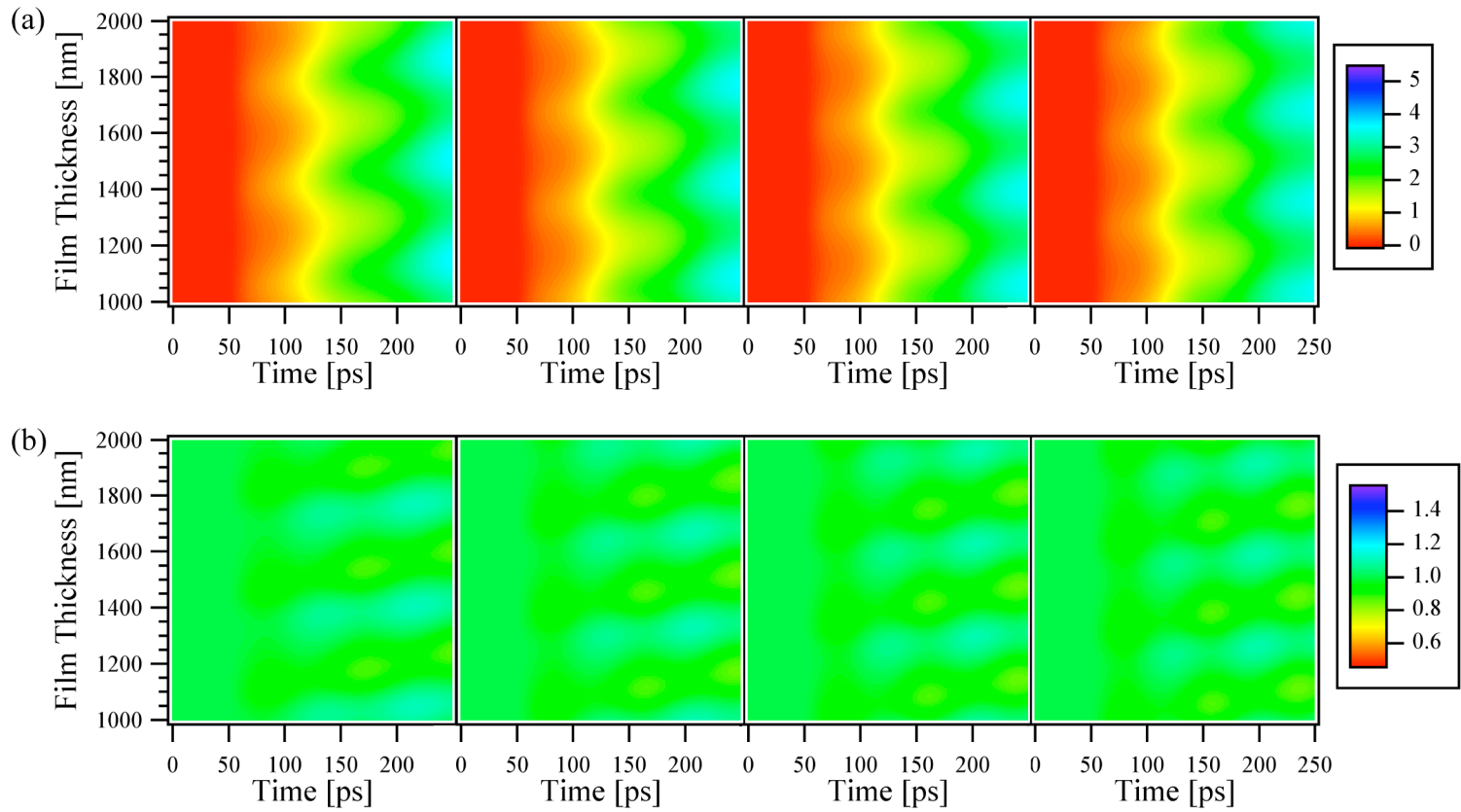


Fig. 5-17. (a) Phase shift and (b) reflectivity data simulated for polycarbonate films with different refractive indices at 63.4° incident angle and p-polarized probe light as a function of the initial thickness of the polycarbonate film. From left to right, the initial refractive indices are 1.450, 1.500, 1.525, and 1.549.

5.4 Polycarbonate¹⁰

The sample consisted of a 120 μm thick glass cover slip that was vapor deposited with 2 μm of Al (Berliner Glas/U.S.). Polycarbonate resin (Acros Organics, M.W. $\sim 45,000$) was dissolved in chloroform to a 6% solution with 0.5% BASF Pluronic L-62 surfactant. This solution was spin-cast at 2500 rpm for 25 s into a layer approximately 1600 nm thick, as measured by white light reflectometry over a wavelength range of 450 to 850 nm (Filmetrics F20).

Shocks of various pressures were created with laser energies from 0.7 to 1.3 mJ. The UDE data collected from one of those shots is shown in Fig. 5-18. The data along a single pixel at the Gaussian center of each shock were fit using the analysis described in §5.2 to yield the shock and particle velocities. Those velocities are plotted in Fig. 5-19 along with the LASL Shock Hugoniot Data⁴ of polycarbonate for comparison. All of the fit parameters for each shot are given in Table 5-2, and the uncertainties in those parameters are given in Table 5-3.

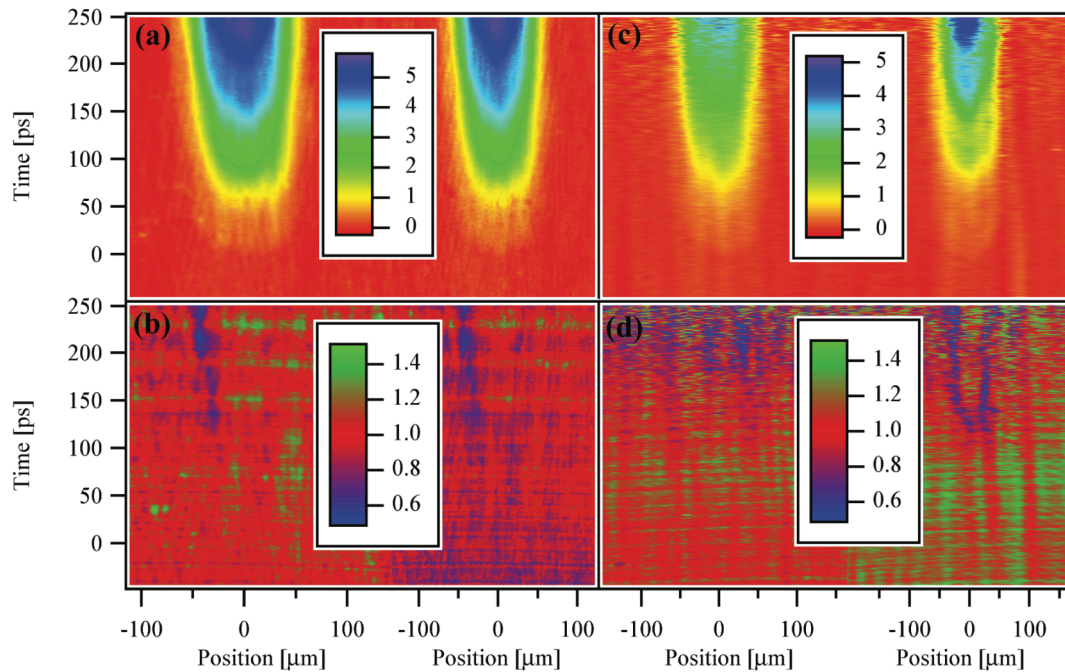


Fig. 5-18. Phase shift and reflectivity data for a 9.5 ± 0.2 GPa shock propagating through a 1580 nm thick polycarbonate film coated onto a 2 μm thick Al film. In each of the four images, the data from the p-polarized probe are on the left and from the s-polarized probe are on the right. (a) Phase shift data at 25.0° . (b) Reflectivity data at 25.0° . (c) Phase shift data at 63.4° . (d) Reflectivity data at 63.4° .

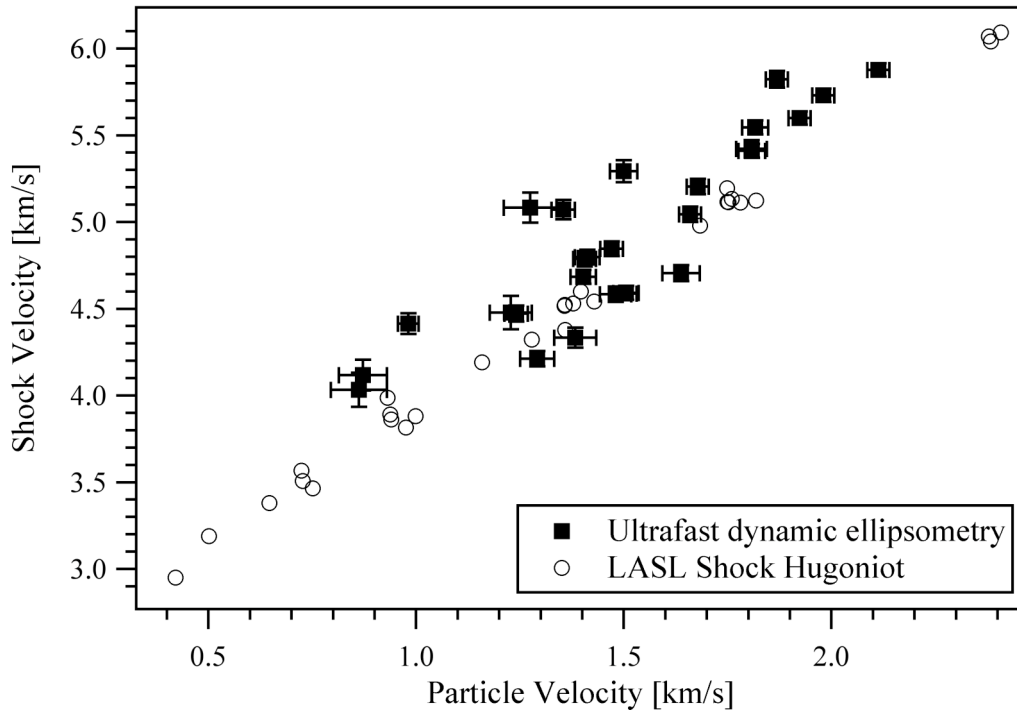


Fig. 5-19. Hugoniot data using ultrafast dynamic ellipsometry for a 1600 nm film of polycarbonate spin-cast from chloroform onto 2 μm Al. For comparison purposes, the LASL Shock Hugoniot Data⁴ are also plotted.

Table 5-2. Polycarbonate data

Shot number	Initial refractive index	Shocked refractive index	Thickness [nm]	Shock velocity [km/s]	Particle Velocity [km/s]	Low angle start time [ps]	High angle start time [ps]
1	1.53	1.73	1550	4.47	1.24	67.1	69.7
2	1.52	1.80	1580	4.59	1.51	67.8	68.6
3	1.52	1.80	1580	4.59	1.50	65.5	62.9
4	1.54	1.82	1573	4.58	1.48	69.7	69.2
5	1.46	1.61	1698	5.08	1.27	81.4	69.1
6	1.53	1.84	1606	4.71	1.64	71.6	65.9
7	1.46	1.66	1644	4.79	1.41	63.6	53.8
8	1.50	1.60	1580	4.41	0.98	58.2	54.5
9	1.32	1.46	1840	5.43	1.54	68.2	63.0
10	1.56	1.81	1568	5.41	1.81	51.1	49.1
11	1.51	1.81	1620	5.88	2.11	43.5	33.9
12	1.44	1.51	1607	7.54	1.62	55.6	61.5
13	1.55	1.81	1589	5.54	1.82	51.3	43.6
14	1.52	1.81	1575	5.73	1.98	44.0	39.6
15	1.51	1.73	1564	5.82	1.87	44.1	46.7
16	1.64	1.99	1481	5.14	1.85	42.4	41.2
17	1.54	1.83	1544	5.60	1.92	44.3	35.0
18	1.58	1.82	1498	4.80	1.41	61.1	49.4
19	1.56	1.79	1525	4.85	1.47	56.2	46.9
20	1.50	1.78	1638	5.42	1.81	71.5	54.7
21	1.50	1.77	1581	5.20	1.68	63.7	60.7
22	1.56	1.78	1542	4.68	1.40	61.2	53.6
23	1.52	1.68	1551	5.07	1.35	55.7	50.6
24	1.50	1.70	1485	5.29	1.50	65.9	63.9
25	1.42	1.64	1728	5.04	1.66	56.4	46.8
26	1.43	1.70	1709	4.33	1.38	69.5	69.7
27	1.48	1.73	1637	4.21	1.29	59.6	70.2
28	1.27	1.38	1986	4.87	1.31	58.7	66.1
29	1.56	1.68	1527	4.12	0.87	88.0	84.3
30	1.53	1.65	1575	4.03	0.86	85.4	64.8
31	1.40	1.59	1803	4.48	1.23	77.3	68.5

Table 5-3. Variances in the fit parameters of the polycarbonate data

Shot number	Initial refractive index	Shocked refractive index	Thickness [nm]	Shock velocity [km/s]	Particle Velocity [km/s]	Low angle start time [ps]	High angle start time [ps]	Mean squared error
1	0.01	0.01	10	0.05	0.03	1.4	1.7	0.02
2	0.01	0.01	10	0.04	0.03	1.2	1.5	0.02
3	0.01	0.01	10	0.04	0.03	1.2	1.5	0.03
4	0.01	0.01	12	0.04	0.04	1.3	1.6	0.02
5	0.01	0.01	21	0.09	0.06	1.5	2.0	0.02
6	0.01	0.01	14	0.05	0.04	1.2	1.5	0.03
7	0.01	0.01	10	0.05	0.03	1.3	1.4	0.02
8	0.01	0.01	11	0.06	0.02	1.6	1.8	0.02
9	0.00	0.01	12	0.07	0.03	1.6	1.4	0.03
10	0.01	0.01	9	0.04	0.03	1.0	1.2	0.03
11	0.00	0.01	8	0.04	0.03	0.9	1.0	0.03
12	0.00	0.01	6	0.13	0.03	0.8	1.0	0.06
13	0.01	0.01	9	0.04	0.03	1.0	1.2	0.03
14	0.01	0.01	8	0.04	0.03	0.9	1.1	0.03
15	0.01	0.01	9	0.05	0.03	0.8	0.9	0.03
16	0.01	0.01	9	0.04	0.03	0.9	1.1	0.04
17	0.01	0.01	8	0.04	0.03	0.9	1.1	0.05
18	0.01	0.01	9	0.04	0.03	1.1	1.6	0.02
19	0.01	0.01	9	0.04	0.03	1.1	1.4	0.02
20	0.01	0.01	11	0.05	0.04	1.1	1.4	0.02
21	0.01	0.01	9	0.05	0.03	1.0	1.3	0.04
22	0.01	0.01	10	0.04	0.03	1.2	1.5	0.02
23	0.01	0.01	9	0.06	0.03	1.1	1.5	0.04
24	0.00	0.01	6	0.06	0.03	1.4	1.0	0.03
25	0.00	0.01	10	0.04	0.03	1.2	1.2	0.07
26	0.01	0.01	18	0.06	0.05	1.5	1.8	0.02
27	0.01	0.01	14	0.05	0.04	1.6	1.8	0.02
28	0.01	0.01	23	0.09	0.04	1.6	1.8	0.05
29	0.01	0.01	19	0.09	0.06	2.2	2.6	0.02
30	0.01	0.01	22	0.10	0.07	2.3	2.8	0.02
31	0.01	0.01	24	0.10	0.05	2.3	2.6	0.02

As shown in Fig. 5-19, the Hugoniot data measured with UDE have more scatter than the LASL Shock Hugoniot data. Since the polycarbonate measured with UDE is spin coated from a volatile solvent, there are likely small variations in the thickness and in the density of the film on a micron scale. These variations are the cause of some of the scatter in the data and some of the deviation from the Hugoniot measured on bulk polycarbonate. Although the thickness of the polycarbonate was measured with white light reflectometry, the reflectometer probes an area approximately 2 mm in diameter. The multiple angles in this technique, which provide 8 sets of spatially resolved data, allow the acquisition of the initial thickness and the initial refractive index with a precision similar to that of a spectroscopic ellipsometer but with a much smaller spot size.

As discussed in §5.2, data with stronger oscillations from thin film effects better constrain the fit. The magnitude of the oscillations depends most heavily on the initial thickness and on the initial and shocked refractive indices of the film. Although the initial thickness of the film was judiciously chosen to maximize the oscillations, the refractive indices are more difficult to manipulate. The initial refractive index is set when the film is made, and the shocked refractive index depends on the amount of compression from the shock wave. Larger changes in refractive index between the initial and shocked layers give stronger oscillations, also resulting in fits that are more tightly constrained. Hence, the uncertainty in the fit parameters is smaller for shocks with higher pressures, as shown in Fig. 5-19.

The refractive index of bulk polycarbonate at 800 nm is 1.549.⁸ Since the fits of the initial refractive index of the shocked film were consistently lower than the bulk refractive index, the refractive index of the film was measured on a spectroscopic ellipsometer (J.A. Woollam Co.) between 300 and 1300 nm, probing at 70° and 80°. The data are shown in Fig. 5-20. The spot size sampled by this ellipsometer was approximately 2 mm in diameter. The data were fit for the thickness and the refractive index, giving a refractive index of 1.50 ± 0.05 at 800 nm. The fit refractive index is shown in Fig. 5-21. The average refractive index of the pristine polycarbonate film for all the shots shown Fig. 5-19 was 1.52 ± 0.05 , which is in agreement with the static spectroscopic ellipsometry data.

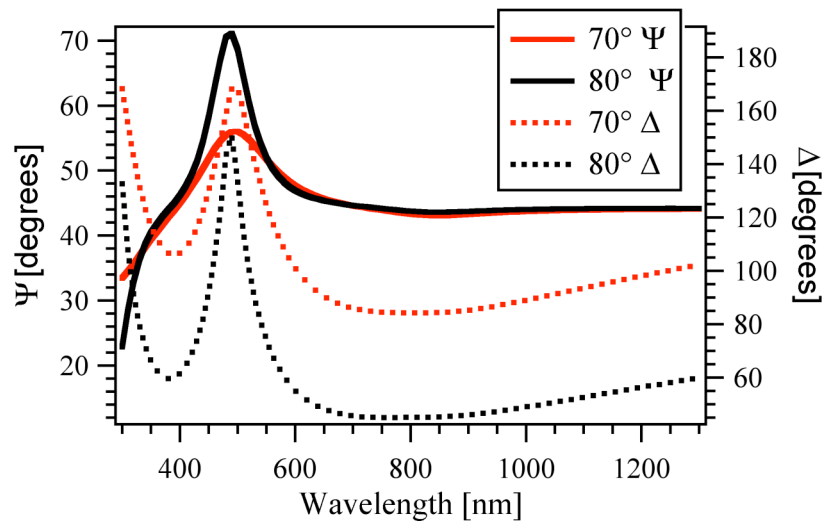


Fig. 5-20. Spectroscopic ellipsometry data for a polycarbonate film spin-coated on 2 μm Al.

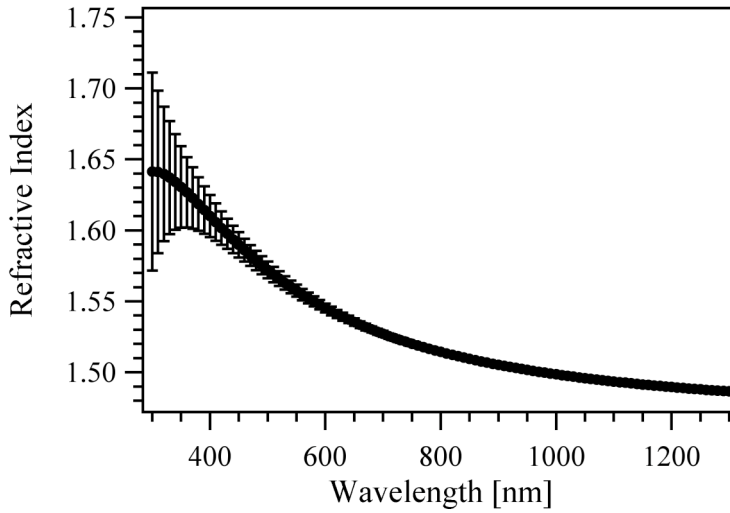


Fig. 5-21. Polycarbonate thin film refractive index data from a fit to the spectroscopic ellipsometry data shown in Fig. 5-20.

Since the optical properties of many polymers conform to the Gladstone-Dale relation under compression, the calculated value for the shocked refractive index according to the Gladstone-Dale relation was compared to the value obtained from the fit. The relationship between these two quantities is plotted in Fig. 5-22. The linear fit to this data yields a slope of 0.93 ± 0.07 and an intercept of 0.11 ± 0.12 , indicating that the refractive index of polycarbonate under shock compression is described well by the Gladstone-Dale relation.

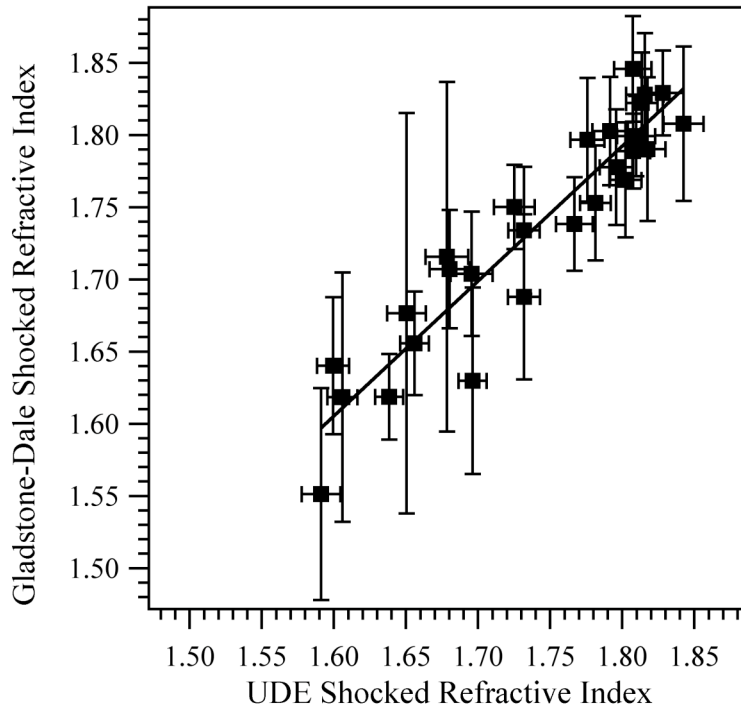


Fig. 5-22. A plot of the shocked refractive index of polycarbonate calculated from the Gladstone-Dale relation, $n_{s,GD}$, versus the shocked refractive index, n_s . The linear fit gives $n_{s,GD} = (0.93 \pm 0.07) n_s + (0.11 \pm 0.12)$.

5.5 PMMA

The sample consisted of a 120 μm thick glass cover slip that was vapor deposited with 2 μm of Al (Berliner Glas/U.S.). Poly(methyl methacrylate) (PMMA) (Acros Organics, M.W. $\sim 93,300$) was dissolved in toluene to a 13.4% solution with 0.6% BASF Pluronic L-62 surfactant. This solution was spin-cast at 2500 rpm for 25 s into a layer approximately 1600 nm thick, as measured by white light reflectometry over a wavelength range of 450 to 850 nm (Filmetrics F20).

Shocks of various pressures were created with laser energies from 0.2 to 1.0 mJ. The data along a single pixel at the Gaussian center of each shock were selected for analysis. The data show phase shifts similar to those seen in the polycarbonate data, however, the reflectivity data are markedly different. One set of data is shown in Fig. 5-23 that demonstrates the typical characteristics. Specifically of note are the increase in reflectivity and the strong accompanying oscillations in the high angle s-polarized reflectivity. The presence of the unexpected characteristics almost exclusively in the reflectivity data suggested that the shocked refractive index might have a nonzero absorption coefficient. To explore this theory, the data was fitted with the model explained in §5.2 with the addition of the imaginary component of the refractive index as a fitting parameter. This fit is shown with the data in Fig. 5-23, along with the fit to only the phase shift data using the model with no absorption coefficient. With the absorption coefficient, the fit in Fig. 5-23 yields the shocked refractive index of $1.58 + i(-0.009)$. The absorption coefficient obtained seems non-physical in that the absorption is less than zero. Resultantly, neither fitting method seems to be appropriate for the PMMA reflectivity data, leading to the conclusion that the existing model is inadequate for this

material. Lacking additional data or knowledge that could lead to a better model, the PMMA phase shift data only was used to fit the data with the existing model. The Hugoniot results of this analysis are provided in Fig 5-24, and the refractive index results are provided in Fig. 5-25. No error estimates are given since only the phase shift data was fitted.

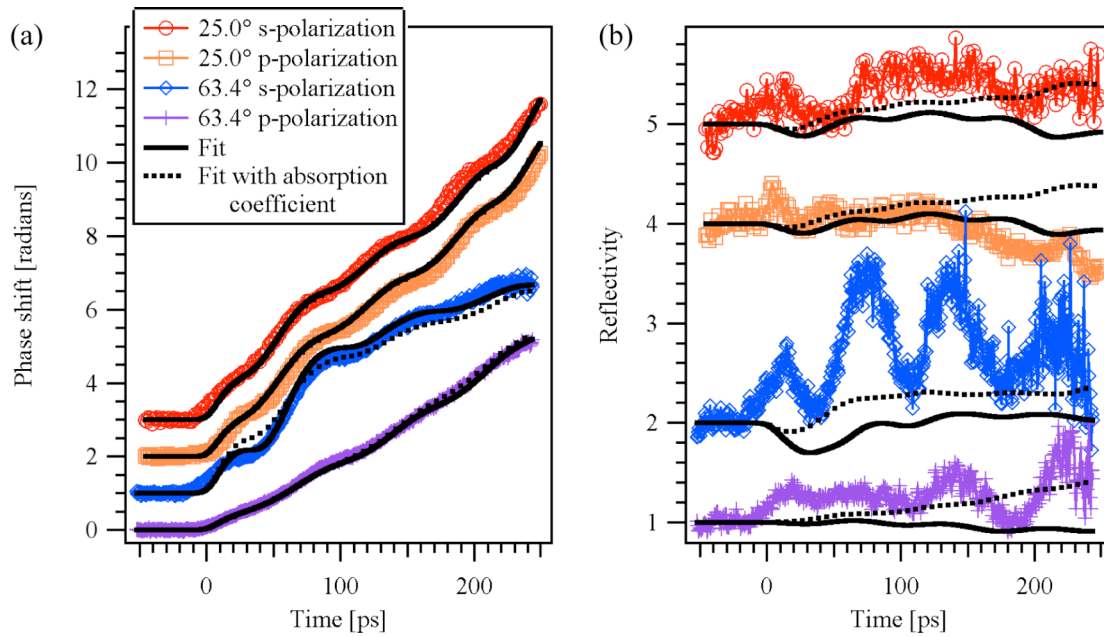


Fig. 5-23. (a) Phase shift and (b) reflectivity data from the two angles and two orthogonal polarizations for an approximately 13 GPa shock in a 1600 nm PMMA film on 2 μm Al. The solid black line is a global fit to the data using the model described in §5.2, including a shocked refractive index with no absorption coefficient. The dotted black line is a global fit to the data using the same model but with a nonzero absorption coefficient. Data are vertically offset for clarity.

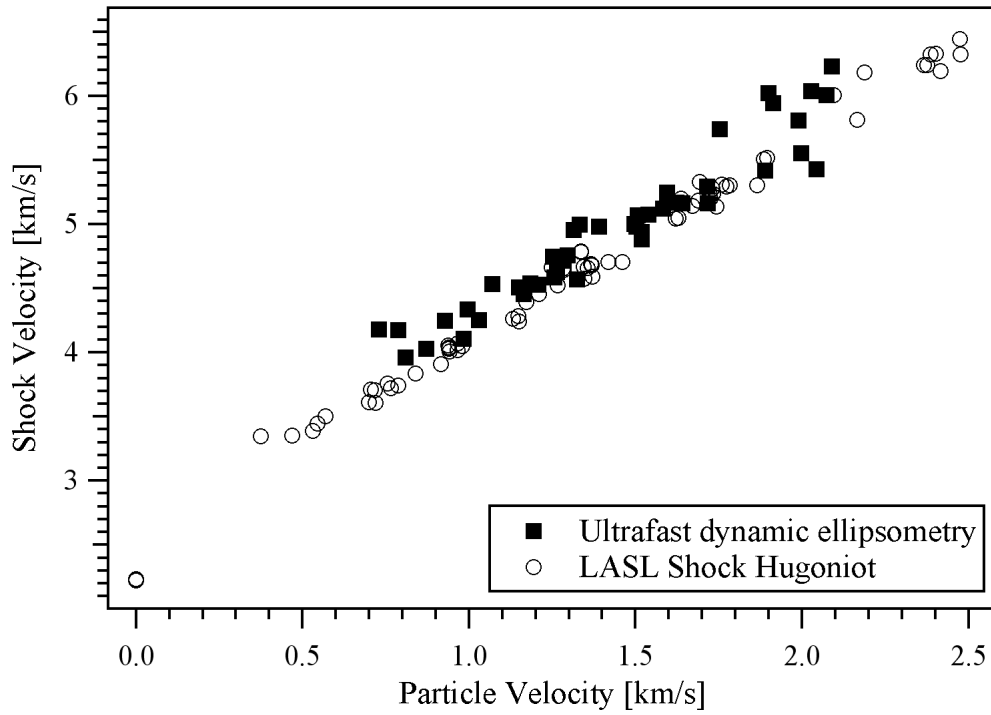


Fig. 5-24. Hugoniot data using ultrafast dynamic ellipsometry for a 1600 nm film of PMMA spin-cast from toluene onto 2 μm Al. For comparison purposes, the LASL Shock Hugoniot Data⁴ are also plotted.

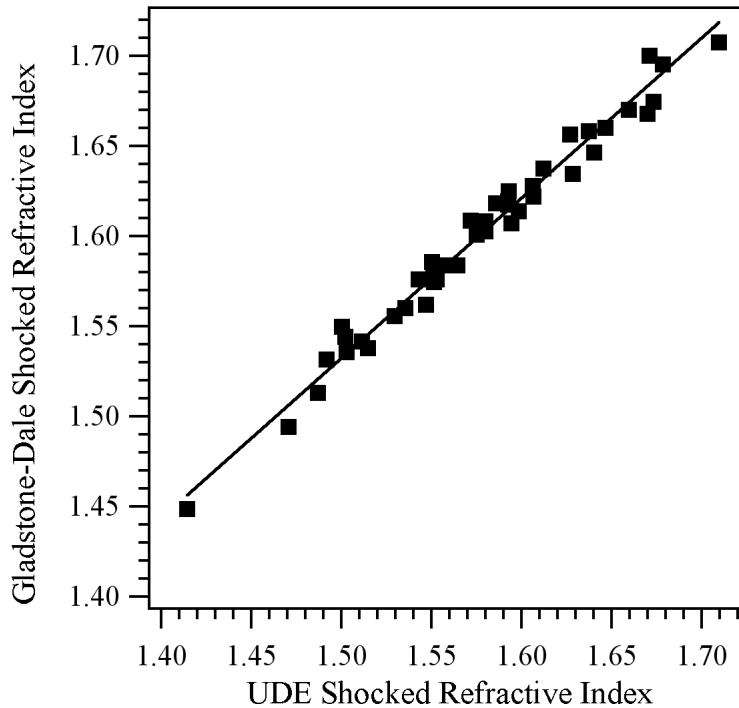


Fig. 5-25. A plot of the shocked refractive index of PMMA calculated from the Gladstone-Dale relation, $n_{s,GD}$, versus the shocked refractive index, n_s . The linear fit gives $n_{s,GD} = (0.89 \pm 0.02) n_s + (0.20 \pm 0.03)$.

5.6 Kel-F 800¹¹

Poly(chlorotrifluoroethylene-*co*-vinylidene fluoride) is a polymer commonly referred to as Kel-F 800 and is frequently used as a binder in plastic bonded explosives, such as PBX 9502. Its use with explosives makes it desirable to know its high pressure equation of state for use in hydrodynamic models. Hugoniot data of Kel-F 800 were obtained using ultrafast dynamic ellipsometry and were compared with previous data on macroscopic samples obtained in plate impact gas gun experiments. The data agree well.

The sample consisted of a 120 μm thick glass cover slip that was vapor deposited with 2 μm of Al (Berliner Glas/U.S.). The Kel-F 800 (FK-800 resin, 3M) was dissolved

in methyl ethyl ketone to a 19% solution with 1.5% BASF Pluronic L-62 surfactant. This solution was spin-cast onto the Al at 5000 rpm for 35 s into a layer approximately 1500 nm thick.

The data were collected and analyzed in the same manner as the other polymer Hugoniot data in this chapter. Fig. 5-26 shows the phase shift and reflectivity data for a shock with a peak pressure of 20.3 ± 0.6 GPa traveling through 1480 nm of Kel-F 800. Lineouts of the data shown in Fig. 5-26 are shown in Fig. 5-27 along with the fit to those data.

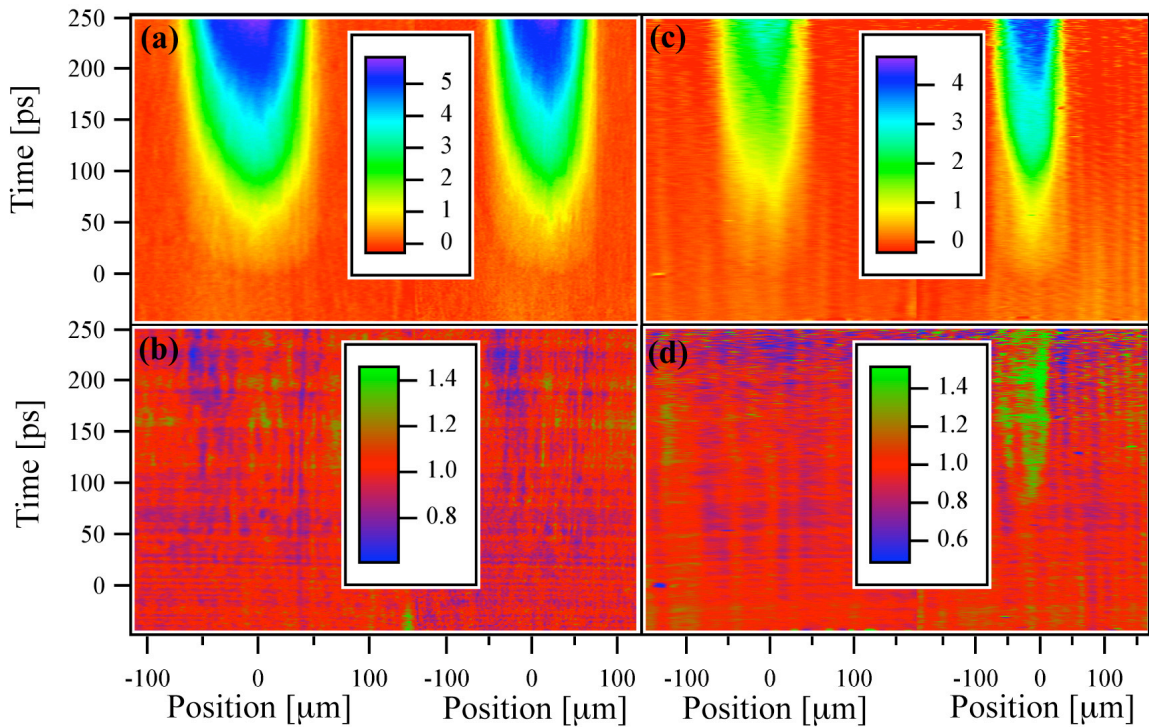


Fig. 5-26. Phase shift and reflectivity data for a 20.3 ± 0.6 GPa shock in 1480 nm of Kel-F 800 on 2 μm of Al. In each of the four images, the data from the p-polarized probe are on the left and from the s-polarized probe are on the right. (a) Phase shift data at 25.0° . (b) Reflectivity data at 25.0° . (c) Phase shift data at 63.4° . (d) Reflectivity data at 63.4° .

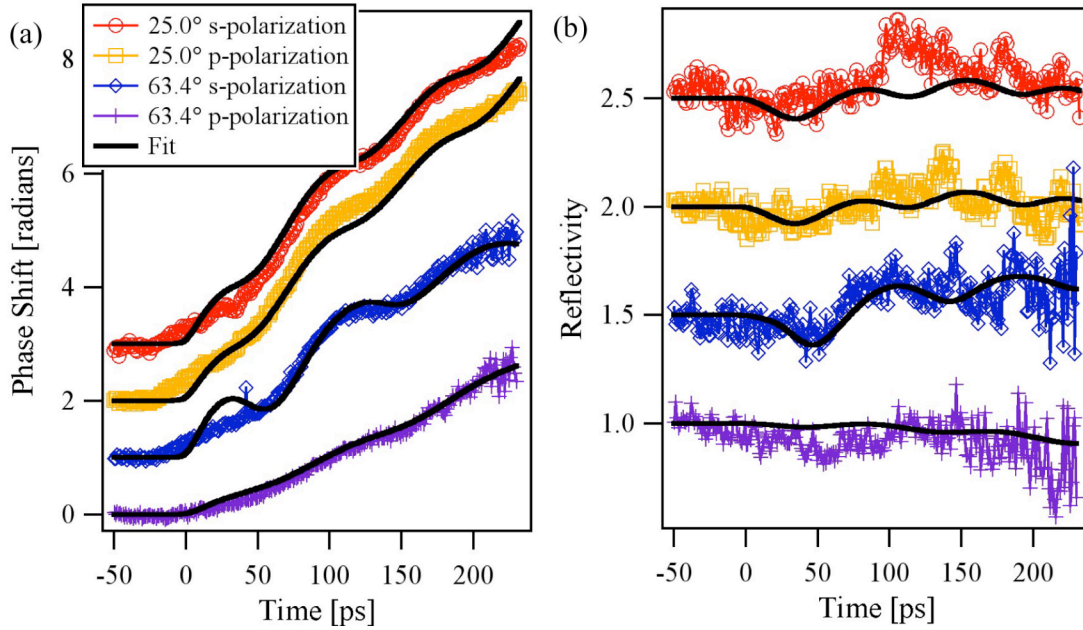


Fig. 5-27. (a) Phase shift and (b) reflectivity data from the two angles and both polarizations along with the fit to the data for a 20.3 ± 0.6 GPa shock in a 1480 nm Kel-F 800 film on 2 μm Al. Data are vertically offset for clarity.

Shocks of various pressures were created with laser energies from 0.7 to 1.0 mJ.

The data along a single pixel at the Gaussian center of each shock were fit, using the analysis previously described, to yield the shock and particle velocities. Those velocities are plotted in Fig. 5-28 along with Kel-F 800 Hugoniot data by Dattelbaum *et al.*¹² for comparison.

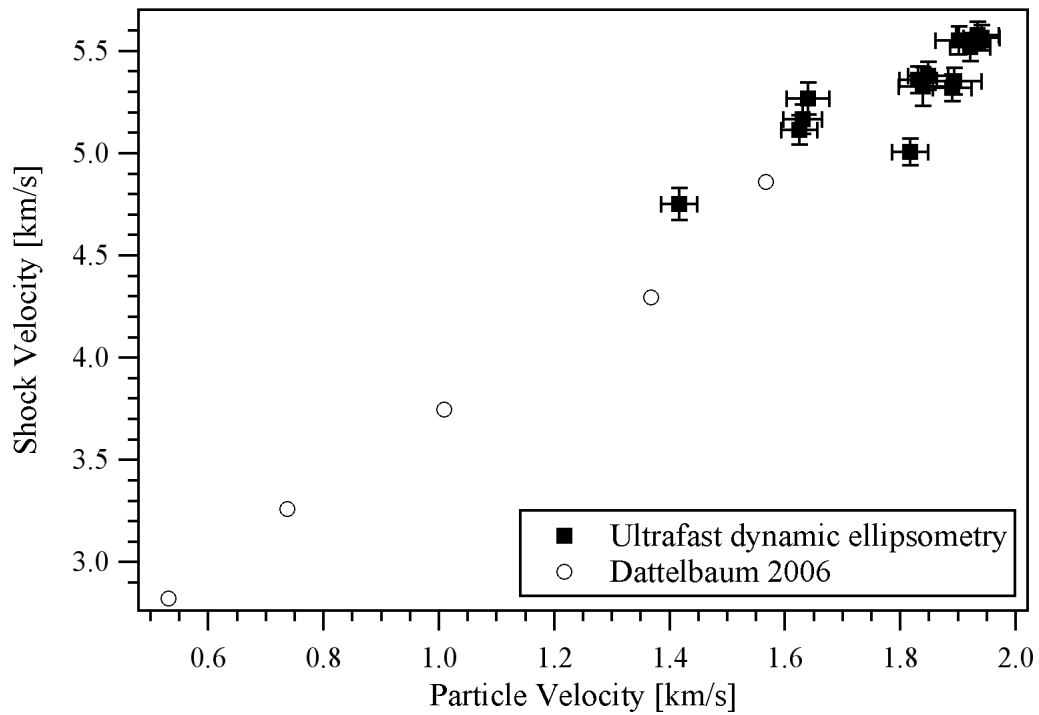


Fig. 5-28. Hugoniot data using ultrafast dynamic ellipsometry for a 1500 nm Kel-F 800 thin film spin-cast from methyl ethyl ketone onto 2 μm Al. For comparison purposes, Hugoniot data from Dattelbaum *et al.*¹² are also plotted.

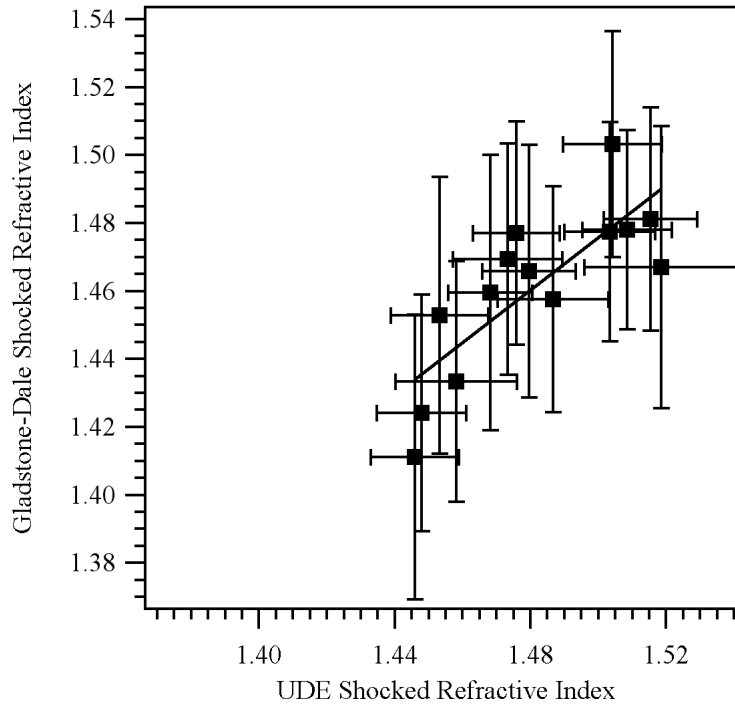


Fig. 5-29. A plot of the shocked refractive index of Kel-F 800 calculated from the Gladstone-Dale relation, $n_{s,GD}$, versus the shocked refractive index, n_s . The linear fit gives $n_{s,GD} = (0.77 \pm 0.17) n_s + (0.32 \pm 0.25)$.

As shown in Fig. 5-28, the Hugoniot data measured with UDE have more scatter than the data by Dattelbaum *et al.*¹² As described earlier, this variation likely results from the variations in the thickness and in the density of the film due to spin-coating.

Table 5-4. Kel-F 800 data

Shot number	Initial refractive index	Shocked refractive index	Thickness [nm]	Shock velocity [km/s]	Particle Velocity [km/s]	Low angle start time [ps]	High angle start time [ps]
1	1.27	1.45	1656	5.33	1.84	76.4	57.5
2	1.32	1.47	1553	5.27	1.64	74.5	57.7
3	1.29	1.45	1567	5.11	1.62	53.8	47.9
4	1.32	1.48	1523	5.17	1.63	65.5	53.3
5	1.31	1.50	1558	5.32	1.89	63.5	49.3
6	1.30	1.52	1479	5.35	1.89	66.0	59.6
7	1.31	1.52	1559	5.01	1.82	58.3	46.5
8	1.32	1.45	1515	4.75	1.42	53.5	48.5
9	1.30	1.49	1539	5.58	1.93	57.3	56.3
10	1.31	1.51	1552	5.56	1.94	49.9	45.5
11	1.28	1.46	1547	5.55	1.90	57.4	56.8
12	1.33	1.50	1519	5.36	1.83	52.8	44.5
13	1.31	1.47	1535	5.38	1.85	48.0	47.8
14	1.31	1.48	1576	5.52	1.92	64.8	45.7

Table 5-5. Variances in the fit parameters of the Kel-F 800 data

Shot number	Initial refractive index	Shocked refractive index	Thickness [nm]	Shock velocity [km/s]	Particle Velocity [km/s]	Low angle start time [ps]	High angle start time [ps]	Mean squared error
1	0.01	0.01	20	0.10	0.04	1.4	1.7	0.04
2	0.01	0.01	15	0.08	0.04	1.6	1.8	0.02
3	0.01	0.01	13	0.07	0.03	1.7	1.7	0.02
4	0.01	0.01	13	0.07	0.03	1.6	1.7	0.06
5	0.01	0.01	12	0.06	0.03	1.4	1.6	0.02
6	0.01	0.02	13	0.06	0.05	1.1	1.4	0.02
7	0.01	0.01	13	0.06	0.03	1.5	1.6	0.04
8	0.01	0.01	14	0.08	0.03	1.8	1.9	0.03
9	0.01	0.02	13	0.07	0.04	1.5	1.5	0.02
10	0.01	0.01	12	0.06	0.03	1.4	1.5	0.03
11	0.01	0.02	15	0.07	0.04	1.5	1.4	0.02
12	0.01	0.01	12	0.06	0.03	1.5	1.6	0.01
13	0.01	0.02	13	0.07	0.03	1.5	1.6	0.02
14	0.01	0.01	12	0.07	0.03	1.4	1.5	0.03

5.7 Sylgard 184

Sylgard 184 is a poly(dimethylsiloxane) polymer manufactured by Dow Corning. It is sold in two parts, consisting of the base, which is primarily dimethylvinyl-terminated dimethyl siloxane, and a curing agent. To prepare the sample, the base and curing agent were mixed in a 10:1 ratio as per the manufacturer's instructions. The mixture was placed under mild vacuum, approximately 380 torr (~ 50 kPa), for 30 minutes to remove residual gas that was incorporated during mixing. The mixture was spin cast at 10,000 rpm for 2 minutes onto a 120 μm thick glass cover slip that was vapor deposited with 2 μm of Al (Berliner Glas/U.S.), resulting in a film that was approximately 8 μm thick. The film was cured at 90°C for 2.5 hours.

To generate the shock waves, laser energies of 0.7 to 2.0 mJ were used. Ultrafast dynamic ellipsometry data were collected and analyzed in the manner previously described.

The shock and particle velocities extracted from fitting the data are plotted in Fig. 5-30 along with explosively-driven Sylgard data from the LASL Shock Hugoniot Data.⁴ All of the fit parameters for each shot are given in Table 5-6, and the uncertainties in those parameters are given in Table 5-7. The UDE laser driven shock data extend the pressure range above the explosively driven data. The scatter in the UDE data is slightly larger than in the LASL data, most likely arising from the non-uniformity of the spin-cast sample.

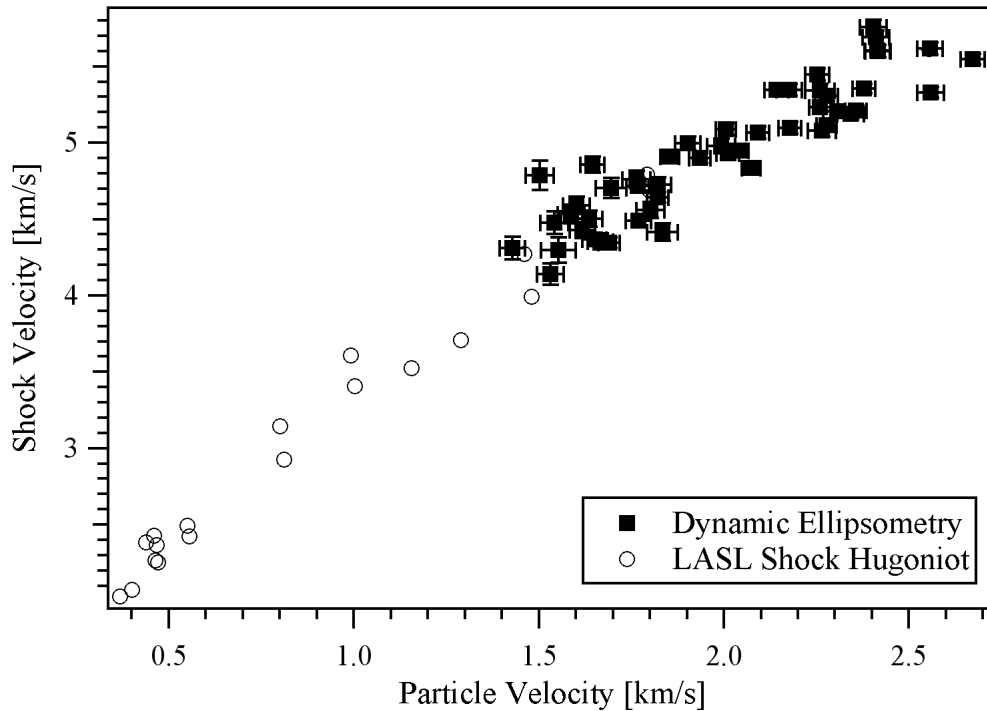


Fig. 5-30. Hugoniot data using ultrafast dynamic ellipsometry for an 8 μm thin film of Sylgard 184 spin-cast onto 2 μm Al. For comparison purposes, Hugoniot data from LASL Shock Hugoniot Data⁴ are also plotted.

The value for the shocked refractive index according to the Gladstone-Dale relation was calculated with the shock velocity, particle velocity and initial refractive index fit parameters using Eq. (5.15). These values were compared to the shocked refractive index obtained from the fit. The relationship between these two quantities is plotted in Fig. 5-31. A linear fit to this data yields a slope of 0.72 ± 0.04 and an intercept of 0.49 ± 0.06 , indicating that Sylgard 184 deviates slightly from a Gladstone-Dale material under shock compression (the slope should be close to 1 with an intercept of zero for a Gladstone-Dale material).

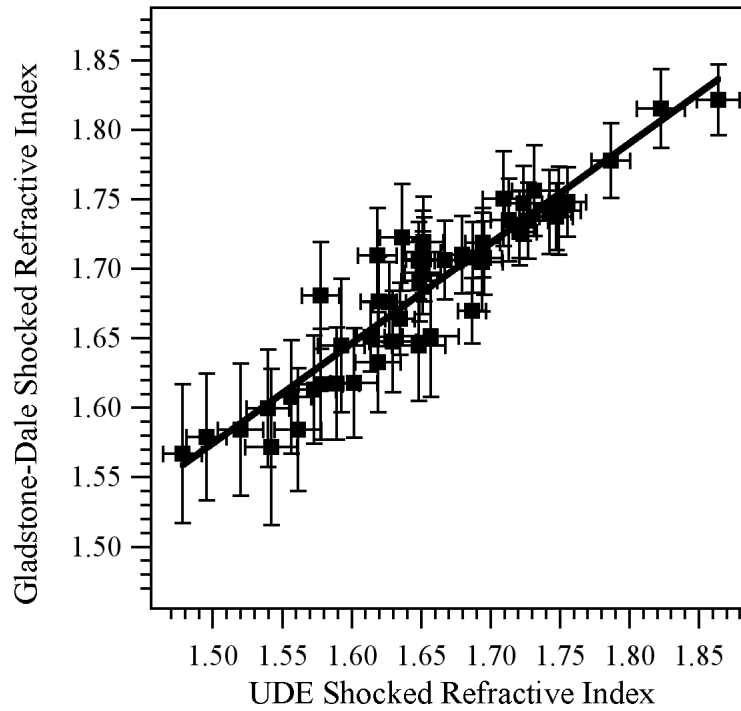


Fig. 5-31. A plot of the shocked refractive index of Sylgard 184 calculated from the Gladstone-Dale relation, $n_{s,GD}$, versus the shocked refractive index, n_s . The linear fit gives $n_{s,GD} = (0.72 \pm 0.04) n_s + (0.49 \pm 0.06)$, showing that Sylgard 184 deviates slightly from a Gladstone-Dale material under shock loading.

Table 5-6. Sylgard 184 data

Shot number	Initial refractive index	Shocked refractive index	Thickness [μm]	Shock velocity [km/s]	Particle Velocity [km/s]	Low angle start time [ps]	High angle start time [ps]
1	1.43	1.86	6.31	5.55	2.67	29.2	20.4
2	1.42	1.82	6.31	5.33	2.56	32.1	24.8
3	1.43	1.71	6.26	5.34	2.26	30.9	25.5
4	1.42	1.71	6.31	5.69	2.41	43.9	23.7
5	1.42	1.79	6.31	5.62	2.56	38.1	20.0
6	1.42	1.68	6.52	5.44	2.25	50.6	44.5
7	1.42	1.72	6.47	5.60	2.42	48.8	44.5
8	1.40	1.70	6.61	5.60	2.41	55.8	49.4
9	1.40	1.65	6.61	5.76	2.40	59.1	45.9
10	1.42	1.65	6.50	5.35	2.18	51.6	40.2
11	1.40	1.72	6.63	5.36	2.38	39.7	26.7
12	1.40	1.69	6.62	5.31	2.28	45.9	28.0
13	1.42	1.73	6.32	5.21	2.31	47.5	29.9
14	1.41	1.74	6.41	5.19	2.34	45.1	25.6
15	1.41	1.69	6.60	5.23	2.26	42.0	32.7
16	1.41	1.63	6.59	5.35	2.14	87.5	75.8
17	1.41	1.67	6.53	5.06	2.09	80.5	74.1
18	1.42	1.73	6.47	5.10	2.18	85.0	81.8
19	1.44	1.62	6.37	5.00	1.90	83.3	67.6
20	1.45	1.58	6.31	4.86	1.65	69.8	64.6
21	1.41	1.76	6.56	5.21	2.36	72.4	77.6
22	1.42	1.72	6.53	4.84	2.07	32.3	38.6
23	1.43	1.65	6.46	4.90	1.94	53.8	44.8
24	1.40	1.63	6.61	5.09	2.01	58.4	51.8
25	1.41	1.75	6.57	5.11	2.28	53.8	48.4
26	1.41	1.61	6.60	4.91	1.85	50.0	43.1
27	1.42	1.69	6.32	4.98	1.99	67.9	35.6
28	1.41	1.75	6.38	5.08	2.27	51.1	34.7
29	1.39	1.69	6.64	4.95	2.04	48.3	46.0
30	1.45	1.64	6.29	4.37	1.65	85.4	76.1
31	1.44	1.65	6.34	4.35	1.69	85.3	77.1
32	1.42	1.65	6.47	4.93	2.01	101.6	99.1
33	1.42	1.65	6.45	4.64	1.82	92.2	77.4
34	1.42	1.62	6.46	4.72	1.77	92.8	76.9
35	1.40	1.56	8.58	4.59	1.60	53.4	41.9
36	1.39	1.59	8.67	4.50	1.64	71.4	65.8
37	1.39	1.63	8.73	4.49	1.77	63.7	54.9
38	1.39	1.48	8.72	4.79	1.50	71.3	57.3
39	1.39	1.57	8.75	4.76	1.76	66.9	57.8
40	1.39	1.62	8.73	4.72	1.82	61.5	56.5
41	1.39	1.58	8.69	4.43	1.62	68.2	54.2
42	1.39	1.54	8.72	4.53	1.59	60.0	56.9
43	1.39	1.50	8.74	4.31	1.43	55.6	61.0
44	1.39	1.65	8.70	4.56	1.80	103.8	126.0
45	1.37	1.56	8.83	4.70	1.70	105.8	117.0
46	1.38	1.52	8.76	4.48	1.54	100.6	106.2
47	1.37	1.54	8.68	4.30	1.55	110.1	76.9
48	1.38	1.60	8.76	4.35	1.67	107.2	103.7
49	1.41	1.59	8.43	4.14	1.53	79.3	89.5
50	1.38	1.66	8.85	4.42	1.83	113.0	85.1

Table 5-7. Variances in the fit parameters of the Sylgard 184 data

Shot number	Initial refractive index	Shocked refractive index	Thickness [μm]	Shock velocity [km/s]	Particle Velocity [km/s]	Low angle start time [ps]	High angle start time [ps]
1	0.001	0.02	0.01	0.04	0.03	1.2	1.1
2	0.001	0.02	0.01	0.04	0.04	1.2	1.2
3	0.001	0.02	0.01	0.05	0.04	1.4	1.3
4	0.001	0.01	0.01	0.04	0.04	1.3	1.3
5	0.001	0.01	0.01	0.04	0.03	1.2	1.2
6	0.001	0.01	0.01	0.04	0.03	1.1	1.2
7	0.001	0.01	0.01	0.04	0.03	1.0	1.1
8	0.001	0.01	0.01	0.04	0.03	1.1	1.1
9	0.001	0.01	0.01	0.05	0.04	1.1	1.0
10	0.001	0.01	0.01	0.04	0.03	1.1	1.2
11	0.001	0.01	0.01	0.03	0.03	1.0	1.0
12	0.001	0.01	0.01	0.03	0.03	1.0	1.0
13	0.001	0.02	0.01	0.04	0.04	1.4	1.3
14	0.001	0.02	0.01	0.04	0.04	1.3	1.3
15	0.001	0.01	0.01	0.03	0.03	1.0	1.1
16	0.001	0.01	0.01	0.04	0.03	1.2	1.1
17	0.001	0.01	0.01	0.04	0.03	1.2	1.2
18	0.001	0.01	0.01	0.04	0.03	1.2	1.2
19	0.001	0.01	0.01	0.04	0.03	1.2	1.3
20	0.002	0.01	0.01	0.05	0.03	1.4	1.4
21	0.001	0.01	0.01	0.04	0.03	1.1	1.1
22	0.001	0.01	0.01	0.03	0.03	1.1	1.2
23	0.001	0.01	0.01	0.04	0.03	1.2	1.2
24	0.001	0.01	0.01	0.04	0.03	1.2	1.1
25	0.001	0.01	0.01	0.03	0.03	1.1	1.0
26	0.001	0.01	0.01	0.04	0.02	1.3	1.2
27	0.001	0.01	0.01	0.05	0.04	1.5	1.6
28	0.001	0.02	0.01	0.04	0.04	1.4	1.4
29	0.001	0.01	0.01	0.03	0.03	1.2	0.9
30	0.002	0.02	0.01	0.04	0.03	1.5	1.5
31	0.002	0.01	0.01	0.04	0.03	1.4	1.4
32	0.001	0.01	0.01	0.04	0.03	1.3	1.2
33	0.001	0.01	0.01	0.04	0.03	1.3	1.3
34	0.001	0.01	0.01	0.04	0.03	1.4	1.4
35	0.001	0.01	0.01	0.06	0.04	1.9	1.7
36	0.001	0.02	0.01	0.05	0.04	1.4	1.9
37	0.001	0.02	0.01	0.04	0.04	1.6	1.8
38	0.001	0.01	0.01	0.10	0.04	1.5	1.7
39	0.001	0.02	0.01	0.06	0.04	1.4	1.7
40	0.001	0.02	0.01	0.05	0.04	1.4	1.7
41	0.001	0.02	0.01	0.05	0.03	1.5	1.8
42	0.001	0.02	0.01	0.06	0.04	1.5	1.8
43	0.001	0.01	0.01	0.07	0.03	1.5	1.8
44	0.001	0.02	0.01	0.05	0.04	1.6	1.9
45	0.002	0.02	0.02	0.07	0.04	1.9	2.0
46	0.001	0.02	0.01	0.07	0.04	1.8	1.9
47	0.001	0.02	0.01	0.08	0.05	2.1	2.3
48	0.002	0.02	0.02	0.05	0.03	1.7	1.9
49	0.001	0.02	0.01	0.07	0.04	2.1	1.8
50	0.001	0.02	0.01	0.06	0.04	1.7	2.1

5.8 Conclusions

Ultrafast dynamic ellipsometry of thin polymer films has provided information on the material and optical responses of polycarbonate, PMMA, Kel-F, and Sylgard 184 to laser driven shock loading. The Hugoniot data measured with UDE matches well with the bulk Hugoniot data for all of these materials. This study has demonstrated that UDE can be used to acquire the Hugoniot equation of state for a transparent material without referencing other data for optical response properties or impedance matching purposes as is typically required in other existing shock wave measurement techniques. These Hugoniot and refractive index data for polycarbonate and for PMMA will likely be used in future gas gun experiments for which these two materials are used as windows. The Hugoniot data on Kel-F 800 and on Sylgard 184 will likely be incorporated into the equations of state for these materials for use in hydrocodes.

References

- ¹ M. Born and E. Wolf, *Principles of Optics: Electromagnetic Theory of Propagation, Interference and Diffraction of Light*, 7th (expanded) ed. (Cambridge University Press, Cambridge, UK ; New York, 2002).
- ² D. J. Funk, D. S. Moore, K. T. Gahagan, S. J. Buelow, J. H. Reho, G. L. Fisher, and R. L. Rabie, "Ultrafast measurement of the optical properties of aluminum during shock-wave breakout," *Phys. Rev. B* **64**, 115114-5 (2001).
- ³ M. A. Meyers, *Dynamic Behavior of Materials* (John Wiley & Sons, Inc., New York, 1994).
- ⁴ S. P. Marsh, *LASL Shock Hugoniot Data* (University of California Press, Berkeley, 1980).
- ⁵ K. T. Gahagan, D. S. Moore, D. J. Funk, R. L. Rabie, S. J. Buelow, and J. W. Nicholson, "Measurement of shock wave rise times in metal thin films," *Phys. Rev. Lett.* **85**, 3205-8 (2000).
- ⁶ E. D. Palik, *Handbook of Optical Constants of Solids II* (Academic Press, San Diego, 1998).
- ⁷ E. D. Palik, *Handbook of Optical Constants of Solids* (Academic Press, San Diego, 1998).
- ⁸ S. E. Caudill and W. T. Grubbs, "Interferometric measurements of refractive index dispersion in polymers over the visible and near-infrared spectral range," *J. Appl. Polym. Sci.* **100**, 65-72 (2006).
- ⁹ J. H. Gladstone and T. P. Dale, "Researches on the refraction, dispersion, and sensitiveness of liquids," *Philos. Trans. R. Soc. London* **153**, 317-343 (1863).
- ¹⁰ C. A. Bolme, S. D. McGrane, D. S. Moore, and D. J. Funk, "Single shot measurements of laser driven shock waves using ultrafast dynamic ellipsometry," *J. Appl. Phys.* **102**, 033513-8 (2007).
- ¹¹ C. A. Bolme, "Single shot dynamic ellipsometry measurements of laser-driven shock waves" in *Shock Compression of Condensed Matter--2007*; Vol. 955, edited by M. L. Elert, M. D. Furnish, R. Chau, N. C. Holmes, and J. Nguyen (American Institute of Physics, Melville, NY, 2007), p. 1211-16.
- ¹² D. M. Dattelbaum, D. L. Robbins, S. A. Sheffield, E. B. Orler, R. L. Gustavsen, R. R. Alcon, J. M. Lloyd, and P. J. Chavez, "Quasi-static and shock compressive response of fluorinated polymers: Kel-F 800" in *Shock Compression of Condensed Matter--2005*; Vol. 845, edited by M. D. Furnish, M. Elert, T. P. Russell, and C. T. White (American Institute of Physics, Melville, NY, 2006), p. 69-72.

Chapter 6

Ultrafast Dynamic Ellipsometry of Deposited Dielectrics

This chapter describes the sample preparation for deposited dielectric thin films of materials used as windows for later shock experiments and the ultrafast dynamic ellipsometry data collected of the window materials on Al.

6.1 Introduction

Ultrafast dynamic ellipsometry (UDE) was developed to probe shock induced ultrafast phase transitions in metals. Since metals are opaque at the optical wavelengths used, UDE only probes the optical properties within the skin depth of the metals. For shock induced phase transformation experiments, a shock is driven into the material, and the surface of the material is confined with a transparent window of similar or higher impedance. In the case of a window material with identical shock impedance to the sample material, the window serves to hold the surface at high pressure until the rarefaction wave from the rear of the sample reaches the sample/window interface. With a window material of higher shock impedance, a portion of the shock wave reflects from the window back into the sample, resulting in a higher pressure at the interface than in the original shock wave. In either of these cases, the window serves to hold the sample surface at high pressure for a length of time adequate to permit the phase transformation.

With a window of lower shock impedance, the material would partially release at the interface, but the material would be held at a pressure below the shock pressure and above ambient pressure until the release wave arrived. Without a window, the sample free surface would continuously release into the ambient air, and the phase transformation could not be observed.

Since UDE measures the reflectance of the sample, the optical and material response of the window will be included with the response of the underlying sample material. As some of the material changes may be subtle and the optical properties of the sample may change with the pressure and temperature rise from the shock wave as well as from the phase transformation, it is prudent to measure the response of the window material separately from the sample of interest.

To measure the window response to laser shock loading with UDE, fused silica and aluminum oxide were deposited on Al thin films that have been extensively studied during laser-driven shock loading.¹⁻⁴ The Al/window samples were shocked, and UDE data were recorded.

6.2 Window deposition

A moderate-volume vacuum chamber was used for electron-beam (e-beam) deposition of fused silica and aluminum oxide. The vacuum chamber consisted of an 18" diameter vacuum bell jar on top of a stainless steel flange of similar diameter. The vacuum was provided by a compound turbomolecular pump (BOC Edwards, EXT255H) backed by a dry scroll pump (BOC Edwards, XDS-10). The pressure was monitored with an ion gauge, a cold cathode gauge, and two convectron gauges. A 3 kW multiple

crucible e-Gun (Thermionics) was used as the e-beam deposition source. This source had a rotary mechanism with 4 crucible wells, allowing the deposition of multiple materials in a single vacuum cycle. The planetary was mounted approximately 8" from the source. A quartz crystal microbalance (QCM) was mounted in the center of the planetary for measuring the thicknesses of the deposited layers, and the substrates were positioned concentrically around the QCM.

The e-beam source was outfitted with an X-Y sweep controller, which supplied a variable current to the electromagnets in the source to sweep the beam over the evaporant and to provide uniform heating. The deposition rate was controlled by varying the current through the e-beam filament and the size of the area of evaporant being swept.

6.3 Fused silica

Fused silica (Cerac Inc.) was deposited on a 2 μm Al film on a 120 μm glass substrate. The 953 nm thick fused silica film was deposited at a rate of 0.10 nm/s onto a substrate that was heated to 260°C under a vacuum of 2×10^{-6} torr.

Using the same experimental configuration as was described in the previous chapter, the fused silica film was shocked with a pump energy of 1.2 mJ. Typical UDE data from this experiment are shown in Fig. 6-1. Due to the lack of oscillations in the phase shift and reflectivity data, the Hugoniot parameters of the fused silica film could not be determined.

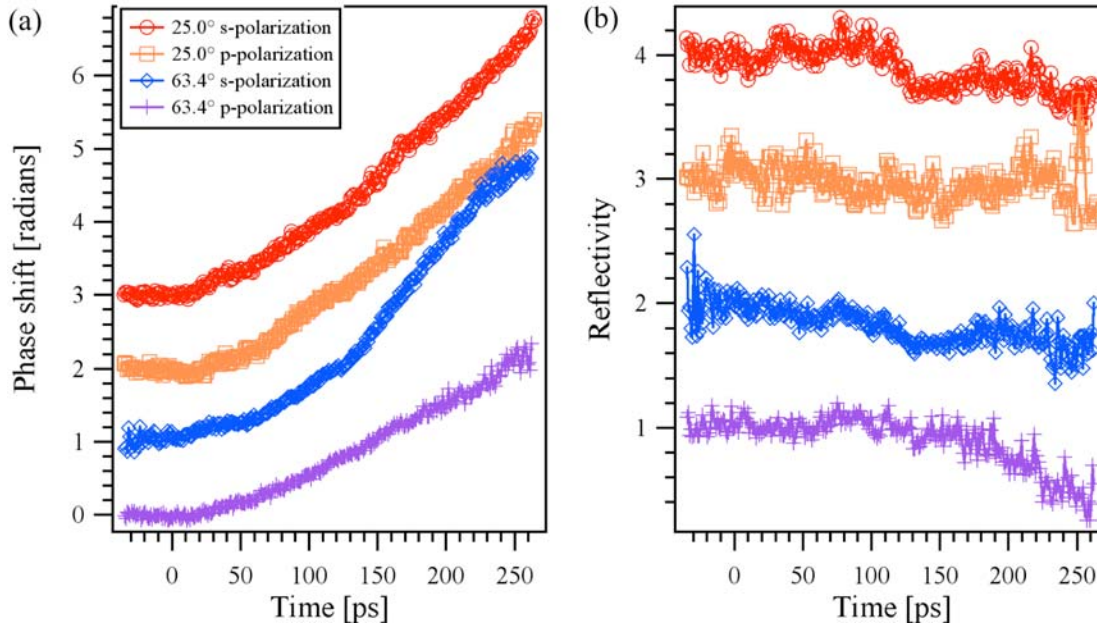


Fig. 6-1. (a) Phase shift and (b) reflectivity data from the two angles and two orthogonal polarizations in a 953 nm thick film of fused silica on 2 μm thick Al. Data are vertically offset for clarity.

6.4 Aluminum oxide

A 1015 nm thick film of aluminum oxide (Alfa Aesar) was grown on a 1 μm Al film on a 120 μm glass substrate. The aluminum oxide film was deposited at a rate of 1.4 nm/s onto a room temperature substrate under a 1×10^{-5} torr vacuum.

The experiment was performed in a manner identical to that described in the previous section, except the pump energy was 1.9 mJ. A typical set of phase shift and reflectivity data from the UDE diagnostic is shown in Fig. 6-2. Similar to the data on fused silica, the Hugoniot properties of the aluminum oxide film could not be determined.

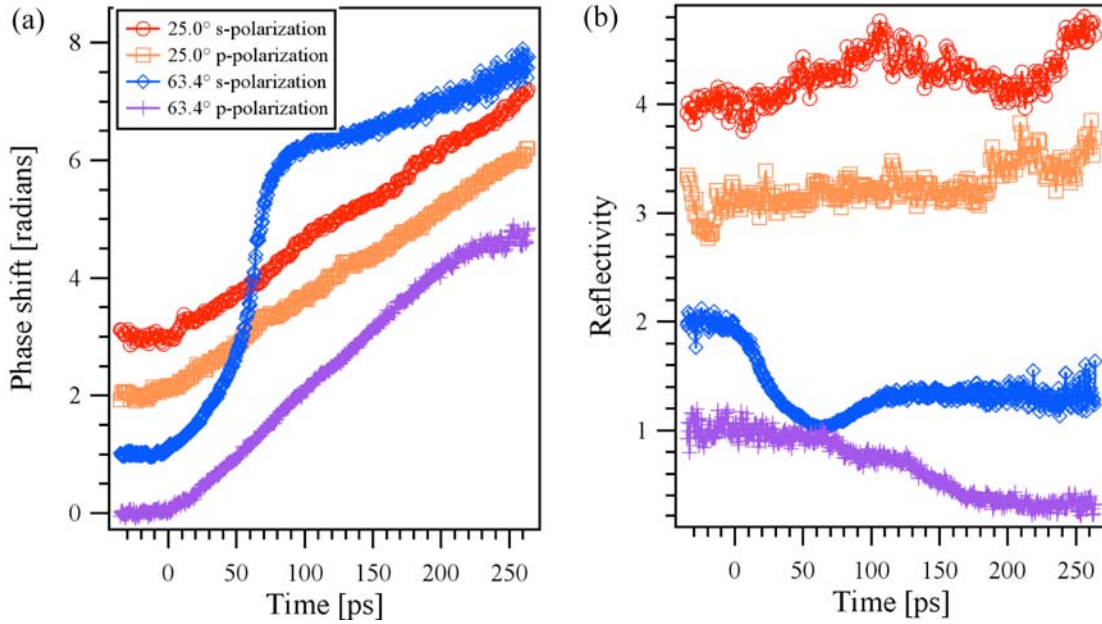


Fig. 6-2. (a) Phase shift and (b) reflectivity data from the two angles and two orthogonal polarizations in a 1015 nm thick film of aluminum oxide on 1 μm thick Al. Data are vertically offset for clarity.

6.5 Discussion

The phase shift and reflectivity data for both the fused silica and aluminum oxide do not show oscillations like the data for the polymer films in the previous chapter. The lack of oscillations resulting from the reflection of the probe light from the Fresnel surface created by the change in refractive index at the shock front is explained by the anomalous behavior of low density glasses under compression.

Wackerle first observed the anomalous compression in fused silica when subjected to shocks below 10 GPa.⁵ These findings were confirmed by Barker and Hollenbach, during their investigation into the optical characteristics of common window materials used in shock loading experiments.⁶ Multiple subsequent experiments showed that for pressures below ~4-5 GPa, fused silica propagates slowly developing ramp waves

instead of shock waves due to its increasing compressibility with pressure.⁵⁻⁹ The decreasing elastic moduli of glasses was also verified under hydrostatic compression by Kondo *et al.*¹⁰ Ng *et al.*⁸ specifically noted the slow build-up time for a strong shock in fused silica under laser driven shock compression.

The UDE phase shift and reflectivity data for fused silica is likely showing a ramp wave similar to the other studies. Although the shock compressed refractive index of fused silica shows behavior close to that of a Gladstone-Dale material,^{6,7} the slow ramp compression would diminish the oscillations that were seen in the polymer data because there would not be a strong Fresnel surface in a well-defined shock front to reflect the probe light. Without further knowledge of the wave structure in the fused silica film, the UDE data cannot be analyzed to yield Hugoniot data.

For a sapphire film, one would also expect the oscillations from the reflection of the probe light off the shock front to be missing. The lack of oscillations would result from the low compressibility of the crystal, and therefore, the small change in density and refractive index.^{6,7,11} However, despite the common chemical composition of sapphire and aluminum oxide, the aluminum oxide film should behave similarly to the fused silica film. Bourne attributed the formation of ramp waves in glasses to their “open structure.”⁹ He confirmed this statement by testing the shock compression of higher density glasses, in which he saw the development of shock waves, typical of most materials, instead of ramp waves.⁹ The e-beam deposition of the aluminum oxide created an amorphous film with a small amount of visible scatter. The scattering of light suggests a high occurrence of defects in the film, which is likely to give it a more open structure and endow it with the related non-linear elastic behavior. As with the fused silica UDE data, additional

knowledge about the wave structure in the aluminum oxide film would be required to obtain the Hugoniot properties.

6.6 Conclusions

Although the amorphous structure of the deposited dielectric films of fused silica and aluminum oxide prevented the acquisition of Hugoniot information, the goal of these measurements was achieved. The UDE measurements on these films were to ascertain their optical response to laser driven shock loading. Even without the Hugoniot information on these films, they may still be used as window materials on metal samples to prevent oxidation and to hold the pressure at the metal surface.

References

- ¹ D. J. Funk, D. S. Moore, K. T. Gahagan, S. J. Buelow, J. H. Reho, G. L. Fisher, and R. L. Rabie, "Ultrafast measurement of the optical properties of aluminum during shock-wave breakout," *Phys. Rev. B* **64**, 115114-5 (2001).
- ² K. T. Gahagan, D. S. Moore, D. J. Funk, R. L. Rabie, S. J. Buelow, and J. W. Nicholson, "Measurement of shock wave rise times in metal thin films," *Phys. Rev. Lett.* **85**, 3205-8 (2000).
- ³ K. T. Gahagan, D. S. Moore, D. J. Funk, J. H. Reho, and R. L. Rabie, "Ultrafast interferometric microscopy for laser-driven shock wave characterization," *J. Appl. Phys.* **92**, 3679-82 (2002).
- ⁴ R. Evans, A. D. Badger, F. Fallies, M. Mahdieh, T. A. Hall, P. Audebert, J. P. Geindre, J. C. Gauthier, A. Mysyrowicz, G. Grillon, and A. Antonetti, "Time- and space-resolved optical probing of femtosecond-laser-driven shock waves in aluminum," *Phys. Rev. Lett.* **77**, 3359-62 (1996).
- ⁵ J. Wackerle, "Shock-wave compression of quartz," *J. Appl. Phys.* **33**, 922-937 (1962).
- ⁶ L. M. Barker and R. E. Hollenbach, "Shock-wave studies of PMMA, fused silica, and sapphire," *J. Appl. Phys.* **41**, 4208-26 (1970).
- ⁷ R. E. Setchell, "Index of refraction of shock-compressed fused silica and sapphire," *J. Appl. Phys.* **50**, 8186-92 (1979).
- ⁸ A. Ng, P. Celliers, and D. Parfeniuk, "Dynamics of laser-driven shock waves in fused silica," *Phys. Rev. Lett.* **58**, 214-217 (1987).
- ⁹ N. K. Bourne, Z. Rosenberg, and A. Ginzburg, "The ramping of shock waves in three glasses," *Proc. R. Soc. London, Ser. A* **452**, 1491-6 (1996).
- ¹⁰ K. Kondo, S. Iio, and A. Sawaoka, "Nonlinear pressure dependence of the elastic moduli of fused quartz up to 3 GPa," *J. Appl. Phys.* **52**, 2826-31 (1981).
- ¹¹ S. C. Jones, M. C. Robinson, and Y. M. Gupta, "Ordinary refractive index of sapphire in uniaxial tension and compression along the c axis," *J. Appl. Phys.* **93**, 1023-31 (2003).

Chapter 7

Single Shot Hugoniot using a Spatially Shaped Pressure Wave

7.1 Introduction

During the development of ultrafast dynamic ellipsometry (UDE) that is detailed in the previous chapters, it was postulated that it might be possible to generate a range of pressures from a single laser pulse using the Gaussian spatial profile of the shock drive laser as well as its specifically shaped temporal profile. From a fit of the measured electric field phase shift and reflectivity change upon reflection from the shocked material, we extract the shock velocity (u_s), particle velocity (u_p), and shocked refractive index (n) at each spatially resolved stress state along a one-dimensional slice across the Gaussian profile with UDE. The small distance traveled by the shock wave with respect to the large width of the shocked region allows the flow to be treated as one-dimensional at each spatial point, an assumption that is verified by hydrocode calculations.

To demonstrate the feasibility and accuracy of using the Gaussian spatial profile of the shock-generating laser to create different pressures in a material and to enable the measurement of the shock state in each region, we measured the Hugoniot of several liquids: cyclohexane, toluene, methanol, and water. The experiment on each material was performed using a chirped and temporally shaped single laser pulse of approximately 300 ps total length. The u_s - u_p responses of the four liquids on this short timescale were

compared to those obtained when using a traditional shock wave technique in which the shocks were generated with high explosives and the velocities were measured with time-of-arrival pins, even though the shock wave rise times and durations in our experiments were shorter by several orders of magnitude. Liquid samples were chosen for these experiments to permit an accurate comparison of the temporal material response without concern about differences in the material due to sample size or microstructure.

In addition to the liquid samples, a polycarbonate thin film was also probed with single shot UDE. The data from the polycarbonate film showed evidence of the inhomogeneity of the film that was incorporated during sample fabrication.

7.2 CTH hydrocode simulation

To test the assumption that the large aspect ratio of the Gaussian stress wave provides essentially one-dimensional flow, V. H. Whitley performed a two-dimensional simulation of the cylindrically symmetric hydrodynamic processes with the hydrocode CTH (Sandia National Laboratory).¹ To simulate the laser driven shock, a 3 μm thick aluminum plate was assigned a Gaussian temperature distribution and no momentum. The stationary plate was placed in contact with a 2 μm thick unheated aluminum plate, on the other side of which was 4 μm of cyclohexane. The temperature of the Al flyer was adjusted to create pressure conditions in the cyclohexane similar to those in the shot shown in §7.3.1. The system was allowed to evolve in time, during which the heated Al plate induced a shock wave in the unheated Al plate that traveled through the cyclohexane. The simulation was run for 250 ps after the shock wave reached the Al/cyclohexane interface, which was the same length of time as in the experiment.

Figure 7-1(a) shows the pressure distribution in the heated Al plate at the beginning of the simulation, and Fig. 7-1(b) shows the pressure distribution at the end of the simulation, 250 ps after the shock wave crossed the Al/cyclohexane boundary. Figure 7-2 shows the radial and axial components of the particle velocity at the end of the simulation. Due to the large diameter of the shocked area in comparison to the distance that the shock wave travels into the cyclohexane during the time for which the data were recorded, the radial and axial velocity components can be approximated as non-interacting. The CTH simulation shows that the radial velocity component is less than 2.1% of the axial velocity component for the area and time over which the Hugoniot data were collected. Neglecting this interaction leads to an error that is of the same order as the error in the UDE fitting parameters. The ratio of the radial portion of the velocity to the axial portion increases as time progresses, which restricts the non-interacting assumption to experiments on very short timescales. The minimal pressure differential between adjacent areas of material allows the areas to be treated as essentially non-interacting flow tubes. The large aspect ratio means that the tilt of the shock wave, even on the steepest part of the Gaussian, is still similar to an impact by a projectile with a small amount of tilt (tens of milliradians).

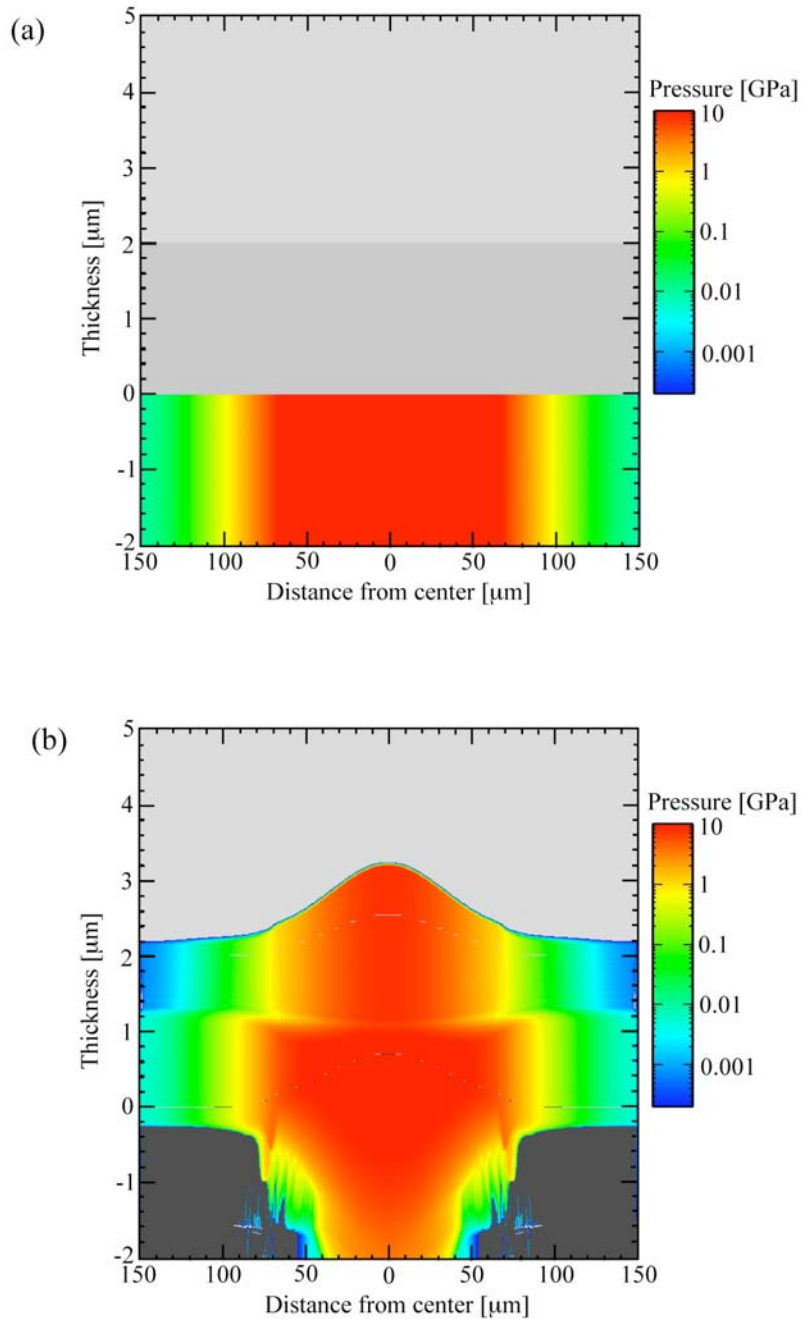


Fig. 7-1. Pressure plots from the CTH simulation. (a) Initial pressure distribution in an Al plate from thickness -2 to 0 μm resulting from an applied Gaussian temperature distribution that is used to generate a shock wave in an adjacent Al plate (thickness = 0 to 2 μm) and in a layer of cyclohexane (thickness = 2 to 5 μm). (b) Pressure distribution in the sample 250 ps after the shock wave crossed the Al/cyclohexane interface that was originally located at thickness = 2 μm . The pressure in the cyclohexane at the center of the sample is 8.25 GPa. Courtesy of V. H. Whitley.

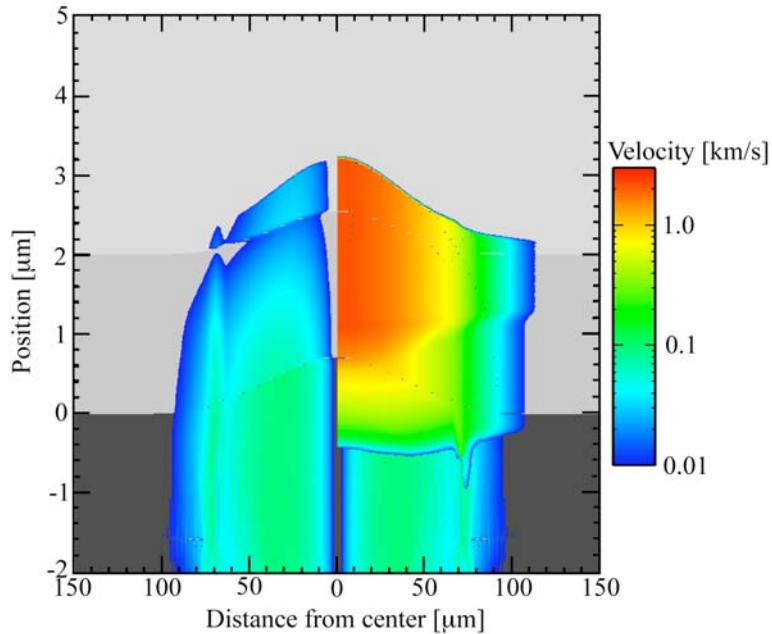


Fig. 7-2. Plot of the radial and axial particle velocity components from the CTH simulation at 250 ps after the shock wave crossed the Al/cyclohexane interface that was originally located at thickness = 2 μm . The radial (horizontal) component of the particle velocity is to the left of the center, and the axial (vertical) component of the particle velocity is to the right of the center in this cylindrically symmetric simulation. Please note the compressed length scale of the horizontal axis with respect to the vertical axis. Courtesy of V. H. Whitley.

7.3 Single shot Hugoniot data of liquids

7.3.1 Experiment

The experimental conditions of the laser for shock generation and UDE probing are the same as in the previous chapter.

The sample consisted of a liquid cell in which one side was a 120 μm thick glass slide that was vapor deposited with 2 μm of aluminum (Berliner Glas) and the other side was a 1 mm thick fused quartz slide that was angled approximately 2° in the direction perpendicular to the incident probe beams to remove the interference from the reflections

off of the surfaces of the slide. The cell was filled with the liquid sample that was approximately 0.75 mm thick. The laser was focused onto the Al/glass interface to generate the shock, which then propagated through the Al layer and into the liquid. The shock response of the liquid was probed from the opposite direction through the quartz slide. A schematic of the cross-section of the liquid cell is shown in Fig. 7-3.

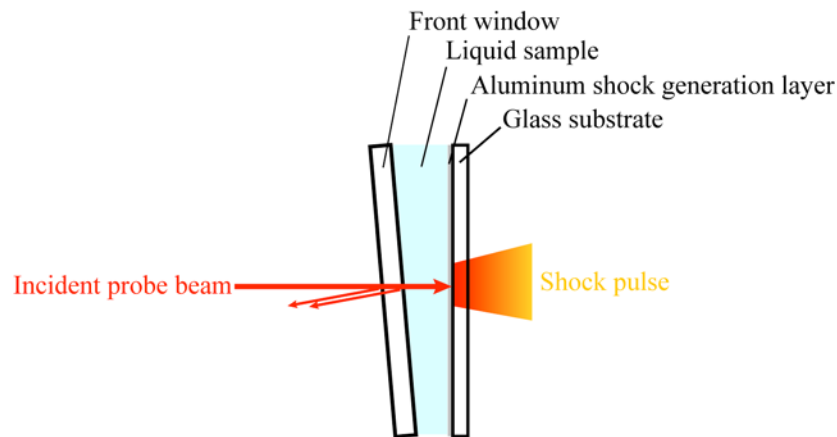


Fig. 7-3. Cross-section schematic of the liquid sample cell. The shock generating pulse is incident from the right and is focused through the glass substrate onto the vapor-plated aluminum layer. The shock travels into the liquid sample and is probed from the left. The incident probe beam is partially reflected downward at the interfaces of the front window, which removes the window reflections from the detected interferogram.

To analyze the data, the thin film model explained in §5.1 was slightly modified. Since the thickness of the liquid was large in comparison to the wavelength of the light, the five layer sample used in the analysis of the thin films was replaced with a sample consisting of four layers: unshocked liquid, shocked liquid, alumina, and aluminum (the air layer was neglected). The refractive index of the unshocked liquid was obtained from the literature, and it was set to that constant value during the fit. The thickness of the

unshocked liquid layer was set to a large value ($d=10^7$ nm), and Snell's law, given in equation (7.1), was used to calculate the incident angle in the unshocked liquid.

$$n_1 \sin \theta_1 = n_2 \sin \theta_2, \quad (7.1)$$

where n_1 is the refractive index of air ($n_1=1$), θ_1 is the incident angle in air, n_2 is the refractive index of the unshocked liquid, and θ_2 is the incident angle in the unshocked liquid. The shock velocity, the particle velocity, and the shocked refractive index of the liquid were allowed to vary when calculating the phase shift and reflectivity from the sample as a function of time. The thickness of the unshocked liquid layer decreased linearly as a function of the shock velocity, and the thickness of the shocked liquid layer increased linearly as a function of the difference between the shock and particle velocities. All eight sets of data (phase shift and reflectivity for each angle and each polarization) were fitted simultaneously at each spatial position across the Gaussian-shaped pressure pulse.

Just as with the thin polymer films in Chapter 5, for UDE to be used to find Hugoniot data in transparent liquids, there must be a change in the refractive index between the shocked and unshocked layers that is large enough to create a Fresnel surface. Therefore, the minimum pressure required to create a Fresnel surface at the shock front dictates the lower limit of the Hugoniot data. That minimum pressure depends on the initial refractive index of the material and on the change in refractive index under shock compression. In the four liquids presented here (cyclohexane, water, methanol, and toluene), the minimum pressure at which UDE data could resolve the movement of the shock front varied. The upper limit on pressure was a result of the maximum intensity at the center of the laser pulse. With this sample configuration, the

maximum pressure was limited by the intensity of the laser light that could be transmitted through the 120 μm glass substrates without self-focusing.

Several decades ago, Woolfolk et al.² empirically derived a formula for the universal Hugoniot curve for liquids. The universal liquid Hugoniot formula is as follows:

$$\frac{u_s}{c_0} = 1.37 - 0.37e^{\frac{-2u_p}{c_0}} + 1.62\frac{u_p}{c_0}, \quad (7.2)$$

where, u_s is the shock velocity, u_p is the particle velocity, and c_0 is the sound speed at ambient pressure. With the single shot Hugoniot for each liquid, the universal liquid Hugoniot will also be plotted.

As in Chapter 5, the shocked refractive index obtained with the Hugoniot data will be compared to the value calculated with the Gladstone-Dale³ formula in Eq. (7.3), which provides a simple density correction for the refractive index.

$$n_{s,\text{GD}} = 1 + \frac{(n_0 - 1)}{\left(1 - \frac{u_p}{u_s}\right)}, \quad (7.3)$$

where $n_{s,\text{GD}}$ is the shocked refractive index according to Gladstone-Dale and n_0 is the initial refractive index of the material at ambient pressure. The shocked refractive index for each of the liquids differs substantially from the Gladstone-Dale expectation.

7.3.2 Cyclohexane

The eight sets of data collected during the shock experiment on cyclohexane (Acros Organics) are shown in Fig. 7-4. The Gaussian spatial profile of the shock generating laser pulse created the smoothly varying pressure distribution across the shocked region.

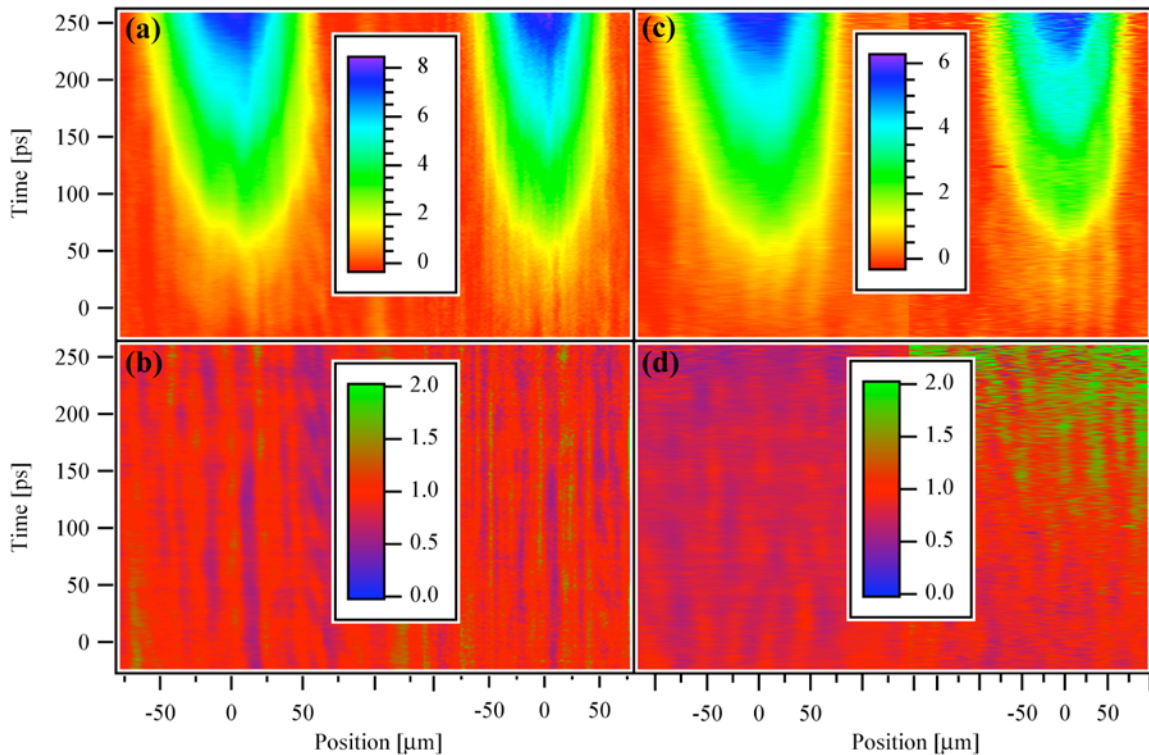


Fig. 7-4. Phase shift and reflectivity data for a shock in liquid cyclohexane that is backed by $2\ \mu\text{m}$ of Al. The maximum pressure of the shock wave is 8.2 ± 0.1 GPa at the center of the shocked area. In each of the four images, the p-polarized data are on the left and the s-polarized data are on the right. (a) Phase shift data at 28.4° . (b) Reflectivity at 28.4° . (c) Phase shift data at 63.1° . (d) Reflectivity data at 63.1° .

The derived Hugoniot data for the shock response of cyclohexane shown in Fig. 7-4 are plotted in Fig. 7-5. These data were obtained using the fitting procedure

described above with the initial refractive index for cyclohexane of 1.4206.⁴ The Hugoniot data show very little scatter in the shock and particle velocities. They also match very well with the previous data on cyclohexane from the LASL Shock Hugoniot Data⁵ and with the calculated universal liquid Hugoniot.² For the LASL data, the shock wave was created with high explosives and the velocities were measured with time-of-arrival pins. The time resolution with which the LASL data were recorded was several orders of magnitude longer than that of the UDE data, but despite this difference, the u_s - u_p response is essentially identical. This similarity suggests that the shock response of cyclohexane is not time-dependent.

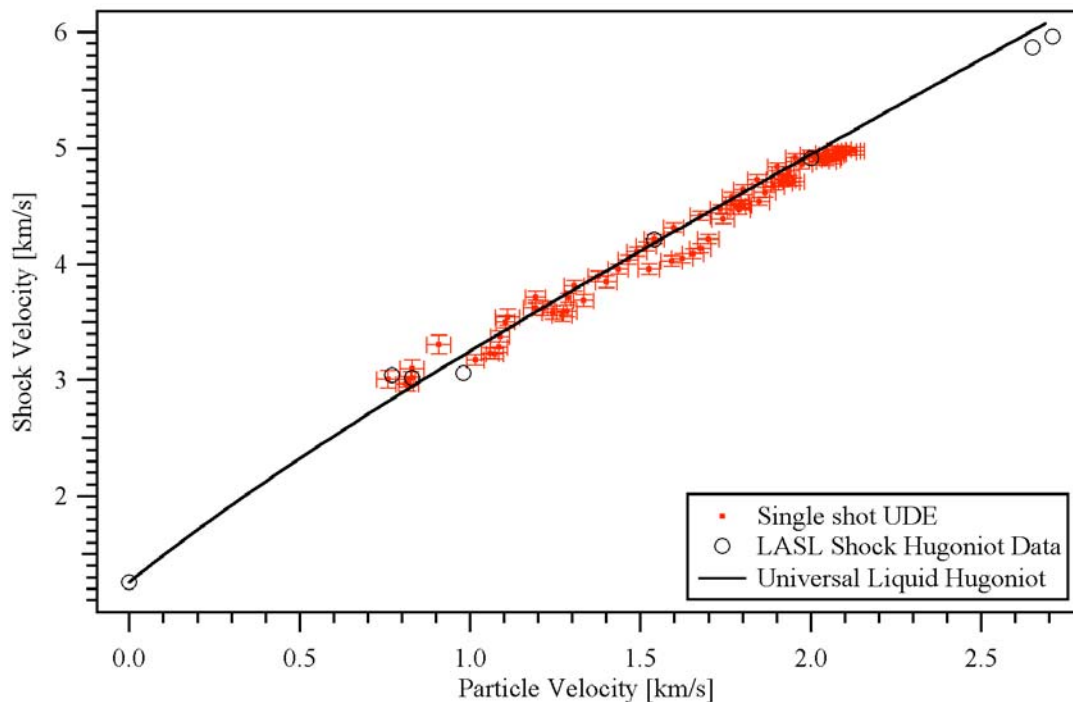


Fig. 7-5. Hugoniot data for cyclohexane from a single laser shot along with data from the LASL Shock Hugoniot Data⁵ and the calculated universal liquid Hugoniot² for comparison.

Figure 7-6 shows the comparison between the shocked refractive index acquired from the fit to the UDE data and the Gladstone-Dale shocked refractive index calculated from Eq. (7.3), using the shock velocity and particle velocity from the fit. The linear fit in Fig. 7-6 shows some deviation of the shocked refractive index from the values expected from the Gladstone-Dale relation, but the difference is within the error of the measurement.

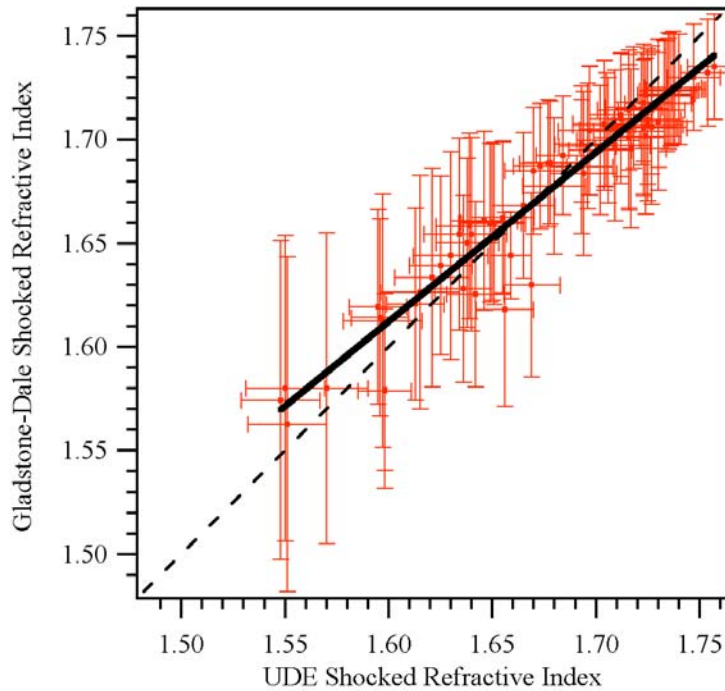


Fig. 7-6. A plot of the shocked refractive index of cyclohexane calculated from the Gladstone-Dale relation, $n_{s,GD}$, versus the shocked refractive index, n_s . The linear fit (solid black line) gives $n_{s,GD}=(0.82 \pm 0.02) n_s + (0.30 \pm 0.04)$. The dashed black line represents Gladstone-Dale behavior.

7.3.3 Toluene

Ultrafast dynamic ellipsometry data were taken of anhydrous toluene (Sigma Aldrich). The Hugoniot data extracted from fitting the data with an initial refractive index of 1.486^4 for toluene are shown in Fig. 7-7. The UDE toluene Hugoniot data are also in good agreement with the data from the LASL Shock Hugoniot Data.⁵ At lower pressures, the UDE toluene Hugoniot data match well with the universal liquid Hugoniot,² but at higher pressures both the LASL data and the UDE data differ from the universal liquid Hugoniot.

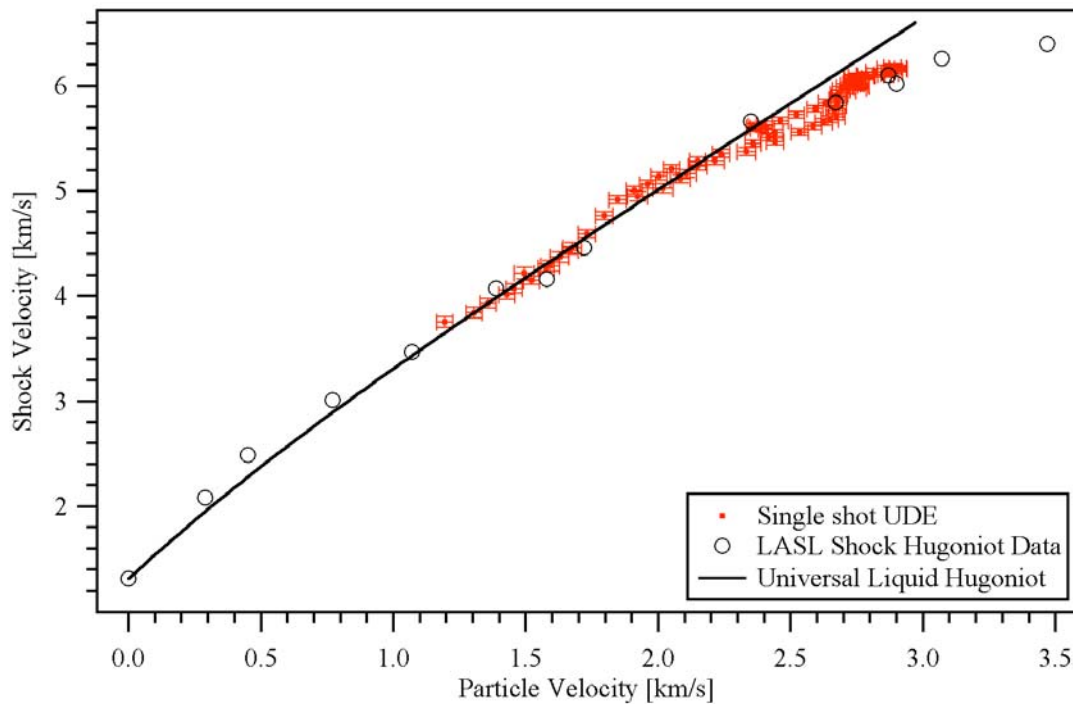


Fig. 7-7. Hugoniot data for toluene from a single laser shot along with data from the LASL Shock Hugoniot Data⁵ and the calculated universal liquid Hugoniot² for comparison.

The shocked refractive index data of toluene from the fitting routine are compared with the shocked refractive index calculated from the Gladstone-Dale relation in Fig. 7-8.

The toluene shocked refractive index data differ dramatically from the values expected from Gladstone-Dale.

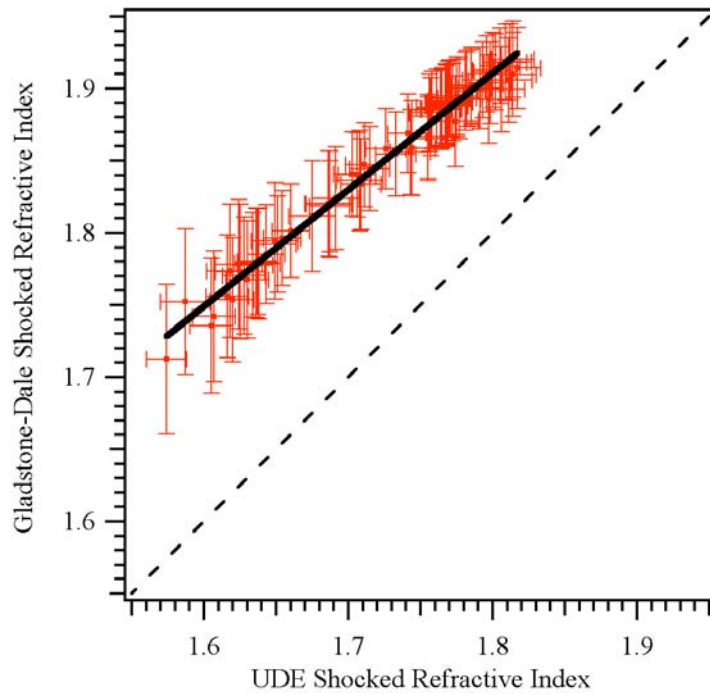


Fig. 7-8. A plot of the shocked refractive index of toluene calculated from the Gladstone-Dale relation, $n_{s,GD}$, versus the shocked refractive index, n_s . The linear fit (solid black line) gives $n_{s,GD}=(0.81 \pm 0.01) n_s + (0.46 \pm 0.02)$. The dashed black line represents Gladstone-Dale behavior.

7.3.4 Methanol

Ultrafast dynamic ellipsometry data were acquired of spectrophotometric-grade methanol (Fisher Chemical). The initial refractive index used for methanol was 1.325.⁴ The Hugoniot data obtained from a single shot in methanol are shown in Fig. 7-9. At higher shock pressures, the UDE data match well with both the LASL data and the universal liquid Hugoniot, but at lower pressures, the data deviate. This deviation might result from the weak interference fringes between the light reflected from the shock front and the light reflected from the Al/methanol interface in the UDE data.

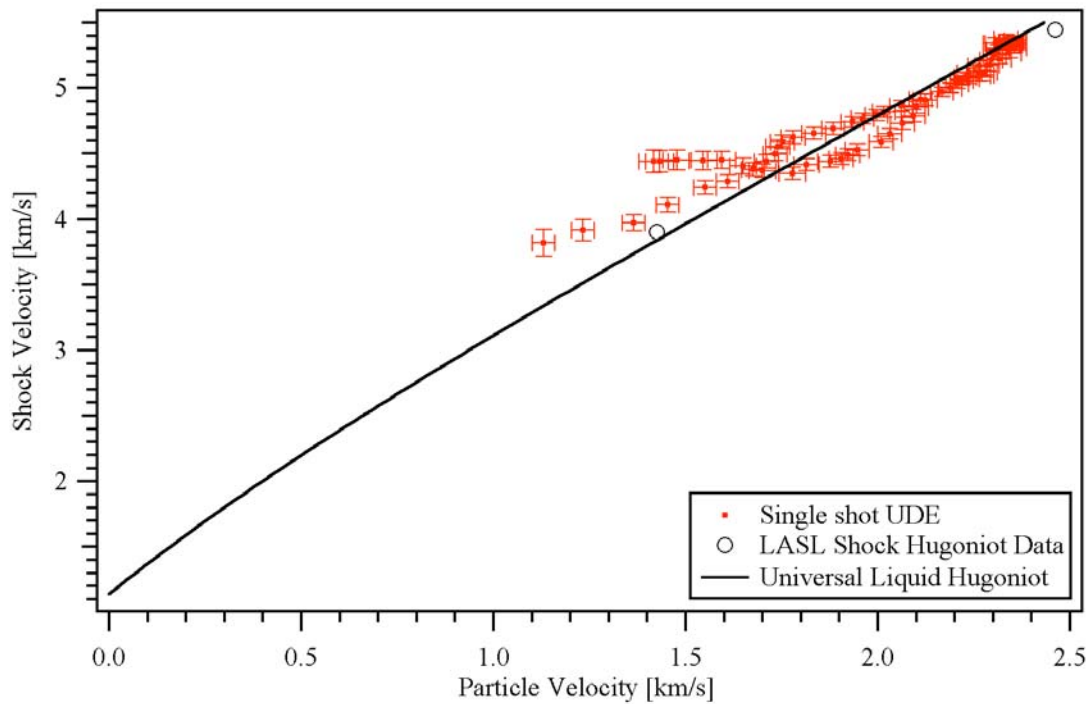


Fig. 7-9. Hugoniot data for methanol from a single laser shot along with data from the LASL Shock Hugoniot Data⁵ and the calculated universal liquid Hugoniot² for comparison.

Figure 7-10 compares the shocked refractive index from the fit of the UDE data to the shocked refractive index calculated from the Gladstone-Dale relation. The shocked

refractive index data of methanol differ slightly more from the Gladstone-Dale expectation than that of cyclohexane but less than that of toluene.

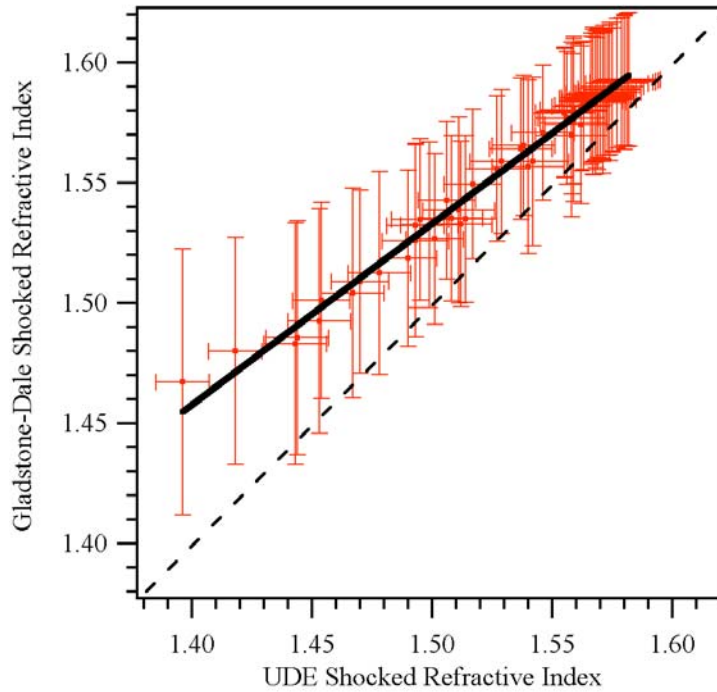


Fig. 7-10. A plot of the shocked refractive index of methanol calculated from the Gladstone-Dale relation, $n_{s,GD}$, versus the shocked refractive index, n_s . The linear fit (solid black line) gives $n_{s,GD}=(0.75 \pm 0.01) n_s + (0.40 \pm 0.02)$. The dashed black line represents Gladstone-Dale behavior.

7.3.5 Water

Ultrafast dynamic ellipsometry data were taken of ultrafiltered deionized water. The Hugoniot data extracted from the fit with an initial water refractive index of 1.326⁶ is shown in Fig. 7-11. The UDE water Hugoniot data lay slightly below the water Hugoniot data from the LASL Shock Hugoniot Data⁵ and the universal liquid Hugoniot.²

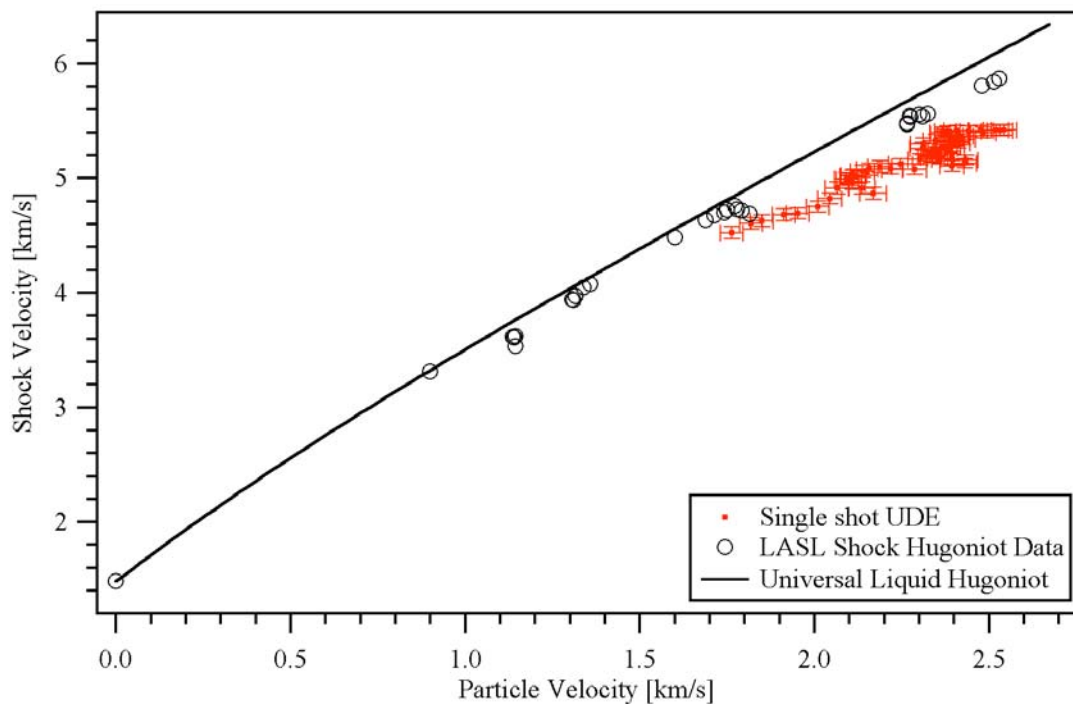


Fig. 7-11. Hugoniot data for water from a single laser shot along with data from the LASL Shock Hugoniot Data⁵ and the calculated universal liquid Hugoniot² for comparison.

Figure 7-12 shows the comparison between the shocked refractive index data acquired from the fit to the UDE data and the calculated Gladstone-Dale shocked refractive index. The shocked refractive index deviates around the Gladstone-Dale expectation but within the error estimate.

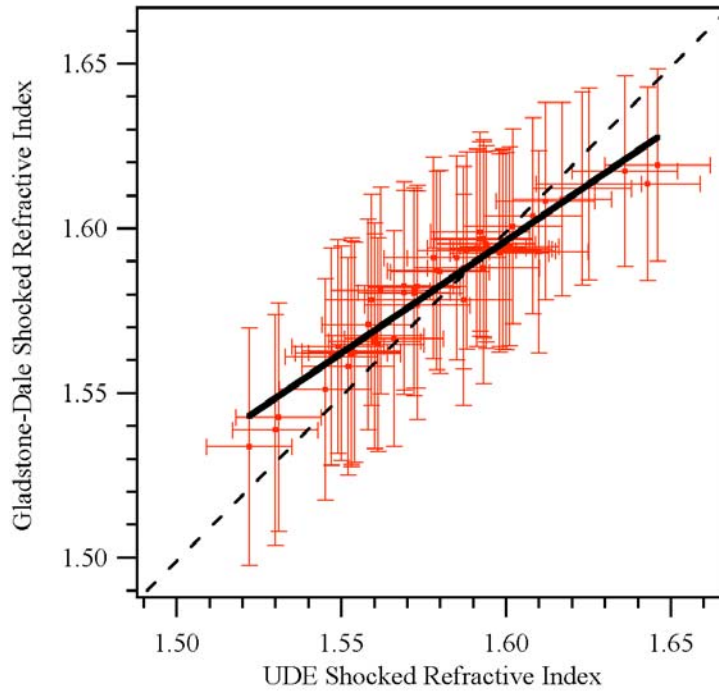


Fig. 7-12. A plot of the shocked refractive index of water calculated from the Gladstone-Dale relation, $n_{s,GD}$, versus the shocked refractive index, n_s . The linear fit (solid black line) gives $n_{s,GD}=(0.68 \pm 0.03) n_s + (0.50 \pm 0.04)$. The dashed black line represents Gladstone-Dale behavior.

7.4 Single shot Hugoniot data of polycarbonate thin film

The single shot method of using the spatial profile of the shock generating laser to create a distribution of pressures in a material was attempted with polymer thin films in addition to liquids. The same polycarbonate film that was used in §5.3 was used for the single shot Hugoniot. As discussed in Chapter 5, the fit parameters for the polymer thin films include the initial refractive index and the thickness of the film in addition to the fit parameter as defined for the liquid samples in the previous section.

In §5.3, it was postulated that the scatter in the Hugoniot data was a product of the inhomogeneity of the polycarbonate film. This postulation was well supported by the variation in the values of the thickness and initial refractive index (and therefore, density) obtained from the fitting of the data. Additionally, small inhomogeneities were visible by eye on the surface of the film. These inhomogeneities were diminished with the use of a surfactant in the solution from which the film was spin-cast, but they were not entirely removed.

When the single shot Hugoniot method was performed on the polycarbonate film, there appeared to be some structure to the resulting Hugoniot data. The Hugoniot data did not show the random scatter seen in the data in §5.3, but instead, showed a continuous pattern that was unique for each shot. Since the film was already known to be inhomogeneous, the curiosity of the pattern in the data was further investigated. Figure 7-13 displays the initial refractive index and the thickness of the film across the shot region for a single laser shot. Clearly, there is a strong correlation between the two parameters. Is this correlation an artificial byproduct of the fitting routine, or does UDE measure the actual properties of the sample?

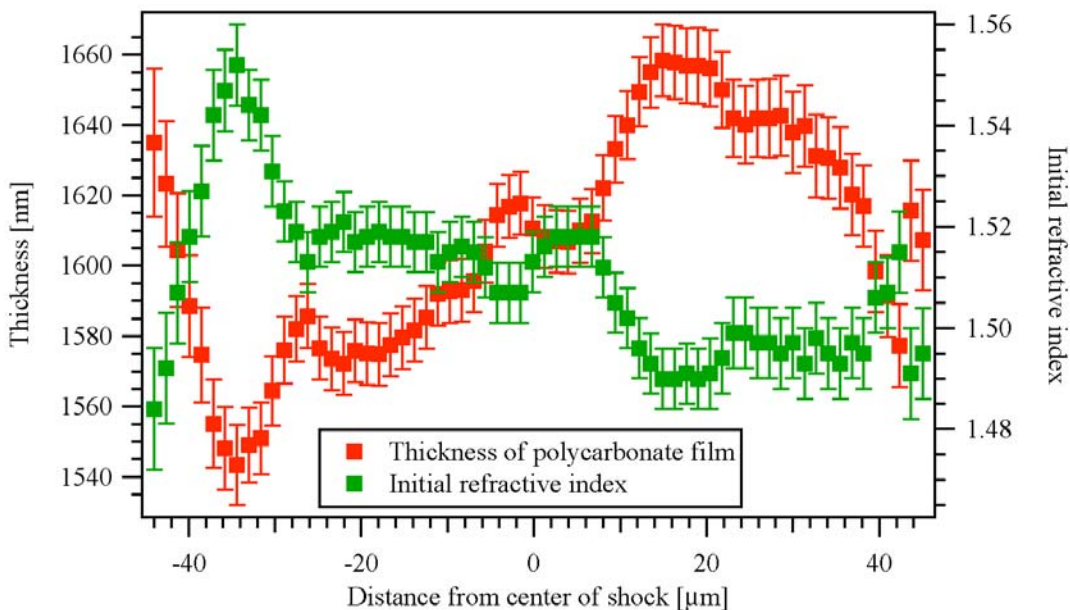


Fig. 7-13. Thickness and initial refractive index data of a polycarbonate film across the shocked region obtained from a single shot Hugoniot UDE measurement and using the fitting routine described in §5.1.

If the initial refractive index and thickness of the film were constant across the shocked region, the optical path length through the material would also be constant (optical path length = refractive index x distance). In this case, the initial refractive index and thickness would not need to be fit parameters but could be set as constants. The variation in those values shown in Fig. 7-13 might have arisen from optimizing the fit while keeping the optical path length unchanged. The other possibility is that UDE probes the actual properties of the sample, and the correlation might have resulted from the way the film was cast. Since the film was spin-cast from a solution of polycarbonate in chloroform, there are numerous ways that the film could have settled to form regions with different thicknesses and densities. For example, the films might have contained regions with various amounts of residual solvent. Upon evaporation of the solvent, the

film could have condensed to form thinner regions with higher densities and therefore higher refractive indices. To test these two hypotheses, the same set of data was fit using a different routine, in which the initial refractive index and thickness were not fit parameters but were set to constant values. The values chosen were the averages of the values shown in Fig. 7-13: initial refractive index=1.51, thickness=1610 nm. Figure 7-14 shows the Hugoniot data resulting from both of the fitting routines.

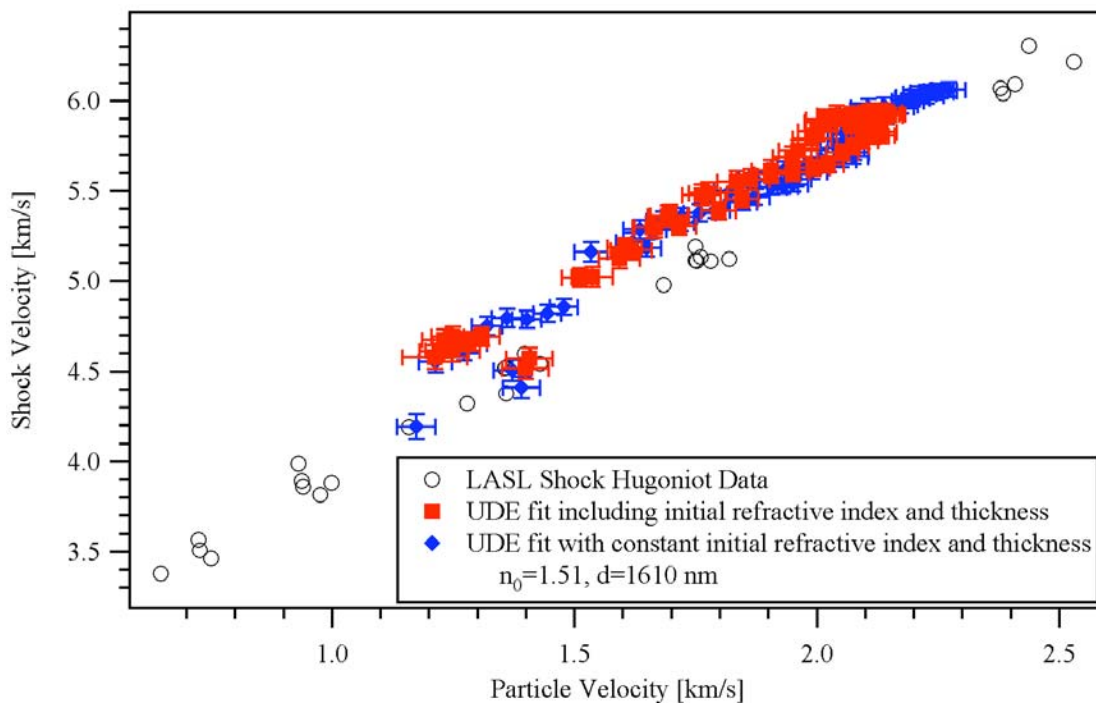


Fig. 7-14. Hugoniot data of a polycarbonate thin film from fitting a single shot. The same UDE data were fit including the initial refractive index and thickness of the film as fit parameters and setting those values to constants. Data from the LASL Shock Hugoniot Data⁵ are included for reference.

Removing the initial refractive index and thickness as fitting parameters decreased some of the structure seen in the data obtained from the fitting that included all of the parameters. However, the mean squared error, shown in Fig. 7-15, is higher when

not using all of the parameters, implying that the initial refractive index and thickness are not constant across the shocked region. These results suggest that UDE probes the actual sample characteristics.

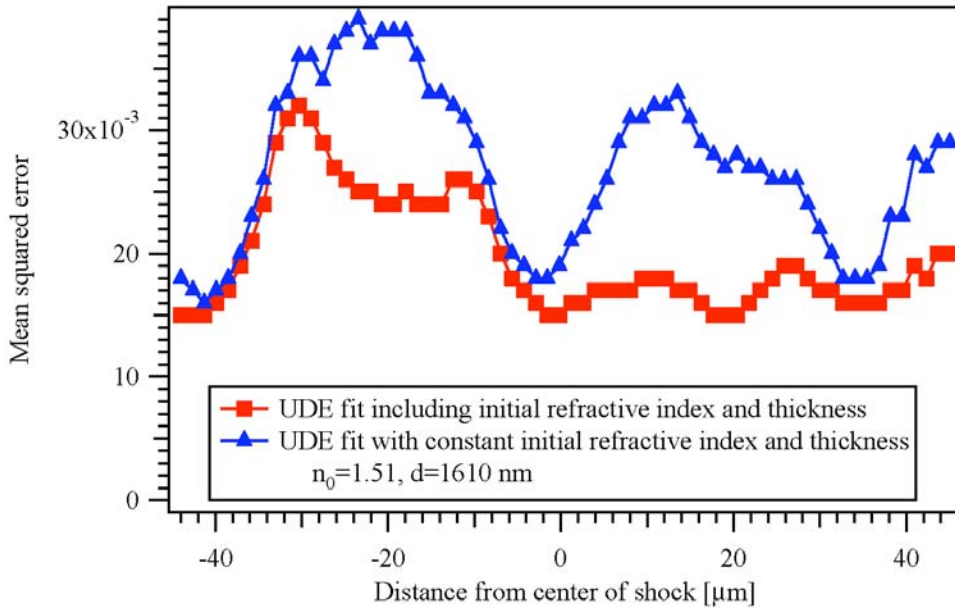


Fig. 7-15. Mean squared errors of the fits that produced the Hugoniot data in Fig. 7-14 across the shocked region of a single shot.

7.5 Discussion

The CTH hydrocode simulation showed that for the short length scales of UDE, the spatial profile of the shock generating laser pulse could be used to create a distribution of differing shock pressures in the sample. The single shot Hugoniot data of cyclohexane and toluene also support the conclusions from the CTH simulation. Use of the spatial profile of the laser to create a range of pressures is limited to experimental configurations with a large aspect ratio and to short times because the radial component of the particle velocity increases with time and shock propagation distance. Just as with

the polymer data in Chapter 5, a change in refractive index of the transparent material is required at the shock front to acquire Hugoniot data from UDE. However, if this condition is met, the UDE technique for obtaining a single shot Hugoniot allows a fast and cost-effective method of collecting Hugoniot data.

The cyclohexane and toluene Hugoniot data match very well with both the LASL Shock Hugoniot Data and the universal liquid Hugoniot. The u_s - u_p responses of the cyclohexane and of the toluene on this short timescale were essentially identical to those obtained when using a traditional shock wave technique in which the shock was generated with high explosives and the velocities were measured with time-of-arrival pins, despite the difference of several orders of magnitude in the time resolution of the measurement methods. The same response of these materials on vastly different timescales is understandable since the materials are without strength and they do not possess any time dependent processes such as phase transitions or chemical reactions in the pressure regions that were probed. These liquid samples permit direct comparison with the longer timescale data since they are uniform and should be identical to the previous samples. It is for this reason that the scatter in the Hugoniot data is much less than for the polymer samples in Chapter 5.

The single shot Hugoniot data of water are interesting since they deviate from the previously measured Hugoniot. The strong hydrogen bonding in the water could provide an explanation for the difference in the response. The structural relaxation and intermolecular bonding in water have been measured to have a time constant on the order of 1-2 ps.⁷⁻¹¹ Although that time is shorter than the time resolution of the UDE data, the slower equilibration time and the strength of the intermolecular bonding might still play a

role in the shock response on the current timescale. In fact, spontaneous Raman scattering from water shocked with a gas gun (experiment duration $\sim 1 \mu\text{s}$) showed that strong intermolecular hydrogen bonds were present up to 12 GPa.¹² It is possible that the hydrogen bonds play a role in the material response that is evident only when the temporal resolution of the measurement is on the same order as the structural relaxation or when the strain rate is high enough to interfere with the vibrational dynamics. Although the structural relaxation times in methanol are similar to water,¹³ the methanol data do not deviate as strongly as the water data, which could be a consequence of the weaker hydrogen bonds. Another possible explanation for the difference is the dramatically higher viscosity of shocked water in the pressure region probed.¹⁴ This higher viscosity is attributed to the partial solidification of the liquid water into ice VII.

The shocked refractive indices of cyclohexane, methanol, and water differ slightly from the values predicted by the Gladstone-Dale relation, but the differences are within the error of the measurement. However, the shocked refractive index of toluene differs significantly from Gladstone-Dale behavior. Since liquids are amorphous and do not have strength, it would be expected that the refractive indices would change as a function of density as predicted by Gladstone-Dale.

The single shot data on polycarbonate show inverse correlation between the initial refractive index and the thickness of the film. Further analysis suggests that UDE probes the material characteristics and is sensitive to small fluctuations in the sample properties.

In terms of the applicability of this technique to other materials, the ease and speed with which these single shot Hugoniot measurements are performed opens up new possibilities for investigating materials at high pressure. Materials that have not

traditionally been investigated as a function of pressure may now be studied using this technique. Most high pressure studies focus on pure materials or high interest materials of a set composition. The speed and cost effectiveness of this technique will allow solutions and mixtures to be studied as a function of composition in a far less labor-intensive way than previously available. Although this is a destructive technique, the small amount of material consumed will also permit testing of high cost samples. In addition to more efficiently measuring high pressure states, the single shot Hugoniot method described in this chapter may be used to extrapolate rate-dependent processes on a very fast timescale, a prospect which will be discussed in more detail in subsequent chapters.

References

- ¹ J. M. McGlaun, S. L. Thompson, and M. G. Elrick, "CTH - A 3-dimensional shock-wave physics code," *Inter. J. Impact Eng.* **10**, 351-360 (1990).
- ² R. W. Woolfolk, M. Cowperthwaite, and R. Shaw, "A "universal" Hugoniot for liquids," *Thermochemica Acta* **5**, 409-414 (1973).
- ³ J. H. Gladstone and T. P. Dale, "Researches on the refraction, dispersion, and sensitiveness of liquids," *Philos. Trans. R. Soc. London* **153**, 317-343 (1863).
- ⁴ J. Rheims, J. Koser, and T. Wriedt, "Refractive-index measurements in the near-IR using an Abbe refractometer," *Meas. Sci. Tech.* **8**, 601-5 (1997).
- ⁵ S. P. Marsh, *LASL Shock Hugoniot Data* (University of California Press, Berkeley, 1980).
- ⁶ E. D. Palik, *Handbook of Optical Constants of Solids* (Academic Press, San Diego, 1998).
- ⁷ G. M. Gale, G. Gallot, F. Hache, N. Lascoux, S. Bratos, and J. C. Leicknam, "Femtosecond dynamics of hydrogen bonds in liquid water: a real time study," *Phys. Rev. Lett.* **82**, 1068-71 (1999).
- ⁸ C. J. Fecko, J. D. Eaves, J. J. Loparo, A. Tokmakoff, and P. L. Geissler, "Ultrafast Hydrogen-Bond Dynamics in the Infrared Spectroscopy of Water," *Science* **301**, 1698-1702 (2003).
- ⁹ C. J. Fecko, J. J. Loparo, S. T. Roberts, and A. Tokmakoff, "Local hydrogen bonding dynamics and collective reorganization in water: Ultrafast infrared spectroscopy of HOD/D2O," *J. Chem. Phys.* **122**, 054506 (2005).
- ¹⁰ J. J. Loparo, S. T. Roberts, and A. Tokmakoff, "Multidimensional infrared spectroscopy of water. I. Vibrational dynamics in two-dimensional IR line shapes," *J. Chem. Phys.* **125**, 194521-1 (2006).
- ¹¹ C. P. Lawrence and J. L. Skinner, "Ultrafast infrared spectroscopy probes hydrogen-bonding dynamics in liquid water," *Chem. Phys. Lett.* **369**, 472-7 (2003).
- ¹² N. C. Holmes, W. J. Nellis, W. B. Graham, and G. E. Walrafen, "Spontaneous Raman scattering from shocked water," *Phys. Rev. Lett.* **55**, 2433-6 (1985).
- ¹³ R. Laenen, G. M. Gale, and N. Lascoux, "IR spectroscopy of hydrogen-bonded methanol: vibrational and structural relaxation on the femtosecond time scale," *J. Phys. Chem. A* **103**, 10708-12 (1999).
- ¹⁴ V. N. Mineev and A. I. Funtikov, "Measurements of the viscosity of water under shock compression," *High Temperature* **43**, 141-150 (2005).

Chapter 8

Hugoniot Measurements of Reactive Liquids

8.1 Introduction

Shock induced chemical reactions have become common since the invention of dynamite by Alfred Noble in 1866. Currently, modern society relies on shock induced chemical reactions in the form of detonating explosives for numerous uses, such as mining, building demolition, pyrotechnics, warfare, and even diamond manufacturing.¹ In spite of the prevalent use of the resulting mechanical work (typically in the form of pressure and temperature) provided from shock induced chemical reactions, the underlying mechanism and kinetics for the transfer of energy from a mechanical insult into the chemistry of breaking and forming chemical bonds is relatively unknown.

The successful development of ultrafast dynamic ellipsometry (UDE) as a single shot optical diagnostic of laser driven shock induced optical and material response has provided a unique opportunity to investigate shock induced chemical reactions. The chemical reaction zone length in shock induced reactions has been inferred by features in the velocity wave profiles of shock experiments,² by curvature of the shock front,³ and by laser velocity interferometry.⁴ The time associated with the chemical reaction zone length can provide an estimate of the time in which the reaction occurs. Some reaction kinetics experiments have used spectroscopy to investigate the molecular vibrations

during shock loading, such as infrared absorption,⁵ Raman spectroscopy,⁶ and reflectivity.⁷ Ultrafast dynamic ellipsometry is unique in its intimate coupling of the measurement of material velocities and optical refractive indices. Although it lacks the definitive nature of some of the other types of spectroscopy for probing the existence of chemical bonds, it can nevertheless provide valuable data about the rates at which changes occur.

Two substances that are well known to undergo chemical reactions upon shock-loading were selected for study with UDE: nitromethane and carbon disulfide. Both chemicals were chosen because of their ready availability and because they react at pressures which were accessible with the existing experimental arrangement.

8.2 Nitromethane

8.2.1 Introduction

Nitromethane is the simplest of the organic nitro-based explosives, and as such, it has been used for numerous experimental and theoretical investigations into shock-induced chemical reactions. If the mechanism and kinetics of the reaction in nitromethane are understood, those ideas may then be transferred to the more complex organic explosives. An additional benefit of nitromethane is that it is a liquid at room temperature and pressure, which removes the influences of sample morphology and plastic heating from the already complex equation.

The length (and time) of the chemical reaction zone has been measured with various techniques.^{3,4,8-10} These measurements tend to range from a few tens of microns (~ 6 ns) to a few hundreds of microns (~ 50 ns). The estimates on the length of the

chemical reaction zone are strongly influenced by the experimental method used for the measurement and on the time-resolution of that method. A common theme emerges from these experiments: The time-resolution of each of the techniques leaves some important dynamics unresolved. To produce information about the kinetics of the chemical reactions, the time-resolution of the measurement is critical, and the ps time resolution of UDE has the ability to shed new light on this problem.

Recently, vastly improved computational methods have been developed that can access the evolution of the material with fs time-resolution.¹¹ These rich computational methods provide extensive amounts of data, but to reduce the computational cost, the simulations are performed with few molecules. (Eight and 16 molecules were used in Ref. 11.)

Ultrafast dynamic ellipsometry has the potential to provide interesting information on the kinetics of nitromethane. The temporal resolution of UDE is in precisely the proper space to fill a critical gap in the knowledge about nitromethane. A recent computation by Reed *et al.*¹¹ has indicated the creation of a semi-metallic layer in the nitromethane during the first 200 ps after being shocked. The optical properties accessed by UDE offer the possibility to confirm or refute those findings. Probing through the depth of the material with the ability to separate the optical changes from the material motion allows a vastly greater amount of information to be obtained than by only probing the interface between nitromethane and an inert material. The UDE results will provide either a lower bound on the kinetics of the reactions or an approximate time scale at which significant changes begin to occur.

8.2.2 Experiment

The experimental apparatus for laser shock generation and for the UDE probe was identical to that described in §7.3.1. A liquid cell of the same design contained the nitromethane (Alfa Aesar, 98+%). One side of the cell consisted of a 330 μm thick sapphire window on which was vapor-deposited 1 μm of Al. The other side of the cell was a 0.5 mm thick fused silica window tilted approximately 2° in the direction perpendicular to the incident probe beams to remove the interference from the reflections off of the surfaces of the window. The liquid sample in the cell was approximately 3 mm thick. The data was analyzed in the same manner as in Chapter 7, starting with the unshocked nitromethane refractive index of 1.382.¹²

8.2.3 Results

Approximately 3.5 mJ was used in the chirped laser pulse to create the shock wave in the nitromethane. The two-dimensional images of the phase shift and reflectivity data resulting from a typical shot are shown in Fig. 8-1. In Fig. 8-1, all four sets of phase shift data show a very clear region in the center of the shocked area where the phase shift is less than that on the sides. As the laser pulse that created the shock wave had a Gaussian spatial profile, the phase shift in the center should be the highest (indicating the largest amount of motion of the Al surface), and the phase shift should smoothly decrease toward the edges of the shocked region (indicating smaller amounts of Al surface motion for the regions of lower shock pressures). In contrast, Fig. 8-1 shows the expected behavior on the edges of the shocked region but a sharp decrease in the center, presumably in the area of higher pressure.

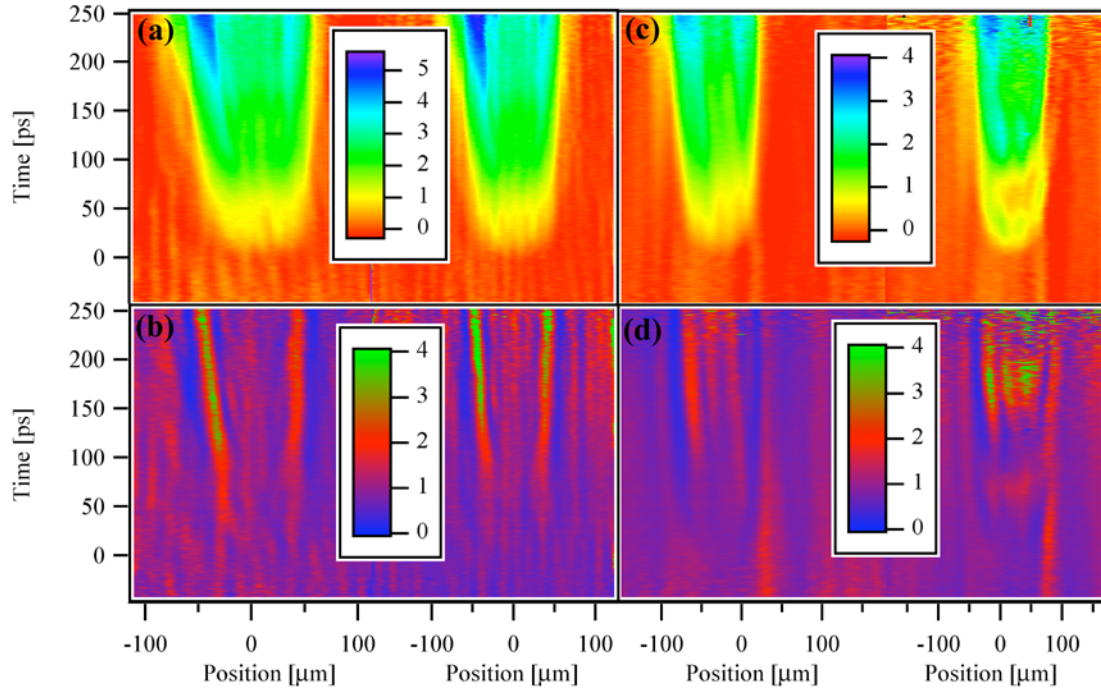


Fig. 8-1. Phase shift and reflectivity data for a shock with a peak pressure of 7.9 ± 0.2 GPa in nitromethane on 1 μm of Al. In each of the four images, the data from the p-polarized probe are on the left and from the s-polarized probe are on the right. (a) Phase shift data at 25.0° . (b) Reflectivity data at 25.0° . (c) Phase shift data at 63.4° . (d) Reflectivity data at 63.4° .

Further inspection of the phase shift data showed a clear change in slope approximately 80-100 ps after the shock front passed from the Al layer into the nitromethane. A set of phase shift and reflectivity data from a single spatial position in the center of the shocked area in Fig. 8-1 is shown in Fig. 8-2. The dotted black lines are the result of the fit to the first 90 ps of data after the shock wave enters the nitromethane. This fit was extended past the first 90 ps to more clearly show the deviation of the data from the expected behavior. The following options were explored in trying to find a model that would reproduce the characteristic shown in the data: 1. Creating an additional layer of material behind the shock front that moved with a separate velocity and had a different refractive index. At the time that this additional layer was created, the

shock and particle velocities of the original shocked layer were also permitted to change to different values. 2. Creating an additional layer of material behind the shock front that moved with a separate velocity and had a different refractive index, while maintaining the same velocity of the shock front. 3. Changing only the velocity of the Al interface at some time after the shock, while maintaining the same shock velocity and the same refractive index of the shocked layer. The first two models described were unsuccessful in that the fitting algorithm was unable to determine a unique set of parameters of best fit. The result of the fitting with the third model is shown in Fig. 8-2 as the solid black line. It is a substantially better fit to the phase shift data, and it seems to properly reproduce the important features. The fits to the reflectivity data are equally poor with all three models, showing that even the more appropriate model is lacking.

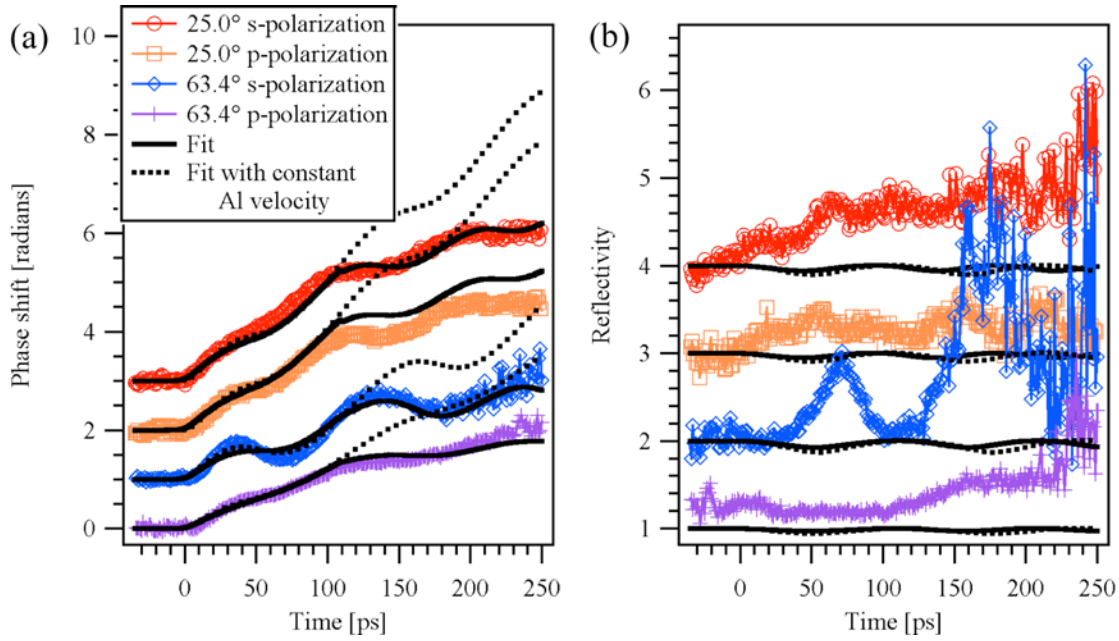


Fig. 8-2. (a) Phase shift and (b) reflectivity data from the two angles and both polarizations for a 7.9 ± 0.2 GPa shock in nitromethane on $1 \mu\text{m}$ Al. The solid black line is the fit to the phase shift data using the model described above, and the dotted black line is the fit to the phase shift data for the first 100 ps after the shock reached the Al/nitromethane interface using the model described in Chapter 7 and extended for later times to show the difference in the data from the behavior expected for constant shock and particle velocities. Data are vertically offset for clarity.

Due to power fluctuations in the 10 Hz laser system, there was one shot of lower pressure in the data set. The two-dimensional phase shift and reflectivity data from that shot are shown in Fig. 8-3. The pressure at the center of this shot was 7.0 ± 0.2 GPa, while the pressure at the center of the shot above in Fig. 8-1 (as calculated from the shock and particle velocities before the change in the velocity of the Al surface) was 7.9 ± 0.2 GPa. In this shot, the total phase shift is lower, indicative of a lower pressure, and the phase shift data are lacking the sudden decrease in phase shift across the center of the shocked area late in time. To additionally illustrate the difference, a set of the phase shift and reflectivity data from the center of the shot in Fig. 8-3 is shown in Fig. 8-4. The data

are accompanied by the fit from the original model (black dotted line). These phase shift data do not show the same late time behavior as in the previous shot.

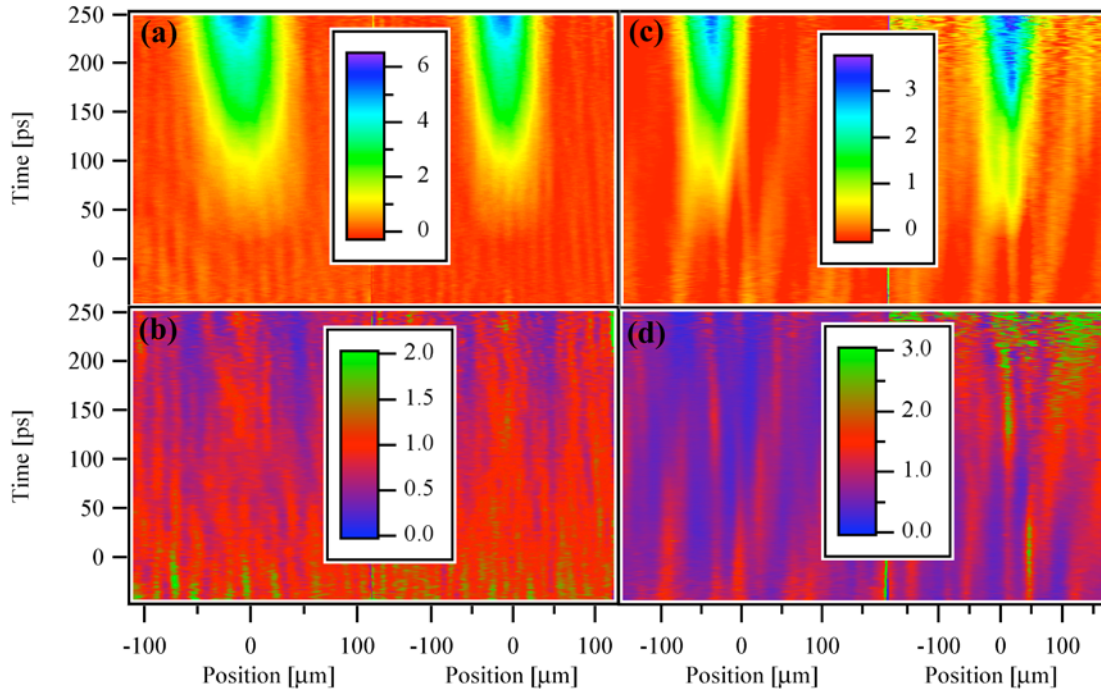


Fig. 8-3. Phase shift and reflectivity data for a shock with a peak pressure of 7.0 ± 0.2 GPa in nitromethane on $1 \mu\text{m}$ of Al. In each of the four images, the data from the p-polarized probe are on the left and from the s-polarized probe are on the right. (a) Phase shift data at 25.0° . (b) Reflectivity data at 25.0° . (c) Phase shift data at 63.4° . (d) Reflectivity data at 63.4° .

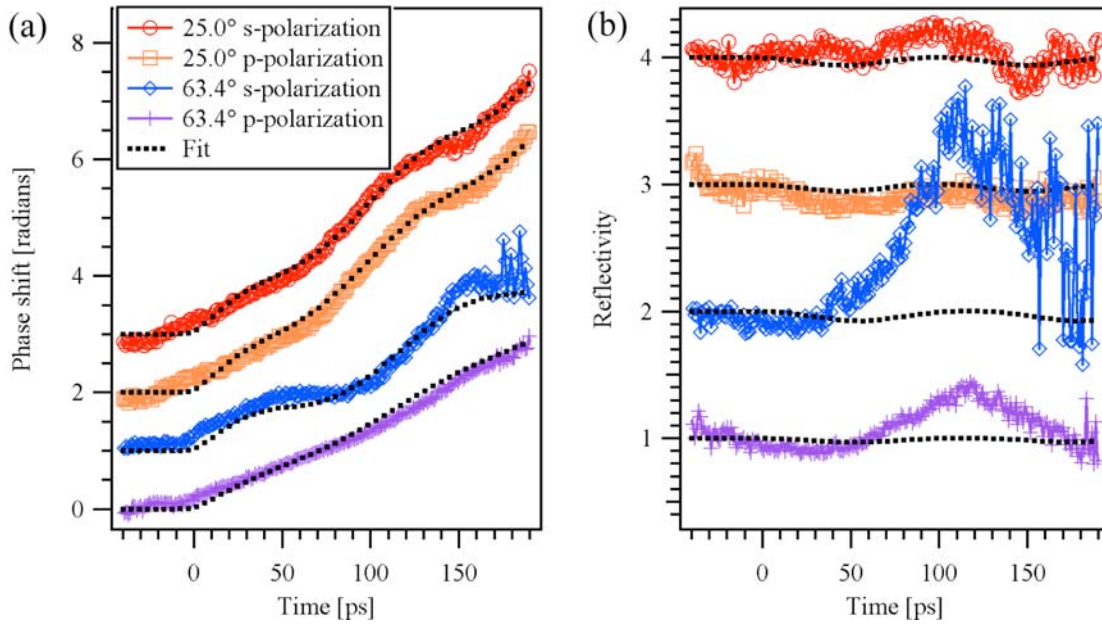


Fig. 8-4. (a) Phase shift and (b) reflectivity data from the two angles and both polarizations for a 7.0 GPa shock in nitromethane on 1 μm Al. The dotted black line is the fit to the phase shift data using the model described in Chapter 7 with constant shock and particle velocities. Data are vertically offset for clarity.

The fits to several different spatial positions across the shock region (and therefore, to several different pressures as explained in Chapter 7) produced the shock and particle velocity data shown in Fig. 8-5. The Hugoniot data are shown to be close to the Hugoniot measured with other techniques, confirming that a shock is being driven into the nitromethane.

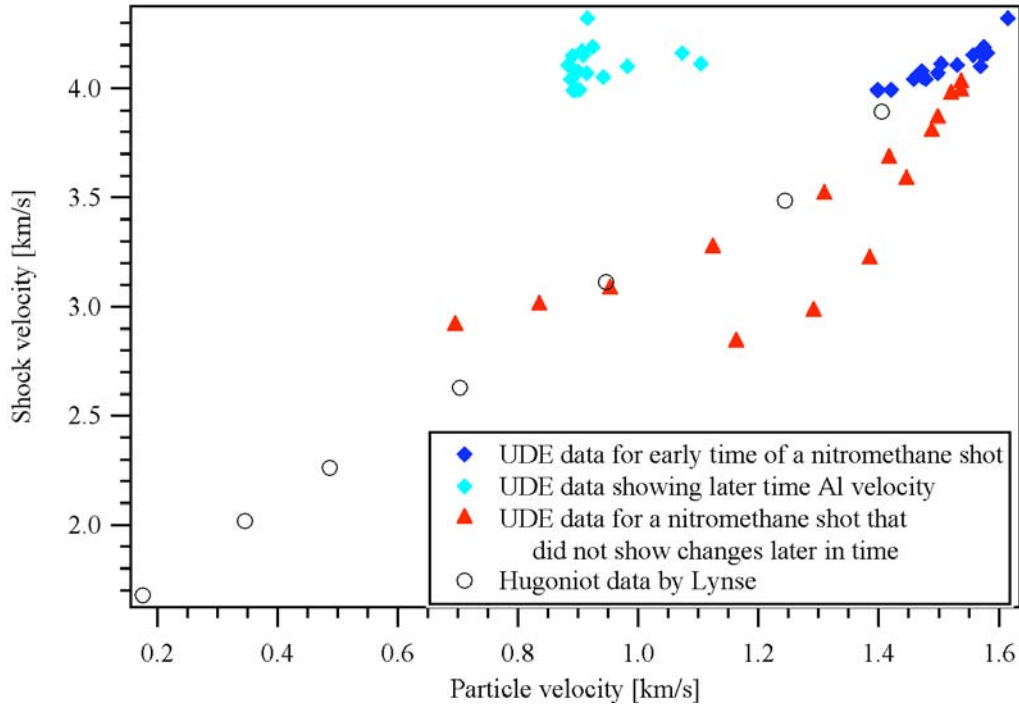


Fig. 8-5. (◆) Hugoniot data for nitromethane fit to the phase shift data for the first 100 ps after the shock reached the Al/nitromethane interface on the shot shown in Fig. 8-1. (◆) Shock velocity versus velocity of the Al interface at later time as explained in the description of the model for the shot shown in Fig. 8-1. (▲) Hugoniot data for the shot shown in Fig. 8-3 fit with constant shock and particle velocities. (○) Hugoniot data by Lynse¹³ for nitromethane at an initial temperature of 50°C.

As in the previous chapters, the shocked refractive index obtained from fitting the ultrafast dynamic ellipsometry data was compared to the value calculated with the Gladstone-Dale¹⁴ formula in Eq. (8.1), which provides a simple density correction for the refractive index.

$$n_{s,GD} = 1 + \frac{(n_0 - 1)}{\left(1 - \frac{u_p}{u_s}\right)} \quad (8.1)$$

where $n_{s,GD}$ is the shocked refractive index according to Gladstone-Dale, n_0 is the initial refractive index of the material at ambient pressure, u_p is the particle velocity, and u_s is

the shock velocity. This comparison is shown in Fig 8-6. The nitromethane data for both shots agree with the Gladstone-Dale model and also with the experimental data by Hardesty.¹⁵ The deviation from Gladstone-Dale by the nitromethane shocked refractive index from the 7.0 GPa shot is almost identical to the deviation of methanol in Chapter 7.

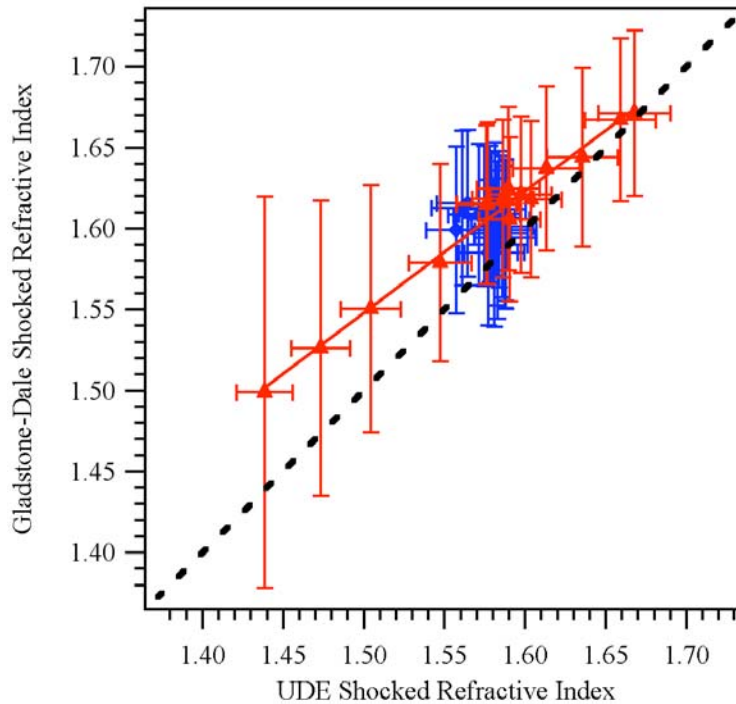


Fig. 8-6. A plot of the shocked refractive index of nitromethane calculated from the Gladstone-Dale relation, $n_{s,GD}$, versus the shocked refractive index, n_s , obtained from the fit to the UDE data. The dashed black line represents Gladstone-Dale behavior. (●) Refractive index from the shot with a maximum pressure of 7.9 ± 0.2 GPa. (▲) Refractive index from the shot with a maximum pressure of 7.0 ± 0.2 GPa. The fit to the refractive index data from the 7.0 GPa shot gives $n_{s,GD} = (0.75 \pm 0.03) n_s + (0.42 \pm 0.04)$.

8.2.4 Discussion

The data shown in Fig. 8-1 are intriguing because they seem to show a sudden decrease in the velocity of the Al surface shortly after the arrival of the shock wave.

What could this data be telling us? One possibility is that the material near the nitromethane/Al interface was becoming less compressible, but one would expect a change in refractive index to accompany this new layer, and a new refractive index was not shown in the analysis of the data. Another possibility is that the material near the interface was expanding, as if a product was being created that was larger than the original volume and began more strongly resisting the movement of the Al surface. This explanation is plausible for the reaction of nitromethane, but again, one would expect a new refractive index at that layer.

The formation of the aci ion shown in Fig. 8-7 is an endothermic reaction commonly theorized to be a critical rate-limiting step in the reaction of nitromethane. The formation of this ion can be facilitated with the addition of a strong base. The base usually chosen for this purpose is the organic base diethylene triamine (DETA). In small amounts, the addition of this base increases the sensitivity of the nitromethane as well as shortens its chemical reaction zone, presumably by facilitating the formation of the aci ion.^{8,10} In contrast, deuterating nitromethane lengthens the chemical reaction zone, presumably by hindering the formation of the aci ion.^{4,16} Some UDE experiments were performed on mixtures of DETA and nitromethane, and the resulting data were qualitatively similar to the data shown in Fig. 8-1 with the same apparent decrease in the velocity of the Al layer 80-100 ps after the shock entered the nitromethane. Repetition of those experiments with the same concentrations of DETA is required before a comparison to the other studies is justified.

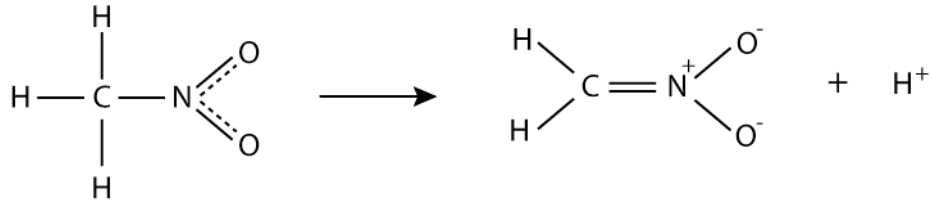


Fig. 8-7. Creation of the aci-ion that is thought to be a critical initial step in the reaction of nitromethane. This reaction is facilitated by the addition of a base, commonly diethylene triamine, which makes the nitromethane easier to initiate.

The shock velocity in the nitromethane does not change when the Al surface velocity apparently decreases, confirming the assumption that any reaction energy being consumed or generated does not have time to feed back into the shock front. This result is consistent with the 3-4 μs time that experiments have shown is required for the detonation to overtake the shock front at approximately 8 GPa.¹⁷

A very interesting facet of this data is the abruptness with which the transition occurs in the spatial dimension between the area where the Al surface moves with a constant velocity and where the Al surface velocity dramatically decreases. In the same way, this effect is completely absent from the shot at 7.0 GPa but prevalent at 7.9 GPa, suggesting a sharp threshold in pressure or in temperature. Also, the time between when the shock wave enters the nitromethane and when the Al surface decreases in velocity does not seem to change as a function of spatial position (and pressure), albeit the pressure differential across that area is small enough that the effect might not be resolvable with these pressure gradients.

Why wasn't this change in interface velocity seen in the many previous experiments on nitromethane? The measurement techniques used in the previous experiments inferred the particle velocity from impedance matching with the projectile

velocity and only measured the shock velocity. The method of using electrical shorting pins to determine velocities would only determine the shock velocity. Streak camera measurements of the shock front are probably lacking the resolution to observe material flow behind the shock front. The most commonly used method of probing shocked materials is VISAR,¹⁸ which often uses a reflective coating on the window of the sample, precluding optical access to the sample itself. There was one set of measurements performed by Hardesty¹⁵ in which the reflective coating for the VISAR was placed on the rear surface of the nitromethane sample so that the VISAR probed through the nitromethane, however, his data showed no evidence of this effect. With all of the techniques except the last by Hardesty, only the shock velocity in the material was measured, and the particle velocity was inferred. The UDE method is unique in its ability to probe both the shock and particle velocities in the material.

8.3 Carbon disulfide

8.3.1 Introduction

The first high pressure experiments that showed the reaction of carbon disulfide were static pressure experiments performed by Bridgman in 1942, during which a black solid slowly formed from compressed and heated carbon disulfide.¹⁹ This solid became known as “Bridgman Black.” A subsequent study by Butcher *et al.* in 1963 mapped out the solid, liquid, and gas phase boundaries of carbon disulfide in temperature-pressure space, as well as the regions in which it reacts and in which the solid Bridgman Black is formed.²⁰ These regions are shown in Fig. 8-8. As shown in Fig. 8-8, Bridgman Black is

only formed in a small region of temperature-pressure space designated in Fig. 8-8 as “black solid.”

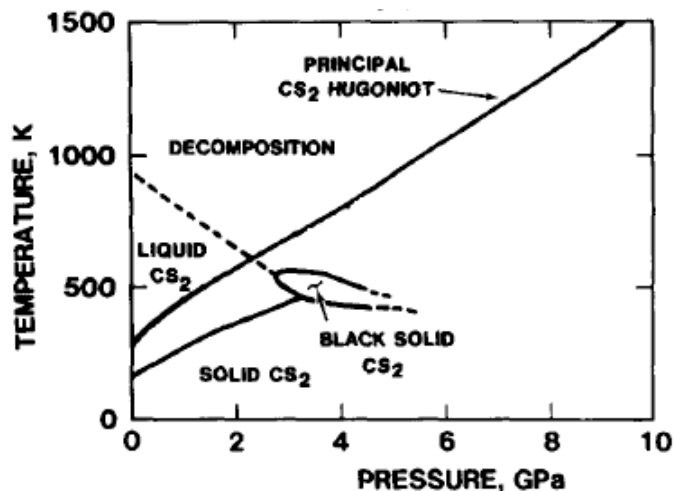


Fig. 8-8. Temperature-pressure phase diagram of carbon disulfide, showing the solid and liquid phases along with the regions in which carbon disulfide reacts in static hydrodynamic experiments. The region labeled black solid CS_2 is also referred to as Bridgman Black. Also shown is the location of the principal Hugoniot relative to the regions of reaction. Reproduced from ref. [2].

In 1960, Whalley elucidated the structure of Bridgman Black by infrared absorption spectroscopy to be a linear polymer with the repeating monomer unit shown in Fig. 8-9.²¹

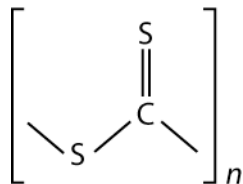


Fig. 8-9. Monomeric unit of the linear polymer that is Bridgman Black, elucidated by Whalley.²¹

Carbon disulfide was first studied under shock loading by Walsh and Rice,²² however, they were restricted to only two accessible pressures, which limited the utility of their data in determining the presence of a chemical reaction under shock loading. A thorough study of the shock loading of carbon disulfide was undertaken by Dick in 1970.²³ Dick's Hugoniot data show a clear discontinuity, which was postulated to be from the onset of chemical reaction, and he speculated that the transformation was from the liquid state to Bridgman Black. Despite one private communication from A. S. Kusubov to Dick reporting the recovery of a black, fluffy solid, it appears that Bridgman Black is not formed under single shock loading of carbon disulfide along the principle Hugoniot. There are no other reports of the creation of Bridgman Black by shock, which is explained by the regions of temperature-pressure space accessible under single shock loading. The temperature-pressure phase diagram showing the location of the principle shock Hugoniot is reproduced from Sheffield² in Fig 8-8. Clearly, the principle Hugoniot does not access the area in which Bridgman Black is formed. Although Bridgman Black is not formed under shock loading, its polymeric structure indicates the type of reaction that occurs in carbon disulfide under pressure.

A number of studies have investigated the complex kinetics of the reactions,²⁴ the products formed,^{21,25} and the effects of shock loading.^{2,7,23,26-28} Under shock compression, the onset of reaction occurs at 5.1 ± 0.05 GPa,²⁹ at which point the compressibility increases, and there is a volume reduction of approximately 26%.²⁸ Recently, a study by Engelke *et al.*²⁸ was published, presenting time-of-flight mass spectrometry results of the product species from shock-loaded carbon disulfide. Thirteen higher molecular weight species were detected when the carbon disulfide was subjected

to a shock produced by the high explosive HMX. The kinetics of the reactions of CS₂ under shock loading have been inferred from shock wave profiles² and from time-resolved spectroscopic reflectance measurements,⁷ with the time resolutions in these studies on the order of tens of nanoseconds.

8.3.2 Experiment

Carbon disulfide (Aldrich) was placed in a liquid cell similar to that used in the nitromethane experiment discussed previously. One side of the cell consisted of a 330 μm thick sapphire window on which was vapor-deposited 1 μm of Al. The other side of the cell was a 0.5 mm thick fused silica window tilted approximately 2° in the direction perpendicular to the incident probe beams to remove the interference from the reflections off of the surfaces of the window. The liquid sample in the cell was approximately 3 mm thick.

The data were analyzed in the same manner as in Chapter 7, with the pristine carbon disulfide refractive index of 1.606 at the wavelength of 800 nm.³⁰ Phase shift and reflectivity data from one of the shots are shown in Fig. 8-10 along with the fit to the data. Particularly notable is the strength of the oscillations, which arises from the large change in refractive index as discussed below.

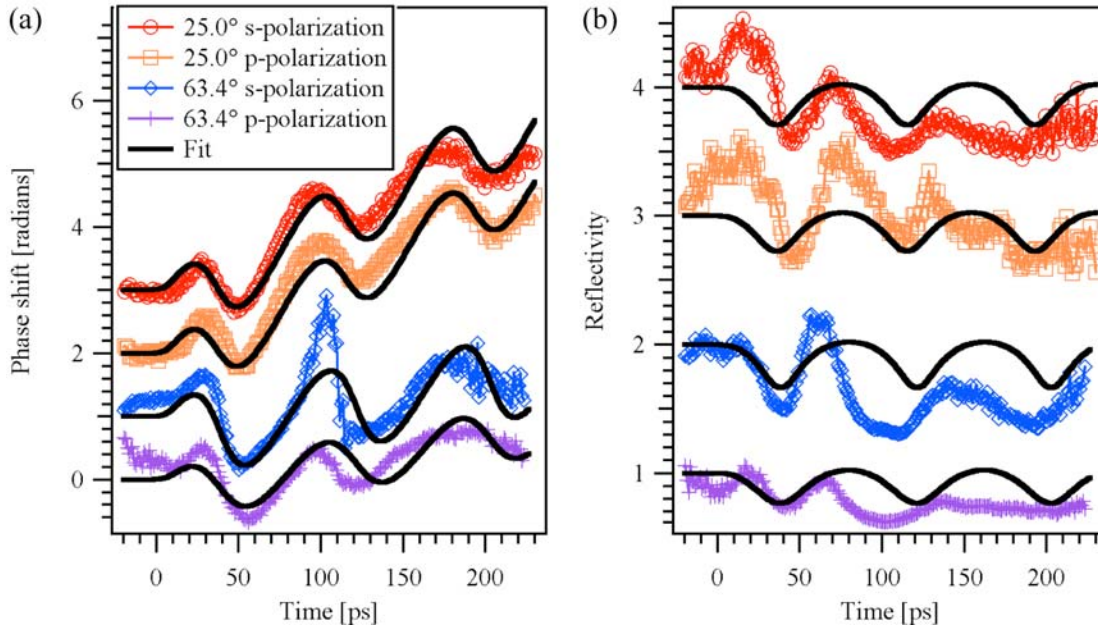


Fig. 8-10. (a) Phase shift and (b) reflectivity data from the two angles and two orthogonal polarizations during a 9.2 ± 0.2 GPa shock in liquid carbon disulfide on $1 \mu\text{m}$ thick Al along with the fit to the data. Data are vertically offset for clarity.

8.3.3 Results

Due to difficulties with the specific sample cell constructed for these experiments, data from only two shots were successfully collected. Nevertheless, the spatially resolved method of data collection explained in Chapter 7 allowed analysis of the data for multiple shock pressures. The Hugoniot data from the two shots are shown in Fig. 8-11 with the Hugoniot data from the LASL Shock Hugoniot Data.³¹ The low pressure shot in blue matches well with the unreacted Hugoniot data, and the high pressure shot in red follows the curve in the Hugoniot above the reaction onset pressure. The data from the high pressure shot appears to deviate toward the unreacted Hugoniot at pressures only slightly above the reaction pressure threshold, which may indicate a pressure dependent reaction rate.

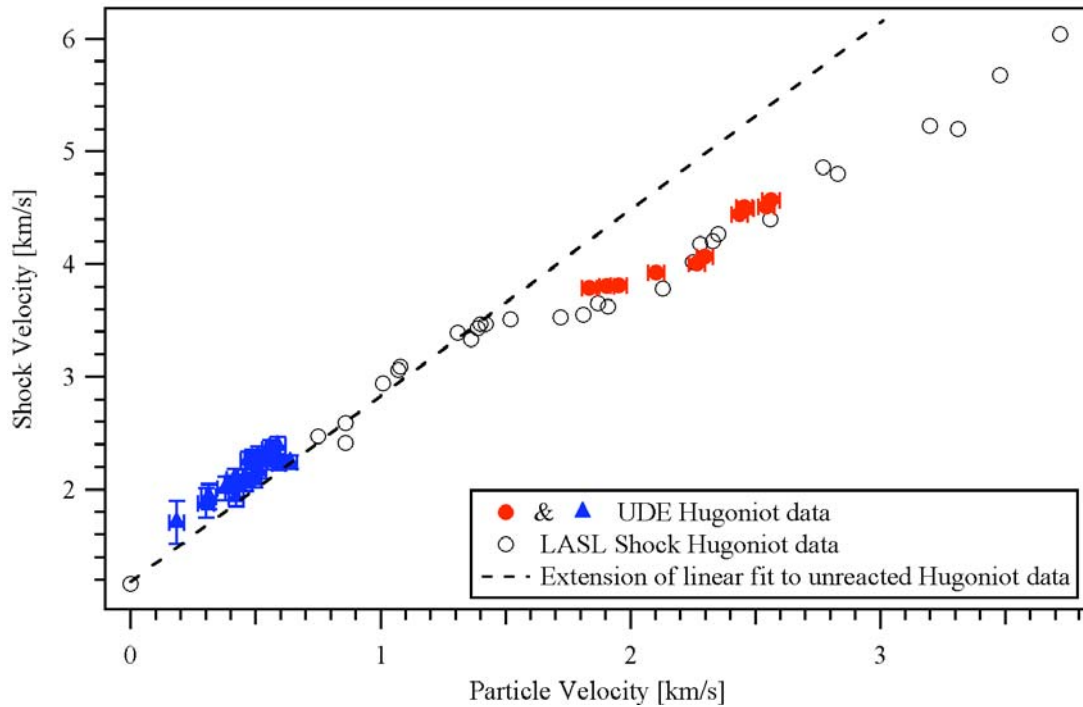


Fig. 8-11. Hugoniot data for carbon disulfide from two single laser shots along with data from the LASL Shock Hugoniot Data.³¹ The data from each shot are shown in a different color. The dashed line is a linear fit to the LASL Shock Hugoniot data at pressures below the onset of reaction, and it is extended above the reaction threshold pressure in the plot to more clearly show the high pressure deviation from the unreacted Hugoniot.

The refractive index data were analyzed in the same manner as previously, and these data are shown in Fig. 8-12. For the data collected at pressures below the onset of reaction, the shocked refractive index of carbon disulfide conforms to the Gladstone-Dale model. However, at pressures above the onset of reaction, the shocked refractive index obtained from the fit is remarkably higher than that expected from the change in the density of the material. This large change between the unshocked and shocked refractive indices in the higher pressure shot caused the large amplitude of the oscillations in the phase shift and reflectivity data shown in Fig. 8-10 as more of the probe light was reflected at the Fresnel surface created by the shock front. Presumably, the deviation

from the Gladstone-Dale prediction for the shocked refractive index results from the formation of the higher molecular weight products.

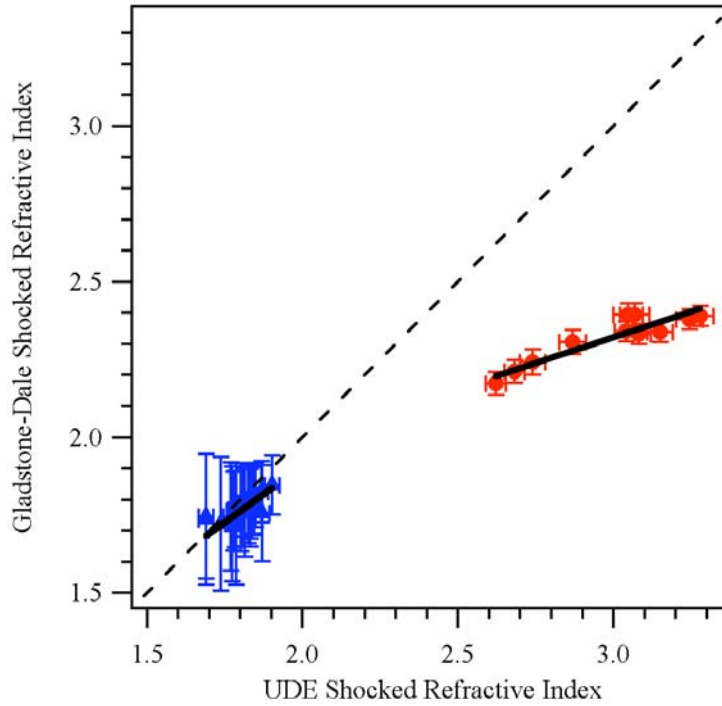


Fig. 8-12. A plot of the shocked refractive index of carbon disulfide calculated from the Gladstone-Dale relation, $n_{s,GD}$, versus the shocked refractive index, n_s . The dashed black line represents Gladstone-Dale behavior. (▲) Refractive index of the lower pressure shot below the reaction threshold. The linear fit to the data gives $n_{s,GD}=(0.73 \pm 0.07) n_s + (0.45 \pm 0.13)$. (●) Refractive index of the high pressure shot above the reaction threshold. The linear fit to the data gives $n_{s,GD}=(0.33 \pm 0.04) n_s + (1.33 \pm 0.12)$.

8.3.4 Discussion

The most significant result from this carbon disulfide experiment is that the Hugoniot measured with UDE during the first 250 ps after the shock entered the carbon disulfide sample shows a similar change from chemical reaction to the Hugoniot

measured with gas guns and explosively driven shock loading. This result implies that the carbon disulfide is reacting on a picosecond or tens of picoseconds time scale.

The recently published data by Engelke *et al.*²⁸ suggest that the time scale for the carbon disulfide reaction is much longer than is seen in this UDE study. Engelke reports the time-of-flight mass spectrometry of carbon disulfide products that were shocked with two different explosives. When shocking the carbon disulfide with hexanitrostilbene (HNS), the mass spectra collected show the same species as when carbon disulfide is evaporated. However, when using a plastic bonded cyclotetramethylene tetranitramine (HMX) explosive to create the shock, they find 13 species more massive than carbon disulfide. They attribute this difference to the different pressures and lengths of time for which the sample was pressurized. With HNS, they calculated that the liquid was shocked above 7.5 GPa for approximately 0.28 μs , and with HMX, the liquid was shocked above 11.0 GPa for approximately 0.25 μs . In contrast, the UDE data show characteristics of reaction for shock pressures that range from 8.8 to 14.8 GPa, and these characteristics are present in the first 250 ps in which the liquid is shocked. The disparity between the mass spectrometry data by Engelke and the UDE data here may be explained by the relatively large quantities of the reaction products necessary for a recordable mass spectrometry measurement. Additionally, one could postulate that reaction intermediates are responsible for the deviation from the unreacted Hugoniot and that those intermediates are formed in the UDE experiments but that formation of stable reaction products requires a longer time at high pressure and temperature. This explanation is reasonable in light of the many and various associative reaction products that have been found from both static and shock loading.^{21,25,28}

To the author's knowledge, the refractive index of carbon disulfide has not been investigated before at 800 nm under shock loading. Gustavsen and Gupta⁷ made time-resolved spectroscopic reflection measurements of carbon disulfide under shock loading and used the data to model the complex refractive index. However, this study used light from 300 to 500 nm, an area of the spectrum where carbon disulfide exhibits absorption bands. Yoo *et al.*³² have also studied CS₂ under shock loading in the wavelength range of 250-700 nm, where carbon disulfide becomes opaque above 9.0 GPa. The much higher values of the shocked refractive index data than those predicted from the Gladstone-Dale relation might be explained by the shift in the absorption bands to higher wavelengths as seen by Gustavsen.⁷ Clearly, some spectroscopy, like infrared absorption or Raman scattering, would do much to explain this behavior in the shocked refractive index.

8.4 Conclusions

The UDE experiments on nitromethane and on carbon disulfide provide valuable and significant new data about the timescales of chemical reactions under shock loading. The nitromethane UDE data show a dramatic decrease in the velocity of the Al surface in contact with the nitromethane approximately 80-100 ps after the arrival of the shock wave, but there is not a change in the velocity of the shock front or in the refractive index, which remains consistent with the Gladstone-Dale model. In carbon disulfide, the Hugoniot measured with UDE tracks closely with the previously measured bulk material Hugoniot, even above the reaction threshold pressure. However, the Hugoniot data above the reaction threshold pressure deviate toward the unreacted Hugoniot, imply that there are time-dependent processes occurring. Further above the reaction threshold

pressure the Hugoniot data are much more aligned with the previously measured data. In the fits to the carbon disulfide UDE data, the fit appears to better match the data earlier in time and slowly begins to stray later on. In the future, these data will be analyzed with a time-dependent model that allows changes in the velocities and the shocked refractive index as a function of time. The refractive index below the reaction threshold pressure is consistent with the Gladstone-Dale model based on the change in density, however the refractive index above the reaction threshold pressure is significantly higher than expected from Gladstone-Dale. The existence of absorption bands at slightly lower wavelengths that move to higher wavelengths when CS₂ is shocked offers an opportunity to probe the refractive index at lower wavelengths, thereby acquiring information about the chemical bonds that are changing on this fast time scale.

References

- 1 I. Society of Explosives Engineers, "The Many Uses of Explosives," Retrieved 26
July 2008 <<http://www.explosives.org/Uses.htm>>.
- 2 S. A. Sheffield, "Response of liquid carbon disulfide to shock compression. II.
Experimental design and measured Hugoniot information," *J. Chem. Phys.* **81**,
3048-63 (1984).
- 3 R. Engelke and J. B. Bdzil, "A study of the steady-state reaction-zone structure of
a homogeneous and a heterogeneous explosive," *Phys. Fluids* **26**, 1210-21 (1983).
- 4 S. A. Sheffield, R. Engelke, R. R. Alcon, R. Gustavsen, D. L. Robbins, D. B.
Stahl, H. L. Stacy, and M. C. Whitehead, "Particle velocity measurements of the
reaction zone in nitromethane," *Research Report LA-UR-02-4331* (Los Alamos
National Laboratory, 2002).
- 5 S. D. McGrane, D. S. Moore, and D. J. Funk, "Shock induced reaction observed
via ultrafast infrared absorption in poly(vinyl nitrate) films," *J. Phys. Chem. A*
108, 9342-9347 (2004).
- 6 G. I. Pangilinan and Y. M. Gupta, "Time-resolved Raman measurements in
nitromethane shocked to 140 kbar," *J. Phys. Chem.* **98**, 4522-4529 (1994).
- 7 R. Gustavsen and Y. M. Gupta, "Electronic and chemical changes in shocked
liquid carbon disulfide inferred from time resolved reflection experiments and
analysis," *J. Chem. Phys.* **95**, 451-66 (1991).
- 8 R. Engelke, S. A. Sheffield, and H. L. Stacy, "Chemical-reaction-zone lengths in
condensed-phase explosives," *Phys. Fluids* **16**, 4143-4149 (2004).
- 9 D. R. Hardesty, "Investigation of the shock initiation of liquid nitromethane,"
Combust. Flame **27**, 229-251 (1976).
- 10 R. Engelke, S. A. Sheffield, H. L. Stacy, and J. P. Quintana, "Reduction of
detonating liquid nitromethanes chemical reaction-zone length by chemical
sensitization," *Phys. Fluids* **17**, 96102-1 (2005).
- 11 E. J. Reed, M. R. Manaa, L. E. Fried, K. R. Glaesemann, and J. D. Joannopoulos,
"A transient semimetallic layer in detonating nitromethane," *Nature physics* **4**, 72-
76 (2008).
- 12 E. E. Toops, "Physical properties of eight high-purity nitroparaffins," *J. Phys.*
Chem. **60**, 304-306 (1956).
- 13 P. C. Lysne and D. R. Hardesty, "Fundamental equation of state of liquid
nitromethane to 100 kbar," *J. Chem. Phys.* **59**, 6512-23 (1973).
- 14 J. H. Gladstone and T. P. Dale, "Researches on the refraction, dispersion, and
sensitiveness of liquids," *Philos. Trans. R. Soc. London* **153**, 317-343 (1863).
- 15 D. R. Hardesty, "On the index of refraction of shock-compressed liquid
nitromethane," *J. Appl. Phys.* **47**, 1994-8 (1976).
- 16 R. Engelke, S. A. Sheffield, and H. L. Stacy, "Effect of deuteration on the
diameter-effect curve of liquid nitromethane," *J. Phys. Chem. A* **110**, 7744-7748
(2006).
- 17 B. Leal-Crouzet, G. Baudin, and H. N. Presles, "Shock initiation of detonation in
nitromethane," *Combust. Flame* **122**, 463-473 (2000).
- 18 L. M. Barker and R. E. Hollenbach, "Laser interferometer for measuring high
velocities of any reflecting surface," *J. Appl. Phys.* **43**, 4669-75 (1972).

- 19 P. W. Bridgman, "Freezing parameters and compressions of twenty-one
substances to 50,000 kg/cm²," Proc. Am. Acad. Arts Sci. **74**, 399-424 (1942).
- 20 E. G. Butcher, J. A. Weston, M. Alsop, and H. A. Gebbie, "Formation and
properties of black form of carbon disulfide," Nature **199**, 756 (1963).
- 21 E. Whalley, "Structure of Bridgman Black carbon disulfide," Can. J. Chem. **38**,
2105-2108 (1960).
- 22 J. M. Walsh and M. H. Rice, "Dynamic compression of liquids from
measurements on strong shock waves," J. Chem. Phys. **26**, 815-823 (1957).
- 23 R. D. Dick, "Shock wave compression of benzene, carbon disulfide, carbon
tetrachloride, and liquid nitrogen," J. Chem. Phys. **52**, 6021-32 (1970).
- 24 S. J. Arnold, W. G. Brownlee, and G. H. Kimbell, "Reactions of shock-heated
carbon disulfide-argon mixtures. 2. Kinetics of dissociation of carbon disulfide,"
J. Phys. Chem. **74**, 8 (1970).
- 25 S. F. Agnew, R. E. Mischke, and B. I. Swanson, "Pressure-induced and
temperature-induced chemistry of carbon disulfide," J. Phys. Chem. **92**, 4201-
4204 (1988).
- 26 M. A. Cook and L. A. Rogers, "Compressibility of solids and liquids at high
pressures," J. Appl. Phys. **34**, 2330-2336 (1963).
- 27 S. A. Sheffield and G. E. Duvall, "Response of liquid carbon disulfide to shock
compression: equation of state at normal and high densities," J. Chem. Phys. **79**,
1981-90 (1983).
- 28 R. Engelke, N. C. Blais, and S. A. Sheffield, "Mass spectroscopic observation of
shock-induced chemistry in liquid CS₂," J. Phys. Chem. A **112**, 58-65 (2008).
- 29 S. A. Sheffield, "Onset of shock-induced reaction in liquid CS₂" in *Shock Waves
in Condensed Matter*, edited by S. C. Schmidt and N. C. Holmes (Elsevier
Science Publishers, Monterey, CA, 1988), p. 463-466.
- 30 A. Samoc, "Dispersion of refractive properties of solvents: Chloroform, toluene,
benzene, and carbon disulfide in ultraviolet, visible, and near-infrared," J. Appl.
Phys. **94**, 6167-74 (2003).
- 31 S. P. Marsh, *LASL Shock Hugoniot Data* (University of California Press,
Berkeley, 1980).
- 32 C. S. Yoo, G. E. Duvall, J. Furrer, and R. Granholm, "Effects of pressure and
dilution on the visible and ultraviolet-spectrum of liquid carbon-disulfide under
shock compression," J. Phys. Chem. **93**, 3012-3021 (1989).

Chapter 9

Laser Ablation of Titanium

This chapter describes research into the type of insult provided by laser ablation in the direct optical initiation (DOI) detonator to initiate reaction in the explosive.

9.1 Introduction

Historically, high-performance detonators have been based on the concept of exploding bridge wire (EBW) initiation. Here, a large voltage with an accompanying current supply is switched across a thin resistive wire. The resulting current flow deposits energy into the wire, forming a hot, exploding plasma, which initiates a low-density pellet of explosive, often pentaerythritol tetranitrate (PETN). Exploding foil initiating detonators (EFI), typically called “slappers,” operate with a different mechanism, in which a large voltage is used to fragment and propel pieces of a polymer into the primary explosive. These traditional explosive detonators have relied on a short high voltage, high current pulse for initiation. Although these detonators are highly reliable, the use of electricity to initiate reaction has raised questions about their safety if they are subject to an unintended electrical pulse, such as lightning or electrostatic discharge. In an effort to improve the safety of explosive detonators, direct optical initiation (DOI) detonators have been developed. Instead of using an electrical pulse for

initiation, DOI detonators use a fiber-optically coupled laser pulse, leaving the detonator electrically isolated from the fireset. In the optically driven detonator of interest to us, a thin layer of titanium (~250 nm) is vapor deposited on a fused quartz substrate, with the PETN pellet pressed onto the Ti coated surface. A laser pulse (usually the output of a Nd:YAG operating at 1064 nm) ablates the titanium, which initiates the explosive.

Diagnostics used to probe ablation dynamics include surface velocity techniques such as the velocity interferometer system for any reflector (VISAR),¹ photonic Doppler velocimetry (PDV),² optically recording velocity interferometer system (ORVIS),³ and Fabry-Perot,⁴ as well as photographic techniques, such as schlieren,⁵ shadowgraphy,^{6,7} and spatial interferometry.⁷ These diagnostics have been applied to image and to obtain both qualitative and quantitative data regarding ablation plume dynamics.

Previous studies of this process using the velocity interferometer system for any reflector (VISAR) and photon Doppler velocimetry (PDV) have gathered data suggesting that the laser ablation does not exclusively yield a hot plasma, but rather, the ablation process yields a fragment field with a range of velocity distributions.^{8,9} The schlieren and ultrafast dynamic ellipsometry methods were used here to provide additional data that help elucidate these mechanistic details.

9.2 Schlieren experiments

9.2.1 Introduction

The schlieren technique uses the refraction in transparent optically inhomogeneous media to image the inhomogeneities.¹⁰ When collimated light travels through an optically inhomogeneous medium, the light rays are bent in proportion to the

gradients in their refractive indices. For schlieren imaging, the light rays are focused after passing through the material of interest, and a knife edge is inserted into the focus. If the entire area of interest had the same refractive index, the knife edge at the focus would remove an equal intensity of light from all areas of the image. However, regions that have changes in refractive index will deviate the path of the light and cause imperfect focusing. Instead of removing equal intensity, the knife edge will remove more or less of the deviated light causing areas of light or dark on the image. In this way, schlieren images the changes in the refractive index of transparent materials in the direction of the knife edge. For materials with refractive indices that vary with density, schlieren images the first derivative of the density.

Due to the large amount of compression present in strong shock waves, schlieren is a useful technique for studying the propagation of shock waves. In this study of DOI detonators, schlieren was used to image the ablation of the Ti thin film that initiates the explosive and to image the shock waves propagating in air and other visualization materials resulting from initiation of the full detonator.

9.2.2 Experiment

The laser system used to initiate the DOI detonator and for these schlieren studies was a Q-switched Nd:YAG laser manufactured by Big Sky Lasers. The laser produced pulses with a wavelength of 1064 nm and a full width at half maximum pulse duration of approximately 10 ns. The laser pulse was focused into a 400 μm diameter fiber with the output end of the fiber placed against the fused quartz substrate. The ablated spot size was approximately 600 μm in diameter.

Previous studies during development of the DOI detonator found that ~50% of the detonators functioned with the laser energy of 12 mJ. Therefore, the energy chosen for reliable initiation of the detonators was 25 mJ, approximately twice the 50% level. All of the data shown below were taken using 25 mJ of ablative energy.

To perform schlieren measurements of explosive detonators, several unique design characteristics were incorporated into the schlieren apparatus. As every detonator shot is not exactly identical to every other, a fast framing camera was used to record a series of images for each shot. Using a single shot gives more accuracy to the results than assembling a composite of data from several different explosive events. A continuous wave laser was used as a backlight for the schlieren measurements, which provided two important benefits. First, the high intensity of the laser light allowed short exposure times of the camera, as short as 5 ns. These short exposures were required to “freeze” the motion due to the high velocity of the materials investigated. Additionally, the monochromaticity of the laser light permitted a narrow bandpass filter to be inserted before the camera, blocking the broadband emission of the ablation and of the explosive reaction from reaching the camera. The final characteristic was the use of a containment vessel in which the test objects were enclosed. The containment vessel was rated for 5 g of trinitrotoluene (TNT) equivalent.

The experimental schlieren apparatus is depicted in Fig. 9-1. An in-line lens-based schlieren configuration was used. A 5W Coherent Verdi laser at 532 nm was used as the backlight. The laser light was focused with a 10x microscope objective and spatially filtered with a 50 μm diameter pinhole. The expanding light was collimated with a 2” diameter lens before entering the containment vessel. Each light port of the

containment vessel had a 1" thick glass window inside of which was a 0.5" thick plexiglass shield. The test object (the Ti coated plate and later the detonator) was placed in the containment vessel. After exiting the containment vessel the laser light was sent through a 532 ± 0.25 nm laser-line bandpass filter before it was focused with another 2" diameter lens. The edge of a straight razor blade was inserted at the focus, using a 3-dimensional x, y, z stage to precisely place the edge for optimal contrast in the schlieren images. A Nikon lens was placed before the camera and the focal lengths and positions of the lenses were varied to image the plane of the test object to the desired magnification for each shot. The fast framing camera was an Imacon 200, which contained seven dual-image 10-bit charge-coupled-devices (CCDs), allowing collection of 14 images during each test. The exposure time could be varied from 5 ns to 2 ms, and the interframe time could be varied from 5 ns to 1 ms.

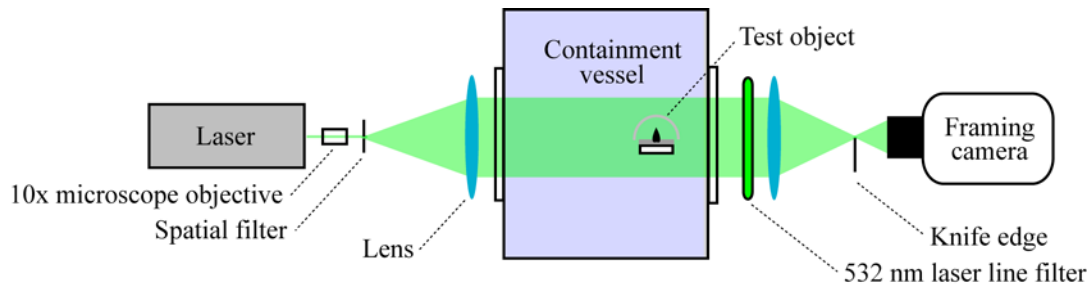


Fig. 9-1. Experimental schematic for schlieren measurements on ablated Ti thin films and DOI detonators.

There were two samples investigated in these experiments. The first was a 1 mm thick fused quartz plate vapor-plated with 250 nm of Ti. The end of the fiber into which the laser was coupled was placed against the non-coated side of the fused quartz, so that the light passed through the quartz before encountering the Ti. The second sample

consisted of the same Ti-coated quartz on top of which the remaining detonator components were assembled. This detonator was designated ER462. An engineering schematic of the detonator is shown in Fig. 9-2, and a photograph of the detonator is Fig. 9-3.

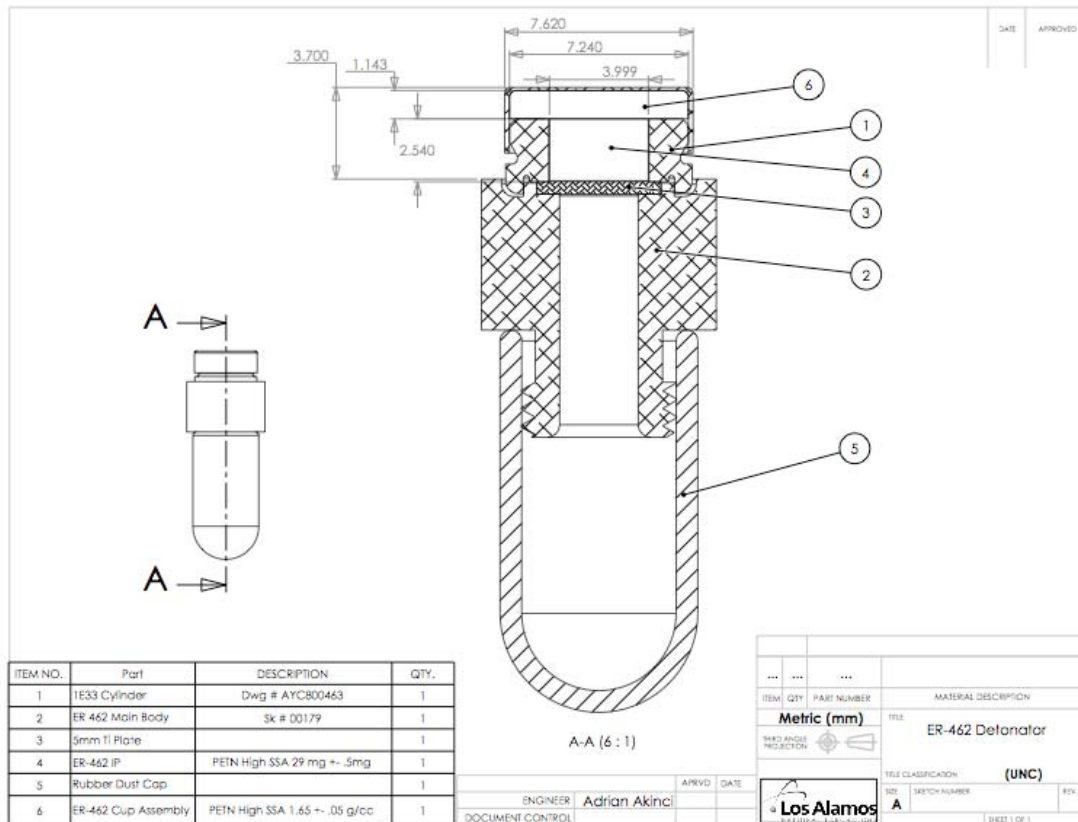


Fig. 9-2. Engineering schematic of the ER462 optically initiated detonator. The optical initiation pulse is delivered by fiber optic cable to the bottom of the device and is incident on the fused quartz substrate that has been vapor-plated with 250 nm of Ti (3). The PETN explosive charge is pressed on top of the Ti at a low density (4) and then in a high density pellet (6). Courtesy of A. Akinci.

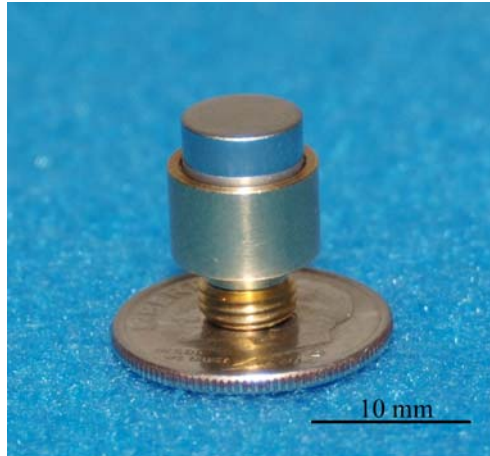


Fig. 9-3. Photograph of the ER462 experimental detonator on a U. S. dime for scale. The fiber optic cable that delivers the optical initiation pulse is screwed onto the threads on the bottom of the device. The explosive charge is inside the metal cup on the top of the detonator. Courtesy of A. Akinci.

9.2.3 Schlieren results

The first series of shots were performed on the Ti-coated fused quartz. The purpose of these shots was to test the newly assembled schlieren apparatus and to determine the nature of the insult provided by the Ti ablation and the speed at which the Ti impacts the energetic constituent of the detonator.

Shown in Fig. 9-4 are the images recorded during a test of the Ti-coating. In this test, the narrow bandpass filter was not used to screen the broadband emission from the camera. The broadband emission from the Ti ablation obscures the initial movement of the Ti and of the expanding shock wave.

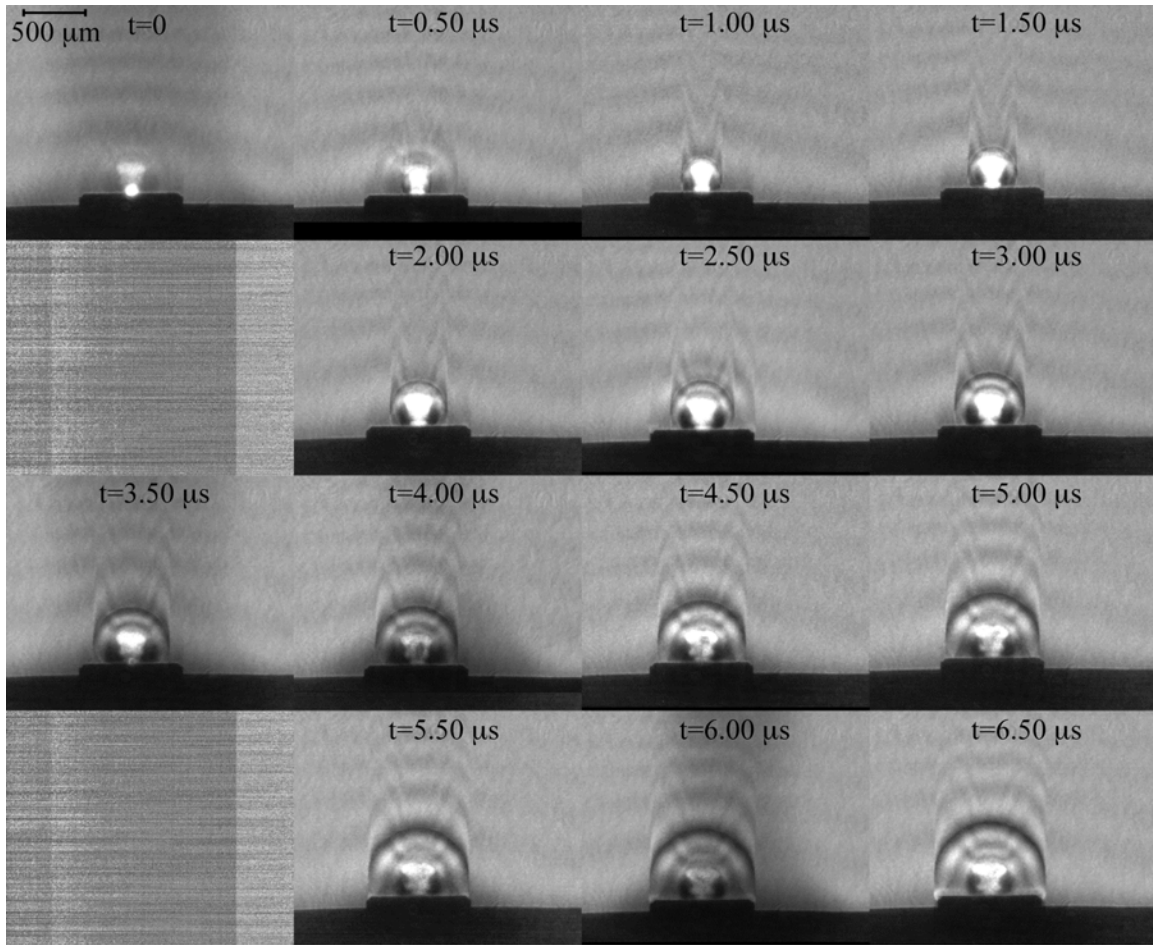


Fig. 9-4. Series of schlieren images recorded from ablation of a 250 nm Ti film. These images were recorded without using a narrow bandpass filter to block the broadband emission. The exposure time was 20 ns, and the interframe time was 500 ns.

The schlieren images were significantly improved with the use of the narrow bandpass filter, as shown in Fig. 9-5, providing clear images of the ablation plume and the expanding shock wave.

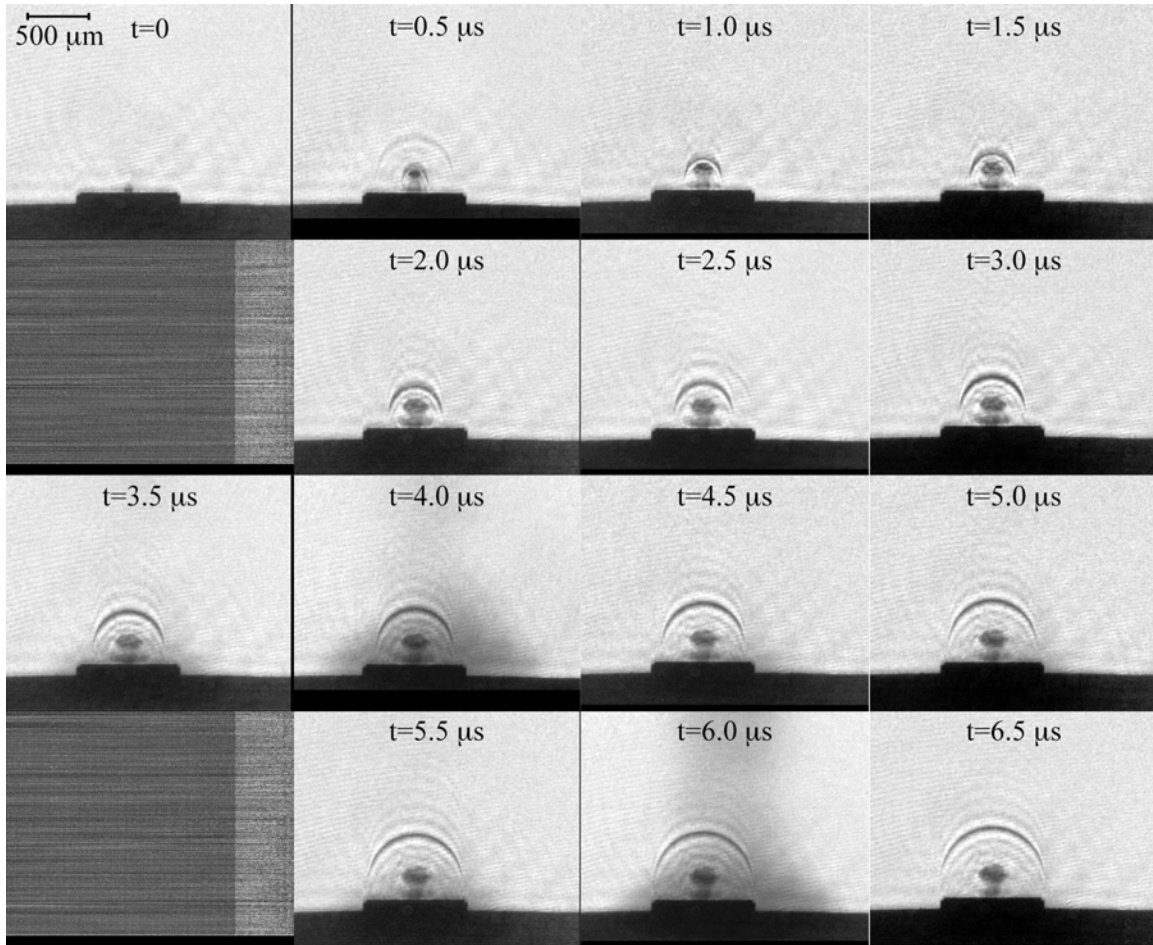


Fig. 9-5. Series of schlieren images recorded from ablation of a 250 nm Ti film, using a narrow bandpass filter to block the broadband emission. The exposure time was 20 ns, and the interframe time was 500 ns.

Schlieren experiments were then performed with the experimental detonator ER 462 using direct optical initiation. Figure 9-6 shows the results of the first schlieren test of the ER462 with its shock wave expanding into the surrounding air.

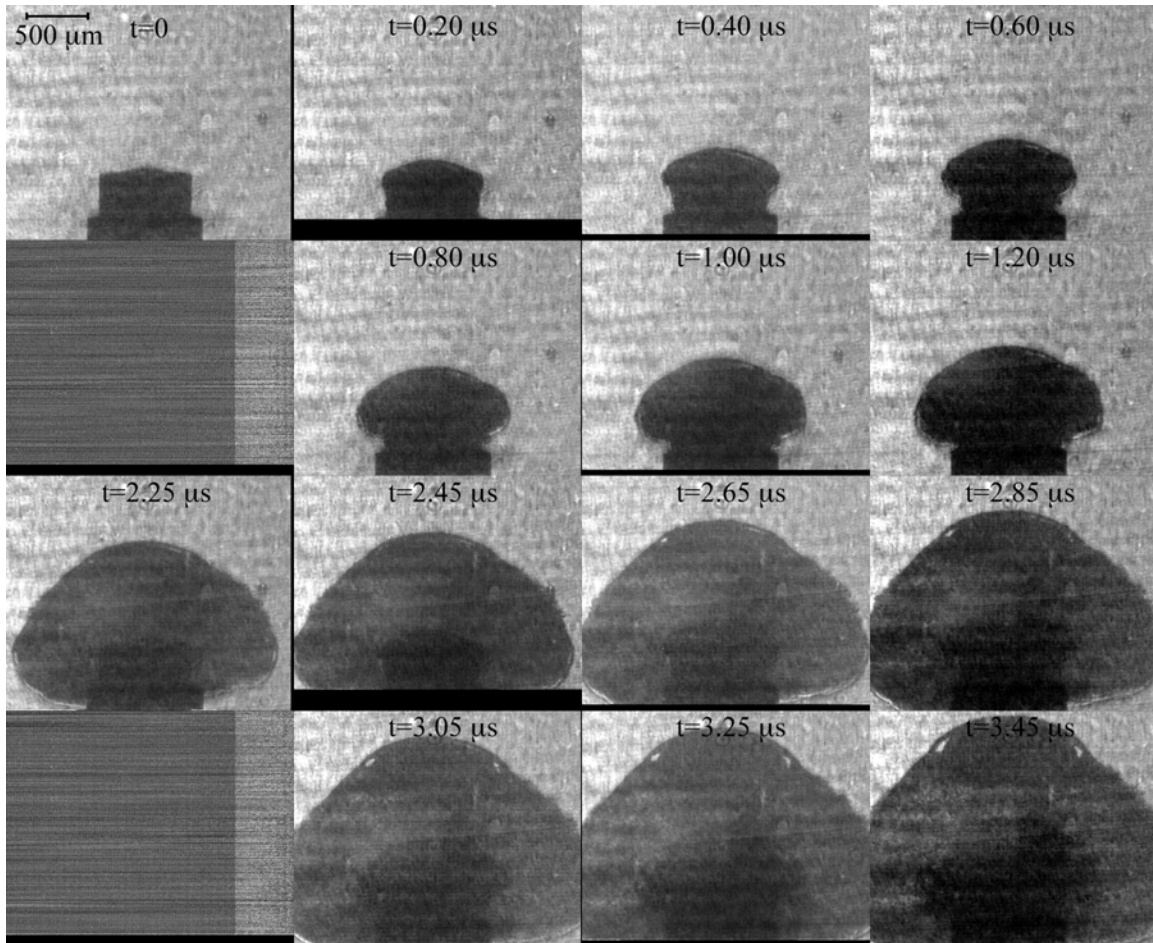


Fig. 9-6. Schlieren images of the shock wave expanding from an ER462 detonator in air. The exposure time was 20 ns, and the interframe time was 200 ns. Due to timing restrictions with the Imacon 200 camera, the interframe time is 1.05 μ s between frames 8 and 9.

To provide higher quality images of the expansion of the shock wave from the ER462, schlieren experiments were performed with plastic imaging blocks in contact with the top of the ER462. Two materials were used for the imaging blocks, poly(methyl methacrylate) (PMMA) and polydimethylsiloxane (PDMS). The results of these tests, showing the shock wave propagating in the plastic block are shown in Figs. 9-7 and 9-8, respectively.

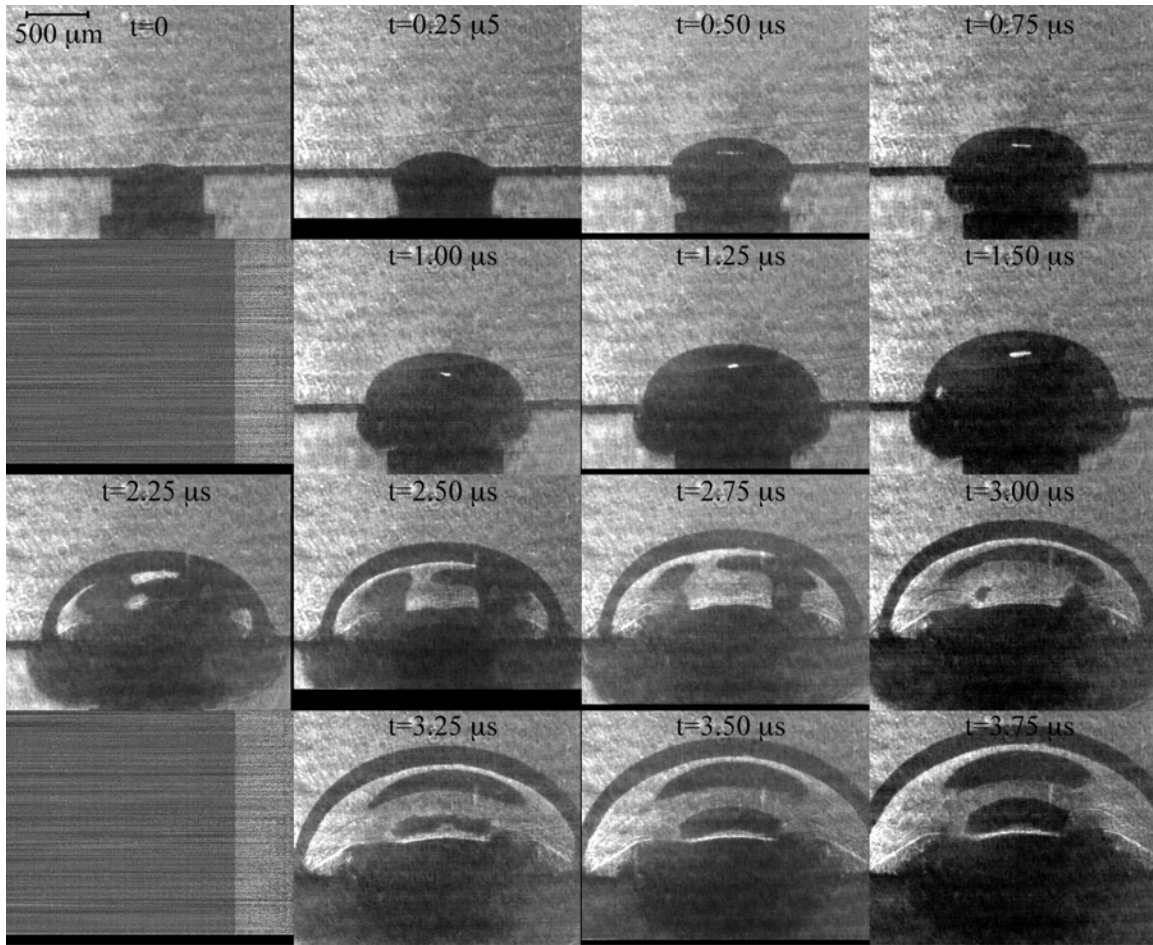


Fig. 9-7. Schlieren images of the shock wave expanding from an ER462 detonator into a PMMA block. The exposure time was 20 ns, and the interframe time was 250 ns. Due to timing restrictions with the Imacon 200 camera, the interframe time is 0.75 μs between frames 8 and 9.

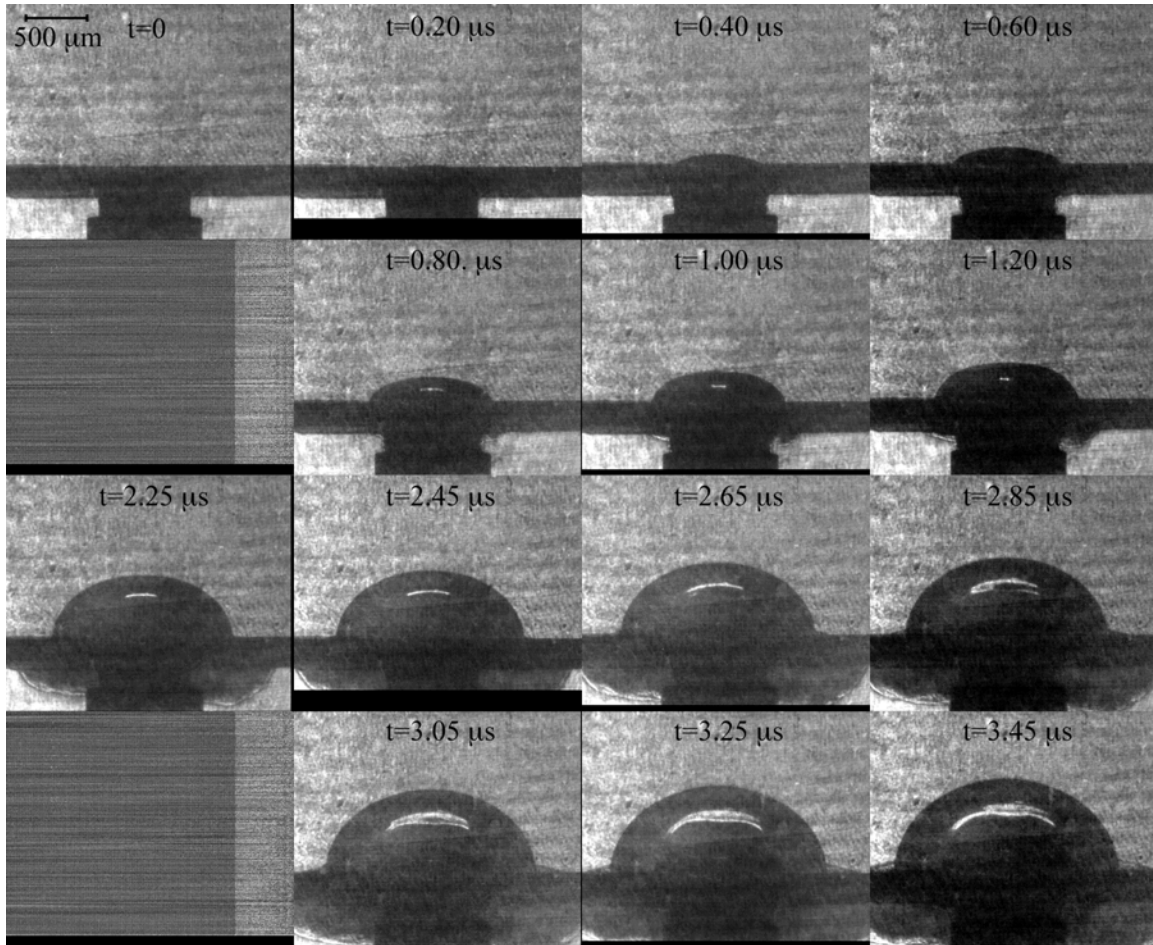


Fig. 9-8. Schlieren images of the shock wave expanding from an ER462 detonator into a PDMS block. The exposure time was 20 ns, and the interframe time was 200 ns. Due to timing restrictions with the Imacon 200 camera, the interframe time is 1.05 μs between frames 8 and 9.

A comparison between the schlieren images in Figs. 9-6, 9-7, and 9-8 shows that the shock wave expansion is much clearer when using the PMMA and PDMS imaging blocks. Especially improved is the visualization of the gradients in the refractive index inside the shocked area. Work is on-going into the analysis of these images with the 2-dimensional finite element hydrocode EPIC. An optimization routine was employed to find the best set of conditions that fit the temporal evolution of the shock wave using

EPIC, after which, the code can supply calculated values for many parameters, such as pressure, temperature, and shear.⁵

Although the schlieren and the framing camera provide insightful data on the full detonator, the data provided of the optical ablation event in Figs. 9-4 and 9-5 do not provide enough information about the state of the material at very early times to determine the nature of the insult provided to the high explosive. The following section describes the subsequent experiments using ultrafast dynamic ellipsometry to study the Ti ablation event.

9.3 Laser ablation with ultrafast dynamic ellipsometry¹¹

9.3.1 Introduction

Previously, phase sensitive techniques such as spectral interferometry have been used to examine the electron temperature and density gradients in thin films under extreme conditions.^{12,13} Here, we apply ultrafast dynamic ellipsometry (UDE) to investigate the ablation dynamics of titanium thin films in an effort to understand the initiation event in optical detonators, such as the ER 462.

Since the optical properties of a material result primarily from its electronic structure (in the visible range), ultrafast dynamic ellipsometry, which is sensitive to changes in the electronic structure as manifested through changes in the material's index of refraction, can potentially probe 1) the phase of a material, 2) its chemical reactivity, and 3) the ablation dynamics, yielding information regarding the electron temperature and electron gradients of the ablation plume. Using the same optical phase shift information as was gathered in the studies of transparent materials described in Chapters

4 through 8, this technique can provide a measurement of the difference in the reflection of s- and p-polarized light from an ablated surface, which can be used to study the properties of the material during ablation.

Previous studies of this ablation process using VISAR, PDV, and schlieren photography have gathered data suggesting that the laser ablation does not exclusively yield a hot plasma, but rather, the ablation process yields a fragment field with a range of velocity distributions.^{8,9} However, since the temporal resolution of these studies was insufficient to resolve the full dynamics of this process, UDE was applied to this problem to provide additional data that will help elucidate these mechanistic details.

9.3.2 Spectroscopic ellipsometry of Ti films

Since the ablation of the Ti films relies heavily on the absorptivity of the metal, the optical constants of the Ti films were measured with spectroscopic ellipsometry. The measurement was performed with a spectrometer by J. A. Woollam. Data were taken through the 1 mm thick fused quartz slide from 400 to 1200 nm at 70° and 80° then fit to yield the optical constants. The spectroscopic ellipsometry data are shown in Fig. 9-9, and the optical constants are plotted in Fig. 9-10. (A more detailed discussion of the spectroscopic ellipsometry is provided in §5.3.) In these UDE experiments, the wavelength of the laser ablation pulse was either 800 nm for a pulse of 300 ps in duration or 532 nm for a pulse of 16 ns in duration. The data in Fig. 9-10 show that the optical constants do not vary a great deal between 1064 nm, the wavelength used in the optical detonator and in the schlieren experiments, and 800 or 532 nm, the wavelengths used for

ablation in the UDE experiments. Hence, the ablation response of the Ti is expected to be similar at all three wavelengths.

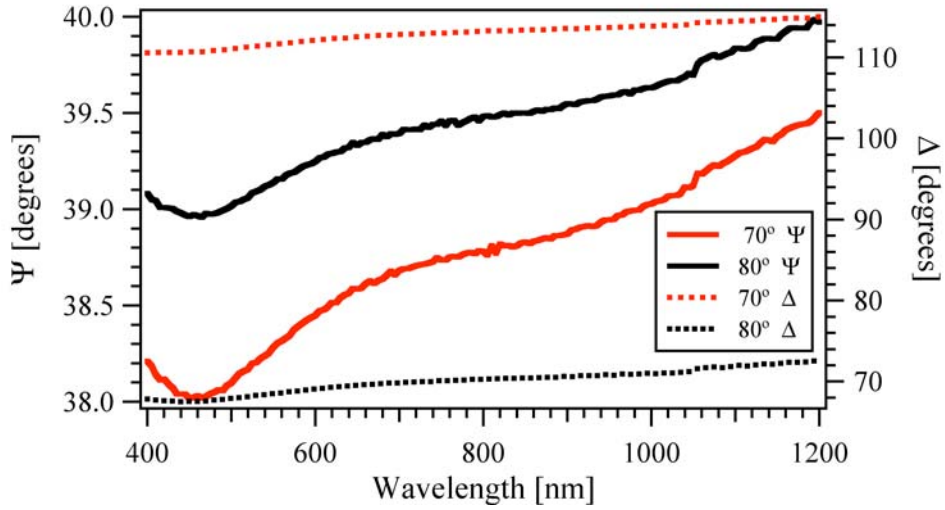


Fig. 9-9. Spectroscopic ellipsometry data for 250 nm Ti film vapor plated on 1 mm fused quartz. Data taken through the fused quartz.

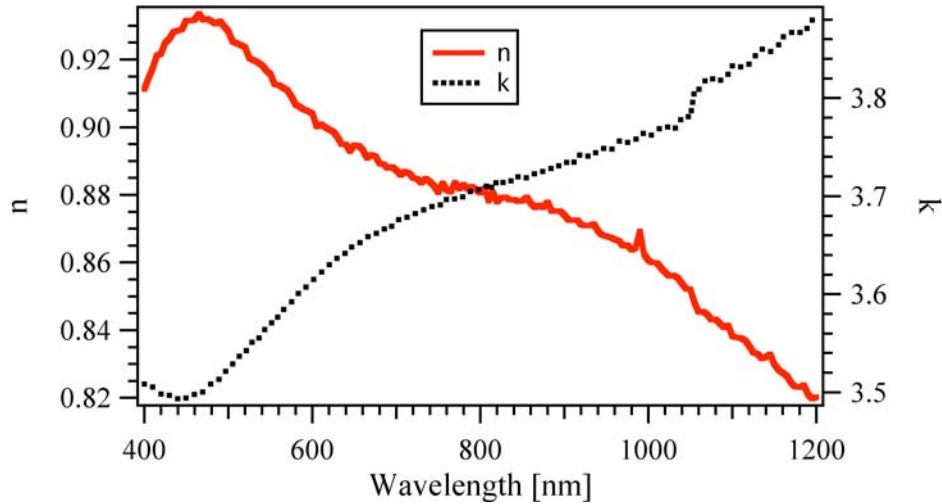


Fig. 9-10. Optical constants from a fit to the spectroscopic ellipsometry data shown in Fig. 9-9 above.

9.3.3 Experiment

Two different lasers and laser wavelengths were used to ablate the Ti. The first laser was the amplified Ti:sapphire laser that was stretched and spectrally shaped for driving a supported shock wave (with a fast rise time and a long duration) and was approximately 300 ps in duration. The details of this laser and its spectral shaping are given in §2.2. The second laser used to ablate the Ti was a small portion of one of the frequency doubled Nd:YAG lasers (Spectra-Physics PRO-190) operating at 532 nm that was normally used for pumping multi-pass amplification of the Ti:sapphire laser. The pulse duration of this laser was 16 ns FWHM. This ns optical drive was used to more closely mimic the conditions of the Ti ablation in the optical detonator and to allow the investigation of the evolution of the Ti ablation over longer times scales than available with the spectrally shaped ps drive. To create the longer delay times, the timing of the Q-switch was delayed with a digital delay generator (SRS DG535). Due to the electrical triggering of the Nd:YAG, there was a timing jitter of approximately 1.5 ns between the Q-switched laser and the probe laser.

In both cases, part of the spectrally shaped pulse was split off and was used for the UDE probe. Details of the probe and of the data analysis are given in Chapter 4.

The sample was 250 nm of Ti vapor-deposited on a 1 mm thick fused quartz microscope slide (Berliner Glas/US). The pump pulse was incident on the sample from the side opposite the probe pulse and was focused through the quartz substrate of the sample onto the Ti layer with an $f/12$ plano-convex lens for the ps drive pulse and an $f/8$ plano-convex lens for the ns drive pulse, creating an ablation region approximately 100 μm in diameter. Between each shot, the sample was translated 600 μm to a pristine area.

Figure 9-11 is a schematic, showing the orientation of the pump and probe pulses relative to the sample.

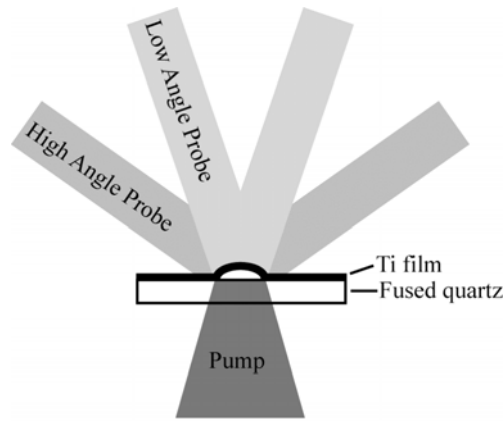


Fig. 9-11. Schematic of the Ti film sample showing ablation orientation. The movement and the optical properties of the Ti film are probed at the free surface.

9.3.4 Ultrafast dynamic ellipsometry results

For examining the mechanism of optical detonator initiation, UDE offers the possibility of characterizing the state of the ablated material, be it plasma, fully dense warm matter, or an intact flyer. Figure 9-12 shows phase shift and reflectivity data for Ti ablated with the ps drive pulse. For materials in which the complex refractive index is not changing with time, the phase shift data show the change in the position of the Ti surface. Clearly visible in the phase shift data is the acceleration of the material at the beginning of the ablation process. Also evident is that the phase profiles show no difference between the s- and p-polarized probed light, nor a difference as a function of probe angle, yielding the same position profiles for both polarizations and incident angles. These results indicate that there is not a measurable change in the complex

refractive index of the Ti during this time and that the Ti does not appear to be forming a plasma under these conditions.

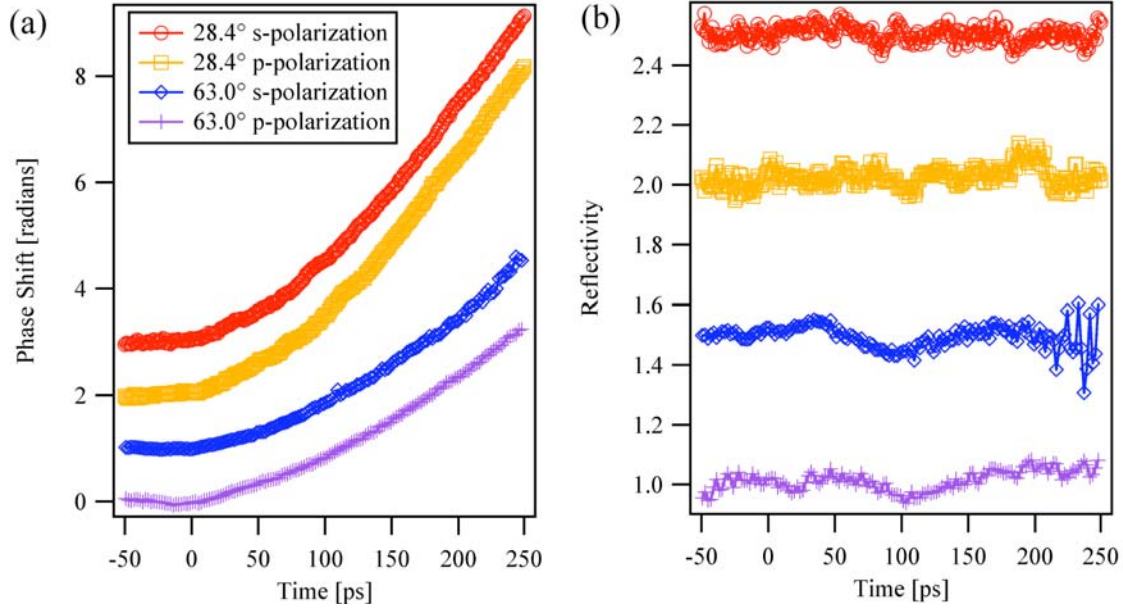


Fig. 9-12. (a) Phase shift and (b) reflectivity data (vertically offset for clarity) during the beginning of ablation of 250 nm of Ti on fused quartz with a spectrally shaped ablation pulse of approximately 300 ps. The phase shift data do not show a difference as a function of polarization of the probe light nor as a function of probe angle. Due to the lack of a measurable change in the refractive index of the Ti, it appears that the ablation launches the Ti as a flyer instead of generating a plasma under these conditions.

To collect a longer time history of data using the ps drive pulse, the motorized delay stage was scanned, varying the time between the arrival of the pump and of the probe pulses at the sample. In the absence of changes in the optical properties of the material, the free surface velocity can be calculated using the change in the phase and the change in time as in Eq. (9.1).

$$u_{\text{fs}} = \frac{\lambda}{4\pi \cos \theta} \frac{\Delta \phi}{\Delta t}, \quad (9.1)$$

where u_{fs} is the free surface velocity, λ is the wavelength of the probe light, θ is the angle of the incident probe light, $\Delta\phi$ is the change in the phase, and Δt is the change in time. Shown in Fig. 9-13 is the derived velocity data taken with UDE of the ablated titanium, at 1.1 mJ, 2.8 mJ and 5.0 mJ. The data result from approximately 70-80 shots at each energy, where 10 shots were collected at each time step, and the pump was delayed by 125 ps relative to the probe between time steps. The velocities shown are linear fits to 50 ps sections across the full 300 ps time scan for each data set, which were averaged at each time point shown. In this way a time history was built up for approximately 1 ns after the start of the ablation process. As stated previously, the similarity of the velocity profiles for both polarizations and angles of incidence indicate the lack of formation of an observable plasma and no measurable changes in the index of refraction of the material with time.

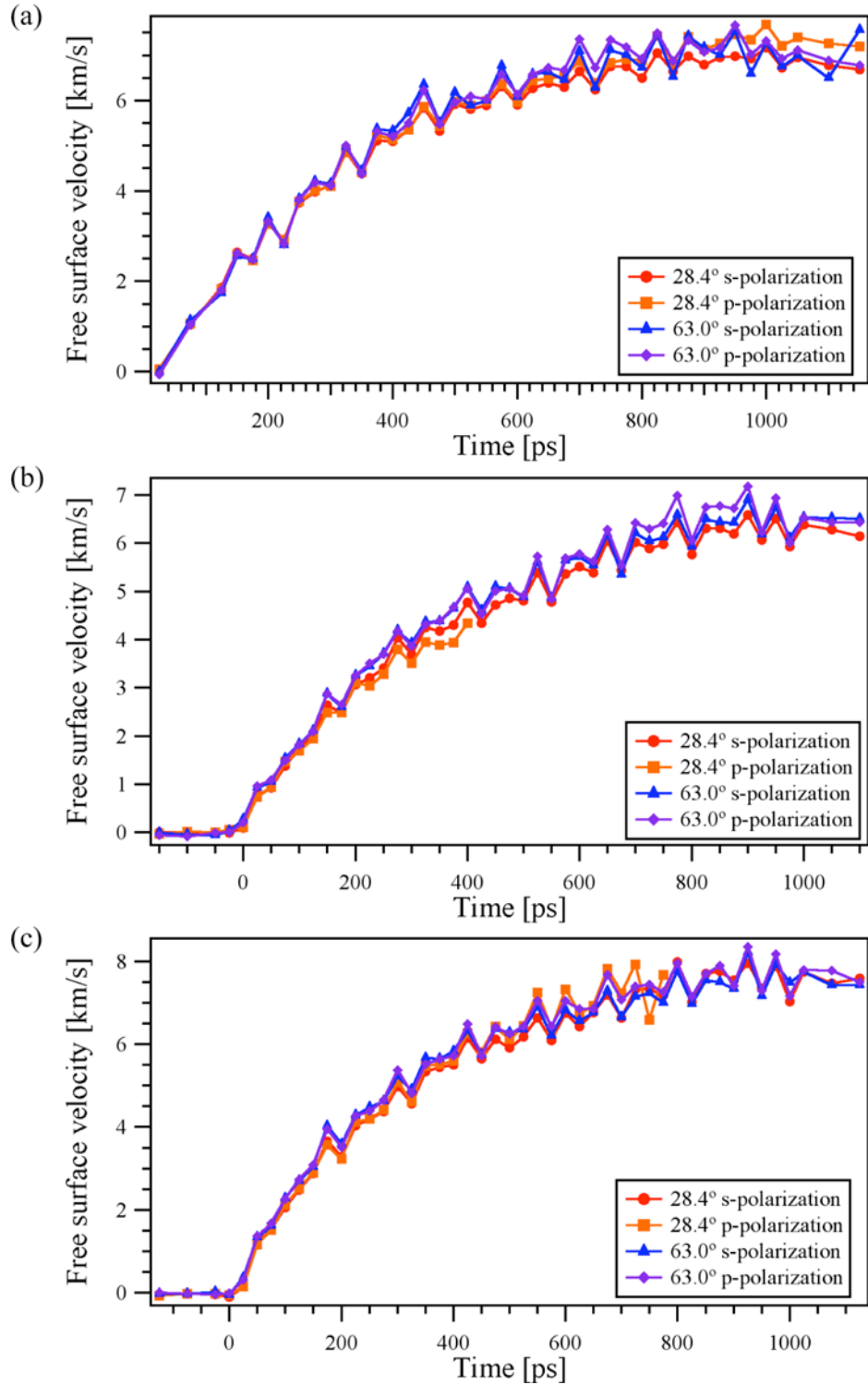


Fig. 9-13. Free surface velocity vs. time for ablation of a 250 nm thick Ti layer when pumped with (a) 1.1 mJ, (b) 2.8 mJ, and (c) 5.0 mJ pulses of 300 ps duration. The phase profiles do not show a difference as a function of polarization or of probe angle, yielding the same velocity profiles for both polarizations and incident angles and indicating that the Ti is launched as a flyer.

The frequency doubled output of a Nd:YAG laser was used to investigate the evolution of the Ti ablation over several nanoseconds, and as a “fairer” comparison to the studies of the ER 462, which uses ns pulses. Due to the one-dimensional spatially resolved nature of the interferometric probe, the contour of the Ti surface was examined as it was ablated. Plotted in Fig. 9-14 are the observed phase shifts across the center of the ablated region at several different times after the arrival of the ns pump pulse. Around 1 ns after the arrival of the pump pulse, the surface had not moved far from its original position ($\sim 0.2 - 0.5 \mu\text{m}$), and the contour of the surface was fairly smooth and followed the profile of the laser pulse. At approximately 3 ns after the arrival of the pump pulse, definite irregularities across the surface of the Ti were observed. At approximately 5 ns, the Ti surface had significant variations in position, likely indicating the onset of hydrodynamic instability. Similar to the variations in surface position, the free surface velocity varied widely across the ablated region of a single shot and between shots. Most of the peak velocities during approximately the first 7 ns probed were 1-3 km/s, which is in the same range as the peak of the velocity distribution using the DOI fireset and measured by PDV.⁸ There is some indication that there are significant differences in the phase shifts of the s- and p-polarized probe light for these shots, however, the lower signal-to-noise ratio using the ns ablation pulse prohibits a conclusive statement that optical effects were observed.

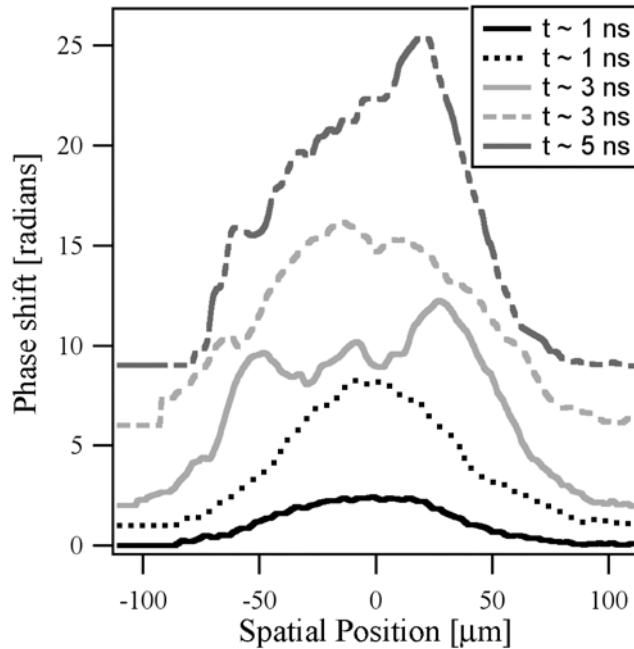


Fig. 9-14. Spatial line outs from UDE data (vertically offset for clarity), showing the accumulated phase at the approximate times noted for the ns ablation of Ti pumped with 2.8 mJ. Note the variability and irregularity of the spatial profiles at later times.

The presence of these irregularities is observed in both the phase shift and the reflectivity. Additionally, the development of the individual irregularities can be observed in a single shot on shorter time scales due to the temporal resolution of the probe method. For example, Fig. 9-15 shows the phase shift and reflectivity data for one shot taken approximately 7 ns after the initial arrival of the pump pulse. In the phase shift data, three large bumps at the surface of the Ti are seen to develop with time, while in the reflectivity data, the reflectivity at each spatial point is shown to be changing, typically decreasing, as a function of time.

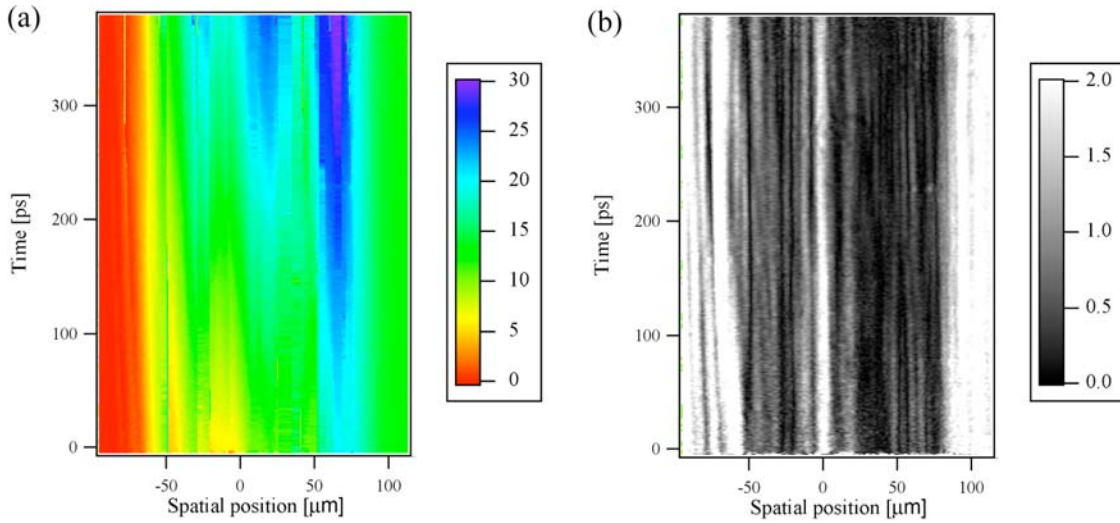


Fig. 9-15. Example of the growth of irregularities observed at later times (~ 7 ns) in both the (a) phase shift and (b) reflectivity. The Ti appears to be breaking up, either due to instabilities caused by the laser profile or due to instabilities in the propagation of the flyer.

With the ps ablation pulse, the phase shift and reflectivity data gathered using UDE suggest that the Ti films are ablated in a manner more consistent with a flyer than with a plasma. Using UDE, we measured no changes in the refractive index of the Ti and recorded only the motion of the Ti free surface. This lack of observable change in the refractive index indicates that the Ti did not become a plasma during the time in which it was probed. Another indication of flyer generation is the time-evolution of the Ti free surface velocity shown in Fig. 9-13. The initial acceleration tapers off to a constant velocity and is consistent with a film that has delaminated from its substrate to become a flyer.

Using the ns ablation pulse, the development of irregularities on the surface of the Ti several nanoseconds after the arrival of the beginning of the pulse is suggestive that the flyer becomes fragmented either from irregularity in the spatial profile of the laser pulse or from hydrodynamic instabilities that develop in the material. Valenzuela *et al.*

used PDV to study the velocity distribution of the Ti ablation for hundreds of nanoseconds.⁸ Their results match very well with this study, in that they observed a wide distribution of velocities up to the limit of their detection range (~7 km/s), similar to the results plotted in Fig. 9-13, and that the peak of their observed velocity profile is in the same region as the majority of velocities observed with UDE using the ns ablation pulse.

The lack of an observable effect on our interferometric data from the plasma and its index of refraction effects likely results from the fact that titanium, as most transition metals, exhibits a large electron-phonon coupling constant, $g=1.3 \times 10^{18} \text{ Wm}^{-3}\text{K}^{-1}$.¹⁴ Thus, the combination of a skin depth of 19 nm and the strong electron-phonon coupling causes rapid heating of the Ti in contact with the quartz substrate. The rapid heating causes expansion of the ablated layer, launching a shock wave, and upon release, launching the entire Ti film. Thus, one might conclude that initiation of PETN, the explosive component of the detonator, might be simply a result of the interaction of a high velocity flyer with the PETN. In fact, a shock-matching calculation indicates that at flyer velocities of 6.6 to 8 km/s, the pressure in PETN (density 1.6 g/cc) is expected to be between 80 and 110 GPa, strongly over-driving the equilibrium detonation pressure of ~26 GPa and indicating that prompt reaction should occur. However, this simple flyer model is somewhat inconsistent with the PDV, schlieren, and ns Nd:YAG driven ablation data, all of which show variation in velocities and the formation of instabilities, much like the fragment initiation mechanism of slapper detonators.⁵ Thus, the initiation of the explosive using ablated Ti, though clearly an unstable process from a hydrodynamic perspective, reliably initiates the PETN in a manner that permits electrical isolation of the detonator.

9.4 Conclusion

Schlieren and UDE have been used to study the dynamics of DOI detonators and the underlying ablation initiation mechanism. The schlieren measurements have shown the creation of a shock wave from the ablation and the creation of a smooth shock wave by the full detonator. Ultrafast dynamic ellipsometry has been used to measure the ablation of Ti thin films. During the first several nanoseconds of the ablation process, the lack of any discernable difference between the s- and p-polarized probe data, the velocity profile of the free surface, and the irregular spatial profile of the ablated region indicate that the ablated material is a fragmented flyer on these short time scales, not an expanding plasma. These results are consistent with earlier studies using PDV. In the application of laser driven ablation of Ti films to optical detonators, these data support the supposition that the method of explosive initiation is similar to the fragmented initiation of slapper detonators.

This study is the first application of UDE to probe the physical state of matter. However, there is an increasing scientific desire for diagnostics of this sort for exploring matter under extreme conditions, for instance, in the fields of plasma physics and high energy density physics. Ultrafast dynamic ellipsometry is very well suited to the single shot nature of experiments in those fields and can provide much new and necessary information.

References

- ¹ L. M. Barker and R. E. Hollenbach, "Laser interferometer for measuring high velocities of any reflecting surface," *J. Appl. Phys.* **43**, 4669-75 (1972).
- ² O. T. Strand, L. V. Berzins, D. R. Goosman, W. W. Kuhlow, P. D. Sargis, and T. L. Whitworth, "Velocimetry using heterodyne techniques" in *26th International Congress on High-Speed Photography and Photonics*, edited by D. L. Paisley, S. Kleinfelder, D. R. Snyder, and B. J. Thompson (SPIE--International Society for Optical Engineering, Bellingham, WA, 2005), p. 593-599.
- ³ D. D. Bloomquist and S. A. Sheffield, "Optically recording interferometer for velocity measurements with subnanosecond resolution," *J. Appl. Phys.* **54**, 1717-22 (1983).
- ⁴ C. F. McMillan, D. R. Goosman, N. L. Parker, L. L. Steinmetz, H. H. Chau, T. Huen, R. K. Whipkey, and S. J. Perry, "Velocimetry of fast surfaces using Fabry-Perot interferometry," *Rev. Sci. Instrum.* **59**, 1-20 (1988).
- ⁵ S. A. Clarke, C. A. Bolme, M. J. Murphy, C. D. Landon, K. A. Thomas, T. A. Mason, R. J. Adrian, A. A. Akinci, and M. E. Martinez, "Using schlieren visualization to track detonator performance" in *Shock Compression of Condensed Matter--2007*, edited by M. L. Elert, M. D. Furnish, R. Chau, N. C. Holmes, and J. Nguyen (American Institute of Physics, Melville, NY, 2007), p. 1089-1092.
- ⁶ G. S. Settles, "High-speed imaging of shock waves, explosions and gunshots - New digital video technology, combined with some classic imaging techniques, reveals shock waves as never before," *Am. Sci.* **94**, 22-31 (2006).
- ⁷ M. Hauer, D. J. Funk, T. Lippert, and A. Wokaun, "Laser ablation of polymers studied by ns-interferometry and ns-shadowgraphy measurements," *Appl. Surf. Sci.* **208-209**, 107-12 (2003).
- ⁸ A. R. Valenzuela, G. Rodriguez, S. A. Clarke, and K. A. Thomas, "Photonic Doppler velocimetry of laser-ablated ultrathin metals," *Rev. Sci. Instrum.* **78**, 013101 (2007).
- ⁹ A. R. Valenzuela, G. Rodriguez, and S. A. Clarke, "Optically-based velocity and topographic measurement systems in the nano-scale for developing optical initiation," *Proc. SPIE Int. Soc. Opt. Eng.* **6662**, A6620-A6620 (2007).
- ¹⁰ G. S. Settles, *Schlieren and shadowgraph techniques: visualizing phenomena in transparent media* (Springer-Verlag, Berlin, 2001).
- ¹¹ C. Bolme and D. Funk, "Ultrafast dynamic ellipsometry measurements of early time laser ablation of titanium thin films," *Appl. Phys. A* (2008).
- ¹² P. Blanc, P. Audebert, F. Fallies, J. P. Geindre, J. C. Gauthier, A. DosSantos, A. Mysyrowicz, and A. Antonetti, "Phase dynamics of reflected probe pulses from sub-100-fs laser-produced plasmas," *J. Opt. Soc. Am. B* **13**, 118-24 (1996).
- ¹³ C. Quoilx, G. Hamoniaux, A. Antonetti, J. C. Gauthier, J. P. Geindre, and P. Audebert, "Ultrafast plasma studies by phase and amplitude measurements with femtosecond spectral interferometry," *J. Quant. Spectrosc. Radiat. Transfer* **65**, 455-62 (2000).

- ¹⁴ Z. Lin, L. V. Zhigilei, and V. Celli, "Electron-phonon coupling and electron heat capacity of metals under conditions of strong electron-phonon nonequilibrium," *Phys. Rev. B* **77**, 075133-1 (2008).

Chapter 10

Metallic Phase Transitions

10.1 Introduction

Molecular dynamics (MD) and electronic structure calculations^{1,2} have been steadily advancing to the current level where they can accurately predict material responses in complex systems and conditions, such as shock loading. Unfortunately, most of the current shock wave diagnostics have time and length scale resolutions that are inadequate to properly benchmark these calculations. More importantly, the missing resolution complicates the process of improving the accuracy of the calculations, such as refinement of the empirical interatomic potentials used in classical MD simulations. Ultrafast dynamic ellipsometry (UDE) was developed to assist in this area by providing experimental data on the material and optical responses at time and length scales similar to those in large calculations.

Several interesting metallic phase transitions have been recently investigated using both experimental and computational methods. The α - ϵ phase transition in Fe was explored in an MD simulation, using several shock pressures and several orientations of the Fe crystal lattice.¹ The orientation of the Fe crystal was found to be critical in determining the kinetics of the phase transition due to the differing accessibilities of slip planes. These simulations were followed by an experiment that used laser driven shock

waves to induce the transition and x-ray diffraction (XRD) to probe the rearrangement of the lattice structure.³ Another metallic phase transition of interest is the γ - α transition in cerium. This isomorphous phase transition occurs with a 16% decrease in volume, and it is theorized that this transition results from the transition of delocalized to localized 4*f*-electrons. Currently, calculations using the Vienna *Ab-initio* Simulation Package (VASP) are underway to map the Ce phase diagram,⁴ and this phase transition is being investigated under gas gun driven shock loading.⁵

This chapter will present the application of UDE to the ultrafast laser-induced melting of silicon, a transition that has already been well studied but was used to test UDE on metallic phase transitions. The remainder of the chapter will describe the progress that has been made toward the fabrication of oriented crystalline Fe and Ce films and the characterization of these films, along with some preliminary UDE data. Finally, there will be a discussion of the next steps to follow this work.

10.2 Ultrafast laser induced melting of silicon⁶

10.2.1 Introduction

The response of crystalline silicon to laser excitation has been extensively studied during the past several decades.⁷⁻¹⁵ The most commonly interrogated property has been the large change in reflectivity upon laser excitation, melting, or ablation. The previous studies have typically probed the reflectivity at a single angle with one polarization of light. Here is presented ultrafast dynamic ellipsometry of laser ablated crystalline silicon that provides a spatially resolved measurement of the change in the refractive index across the region subjected to a 100 fs laser pulse. The resulting refractive index data

show only a slight change in the real component and a significant increase in the extinction coefficient, indicative of the melting of silicon. The change is strongest in the central area of the ablation region with more minor changes toward the edges.

In this particular application, we are not looking to temporally resolve the melt dynamics, as those have been thoroughly studied using reflectivity.⁷⁻¹⁵ Instead, we are using this well-established ultrafast melting process to demonstrate that UDE is able to determine metallic phase transitions before turning to materials in which the phase transition kinetics and optical characteristics are unknown.

10.2.2 Experiment

The same 10 Hz laser system was used in this experiment as in the rest of this thesis. As before, a portion of the pulse energy was spectrally narrowed and compressed to 400 fs after amplification, then it was used to measure the time-dependent frequency of the chirped pulse used for the UDE probe. (A more complete description of this process is provided in §4.2.) After measuring the time-dependent frequency, the spectral narrowing of the compressed pulse was removed, and the full bandwidth of the pulse was compressed, yielding a pulse duration of approximately 100 fs. Contrary to the other experiments in this thesis, this pump pulse was incident on the sample on the same side as the probe. The 100 fs pump pulse contained 0.18 mJ and was directed onto a 250 μm thick wafer of Si(111) at normal incidence and focused to approximately 200 μm in diameter. The incident fluence was 0.6 J/cm^2 , approximately 3.5 times the melting threshold of 0.17 J/cm^2 .¹² An experimental schematic is provided in Fig. 10-1, and interferograms recorded before and during the ablation are shown in Fig. 10-2.

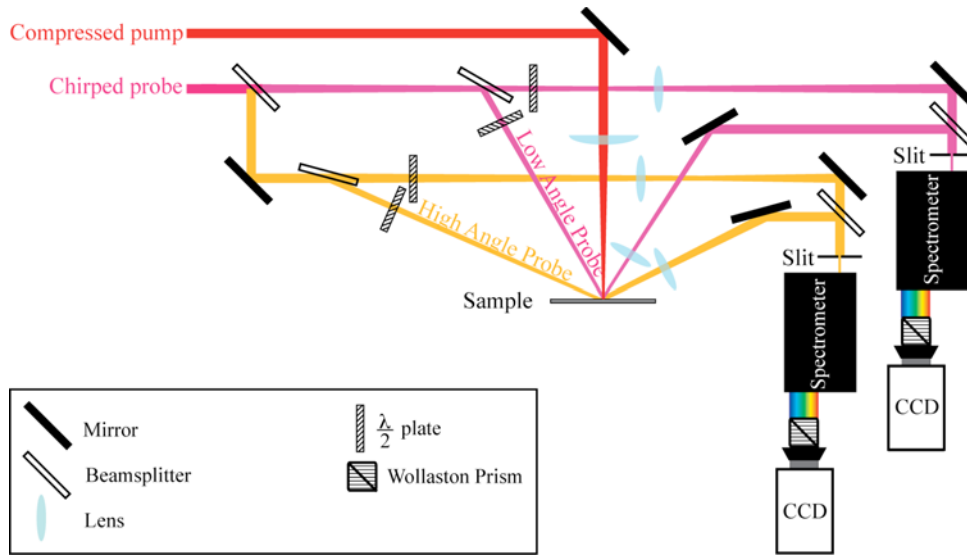


Fig. 10-1. Experimental schematic for ultrafast dynamic ellipsometry diagnostic showing the orientation of the 100 fs compressed pump pulse.

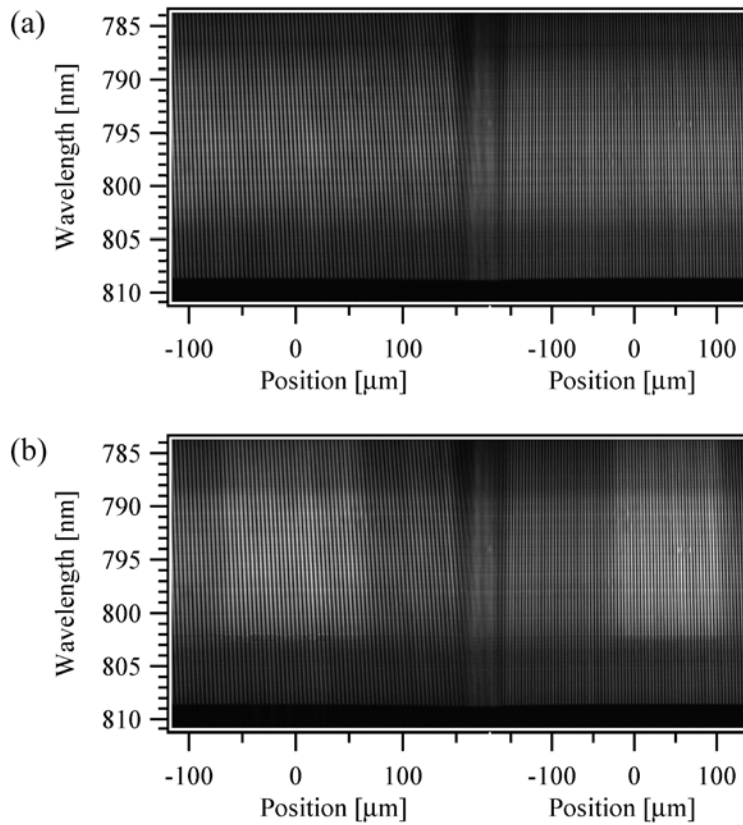


Fig. 10-2. Interferograms of the 25.8° probe with the p-polarized light on the left and the s-polarized light on the right. Interferograms were recorded (a) before and (b) during the ablation of a Si(111) wafer with 0.6 J/cm².

The interferograms were processed in the same manner as described in §4.3.

Figure 10-3 shows the resulting phase shift and reflectivity data from the interferograms in Fig. 10-2.

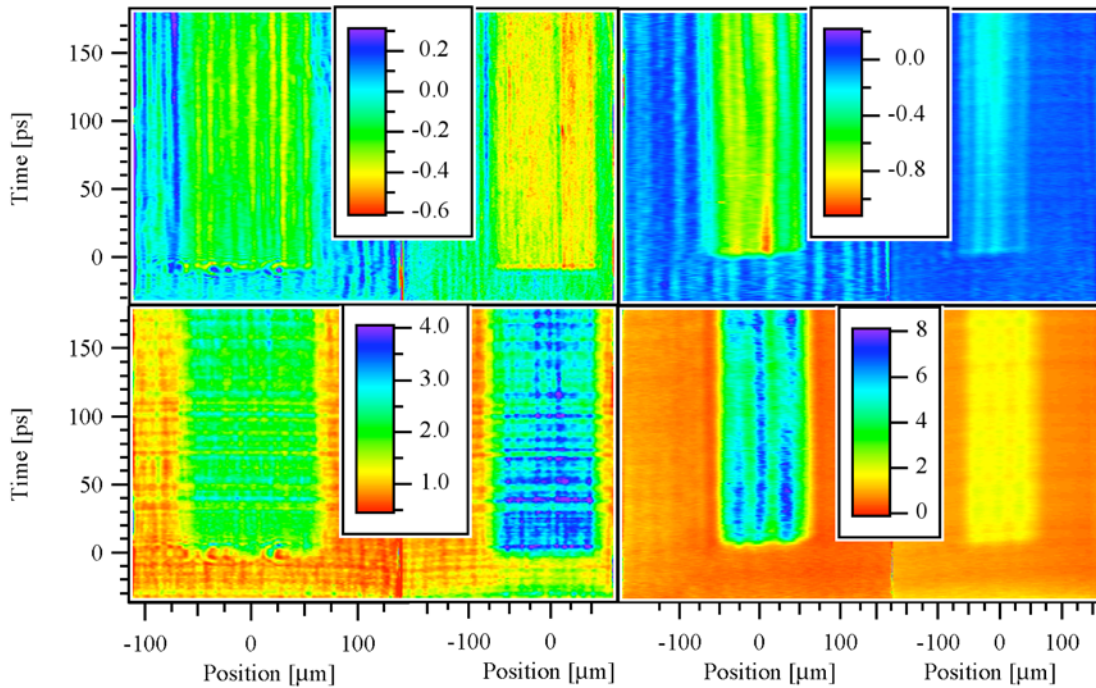


Fig. 10-3. Phase shift and reflectivity data of Si(111) ablated with 0.6 J/cm^2 . In each of the four images, the data from the p-polarized probe are on the left and from the s-polarized probe are on the right. (a) Phase shift data at 25.8° . (b) Reflectivity data at 25.8° . (c) Phase shift data at 62.7° . (d) Reflectivity data at 62.7° . The phase shift and reflectivity data are given relative to the initial values (prior to the arrival of the pump pulse).

10.2.3 Results

In this experiment, the absolute reflectance of the light is not measured, but rather the measured quantity is the change in reflectance. The phase shift is a measurement of changes in the optical properties and the path length of the reflected light. The reflectivity primarily measures the changes in the extinction coefficient. Both quantities

are measured relative to the reflectance before the arrival of the laser ablation pulse. Due to the relative nature of the measurement, the phase shift is adjusted such that the phase shift before the arrival of the ablation pulse is 0, and the reflectivity is normalized to the value before the arrival of the ablation pulse.

The data seem to show a change from the refractive index before the ablation pulse to a second refractive index afterward that appears to stay constant for the duration of the measurement. There is not an indication that the material is in motion after the arrival of the ablation pulse because the phase shift is not changing; in other words, the path length is not changing. Additionally, the interferograms recorded 200-300 ms after the ablation event support the approximation of stationary material because they show that the surface has sustained only minor damage without a large loss of material. The model used to fit the data was adjusted for these characteristics. The model sets the material motion to 0, and it changes the optical constants from an initial value to a final value. A time constant for the transformation of the optical properties is also included in the model. The time-dependent refractive index was given the empirical form of Eq. (10.1), which smoothly varies the optical constants from the initial to final values with a variable time constant, τ .

$$\tilde{n}(t) = \tilde{n}_0 + \int \frac{1}{2} [1 + \tanh(\frac{t-t_0}{\tau})] (\tilde{n}_f - \tilde{n}_0) dt \quad (10.1)$$

where $\tilde{n}(t)$ is time-dependent complex refractive index, \tilde{n}_0 is the initial complex refractive index, \tilde{n}_f is the final complex refractive index, t is time, t_0 is the center time of the change in refractive index, and τ is the time constant of the change.

For an accurate measurement of the initial refractive index of the Si wafer, it was measured on a spectroscopic ellipsometer (J.A. Woollam Co.). The wafer was probed at

70° and 80° from 400 to 1200 nm, and the resulting data were fit for the refractive index. At 800 nm, the refractive index was $(3.66 \pm 0.10) + i(0.13 \pm 0.17)$, and this value for the refractive index was used in the fitting. This value agrees with the literature value of $3.688 + i0.006$ at 805.1 nm.¹⁶

Phase shift and reflectivity data were averaged in sets of 5 pixels along the spatial axis. The averaged data as a function of time were extracted from the data shown in Fig. 10-3. The eight sets of data were extracted for the same spatial position at each point across the ablation region.

Using equations for the reflectance explained in Chapter 4 and Eq. (10.1) for the time-dependence of the complex refractive index, all eight sets of data were simultaneously fit for the real and imaginary components of the refractive index and the time constant of the change in the optical properties using the Levenberg-Marquardt least squares fitting algorithm. An example set of data and their fit are shown in Fig. 10-4.

The optical constants ($\tilde{n} = n + ik$) resulting from the fits to the data as a function of position across the ablation region are shown in Fig. 10-5. The real portion of the refractive index does not change much due to ablation, but the imaginary portion shows a large change, especially toward the center of the ablation region.

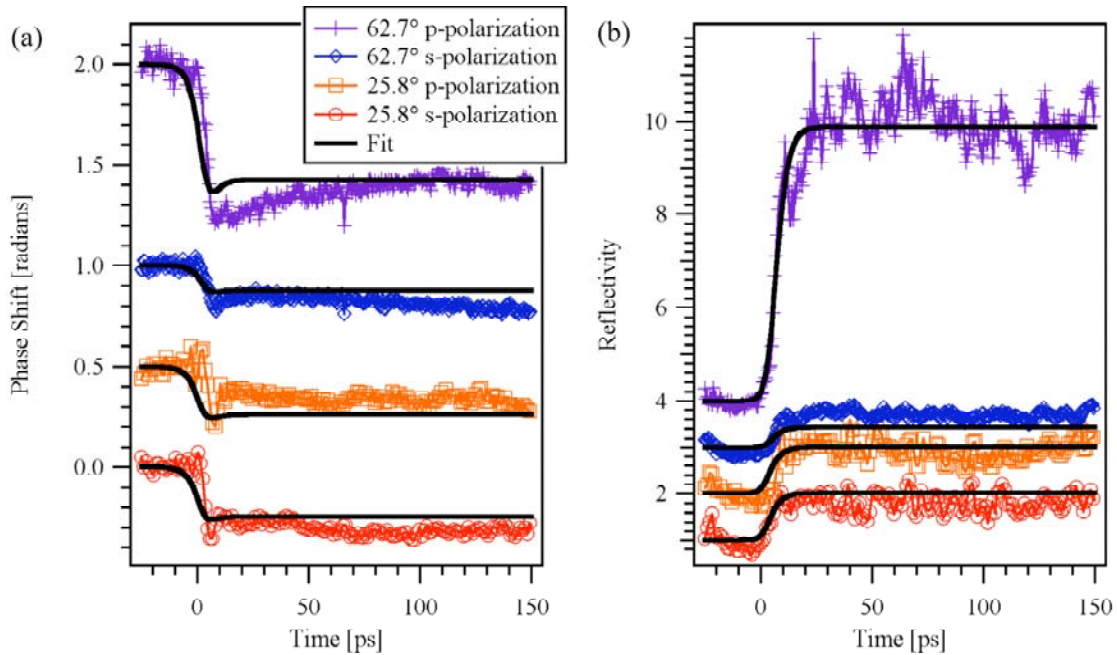


Fig. 10-4. (a) Phase shift and (b) reflectivity data from the two angles and both polarizations along with the fit obtained from simultaneously fitting all eight sets of data for the Si ablation. The data are plotted relative to the initial values, in that before the arrival of the pump pulse, the phase shift is set to 0 and the reflectivity is normalized to 1. Data are vertically offset for clarity.

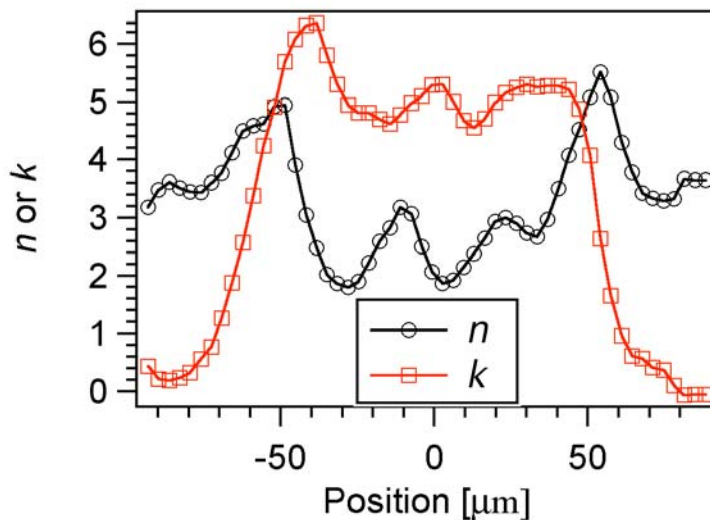


Fig. 10-5. The real (n) and imaginary (k) parts of the refractive index obtained from the fit to the data from 30 ps before to 150 ps after the arrival of the pump pulse as a function of the spatial position across the center of the ablated region.

The majority of the time constants τ from the fits to the data ranged between 4 and 8 ps. However, since the time resolution of the measurement is 3.5 ps (due to the spectral resolution of the spectrometers as discussed in §4.3), the time constant is not indicative of the dynamics of the transition.

10.2.4 Discussion

The spatially resolved ultrafast dynamic ellipsometry data provide a measurement of the refractive index across the center of the ablation region. The silicon surface should melt when exposed to the fluence used in the ablation pulse. The refractive index of liquid silicon at 700 nm was measured by Shvarev *et al.* to be $3.3+i5.6$.¹⁷ The real component of the refractive index oscillates near the liquid value; however, it is not a definitive indicator of the liquid phase because the solid and liquid values are too similar to be distinguished by the data.

The more interesting data are of the spatially resolved extinction coefficient. The value of the extinction coefficient rises from that of solid silicon at the edges of the ablation region to that of liquid silicon in the center, providing a one-dimensional spatially resolved probe of the ultrafast laser induced melting of crystalline silicon. The spatial profile of the extinction coefficient is understandable in terms of an energy threshold for the melt that is reached on the edges of the pulse with a fairly constant value in the center where the material is melted.

Although the ultrafast laser induced melting of silicon is a well-known and thoroughly studied phenomenon, the technique of ultrafast dynamic ellipsometry has demonstrated that it can make a single-shot temporally and spatially resolved

measurement of a phase transition. As far as the silicon is concerned, the resulting refractive index data show how the material response is different at the edges of the ablation region from the response in the center. Additionally, the multiple angles and multiple polarizations of ultrafast dynamic ellipsometry provide significantly more information than a single reflectivity measurement, allowing a determination of both the real and imaginary portions of the refractive index. To investigate the kinetics of this transition, this experiment could be modified to achieve a time resolution comparable with the bandwidth-limited probe pulse duration (<50 fs) using a signal reconstruction method described by Geindre *et al.*¹⁸

10.3 Iron and cerium metal films

10.3.1 Fabrication of metal films

The electron-beam deposition system in the bell jar vacuum chamber described in §6.2 was used to deposit the metal films. Both iron and cerium readily oxidize, so the ability to deposit multiple materials, such as the metal film and the protective window layer, without breaking vacuum and exposing the metals to atmospheric oxygen was utilized in the creation of these films.

The approach used in creating these films was the same as described by Meserole *et al.*^{19,20} Briefly, the substrate material and orientation was chosen such that the lattice spacing of the substrate closely resembled the lattice spacing of the desired crystalline orientation. The Fe(100) orientation was desired, and so (100)-oriented magnesium oxide (MgO) substrates 10 mm x 10 mm x 0.5 mm that were polished to an optical finish on both sides were used for the iron films, identical to the substrates of Meserole.^{19,20}

These substrates were sonicated for 5 minutes in methanol and then UV/ozone cleaned on both sides prior to the deposition. Iron wire that was 1.0 mm in diameter (Puratronic, 99.995%) was manually coiled and placed in a graphite crucible liner for deposition. The lattice spacing of γ -Ce is well matched to the lattice spacing of MgO(111). MgO(111) substrates 10 mm x 10 mm x 0.5 mm that were polished to an optical finish on both sides were used for the Ce films and were cleaned in the same manner as the substrates for the Fe. High purity Ce shot (99.95%, Ames Laboratory) was used for the Ce films. The Ce shot had a subtle blue iridescent sheen, and a photograph of the material is shown in Fig. 10-6. The Ce arrived packaged in Ar and was stored in nitrogen after opening to reduce the extent of oxidation.



Fig. 10-6. Photograph of Ce shot used for electron beam deposition.

After deposition, the films were measured with XRD (Rigaku, Ultima III) using Cu $K\alpha$ radiation (wavelength $\lambda=1.54059 \text{ \AA}$). The XRD spectra of a bare MgO(100) substrate and of a MgO(100) substrate with a 600 nm Fe film and a 500 nm fused silica window is shown in Fig. 10-7. The doublet at two theta angle around 43° in both spectra is the MgO(100) peak. (The splitting of this peak into a doublet is an artifact of the

orientation of the sample with respect to the diffraction angle. When the sample is rotated 90° on the sample stage, the doublet becomes the expected single MgO(100) peak and when it is rotated another 90° , the doublet returns.) In Fig. 10-7, the spectrum of the substrate appears identical to the spectrum of the sample.

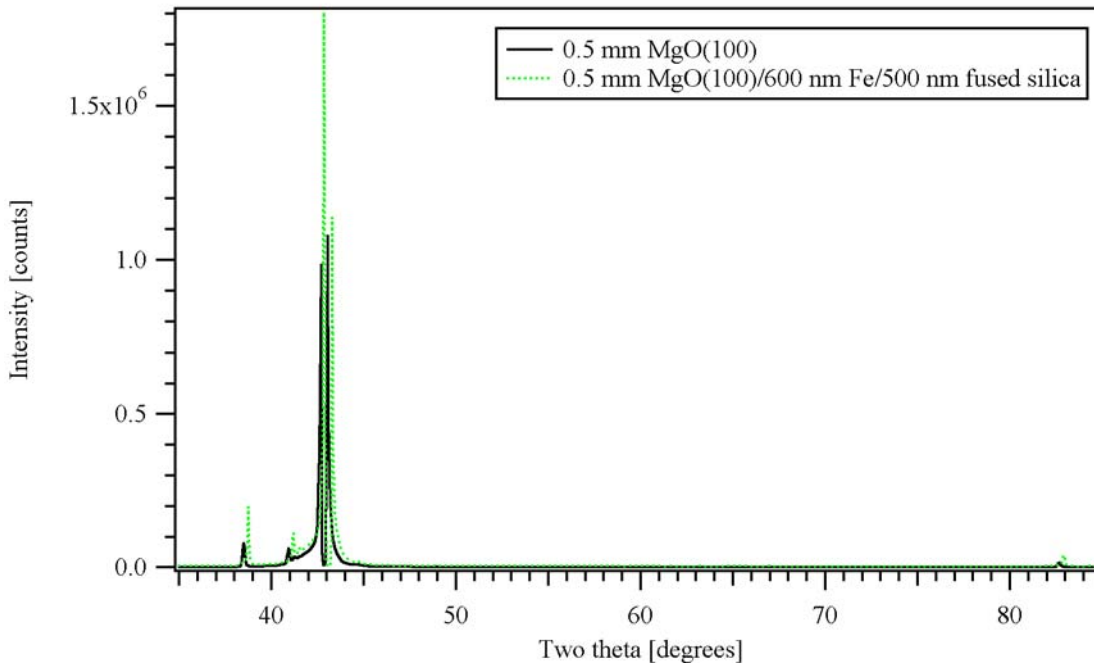


Fig. 10-7. XRD spectra of a 0.5 mm MgO(100) substrate and of a 0.5 mm MgO(100) substrate that was deposited with 600 nm Fe and capped with 500 nm fused silica. There are differences in the intensities of the peaks, but all of the peaks present in the Fe sample are also present in the spectrum of the bare MgO(100) substrate.

A small Fe(020) peak should be present at 65° . To look for this peak, the scan angle was narrowed to $62\text{--}68^\circ$ and the data collection time was increased. The data for a MgO(100) substrate and for a 120 nm Fe film on a MgO(100) substrate are shown in Fig. 10-8. There is a broad peak centered about 64.9° in both spectra, but the Fe sample also shows a small, sharp peak at 66.0° . The spectrum from the Fe films shows a distinct

difference from the spectrum of the substrate, and it appeared consistently from this and other samples.

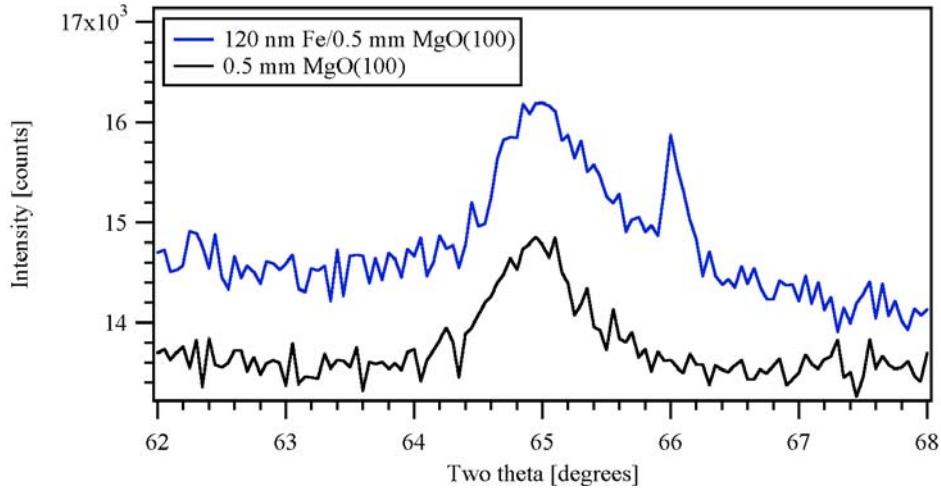


Fig. 10-8. XRD spectra of a bare 0.5 mm MgO(100) substrate and of a 0.5 mm MgO(100) substrate that was deposited with 120 nm Fe. The dwell time on these scans was 6 seconds and data were collected at each 0.05 degrees. Data are vertically offset for clarity.

The XRD spectra for an MgO(111) substrate and for an MgO(111) substrate with a 1900 nm Ce film and a 25 nm aluminum oxide window (to passivate the oxidation) are shown in Fig. 10-9. As with the Fe XRD data, these show a very close match between the bare substrates and the samples. These data show that the high energy Cu $K\alpha$ x-rays penetrate too deeply into the substrate to allow a reasonable measurement of the thin film diffraction spectrum. A Cr x-ray source is currently being acquired because the lower energy photons from the Cr will penetrate less deeply into the substrate and will increase the amount of diffraction from the film relative to the amount of diffraction from the substrate.

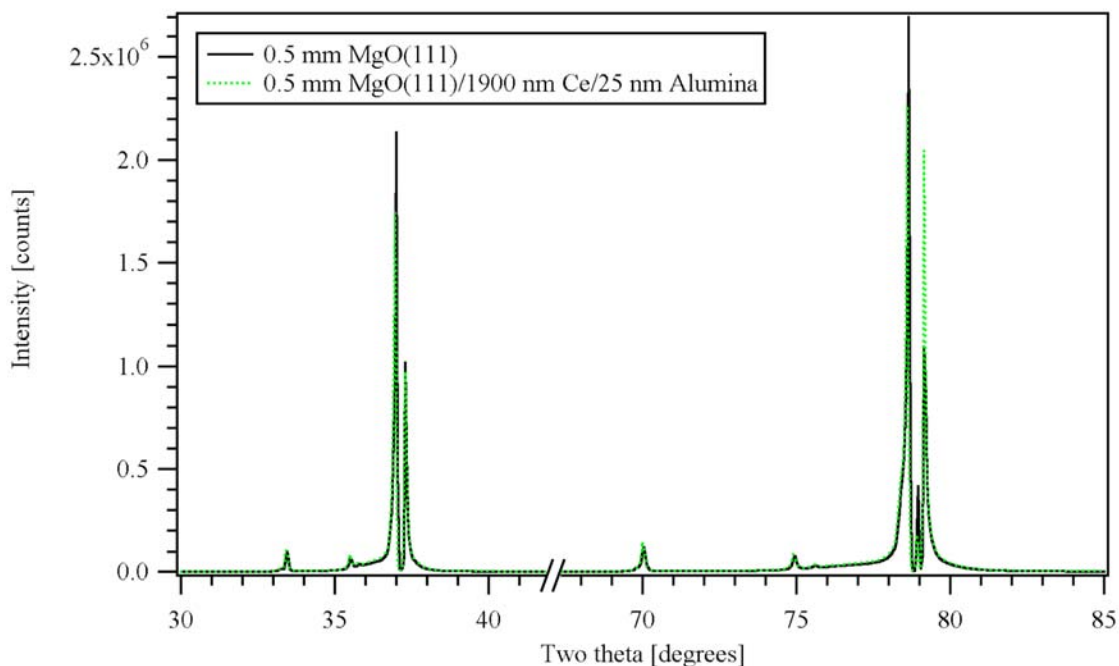


Fig. 10-9. XRD spectra of a 0.5 mm MgO(111) substrate and of a 0.5 mm MgO(111) substrate that was deposited with 1900 nm Ce and capped with 25 nm alumina to prevent oxidation of the Ce. The doublet at 38° is from MgO(111), and the doublet at 79° is from MgO(222). There are differences in the intensities of the peaks, but all of the peaks present in the Ce are also present in the spectrum of the bare MgO(111) substrate.

Since the x-rays from the Cu K α source were too penetrating to provide a clear picture of the crystalline structure of the film, orientation imaging microscopy (OIM) was tested. Orientation imaging microscopy uses a scanning electron microscope (SEM) with the electrons incident on the sample at a grazing angle, commonly 70°, to diffract electrons from the surface of the sample. The data obtained form an image containing many crossed straight lines, called an electron backscatter pattern, and analysis of the image reveals the orientation of the crystal on the surface of the sample. By scanning across the sample surface, the orientations of the various faces of the surface crystals can be obtained. This measurement was performed on both the Ce and the Fe samples, and neither of the samples showed the slightest hint of any scattered pattern.

It was possible that the crystals present in the films were of such a small size (sub-micron) that the lack of pattern was a result of too many orientations being probed at each spot. To increase the size of the crystals, the bell jar deposition system was outfitted with substrate heaters so that the samples could be grown on a high temperature substrate and so that the sample could be annealed in vacuum. The new samples were also probed with OIM and still did not show a pattern from the crystals. Currently, a Ce sample is being prepared for transmission electron microscopy (TEM), which should produce a definitive answer about the crystallinity, the orientation, and the sizes of the crystals in the metal films.

10.3.2 Preliminary UDE data

Preliminary UDE data has been recorded from both Fe and Ce while subjecting them to laser driven shock loading. Phase shift and reflectivity data for a shock in a 580 nm Fe film with a 1400 nm PMMA window is shown in Fig. 10-10. The oscillations are visible in the 25.0° phase shift data, similar to those shown in Chapter 5 for PMMA, but the rest of the data appear to be different from the PMMA data shown in Chapter 5. Most notably, the high angle reflectivity data do not have the increase in reflectivity that was shown in the data of PMMA on an Al film. As the changes in the complex refractive index of metals appear most prominently in the reflectivity data, the differences between the data of PMMA on Al and of PMMA on Fe might be showing changes in the refractive index of the Fe. However, the optical properties of Fe in the α and ϵ phases along the principle Hugoniot have been calculated with quantum MD, and they show

very little change between the α and ϵ phases at the temperature and pressure where the principle Hugoniot intersects the α - ϵ phase boundary.²¹

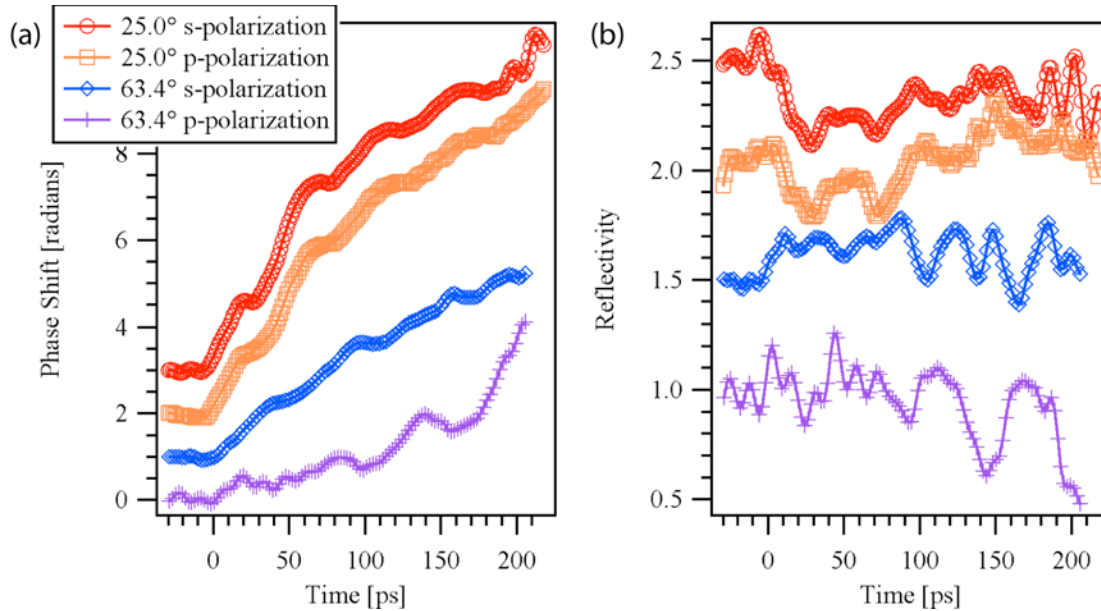


Fig. 10-10. (a) Phase shift and (b) reflectivity data from the two angles and both polarizations using UDE. The shock was created by a 3 mJ chirped pulse into a 580 nm Fe film on 0.5 mm MgO(100) and capped with 1400 nm PMMA. Data are vertically offset for clarity.

Phase shift and reflectivity data from a 1920 nm thick cerium film capped with 1440 nm Al_2O_3 are shown in Fig. 10-11. The data show some features that may result from the isomorphic phase transformation or may be a result of optical effects in the Al_2O_3 window. Further data collection on samples with known crystallinity will be required to understand the UDE data. This interpretation will also be augmented with quantum MD calculations of the optical properties of two Ce phases where the Hugoniot intersects the γ - α phase boundary.

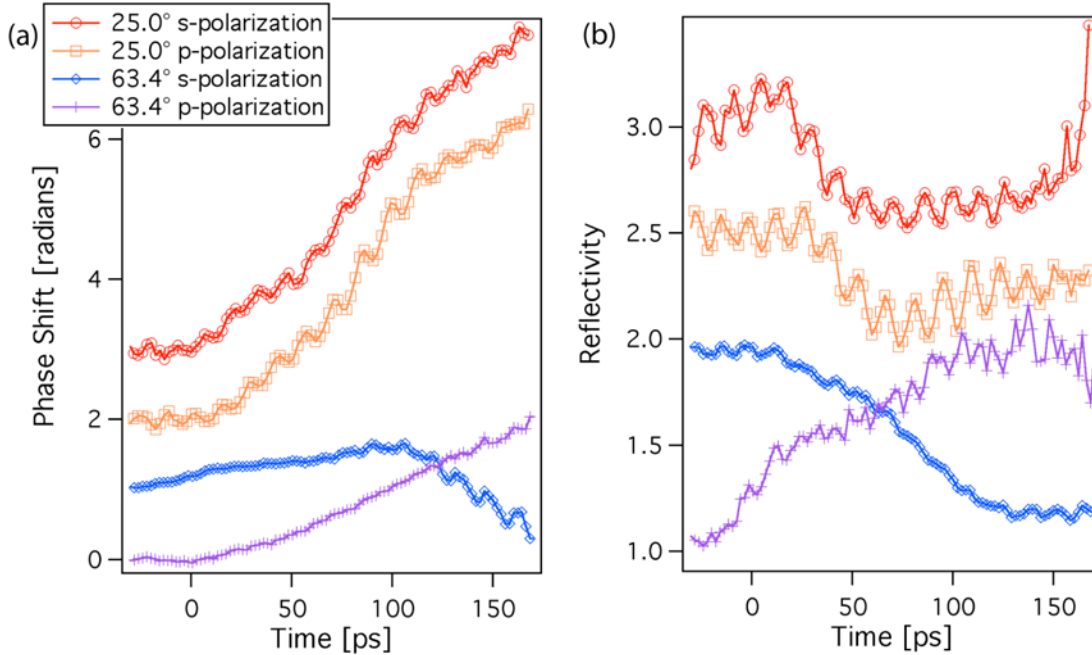


Fig. 10-11. (a) Phase shift and (b) reflectivity data from the two angles and both polarizations using UDE. The shock was created by a 0.3 mJ chirped pulse into a 1920 nm Ce film on 0.5 mm MgO(111) and capped with 1440 nm Al₂O₃. Data are vertically offset for clarity.

10.4 Discussion

Ultrafast dynamic ellipsometry has successfully determined the change in the complex refractive index of silicon during ultrafast laser induced melting.

Two solid-solid phase transformations are of particular interest, the α - ϵ transition in Fe and the γ - α transition in Ce, and both are being investigated with computational and experimental methods. Thin films of Fe and Ce were fabricated with electron beam deposition. Both XRD and OIM were unsuccessful in conclusively determining the structure of the films, and TEM studies are currently underway.

Although the measurement of the iron and cerium phase transition kinetics has not yet been accomplished, the development of UDE was critical to providing a means by

which those measurements are now accessible on time and length scales that may be readily compared to the results of MD calculations of these phenomena.

References

- 1 K. Kadau, T. C. Germann, P. S. Lomdahl, and B. L. Holian, "Microscopy view of structural phase transitions induced by shock waves," *Science* **296** (2002).
- 2 E. J. Reed, M. R. Manaa, L. E. Fried, K. R. Glaesemann, and J. D. Joannopoulos, "A transient semimetallic layer in detonating nitromethane," *Nature physics* **4**, 72-76 (2008).
- 3 D. H. Kalantar, J. F. Belak, G. W. Collins, J. D. Colvin, H. M. Davies, J. H. Eggert, T. C. Germann, J. Hawreliak, B. L. Holian, K. Kadau, P. S. Lomdahl, H. E. Lorenzana, M. A. Meyers, K. Rosolankova, M. S. Schneider, J. Sheppard, J. S. Stolken, and J. S. Wark, "Direct observation of the alpha - epsilon transition in shock-compressed iron via nanosecond X-ray diffraction," *Phys. Rev. Lett.* **95**, 075502-4 (2005).
- 4 D. L. Preston and L. Burakovsky, private communication (2008).
- 5 B. J. Jensen, private communication (2008).
- 6 C. A. Bolme, S. D. McGrane, D. S. Moore, and D. J. Funk, "Ultrafast dynamic ellipsometry of laser ablated silicon" in *High Power Laser Ablation VII*; Vol. 7005, edited by C. R. Phipps (SPIE, 2008), p. 70050M.
- 7 C. V. Shank, R. Yen, and C. Hirlimann, "Time-resolved reflectivity measurements of femtosecond-optical-pulse-induced phase transitions in silicon," *Phys. Rev. Lett.* **50**, 454-7 (1983).
- 8 T. Y. Choi, A. Chimmalgi, and C. P. Grigoropoulos, "Ultra-fast laser-induced processing of materials: Fundamentals and applications in micromachining," *Proc. SPIE Int. Soc. Opt. Eng.* **4637**, 204-211 (2002).
- 9 T. Y. Choi and C. P. Grigoropoulos, "Observation of femtosecond laser-induced ablation in crystalline silicon," *J. Heat Transfer* **126**, 723-6 (2004).
- 10 D. von der Linde and N. Fabricius, "Observation of an electronic plasma in picosecond laser annealing of silicon," *Appl. Phys. Lett.* **41**, 991-3 (1982).
- 11 K. Sokolowski-Tinten, J. Bialkowski, and D. von der Linde, "Ultrafast laser-induced order-disorder transitions in semiconductors," *Phys. Rev. B* **51**, 14186-98 (1995).
- 12 K. Sokolowski-Tinten and D. von der Linde, "Generation of dense electron-hole plasmas in silicon," *Phys. Rev. B* **61**, 2643-50 (2000).
- 13 K. Sokolowski-Tinten, A. Cavalleri, and D. von der Linde, "Single-pulse time- and fluence-resolved optical measurements at femtosecond excited surfaces," *Appl. Phys. A* **69**, 577-579 (1999).
- 14 D. von der Linde and K. Sokolowski-Tinten, "Physical mechanisms of short pulse laser ablation," *Proc. SPIE Int. Soc. Opt. Eng.* **3734**, 2-9 (1999).
- 15 K. Sokolowski-Tinten, J. Bialkowski, A. Cavalleri, and D. von der Linde, "Observation of a transient insulating phase of metals and semiconductors during short-pulse laser ablation," *Appl. Surf. Sci.* **127-129**, 755-60 (1998).
- 16 E. D. Palik, *Handbook of optical constants of solids* (Academic Press, San Diego, 1998).
- 17 K. M. Shvarev, B. A. Baum, and P. V. Gel'd, "Optical properties of liquid silicon," *Soviet physics, Solid state* **16**, 2111-2112 (1975).

- 18 J. P. Geindre, P. Audebert, S. Rebibo, and J. C. Gauthier, "Single-shot spectral
interferometry with chirped pulses," *Opt. Lett.* **26**, 1612-14 (2001).
- 19 C. A. Meserole, G. L. Fisher, D. J. Hilton, Q. X. Jia, R. D. Averitt, D. J. Funk, and
A. J. Taylor, "Fe(001) thin films for x-ray diffraction and terahertz emission
studies," *J. Vac. Sci. Technol., A* **24**, 1509-13 (2006).
- 20 C. A. Meserole, G. L. Fisher, D. J. Hilton, R. D. Averitt, D. J. Funk, and A. J.
Taylor, "Growth of thin Fe(0 0 1) films for terahertz emission experiments,"
Appl. Surf. Sci. **253**, 6992-7003 (2007).
- 21 S. Mavezet, private communication (2007).

This work was performed at Los Alamos National Laboratory under the auspices of the U.S. Department of Energy under contract DE-AC52-06NA25396.

Cynthia A Bolme

Education: **Massachusetts Institute of Technology** - Sept 2002 – Sept 2008
Ph.D. Physical Chemistry

University of California, San Diego - Sept 1999-June 2002
B.S. Chemistry, *Summa Cum Laude*

Research Experience:

Los Alamos National Laboratory

Jan 2005 – Aug 2008 Graduate Research Assistant; MIT Non-Resident Doctoral Research
Investigated the temporal shaping of laser driven shock waves using layered metal targets.
Developed ultrafast dynamic ellipsometry using chirped pulse interferometry to measure the optical properties and material motion of shocked materials in a single shot.
Rebuilt a vacuum electron beam deposition system with enhanced deposition capabilities and control.

Massachusetts Institute of Technology

Jun 2003 - Jan 2005 Research Assistant, MIT Institute of Soldier Nanotechnology
Designed and set up a new laser lab to study the mechanical response of viscoelastic polymers to laser-driven shock waves using impulsive stimulated thermal scattering.
Sept 2002 - June 2003 Teaching Assistant
Principles of Chemical Science (5.112)
Intermediate Chemical Experimentation (5.32)

Los Alamos National Laboratory

Jun 1999 - Aug 2002 (summers & college breaks) Undergraduate Research Assistant, High Explosives Science and Technology
Investigated combustion properties of traditional high explosives and of new high nitrogen energetic materials.

Honors, Fellowships and Awards:

NNSA Defense Programs Award of Excellence 2005--“Ultrafast Dynamic Ellipsometry”
Harold C. Urey Award for Outstanding Scholarship in Chemistry, awarded for the most outstanding scholarship among graduating chemistry majors, UCSD, June 2002
G.T. Seaborg Institute for Transactinium Science Fellow and Fellowship, 2001 & 2002

Selected Publications:

- C. A. Bolme, S. D. McGrane, D. S. Moore, and D. J. Funk, "Ultrafast dynamic ellipsometry of laser ablated silicon" in *High Power Laser Ablation VII*; Vol. 7005, edited by C. R. Phipps (SPIE, 2008), p. 70050M.
- C. A. Bolme and D. J. Funk, "Ultrafast dynamic ellipsometry measurements of early time laser ablation of titanium thin films," *Appl. Phys. A* (2008).
- C. A. Bolme, "Single shot dynamic ellipsometry measurements of laser-driven shock waves" in *Shock Compression of Condensed Matter--2007*; Vol. 955, edited by M. L. Elert, M. D. Furnish, R. Chau, N. C. Holmes, and J. Nguyen (American Institute of Physics, Melville, NY, 2007), p. 1211-16.
- S. A. Clarke, C. A. Bolme, M. J. Murphy, C. D. Landon, K. A. Thomas, T. A. Mason, R. J. Adrian, A. A. Akinci, and M. E. Martinez, "Using schlieren visualization to track detonator performance" in *Shock Compression of Condensed Matter--2007*, edited by M. L. Elert, M. D. Furnish, R. Chau, N. C. Holmes, and J. Nguyen (American Institute of Physics, Melville, NY, 2007), p. 1089-1092.
- C. A. Bolme, S. D. McGrane, D. S. Moore, and D. J. Funk, "Single shot measurements of laser driven shock waves using ultrafast dynamic ellipsometry," *J. Appl. Phys.* **102**, 033513-8 (2007).
- D. S. Moore, C. A. Bolme, S. D. McGrane, and D. J. Funk, "Single pulse ultrafast dynamic ellipsometry," in *High Power Laser Ablation VI*; Vol. 6261I, edited by C. R. Phipps (SPIE, 2006).